https://doi.org/10.15388/vu.thesis.215
https://orcid.org/0000-0001-8505-3686

VILNIUS UNIVERSITY
CENTER FOR PHYSICAL SCIENCES AND TECHNOLOGY

Lauryna
KAVALIAUSKIENĖ

# Tricalcium phosphate polymorphs: The role of ionic substitutions and processing conditions on phase-selective synthesis and properties

**DOCTORAL DISSERTATION**

Natural sciences,
Chemistry (N 003)

VILNIUS 2021

This dissertation was written between 2017 and 2021 at Vilnius University.

**Academic supervisor – Assist. Prof. Dr. Aleksej Žarkov** (Vilnius University, Natural sciences, Chemistry – N 003).
**Academic consultant – Prof. Dr. Stasys Tautkus** (Vilnius University, Natural sciences, Chemistry – N 003).

This doctoral dissertation will be defended in a public meeting of the Dissertation Defence Panel:
**Chairman** – **Prof. Habil. Dr. Audrius Padarauskas** (Vilnius University, Natural Sciences, Chemistry **–** N 003).
**Members:**
**Prof. Dr. Jurgis Barkauskas** (Vilnius University, Natural Sciences, Chemistry – N 003);
**Prof. Dr. Almira Ramanavičienė** (Vilnius University, Natural sciences, Chemistry – N 003);
**Dr. Loreta Tamašauskaitė-Tamašiūnaitė** (Center for Physical Sciences and Technology, Natural Sciences, Chemistry – N 003);
**Prof. Dr. Tomas Tamulevičius** (Kaunas University of Technology, Technological Sciences, Materials Engineering – T 008).

The dissertation shall be defended at a public meeting of the Dissertation Defence Panel at 2 pm on 24th of September 2021 in Inorganic Chemistry auditorium 141 of the Faculty of Chemistry and Geosciences, Vilnius University.
Address: Naugarduko st. 24, Vilnius, Lithuania
Tel. +37052193105; e-mail: info@chgf.vu.lt

The text of this dissertation can be accessed at the libraries of Vilnius University and Center for Physical Sciences and Technology, as well as on the website of Vilnius University:
*www.vu.lt/lt/naujienos/ivykiu-kalendorius*

https://doi.org/10.15388/vu.thesis.215
https://orcid.org/0000-0001-8505-3686

VILNIAUS UNIVERSITETAS
FIZINIŲ IR TECHNOLOGIJOS MOKSLŲ CENTRAS

Lauryna
KAVALIAUSKIENĖ

# Trikalcio fosfato polimorfai: jonų pakaitų ir sintezės sąlygų įtaka faziškai selektyviai sintezei ir savybėms

**DAKTARO DISERTACIJA**

Gamtos mokslai,
Chemija (N 003)

VILNIUS 2021

Disertacija rengta 2017 – 2021 metais Vilniaus universitete.

**Mokslinis vadovas – dr. Aleksej Žarkov** (Vilniaus universitetas, gamtos mokslai, chemija – N 003).
**Mokslinis konsultantas – prof. dr. Stasys Tautkus** (Vilniaus universitetas, gamtos mokslai, chemija – N 003).

Gynimo taryba:
Pirmininkas – **prof. habil. dr. Audrius Padarauskas** (Vilniaus universitetas, gamtos mokslai, chemija – N 003).
Nariai:
**prof. dr. Jurgis Barkauskas** (Vilniaus universitetas, gamtos mokslai, chemija – N 003);
**prof. dr. Almira Ramanavičienė** (Vilniaus universitetas, gamtos mokslai, chemija – N 003);
**dr. Loreta Tamašauskaitė-Tamašiūnaitė** (Fizinių ir technologijos mokslų centras, gamtos mokslai, chemija – N 003);
**prof. dr. Tomas Tamulevičius** (Kauno technologijos universitetas, technologijos mokslai, medžiagų inžinerija – T 008).

Disertacija ginama viešame Gynimo tarybos posėdyje 2021 m. rugsėjo mėn. 24 d. 14 val. Vilniaus universiteto Chemijos ir geomokslų fakulteto Neorganinės chemijos auditorijoje. Adresas: Naugarduko g. 24, Vilnius, Lietuva, tel. +37052193105; el. paštas info@chgf.vu.lt.

Disertaciją galima peržiūrėti Vilniaus universiteto, Fizinių ir technologijos mokslų centro bibliotekose ir VU interneto svetainėje adresu: *https://www.vu.lt/naujienos/ivykiu-kalendorius*

TABLE OF CONTENTS

# LIST OF ABBREVATIONS

ACP – Amorphous Calcium Phosphate

AC – Acetone

ACN – Acetonitrile

CDHA – Calcium Deficient Hydroxyapatite

CHAp – Calcium Hydroxyapatite

CP – Calcium Phosphate

DCS – Decomposition Combustion Synthesis

DTA – Differential Thermal Analysis

DTG – Derivative Thermogravimetry

EPR – Electron Paramagnetic Resonance

EtOH – Ethanol

FTIR – Fourier Transform Infrared Spectroscopy

ICP-OES – Inductively Coupled Plasma Optical Emission Spectrometry

i-PrOH – Isopropanol

PL – Photoluminescence

SBF – Simulated Body Fluid

SEM – Scanning Electron Microscopy

SHS – Self-propagating High Temperature Synthesis

TG – Thermogravimetric Analysis

XRD – X-Ray Diffraction

TCP – Tricalcium Phosphate

# INTRODUCTION

It is a well-known fact that human life expectancy and a number of elderly people have steadily increased due to better medical care and living conditions. However, aging people tend to have more bone related diseases such as bone cancer or osteoporosis [1]. Since elderly people have weaker bones due to the bone mass loss and decrease in bone density, the risk of fracture in bone markedly increases. For example, in 1990, there were 1.6 million hip fractures per year worldwide and this number is expected to reach 6 million by 2050. Due to the increase in these musculoskeletal disorders, governments have to spend more money each year on healthcare [2, 3].

Normally, after minor fractures the bone repairs by itself. Depending on bone defect size, lacking blood flow or infection injured the bone may not be capable to repair by itself. Nonuous bone fractures or large bone voids supposed to be treated using autographs harvested from patients own bone or using artificial bone substitutes [4, 5]. The ideal synthetic material to replace bone tissue should be biocompatible, bioresorbable, osteoconductive, osteoinductive, structurally similar to bone, porous, mechanically resistant, easy to use, safe, and cost-effective [6, 7].

Nowadays, many synthetic bone substitutes such as bioglasses, calcium sulphate, calcium phosphate (CP) ceramics or cements or even polymer-based substitutes are used for bone defect healing. Due to the reason that about two thirds of human bone are made of carbonated calcium hydroxyapatite various CPs are often chosen as a material for bone defect healing. CPs are getting a lot of attention in medicine and dentistry as bone substitute materials because of their positive *in vivo* responses like biocompatibility, bioactivity, osteoconductivity and relatively low cost [8]. For medical purposes, CPs can be used in different forms varying from thin coatings on metallic implants, used to aid implant fixation into bone, to sintered bioceramics, to be used as synthetic bone graft substitutes [9-11].

One of the most remarkable CPs, which is widely used in regenerative medicine, is tricalcium phosphate ($Ca_3(PO_4)_2$, TCP). This material has two stable polymorphs: α- and β-TCP. They both have same chemical composition, but due to the different crystal structure, density and solubility, more reactive α-TCP is usually used as powder component of CP-based bone cements while β-TCP – as biodegradable ceramics [12]. Both TCP polymorphs cannot be naturally precipitated under physiological conditions, but they can be prepared by different chemical routes. Taking into account a broad variety of different CPs, the synthesis conditions play a crucial role in the formation of the final product. For specific application of CPs, it is very

important to develop phase-selective synthesis methods in order to achieve aspired structure with minimal amount of impurity phases [13].

Partial substitution of Ca ions by other biologically active ions is assumed to be a promising tool to superior biological properties of synthetic CPs. It is well known that presence of foreign ions in CP matrix can modify significantly physicochemical, mechanical and anti-bacterial properties of materials, to promote changes in morphology, solubility and kinetics of ion release. Therefore, partial substitution of $Ca^{2+}$ ions in CP matrix by biologically active inorganic ions is a promising strategy to improve bone defect healing [9, 14, 15]. Moreover, substitution-induced properties allow to combine biocompatibility of CPs with newly obtained properties resulting in application of these materials in new areas such as various imaging modalities including fluorescence, magnetic resonance or multimodal imaging, as well as for various therapeutic approaches including chemotherapy, gene therapy, hyperthermia or combination therapy [16].

The purpose of this study was to investigate the influence of selected ionic substitutions and processing conditions on the phase-selective synthesis and properties of TCP polymorphs. In order to achieve this goal, the following tasks were formulated:

- to evaluate the effect of synthesis conditions on phase-selective synthesis of TCP polymorphs by wet precipitation method;
- to investigate the influence of Mn doping on the phase-selective synthesis of TCP polymorphs;
- to examine the influence of Mn doping on hydrolysis rate of low-temperature synthesized metastable α-TCP;
- to investigate the luminescent properties high-temperature synthesized Mn-doped α-TCP;
- to investigate the influence of divalent cations of different size (Mg, Zn, Sr, and Ba) on thermally induced crystallization and phase evolution of ACP;
- to investigate the effect of Fe and Zn co-substitution on structural, magnetic, mechanical and biological properties of β-TCP.

# 1. LITERATURE SURVEY

## 1.1. Human bone

Bone is a rigid yet lightweight, self-healing organ with a unique organic-inorganic composition. In human body, it is responsible for several physiological functions including facilitation of movement, support and protection of other internal organs, blood production, mineral storage and homeostasis, blood pH regulation and others [5, 17]. The properties of bone depend on macro-, micro- and nano- hierarchical structure. The macroscale organization of osteons, osteoids, and haversian canals is responsible for providing long bones with their characteristic mechanical anisotropy. The microscale porosity of bone is suitable for cell migration and vascularization, whereas the nanoscale features are responsible for cell and mineral binding structure. The hierarchical structure of bone is shown in Fig. 1 [5, 18].

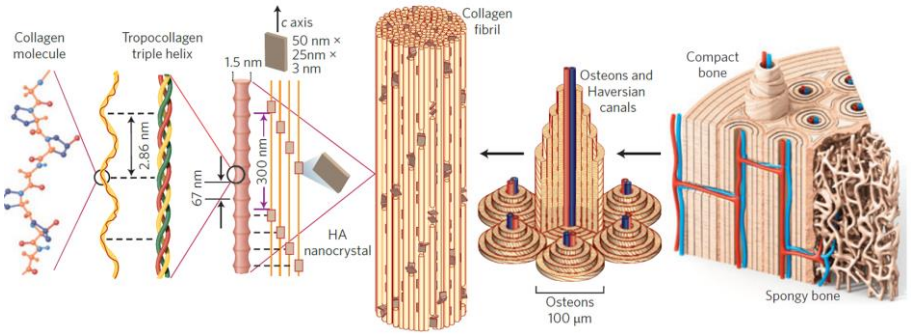


Fig. 1. The hierarchical structure of natural bone [18].

The main constituents of human bones are CPs (~60–70 wt%), collagen (~20–30 wt%), cells, lipids and water (up to 10 wt%) [19, 20]. In general, bone is composed of highly ordered sequence of mineralized collagen fibrils. Collagen fibrils are composed of ~300 nm long, ~1.5 nm in diameter collagen molecules (mainly type-I collagen) and plate-shaped, 50 nm × 25 nm in size, 1.5–4 nm thick biological apatite nanocrystals, which are oriented *c*-axis parallel collagen fibril and possess periodic arrangement [18]. The chemical composition of bone is shown in Table 1 [21-23].

Table 1. Chemical composition of bone [23]

| Inorganic part | Organic part |
|---|---|
| CHAp (~60 wt%) | Collagen (~20 wt%) |
| $H_2O$ (~9 wt%) | Non-collagenous proteins: osteocalcin, osteonectin, osteopontin, sialoprotein, thrombospondin, morphogenetic proteins, serum proteins (~3 wt%) |
| $CO_3^{2-}$ (~4 wt%) | |
| Citrate (~0.9 wt%) | |
| $Na^+$ (~0.7 wt%) | |
| $Mg^{2+}$ (~0.5 wt%) | |
| $Cl^-$ (~0.13 wt%) | Traces: polysaccharides, lipids, cytokines. |
| Others: $K^+$, $F^-$, $OH^-$, $Zn^{2+}$, $Fe^{2+}$, $Cu^{2+}$, $Sr^{2+}$, $Pb^{2+}$, $Mn^{2+}$, $Cr^{3+}$ | Primary bone cells: osteoblasts, osteocytes, osteoclasts |

The inorganic part of bone consists of biological apatite – a non-stoichiometric, low-crystalliny calcium hydroxyapatite ($Ca_{10}(PO_4)_6(OH)_2$, CHAp) substituted with different ions, which is the main reason of non-stoichiometry of CHap in hard tissue. $Ca^{2+}$ can be partially replaced by other metal ions including $Mg^{2+}$, $Sr^{2+}$, $K^+$, $Zn^{2+}$, etc., while $OH^-$ and $PO_4^{3-}$ may be partly replaced by $F^-$, $Cl^-$, $CO_3^{2-}$ and $HPO_4^{2-}$. The $OH^-$ site also can be left vacant [24]. The main substituting ions are $CO_3^{2-}$, $Mg^{2+}$, and $HPO_4^{2-}$, along with other trace elements their content depends on diet, age, diseases and bone condition [20, 25, 26]. The $CO_3^{2-}$ amount in human hard tissue varies from 4 to 8 wt%. This ion can substitute CHAp in two anionic sites: at $OH^-$ (A-type carbonation) and at $PO_4^{3-}$ sites (B-type carbonation) [27]. The average composition of bone can be represented by the following formula $Ca_{8.3}(PO_4)_{4.3}(CO_3)_x(HPO_4)_y(OH)_{0.3}$, where y decreases and x increases with age and the sum of x and y is 1.7 [28, 29].

The organic part is made of collagen, other non-collagenous proteins, polysaccharides, lipids, cytokines and primary bone cells including osteoblasts, octeoclasts and osteocytes [25, 29]. About 90% of organic matrix of hard tissue is made of type-I collagen, 5% of non-collagenous proteins (NCPs) and 2% of lipids. Looking from physiological point of view, inorganic part of bones is responsible for their toughness and the ability to withstand pressure, while the organic part of bones provides elasticity and resistance to stress, bending and fracture.

Bone tissue continuously undergoes growth, repair and renewal processes during resorption by cells called osteoclasts and formation by type of cells called osteoblasts. The main purpose of remodeling is calcium and phosphorus homeostasis and the repair of micro-damaged bones from everyday stress. Firstly, bone remodeling starts with differentiation and migration of osteoclasts to discrete bone surface, where bone dissolution caused by

secreted enzymes begins. Osteoblasts are responsible for the synthesis of new collagenous organic matrix and regulation of matrix mineralization by releasing small, membrane-bound matrix vesicles that concentrate calcium and phosphate ions and enzymatically demolish mineralization inhibitors. Osteoblasts become partly entrapped inside the mineralized tissue and become osteocytes, which are bone-lining cells that regulate bone resorption and formation processes [19, 30, 31]. Bone remodeling process is given in Fig. 2 [32].

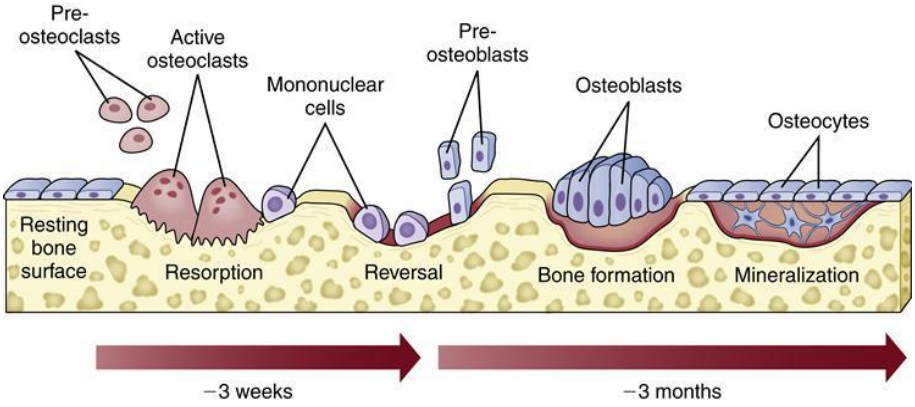


Fig. 2. Bone remodeling process [32].

Sometimes bones are not able to heal themselves, because of huge voids resulting from traumas, bone cancer, teeth removal, etc. Due to these reasons, the need of bone substitute materials like CPs is becoming essential for bone remodeling.

## 1.2. Calcium phosphates

CPs are minerals composed of calcium cations and phosphate anions such as $H_2PO_4^-$, $HPO_4^{2-}$ and $PO_4^{3-}$. CP that also contains $OH^-$, belongs to the apatitic CaP family and is known as calcium hydroxyapatite (CHAp) [33]. In CHAp the $OH^-$ ions can be substituted by $F^-$ or $Cl^-$ ions forming fluorapatite ($Ca_{10}(PO_4)_6F_2$) and chlorapatite ($Ca_{10}(PO_4)_6Cl_2$), respectively. Whereas biological CPs are the main inorganic part of biological hard tissues such as bones or teeth, synthetic CPs are also known for their biocompatibility, bioactivity, nontoxicity and osteoconductivity. Due to this reason different synthetic CPs have been used as bone substitutes for the reconstruction of bone defect in oral implantology, periodontology, oral and maxillofacial

surgery as well as orthopedics in a form of bone grafts, bone fillers and coating materials [26].

Among the most important parameters of CPs are molar Ca/P ratio, basicity or acidity and solubility. The lower the Ca/P molar ratio is, the more acidic and water-soluble the CP is. Usually, Ca/P molar ratio in CPs varies from 0.5 to 2.2. Due to the large number of possible combinations of calcium and phosphate ions, there is a broad variety of different CPs. The most popular non-ion-substituted CPs that are used in medicine are shown in Table 2 [19, 34, 35].

Table 2. The most popular CPs used in medicine [34].

| Compound | Chemical formula | Ca/P ratio | Solubility at 25°C, -log($K_s$) |
|---|---|---|---|
| Monocalcium phosphate monohydrate (MCPM) | $Ca(H_2PO_4)\cdot H_2O$ | 0.5 | 1.14 |
| Monocalcium phosphate anhydrous (MCPA) | $Ca(H_2PO_4)_2$ | 0.5 | 1.14 |
| Dicalcium phosphate dihydrate (DCPD) | $CaHPO_4\cdot 2H_2O$ | 1.0 | 6.59 |
| Dicalcium phosphate anhydrous (DCPA) | $CaHPO_4$ | 1.0 | 6.90 |
| Octacalcium phosphate (OCP) | $Ca_8(HPO_4)_2(PO_4)_4\cdot 5H_2O$ | 1.33 | 96.6 |
| α-tricalcium phosphate (α-TCP) | $\alpha\text{-}Ca_3(PO_4)_2$ | 1.5 | 25.5 |
| β-tricalcium phosphate (β-TCP) | $\beta\text{-}Ca_3(PO_4)_2$ | 1.5 | 28.9 |
| Amorphous calcium phosphate (ACP) | $Ca_xH_y(PO_4)_z\cdot nH_2O$ n=3-4.5, 15-20% $H_2O$ | 1.2-2.2 | * |
| Calcium-deficient hydroxyapatite (CDHA) | $Ca_{10-x}(HPO_4)_x(PO_4)_{6-x}(OH)_{2-x}$ (0<x<1) | 1.5-1.67 | ~85.1 |
| Hydroxyapatite (CHAp) | $Ca_{10}(PO_4)_6(OH)_2$ | 1.67 | 116.8 |
| Tetracalcium phosphate (TTCP) | $Ca_4(PO_4)_2O$ | 2.0 | 38-44 |

*Cannot be measured precisely. However, the following values were found: 25.7 ± 0.1 (pH = 7.40), 29.9 ± 0.1 (pH = 6.00), 32.7 ± 0.1 (pH = 5.28)

Structural and compositional differences between the CPs lead to the different properties such as density, solubility, biodegradability and reactivity under physiological conditions, which determine their biological properties and clinical applications [12]. For the first time, the differences between α-

and β-TCP were distinguished in 1932 [36]. All structural differences between α-, β-TCP and ACP will be discussed in detailed in the following chapters.

## 1.3. Tricalcium phosphate

There are two known room temperature stable TCP polymorphs: the low-temperature β-TCP and the high-temperature α-TCP. Moreover, there is α'- TCP polymorph, but it is not suitable for practical application, because it only exists at temperatures between ~1450 °C and its melting point (~1756 °C). To distinguish phase relationship between α- and β-TCP phases an anhydrous $CaO-P_2O_5$ phase diagram at temperatures within the range of 200-2200 °C was proposed (Fig. 3) [36].

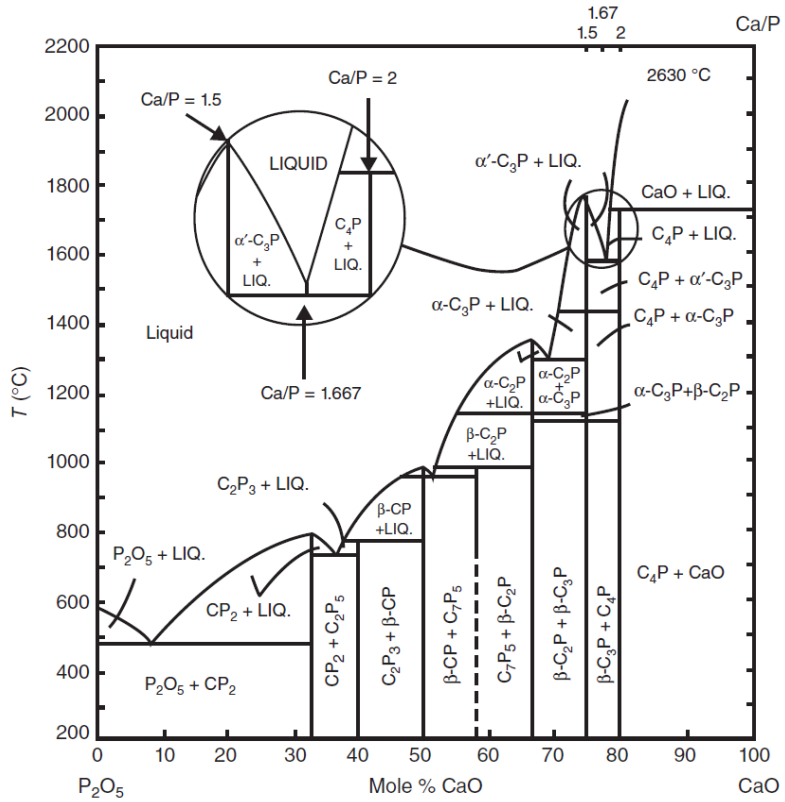


Fig. 3. Phase diagram of the system $CaO-P_2O_5$ at elevated temperatures, where C=CaO, P=$P_2O_5$ [36].

### 1.3.1. Crystal structure of α-TCP

The crystal structure of α-TCP for the first time was described in detail by Mathew et al. [37] in 1977. The α-TCP crystallizes in the monoclinic structure with a space group $P2_1/a$ and lattice parameters $a$=12.887(2) Å, $b$=27.280(4) Å, $c$=15.219(2) Å, $\alpha=\gamma=90°$ and $\beta$=126.20(1)°. The unit cell contains 312 atoms and 24 $Ca_3(PO_4)_2$ formula units, where the number of existing independent sites are 18 for calcium, 12 for phosphorus and 48 for oxygen [37, 38]. Each formula unit occupies 180 $Å^3$, theoretical density is 2.866 g $cm^{-3}$ and cell volume is 4310 $Å^3$. [39]. The crystal structure of α-TCP is demonstrated in Fig. 4 [38].

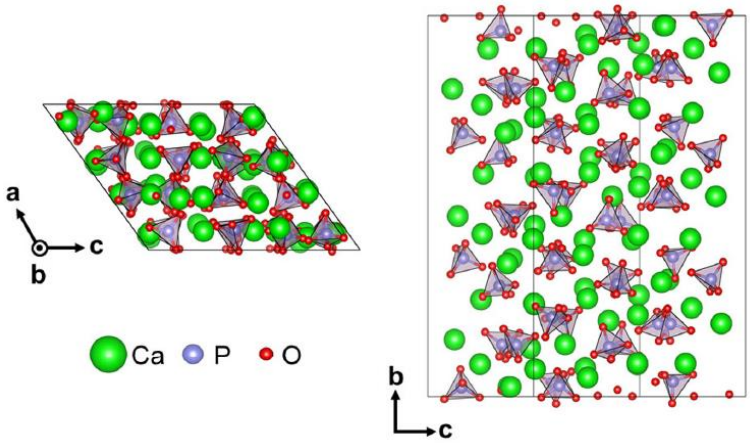


Fig. 4. The crystal structure of α-TCP. The $PO_4^{3-}$ groups are represented by tetrahedra [38].

The crystal lattice of α-TCP consists of calcium and phosphate ions, which are packed in two sorts of ion columns along the [001] direction. The first one contains only $Ca^{2+}$ ions (cation-cation column, C-C) and another – $Ca^{2+}$ and $PO_4^{3-}$ ions (cation-anion column, C-A). In the C-A column calcium and phosphate ions are packed in the following order: $PO_4^{3-}$, $Ca^{2+}$, $PO_4^{3-}$, vacancy, $PO_4^{3-}$, $Ca^{2+}$, $PO_4^{3-}$, vacancy, etc. Schematic representation of the projection of the α-TCP unit cell along the [001] direction is depicted in Fig. 5 [12, 38].

Calcium ions have a wide range of coordination numbers and geometries making α-TCP structure quite complex. In the C-A column Ca ions have at least 7 oxygen neighbors and the most frequently observed geometry is pentagonal bipyramids. Furthermore, in the C-C column Ca ions have coordination numbers from 5 to 7 and the most often observed configuration is 7 oxygen atoms arranged in an irregular polyhedron. These columns are arranged to form a pseudohexagonal pattern: each C-C column is surrounded

by 6 C-A columns and each C-A column is surrounded by alternating C-C and C-A columns [37, 39]. Similar arrangement can be seen in mineral glaserite ($K_3Na(SO_4)_2$) structure or even in other biomaterial – CHAp [40]. The dashed line rhombus in Fig. 5 outlines a cell related to the apatite structure, which can be obtained from α-TCP by replacing the C-C columns at the cell corners of the apatite cell by $OH^-$. Comparably, the C-A columns in CHAp may be considered as very distorted C-A columns, where each column is surrounded by 3 C-A columns as in α-TCP, and by 2 C-C and 1 $OH^-$ columns [33, 37].

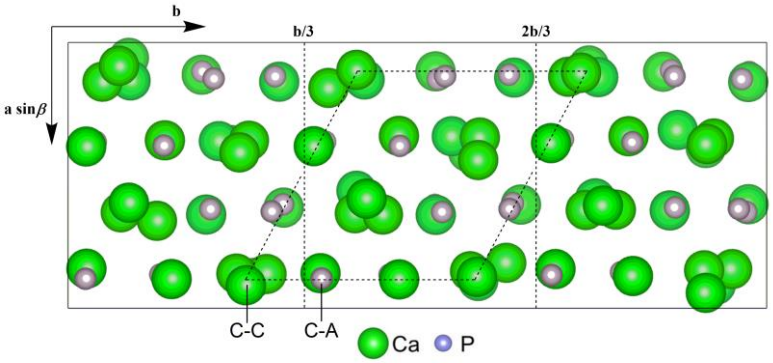


Fig. 5. Schematic representation of the projection of the α-TCP unit cell along the [001] direction. The dashed line outline the apatite unit cell [33].

### 1.3.2. Synthesis of α-TCP

Neither of TCP polymorphs cannot be precipitated directly from aqueous solution under physiological conditions, therefore this material cannot be found in biological tissues. Nevertheless, TCP can be prepared employing different synthetic methods. For instance, high-temperature or low-temperature metastable α-TCP can be obtained by the following approaches:

- Thermal transformation of precursors;
- Solid-state synthesis;
- Self-propagating high temperature synthesis (SHS);
- Decomposition combustion synthesis (DCS) [12, 26].

The α-TCP is usually prepared by thermal treatment of a precursor with a molar ratio of Ca/P ≈ 1.5 (CDHA, ACP or β-TCP). Precursors are usually synthesized from $Ca(NO_3)_2$ and $(NH_4)_2HPO_4$ at alkaline pH by wet precipitation method [41, 42]. Thermally induced transformations of CDHA, ACP and β-TCP into α-TCP are given in Equations 1-3, respectively.

$$Ca_9(HPO_4)(PO_4)_5(OH) \xrightarrow{\geq 1150\ ^\circ C} 3\alpha\text{-}Ca_3(PO_4)_2 + H_2O \quad (1)$$

$$Ca_9(PO_4)_6 \cdot nH_2O \xrightarrow{600-700\ ^\circ C} 3\alpha\text{-}Ca_3(PO_4)_2 + nH_2O \quad (2)$$

$$\beta\text{-}Ca_3(PO_4)_2 \xrightarrow{1125-1430\ ^\circ C} \alpha\text{-}Ca_3(PO_4)_2 \quad (3)$$

Both decomposition of CDHA [43-46] and ACP [47-49] can be applied in order to obtain α-TCP. However, high temperature β- to α-TCP crystalline phase transition is the most direct, cheapest and probably the simplest way to synthesize α-TCP [12, 50-52]. It can be seen (Fig. 5) that β- to α-TCP transition temperature is about 1125 °C, however, calcination is usually performed at temperatures above 1200 °C [36]. Due to the reason that this transition is reversible and highly sensitive to impurities, the thermal quenching is often required in order to stabilize α-TCP phase [53, 54]. Even though β-TCP is assumed to be a low-temperature polymorph, upon heating ACP first crystallizes to low-temperature metastable α-TCP. This process is in agreement with Ostwald step rule, according to which crystallization often occurs in such a way that thermodynamically less stable phase is obtained first, followed by thermodynamically more stable [55, 56].

Most commonly used solid-state reaction scheme consists of few steps: milling the powder mixture, putting the ground mixture under pressure and heating it. The first two stages are required to reduce the particle size, mix them homogeneously and increase the contact area. After milling, the mixture of powders or previously pressed pellet may be directly heated above the β- to α-TCP transformation temperature. The recommended temperature ranges from 1250 to 1500 °C and the sintering time may vary from 2 to 48 h. To avoid the reversion of the crystal phase, thermal quenching is often employed. The most frequently applied synthesis routes are given in Equations 4-7 [57-71].

$$CaCO_3 + 2CaHPO_4 \rightarrow \alpha\text{-}Ca_3(PO_4)_2 + CO_2 + H_2O \quad (4)$$

$$3CaCO_3 + 2NH_4H_2PO_4 \rightarrow \alpha\text{-}Ca_3(PO_4)_2 + 3CO_2 + 3H_2O + 2NH_3 \quad (5)$$

$$CaCO_3 + Ca_2P_2O_7 \rightarrow \alpha\text{-}Ca_3(PO_4)_2 + CO_2 \quad (6)$$

$$Ca_{10}(PO_4)_6(OH)_2 + 2CaHPO_4 \rightarrow 4\alpha\text{-}Ca_3(PO_4)_2 + 2H_2O \quad (7)$$

There are also other, less popular α-TCP preparation techniques like SHS and DCS. They are based on preparation of a solid pellet or solution, containing a mixture of Ca and P precursors, which is exposed to thermal treatment. For SHS, the heat is applied from an external source like heating a

tungsten filament to the point of igniting the bottom of the reactant pellet, while in case of the DCS, the reagent mixture contains an organic, inflammable fuel that acts as a catalyst for the self-combustion of the mixture [12, 26, 72]. SHS synthesis was applied by R. Ayers et al. [73] using CaO and $P_2O_5$ as starting materials, as a result α-TCP containing significant amounts of CHAp and β-TCP was obtained.

For DCS $Ca(NO_3)_2$ and $(NH_4)_2HPO_4$ were used as primary reactants, while third component urea during the decomposition energetically sustained the reaction. This synthesis method was employed by Volkmer et al. [74, 75].

### 1.3.3. Application of α-TCP

Structural differences between TCP polymorphs are responsible for their different chemical and biological properties, such as solubility and biodegradability [12]. These differences in chemical properties of TCP polymorphs define their practical applications. The α-TCP is more reactive in aqueous systems, it has higher specific energy and in aqueous medium it easily hydrolyzes to CDHA (Eq. 8), which is similar to bone CHAp [21, 36, 76].

$$3\alpha - Ca_3(PO_4)_2 + H_2O \rightarrow Ca_9(HPO_4)(PO_4)_5(OH) \quad (8)$$

Both TCP polymorphs promote bone growth where implanted and support the proliferation of fibroblasts, osteoblasts and other bone cells [77]. In medicine, α-TCP is widely used as a major powder component of various bone cements due to its biocompatibility and biodegradability. The biggest advantages of these cements, that they are injectable, easily shaped, harden inside the damaged bone tissue and generate low heat transfer to CDHA that avoids the premature death of surrounding cells [57]. Mostly, α-TCP ceramics are used for bone substitution and scaffold for tissue engineering, when higher bioresorbability (higher degradation rate in the body can be expected) is required compared to that of β-TCP. However, chemically pure α-TCP ceramics due to its quick resorption compared to the bone formation rate and poor mechanical properties, which limit its application in load bearing situations, is less applied in regenerative medicine compared to other CP-based ceramics [78-80]. Moreover, α-TCP can be used in agriculture as a slow release fertilizer for acidic soils [36].

### 1.3.4. Crystal structure of β-TCP

The structure of pure β-TCP was determined by single-crystal XRD by Dickens et al. [81] in 1974 and almost 30 years later using neutron powder diffraction confirmed by Yashima et al. [82]. The β-TCP crystallizes in the rhombohedral structure with a space group *R*3*c* and unit-cell parameters $a=b=10.4352(2)$ Å, $c=37.4029(5)$ Å, $\alpha=\beta=90°$ and $\gamma=120°$ in the hexagonal setting [81, 82]. Unit cell contains 21 formula units. Each formula unit occupies 168 $Å^3$, theoretical density is 3.066 g $cm^{-3}$ and cell volume is 3527 $Å^3$. The total number of atoms in the hexagonal unit cell is 273. There are 5 inequivalent sites for calcium, 3 for phosphorus and 10 for oxygen. The crystal structure of β-TCP is shown in Fig. 6 [38].

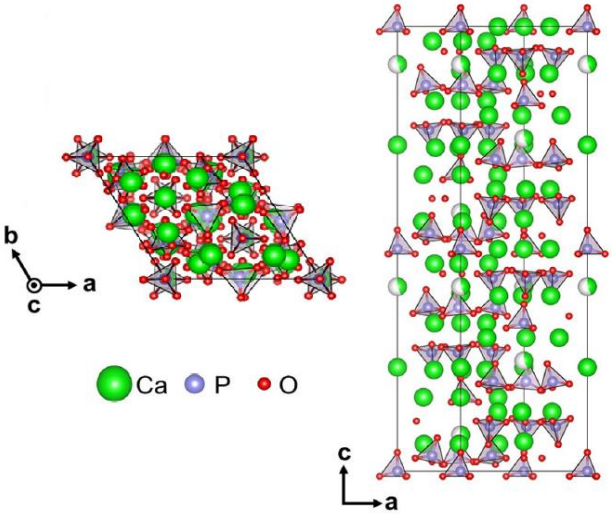


Fig. 6. The crystal structure of β-TCP. The $PO_4^{3-}$ groups are represented by tetrahedra [38].

The crystal structure of β-TCP consists of two type of columns (A and B), which are aligned along the *c*-axis. Column A contains the Ca(4) and the Ca(5) sites, whereas the sites Ca(1), Ca(2) and Ca(3) are coordinated in column B. Column A has a form of $\cdots P(1)O_4\ Ca(4)O_3\ Ca(5)O_6\ P(1)O_4\cdots$, while more densely packed column B $\cdots P(3)O_4\ Ca(1)O_7\ Ca(3)O_8\ Ca(2)O_8\ P(2)O_4\ P(3)O_4\cdots$. Each A column is surrounded by six B columns, while column B by 2 A and 4 B columns. In the A column all the *x* and *y* atomic coordinates of Ca(4), Ca(5) and P(1) have the value of zero, showing that these atoms are located on the straight line. Meanwhile, in the column B the *x* and *y* atomic coordinates of Ca(1), Ca(2), Ca(3), P(2) and P(3) have different values from each other, indicating that column B is distorted compared with column A

from the point of view of atomic positions [81, 82]. The schematic presentation of the β-TCP unit cell on the [001] plane and along the *c*-axis is presented in Fig. 7 [83].

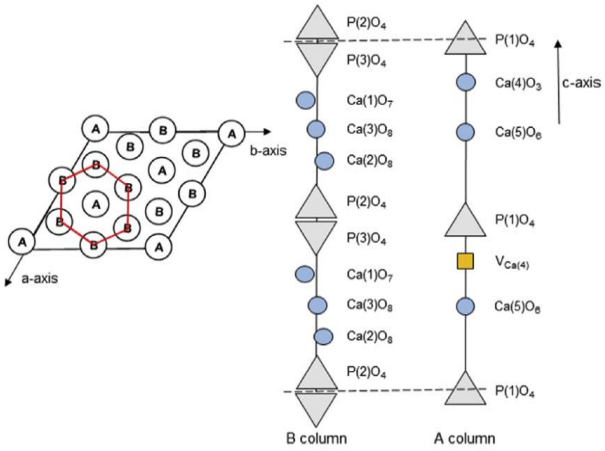


Fig. 7. Schematic representation of the β-TCP unit cell on the [001] plane and along the *c*-axis [83].

As mentioned above, calcium atoms in β-TCP are located at five crystallographic sites from Ca(1) to Ca(5) and have coordination numbers from 3 to 8. The coordination numbers from Ca(1) to Ca(5) are 7, 6 or 8, 8, 3 and 6, respectively. Ca(2) possess two different coordination numbers on the basis of Ca and O distances – Ca(2) is coordinated strongly by 6 oxygens and less strongly by two others. All Ca sites are fully occupied by calcium, while Ca(4) site shows only an occupancy factor of 0.43(4). Since the hexagonal unit cell has 6 Ca(4) sites, 3 Ca vacancies are presented at the Ca(4) site per cell [38, 81, 82]. Local environment of calcium crystallographic sites are presented in Fig. 8 [84].

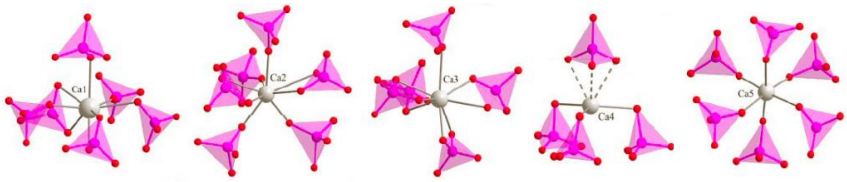


Fig. 8. Local environment of calcium crystallographic sites. The $PO_4^{3-}$ groups are represented by tetrahedra [84].

### 1.3.5. Synthesis of β-TCP

The preparation of β-TCP does not differ significantly from that of α-TCP in terms of synthesis methods. The main difference is usually observed in final annealing temperature, which is lower for β-TCP. The most used ways to obtain β-TCP are:

- Thermal transformation of the precursors;
- Solid-state synthesis;
- Precipitation in organic media [85].

Same as α-TCP, β-TCP cannot be precipitated from aqueous solutions. It is prepared at temperatures above 800 °C by thermal decomposition or crystallization of CP precipitates with Ca/P molar ratio of 1.5 such as CDHA or ACP. The precursors are usually obtained in the same way as it was discussed in 1.3.2 section (Eq. 1 and 2) [26, 36, 50, 86, 87].

For solid-state synthesis as starting materials calcium-rich ($CaCO_3$, $Ca(OH)_2$ and CHAp) and phosphate-rich phases ($CaHPO_4$, $CaHPO_4 \cdot 2H_2O$, $Ca_2P_2O_7$ and $(NH_4)_2HPO_4$) are commonly used [71, 88-91]. The synthesis procedure and reaction equations are the same as it was discussed in 1.3.2 section (Eq. 4-7). The only difference is the heat treatment parameters, which should be chosen to prevent β- to α-TCP phase transition [26]. However, to obtain pure β-TCP starting materials should be mixed homogenously in order not to obtain impurities like CHAp or calcium pyrophosphate [85].

The β-TCP can be precipitated in organic media at low temperatures, for example in ethylene glycol, methanol or tetrahydrofuran [92-97]. In general, separately prepared calcium and phosphate ions containing organic solutions are mixed together and bathed for some time to obtain β-TCP at relatively low temperature. Tao et al. [93] have prepared β-TCP using $CaCl_2 \cdot 2H_2O$, $Na_2HPO_4$ and NaOH in ethylene glycol. Reaction mixture was bathed at 190 °C for 90 minutes. It was discovered that formed β-TCP crystals were hexagonal plates and their sizes can be controlled successfully. The β-TCP can also be obtained during autoclaving of ACP and α-TCP [85].

Other methods like sol-gel, DCS, flame-spray pyrolysis or microwave combustion synthesis can also be employed. Since various synthesis methods have a particular effect on the particle size, crystallite size, morphology, etc., specific synthesis method should be chosen. For example, sol-gel method is used to synthesize smaller nano-sized particles compared to other methods because of its excellent homogenous molecular mixing [98-101].

### 1.3.6. Application of β-TCP

β-TCP is one of the most attractive bone graft substitutes due to its synthetic nature, osteoconduction, osteoinduction and cell-mediated resorption. *In vivo* β-TCP is resorbed by osteoclasts, also it can release a large quantity of $Ca^{2+}$ and $PO_4^{3-}$ which are used for bone repair, meanwhile preserving structural stability, which makes it excellent material for bone tissue regeneration [85, 102, 103].

In medicine and dentistry, β-TCP is used in the form of mono- or biphasic self-setting CP cements, granules or scaffolds for large bone defect healing [76, 85, 104]. Moreover, β-TCP can be used as carrier for growth factor or drug delivery, which could accelerate bone healing process [105-107]. Also, pure β-TCP is added to some toothpaste as a gentle polishing agent [108]. There are also other, non-health related β-TCP applications like using it as component of multivitamin complex, as a texturizer, bakery improver, and anti-clumping agent for dry powdered food, for example: flour, milk powder, dried cream, cocoa powder. Moreover, it is added as a dietary or mineral supplement to food and feed, where it is marked as E341, as inert component in pelleted drugs. Like α-TCP, β-TCP can be used in agriculture as a slow release fertilizer for acidic soils [36, 109].

## 1.4. Amorphous calcium phosphate

### 1.4.1. Structure of ACP

In general, ACP is a hydrated CP with varying Ca/P molar ratio (1.2-2.2), which depends on synthesis method and conditions [110]. In 1970s Betts and Posner [111] using X-ray experiments discovered that ACP is made of randomly aggregated 0.95 nm size roughly spherical units with a Ca/P molar ratio of 1.5 and with approximately 15-20 wt% of tightly bound water in the gaps. These units are called Posner's clusters with a chemical composition of $Ca_9(PO_4)_6$. [36, 55]. Moreover, theoretical investigations on the stability of different $Ca^{2+}$ and $PO_4^{3-}$ clusters with a different number of ions have confirmed that Posner's clusters are the most stable arrangement. It was later suggested that these clusters possess a $S_6$ symmetry and are short range ordered in ACP [112-114]. A model of ACP structure with Posner's cluster with $S_6$ symmetry is shown in Fig. 9 [112, 115].

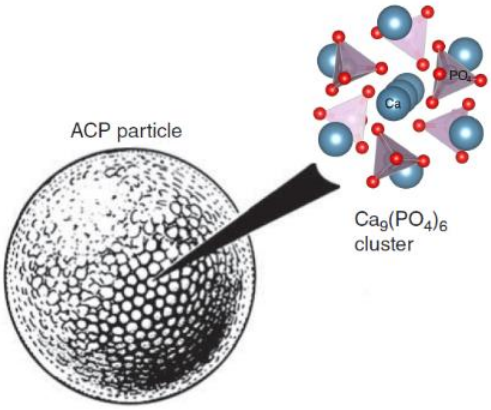


Fig. 9. A model of ACP structure with Posner's cluster with $S_6$ symmetry [112, 115].

### 1.4.2. Synthesis of ACP

Mostly, ACP is obtained by two routes: wet and dry. The wet preparation route is based on synthesis in aqueous medium at low temperature, meanwhile dry method is based on using high energy processing. As it was mentioned before, based on synthesis method and conditions, synthetic ACP can exhibit different Ca/P ratio [55]. In this chapter, synthesis methods of ACP with various Ca/P ratios will be discussed.

The wet synthesis of ACP is based on the double decomposition of calcium and phosphate salt in aqueous or water-alcohol solutions [55]. ACP powders can be synthesized by wet chemical precipitation at room temperature by mixing concentrated aqueous solutions of calcium and phosphate ions and filtering obtained precipitates. For example, combination of $Ca(NO_3)_2$ and $(NH_4)_2HPO_4$ are usually used as starting materials and $NH_4OH$ is used to adjust the pH of solution. Afterwards, precipitates are washed with deionized water and filtered. Washed precipitates are usually lyophilized. Before lyophilization, precipitates have to be frozen in order to prevent phase transformation [116-118]. Other precursors like $CaCl_2$, $Ca(OH)_2$, $H_3PO_4$, $(NH_4)_3PO_4$, $Na_2HPO_4$, etc., can be also employed to prepare ACP, but overall synthesis principle stays the same [119-122].

It is known that ACP in aqueous medium is unstable and converts to thermodynamically favorable crystalline CP phase, usually CDHA. In order to stabilize ACP, ionic stabilizers like $Sr^{2+}$, $Mg^{2+}$, $Zn^{2+}$, $P_2O_7^{4-}$, $CO_3^{2-}$, citrate ions and polymers like polyethylene glycol are used. Utilization of organic washing solutions like ethanol may also stabilize ACP [21, 123-128].

Moreover, ACP can be obtained in water-alcohol solutions or during sol-gel process. Mostly, ethanol, methanol, polyethylene glycol are used as organic solvents [96, 129-137]. Using them in reaction mixture favours the existence of protonated species such as $HPO_4^{2-}$, moreover ions in solutions tend to be less hydrated than those in water. The result of this is a strong decrease of solubility and an increase in precipitation, which favors ACP formation [138]. Synthesis of ACP by sol-gel synthesis was demonstrated by P. Layrolle and A. Lebugle using calcium diethoxide and phosphoric acid as starting materials in a dry argon atmosphere [134].

ACP can also be prepared using mechano-chemical or spray pyrolysis techniques. However, these preparation methods are less popular in comparison with wet synthesis, because some impurities after synthesis might be present, moreover it requires more time to prepare relatively large amounts of ACP [55, 110]. For example, Yu et al. [139] have prepared ACP by a dry mechano-chemical technique from a mixture of DCPD and $Ca(OH)_2$ with a Ca/P ratio of 1.67. Moreover, it was demonstrated by other authors that prolonged high energy ball milling of α-TCP or β-TCP powders in ethanol also leads to the formation of ACP [140-142]. However, there is a risk of powder contamination because of ball wear when using this processing route over extended periods of time to obtain ACP [55].

For the first time flame spray pyrolysis technique was employed by Loher et al. [49, 101, 143] and used by other scientists to prepare ACP. The precursor solution was prepared from calcium 2-ethylhexanoate and tributyl phosphate with Ca/P molar ratio between 1.43 and 1.67. This solution was then dispersed in oxygen gas and fed into a methane/oxygen flame. During flame-spray synthesis, the ACP nanoparticles have formed in a high-temperature environment (1500-2000 °C) and were rapidly quenched by air entrainment from the surrounding. Fast cooling after formation in the flame prevents crystallization and leads to the formation to ACP nanoparticles. These nanoparticles were collected on a filter placed above flame. This method is less used in comparison with other methods, because it is more expensive mainly due to the high energy flame production and the use of appropriate precursors [55]. Moreover, ACP was obtained by direct spray drying using phosphoric acid and calcium acetate solution at 160 °C with Ca/P molar ratios of 1.3 and 1.67 [144].

### 1.4.3. Application of ACP

ACP can be used as bone substitute biomaterial in the form of coatings on metal implants, cements and composites [55]. Additionally, synthetic ACP can be used as a precursor for the synthesis of crystalline CPs [127, 145-147]. Most frequently ACP is used as a component of injectable self-setting CP-based cement [76]. Moreover, metal implants and orthopedic prostheses are coated with ACP in order to enhance bone and implant bonding after implantation and to ensure early and long-term performance [55, 148]. In dentistry, bioactive ACP and polymer composites in acidic environment are able to release calcium and phosphate ions, which may favor enamel mineralization. These biocomposites are used mainly as anticariogenic and/or remineralizing agents (for example, in chewing gums) sugar confections, tooth mousses, bleaching gels, mouth rinses, various drinks or even in milk [22, 108]. Furthermore, ACP-based resorbable cement can be employed as a drug delivery system for antibiotics, growth factors for orthopedic applications. The ability to incorporate growth factors into these cements may accelerate bone healing *in vivo* [55].

ACP also finds its application in non-medical field. It can be used as mordants in fabric dyeing, moreover, in glass and pottery production. In food industry, ACP are used for syrup clearing. Like β-TCP, they might be used as inert fillers in pelleted drugs [36].

## 1.5. The role of trace elements in biological and synthetic CPs

It is well known that some CPs have structural capacity to accept other bioactive ions, which can influence not only crystal structure, but also important materials properties. The presence of foreign ions in CP matrix can affect physiochemical and mechanical properties and cause changes in morphology, density, bioactivity, biocompatibility, solubility in a biological medium and kinetics of ion release [16, 21]. There are two main directions in ionic modification of CaPs. One of them is improving the properties of CaP, while the second one is stabilizing of particular crystal phases [26].

As it was mentioned before, biological apatite depending on human age, diet and condition of the tissue, contains other substituting bioactive ions. Some of them play a crucial role in mineralized tissue metabolism and formation through stimulation of biochemical processes, which support bone tissue growth. In this chapter a beneficial effect that each ion, used in this work, gives for bone metabolism and formation will be discussed.

Each element contributes differently to bone metabolism process. Mn as an element in human organism plays important role for normal bone formation and development. It acts as a cofactor of several enzymes like glycosyltransferases, which are involved in formation of bone and cartilage matrix. However, its deficiency impairs cartilage matrix formation resulting in bone abnormalities like osteoporosis. On the positive side, studies have showed that $Mn^{2+}$ enhances ligand binding affinity of integrin, activates cell adhesion, enhances osteoblast adhesion and has positive impact on the osteointegration [149-151].

Fe is an essential element involved in collagen, which is the main organic part of human bone, synthesis and metabolism of vitamin D. However, both iron overload and deficiency lead to bone resorption, which is associated with decreased bone mass, osteoporosis, altered bone microarchitecture and biomechanics, as well as frequent bone fractures. Fe overload increases osteoclast differentiation and activity, while inhibiting osteoblast differentiation and function, while Fe deficiency negatively affects bone through different mechanisms like inhibition of collagen synthesis, participation in vitamin D metabolism or through hypoxia, which is responsible for bone resorption stimulation [152-154].

Zn is the second most abundant trace element in the human body. About 86% of the total amount of Zn is found in skeletal muscles and bone tissue. It is required for bone growth and development and its deficiency can lead to skeletal abnormality including growth retardation, abnormal mineralization and osteoporosis. At the cellular level, $Zn^{2+}$ promotes both differentiation and proliferation of osteoblasts. Moreover, $Zn^{2+}$ stimulates osteoblastogenesis and suppresses osteoclastogenesis through osteoclastic differentiation [155, 156]. Also, *in vitro* studies showed that Zn stimulates the osteoblastic production of some growth factors, which promote bone formation [26]. Furthermore, doping with Zn may provide antibacterial properties to biomaterials and accelerate bone fracture healing [157, 158].

Sr is another bioactive ion, which is involved in biochemical processes like stimulation of DNA and bone collagen synthesis [159]. About 98% of Sr is localized in human bone tissue [26]. It has been recognized that $Sr^{2+}$ stimulates the proliferation and osteogenic differentiation in osteoblastic cells and inhibits osteoclast activity *in vitro*. Moreover, Sr is used as a treatment for osteoporosis in the form of Sr ranelate, which inhibits bone resorption and stimulates bone formation, resulting in increase of bone mass [160-162]. Also, the presence of $Sr^{2+}$ in bone regenerating materials can enhance osteoinduction and osseointegration at the bone-implant interface after

implantation, reduce bone resorption and can contribute to faster healing after implantation [163].

Mg is the fourth most abundant element in the human body, approximately 60% of Mg is stored in bone, dentin and enamel. An appropriate level of Mg is crucial for preventing osteoporosis, osteopenia, impaired bone growth and other bone fragility. It stimulates osteoblast activity, moreover, Mg ions have impact on the secretion of parathyroid hormone and vitamin D. Mg deficiency lowers parathyroid hormone and vitamin D production, which may lead to hypocalcaemia – bone resorption. Furthermore, deficiency of $Mg^{2+}$ leads to decrease in osteoblast and increase in osteoblast activity resulting in bone mass loss [26, 156].

Ba is not commonly used for bone regeneration due to its toxicity for human organism [164]. However, Kikuchi et al. [165] reported that Ba-doped CHAp showed no cytotoxicity. Some other studies on Ba-substituted CHAp are also known [166, 167]. Moreover, it was proposed that the piezoelectric property could be used as a charge supply to stimulate the bone implant healing process. For this reason, CHAp and $BaTiO_3$ composites have been investigated. It was proposed by Zhang et al. [168] that this composite exhibited a higher piezoelectric coefficient than natural bone. In addition, cytotoxicity studies with human osteoblasts and fibroblast cells showed that this composite is non-toxic indicating that it could be used for bone regeneration [159, 168, 169].

# 2. EXPERIMENTAL

## 2.1. Materials and reagents

The following starting materials and solutions were used for the synthesis and elemental analysis:

- Calcium nitrate tetrahydrate ($Ca(NO_3)_2 \cdot 4H_2O$, ≥99%, Roth);
- Diammonium hydrogen phosphate ($(NH_4)_2HPO_4$, ≥98%, Roth);
- Manganese (II) nitrate tetrahydrate ($Mn(NO_3)_2 \cdot 4H_2O$, 98%, Alfa Aesar);
- Iron (III) nitrate nonahydrate ($Fe(NO_3)_3 \cdot 9H_2O$, ≥98%, Alfa Aesar);
- Zinc (II) nitrate hexahydrate ($Zn(NO_3)_2 \cdot 6H_2O$, ≥98%, Chempur);
- Magnesium (II) nitrate hexahydrate ($Mg(NO_3)_2 \cdot 6H_2O$, 99%, Chempur);
- Strontium nitrate ($Sr(NO_3)_2$, ≥98%, Carl Roth);
- Barium nitrate ($Ba(NO_3)_2$, Lach-Ner);
- Ammonia solution ($NH_4OH$, 25%, Carl Roth);
- Acetone (AC, ≥99.8%, Carl Roth);
- Acetonitrile (ACN, ≥99.5%, Carl Roth);
- Ethanol (EtOH, 96%, Carl Roth);
- Isopropanol (i-PrOH, ≥99.5%, Carl Roth);
- Single element ICP standard solutions of Ca, P, Mn, Fe, Zn, Mg, Sr and Ba (1000 μg/mL, Carl Roth) were used for ICP-OES;
- Nitric acid ($HNO_3$, ROTIPURAN® Supra 69%, Carl Roth).

## 2.2. Synthesis of undoped TCP polymorphs

All compounds were synthesized by wet precipitation method using $Ca(NO_3)_2$ and $(NH_4)_2HPO_4$ as starting materials. An appropriate amount of $(NH_4)_2HPO_4$ was dissolved in deionized water to obtain a 0.5 mol/L solution, to which $NH_4OH$ was added under constant stirring in order to adjust the pH value to 10. An aqueous solution of calcium nitrate (0.75 mol/L) was rapidly added to the above mixture resulting in the instantaneous formation of white precipitates. Initial Ca/P ratio was kept 1.5. The obtained precipitates were stirred in the reaction mixture for 10 min, afterwards vacuum filtered, washed with 100 mL deionized water following by washing with different volumes (20, 40, 60, 80 and 100 mL) of five different washing liquids: deionized water, AC, ACN, EtOH and i-PrOH. After washing the precipitates were dried at

50 °C overnight in the oven. Dry powders were ground and annealed in the furnace at 750 and 775 °C temperature for 5 h in air atmosphere with a heating rate of 5 °C/min. The synthesis scheme of TCP by wet precipitation method is presented in Fig. 10.

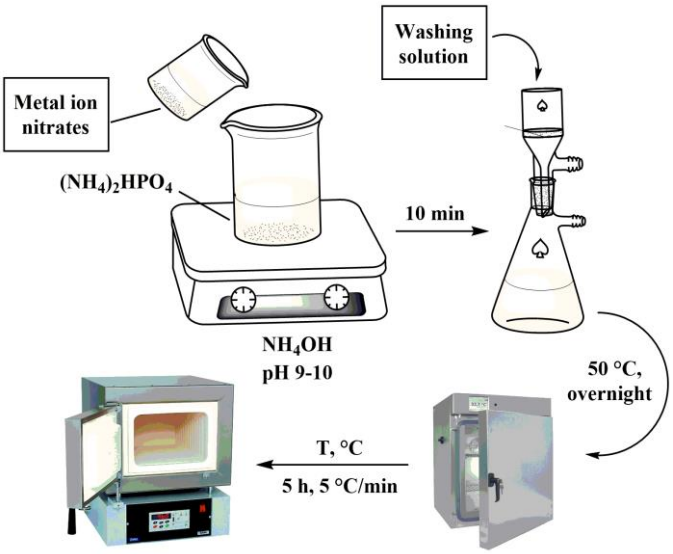


Fig. 10. Synthesis scheme of TCP by wet precipitation method.

## 2.3. Synthesis of Mn-doped TCP polymorphs

Mn-doped α- and β-TCP with Mn concentrations ranged from 0 to 5 mol% with a step of 1 mol% were synthesized by wet precipitation method (based on section 2.2). An appropriate amount of $Mn(NO_3)_2 \cdot 4H_2O$ was added into metal ions solution in accordance to desired stoichiometry. The pH of $(NH_4)_2HPO_4$ solution was adjusted to 10. The solutions were mixed at metal ions to phosphorus ratio of 1.5. In order to obtain ACP as precipitates, 100 mL of deionized water and 100 mL of EtOH were used as washing liquids. Dried and ground precipitates were annealed in the furnace at 700 °C for 5 h in air atmosphere with a heating rate of 5 °C/min.

## 2.4. Investigation of hydrolysis of Mn-doped α-TCP

For the investigation of hydrolysis of Mn-doped α-TCP, pure, 0.5 and 1.0 mol% Mn-doped α-TCP powders were synthesized in the same way as described in section 2.3. Hydrolysis of α-TCP powders was carried out in

deionized water at 37 °C. For this purpose, 400 mg of α-TCP powders were soaked in 15 mL of deionized water and stored for different periods of time. Then the products were filtered, rinsed with deionized water and dried. All samples were investigated in triplicate.

### 2.5. High-temperature synthesis of Mn-doped α-TCP

A series of α-TCP powders doped with different amounts of $Mn^{2+}$ (from 0 to 1.0 mol% with a step of 0.2) were synthesized by wet precipitation method (based on section 2.2). The $Ca^{2+}$ and $Mn^{2+}$ nitrates solution was rapidly added to the $(NH_4)_2HPO_4$ solution, in which pH was adjusted to 10. Metal ions to phosphorus ratio was kept 1.5. Obtained precipitates were vacuum filtered, washed with 100 mL deionized water and 100 mL EtOH afterwards dried in oven at 50 °C overnight. In order to obtain α-TCP phase, the ground precipitates were transferred to alumina crucible, annealed at 1250 °C for 12 h with a heating rate of 5 °C/min and rapidly cooled down on a metal plate.

### 2.6. Synthesis of Mg-, Zn-, Sr- and Ba-substituted ACP

The Mg-, Zn-, Sr- and Ba-substituted ACP powders with metal concentrations ranged from 0 to 10 mol% were synthesized by wet precipitation method (based on section 2.2). An appropriate amount of substituting metal nitrate was added into calcium nitrate solution according to the desired stoichiometry. The pH of $(NH_4)_2HPO_4$ solution was adjusted to 10 (in the case of Zn-substituted ACP the pH was adjusted to 9). The prepared solutions were mixed at metal ions to phosphorus ratio of 1.5. In order to obtain ACP as precipitates, 100 mL of deionized water and 100 mL of EtOH were used as washing liquids. Dried and ground precipitates were annealed in a muffle furnace at different temperatures for 5 h with a heating rate of 5 °C/min.

### 2.7. Synthesis of Fe and Zn co-doped β-TCP

β-TCP powders substituted with equal amounts of Fe and Zn ions (from 0 to 5 mol% with a step of 1 mol%) were obtained by wet precipitation method (based on section 2.2). The $Ca^{2+}$, $Fe^{3+}$ and $Zn^{2+}$ nitrates solution was rapidly added to the $(NH_4)_2HPO_4$ solution, in which pH was adjusted to 9. Metal ions to phosphorus ratio was kept 1.5. The obtained precipitates were vacuum

filtered, washed with 100 mL deionized water and afterwards dried in the oven at 50 °C overnight. Dried and ground precipitates were annealed in a furnace at 800 °C for 5 h in air atmosphere with a heating rate of 5 °C/min.

For the preparation of β-TCP ceramics, polyvinyl alcohol was used as a binder. Powders were uniaxially pressed in 15 mm die using cold isostatic pressing at 200 MPa and sintered at 1100 °C for 5 h in air atmosphere.

## 2.8. Instrumentation and characterization techniques

Thermal decomposition of the as-prepared precipitates was analyzed through thermogravimetric analysis (TGA) using Perkin Elmer STA 6000 Simultaneous Thermal Analyzer. Samples of about 5-10 mg were heated from 25 to 900 °C at a heating rate of 10°C/min in a dry flowing air (20 mL/min).

Powder X-ray diffraction data were collected using Ni-filtered Cu Kα radiation on Rigaku MiniFlex II and Bruker D8 Advance diffractometers working in Bragg-Brentano (θ/2θ) geometry. The data were collected within 2θ angle range from 10 to 60° at a step width of 0.01° and scanning rate of 5°/min. The composition and phase purity of samples were identified using Match! software. Lattice parameters were refined by the Rietveld method using FullProf suite in the profile matching mode. For Rietveld refinement data were recorded within 2θ angle range from 10 to 110° at a step width of 0.01° and integration time 1.5 s, respectively. The average size of crystallites was calculated by Scherrer equation (Eq. 8):

$$\tau = \frac{0.9\lambda}{B\cos\theta} \tag{8}$$

Fourier transform infrared spectra (FTIR) were taken in the range of 4000-400 $cm^{-1}$ with Bruker ALPHA ATR spectrometer with 4 $cm^{-1}$ resolution.

Raman spectra were recorded at room temperature using combined Raman and scanning near field optical microscope (SNOM) WiTec Alpha 300R equipped with 532 nm excitation laser source.

Morphology of the synthesized products was analyzed with a Hitachi SU-70 field-emission scanning electron microscope (FE-SEM).

Elemental analysis of the synthesized samples was performed by inductively coupled plasma optical emission spectrometry (ICP-OES) using Perkin Elmer Optima 7000DV and Agilent 5110 spectrometers. Samples of about 0.02 g were dissolved in 5% nitric acid and diluted to an appropriate volume with deionized water.

Electron paramagnetic resonance (EPR) spectra were recorded using a conventional X-band (microwave frequency ≈ 9.18 GHz) RE 13-06 spectrometer with 100 kHz field modulation at room temperature. The magnetic field was calibrated with DPPH reference sample with $g = 2.0036 \pm 0.0002$. For some samples EPR spectra were obtained with Bruker ELEXSYS-II E500 CW-EPR spectrometer. Power of 9.46 GHz microwaves was set at 0.6325 mW. The magnetic field was modulated at 100 kHz with 0.4 mT modulation amplitude. EPR signal intensities have been normalized to the sample mass.

Excitation and emission spectra were obtained on the Edinburgh Instruments FLS980 spectrometer equipped with double excitation and emission monochromators, 450 W Xe arc lamp, a cooled (-20 °C) single-photon counting photomultiplier (Hamamatsu R928), and mirror optics for powder samples. The photoluminescence (PL) emission spectra were corrected by a correction file obtained from a tungsten incandescent lamp certified by NPL (National Physics Laboratory, UK). When measuring excitation spectra ($\lambda_{em}$ = 670 nm), excitation and emission bandwidths were set to 1.60 and 5.00 nm, respectively. When measuring emission spectra ($\lambda_{ex}$ = 408 nm), excitation and emission bandwidths were set to 4.00 and 1.60 nm, respectively. For both measurements, step width was 1.00 nm and integration time was 0.2 s.

The PL decay kinetics were performed on the same Edinburgh Instruments FLS980 spectrometer. Xe μ-flash lamp μF920 was used as an excitation source. Excitation wavelength were 408 nm while emission was monitored at 670 nm. The effective PL lifetime values were calculated using the following equation (Eq. 9):

$$\tau_{eff} = \frac{\int_0^\infty I(t)tdt}{\int_0^\infty I(t)dt} \quad (9)$$

where $I(t)$ is the PL emission intensity at a time $t$ after the cutoff of excitation light.

Dependence of magnetization of samples on the strength of magnetic field were recorded using magnetometer consisting of the lock-in amplifier SR510 (Stanford Research Systems) the gauss/teslameter FH-54 (Magnet Physiscs) and the laboratory magnet supplied by the power source SM 330-AR-22 (Delta Elektronika).

Density of the sintered pellets was measured by Archimedes' method in deionized water.

Vickers hardness of the prepared sample ceramics was measured using Future-Tech Vickers hardness tester FV-310e. Ten indentations of a single load of 1 kg (9.8 N) and holding time of 15 s were used for the pellets of each composition.

The cytotoxicity of the synthesized samples was evaluated by means of MTT assay using HEK 293 cells. HEK 293 cells (150 μL of 7.5×104 cells/mL) were cultured in a 96-well plate at 37 °C, 5% $CO_2$ for 24 h. The samples with different concentrations of TCP powders (25, 50 and 100 μg/mL dispersed in sterile cell medium) were added (200 μL) to 96-well plate and incubated over a period of 6, 24 and 48 h at 37 °C. HEK 293 cells treated only with culture media were fixed as a positive control. To each well, MTT (5 mg/mL) was added for 2 h incubation at 37 °C. Afterwards, the supernatant was removed, and 150 μL of DMSO/well were added to resolve the formazan crystals. The absorbance was measured at 630 nm using Elisa reader multiplate (ELX 800, BioTek Instruments).

Zebrafish embryo toxicity assay was investigated in order to evaluate acute toxicity and developmental defects of specimens. Zebrafish embryos were exposed to solutions containing 1 wt% of various Fe:Zn co-substituted β-TCP powders under temperature of 28 °C. E3 medium (5 mM NaCl, 0.17 mM KCl, 0.33 mM $CaCl_2$, and 0.33 mM $MgSO_4$) was used for the control group. Fertilized wild-type zebrafish (*Danio rerio*) eggs 1 h post fertilization (1 hpf) were pipetted into polystyrene Petri dishes (35 mm × 10 mm, sterile, stackable, Fisher Scientific) with 10 embryos per plate (N = 10) and the data were recorded at representative stages (24, 48, and 72 hpf). The survivability and conditions of the embryos were captured under a light microscope (Olympus SZX16, Shinjuku-ku, Tokyo, Japan) and a digital camera (Canon EOS 550D, Ohta-ku, Tokyo, Japan) under 40× and 100× magnifications. Percentage survival of the embryos was evaluated and scored for lethal or teratogenic effects.

# 3. RESULTS AND DISCUSSION

## 3.1. Effect of washing procedure on phase-selective synthesis of TCP polymorphs

CPs were precipitated in aqueous medium and washed with 5 different liquids. The XRD patterns of the as-prepared precipitates washed with 100 mL of the solvent before and after the thermal treatment at 775 °C ($H_2O$ and AC) or 750 °C (ACN, EtOH and i-PrOH) are given in Fig. 11.

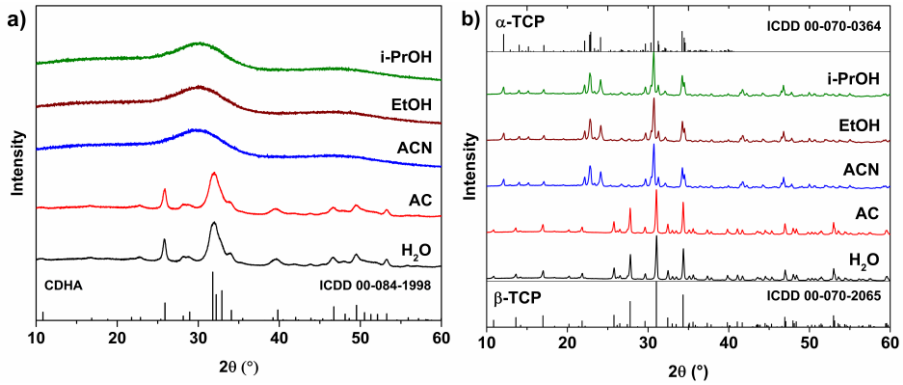


Fig. 11. XRD patterns of the as-prepared precipitates washed with 100 mL of the solvent before (a) and after (b) the thermal treatment at 775 °C ($H_2O$ and AC) or 750 °C (ACN, EtOH and i-PrOH).

Phase composition analysis revealed that using $H_2O$ and AC as washing agents, the crystalline phase corresponding to CDHA was obtained (Fig. 11a). The crystal phase was found to be independent of the used amount of $H_2O$ and AC. In the case of ACN, EtOH and i-PrOH no sharp diffraction peaks were detected in the XRD patterns of these samples, only very broad beak at around 30°, which is characteristic of ACP [138]. Amorphous powders were obtained only using 100 mL and higher volume of the solvent, while CDHA was formed with lower amount of the solvent. Increasing volumes of ACN, EtOH and i-PrOH led to degradation of CDHA phase.

In the case of $H_2O$ and AC, the powders after annealing at 775 °C crystallized to β-TCP phase (Fig. 11b). All diffraction peaks match very well the standard XRD data of rhombohedral $Ca_3(PO_4)_2$ (ICDD 00-070-2065). And in the case of treatment with ACN, EtOH and i-PrOH the samples after annealing at 750 °C crystallized to α-TCP polymorph. The XRD patterns of these samples match the standard XRD data of monoclinic $Ca_3(PO_4)_2$ (ICDD 00-070-0364). Crystal structure of the final product was found to be independent of the volumes of $H_2O$ and AC used for washing procedure,

β-TCP phase was obtained after annealing in all cases. Oppositely, in the case of ACN, EtOH and i-PrOH crystal structure of the annealed products was found to be strongly dependent on the used amount of the solvent.

Unfortunately, it was not possible to obtain single-phase polymorphs at exactly the same temperature. The α-TCP was found to be monophasic only at ≤750 °C, while at higher temperatures small amount of β-TCP was observed. Single-phase β-TCP polymorph was not obtained at 750 °C, since its CDHA precursor does not decompose completely at this temperature.

Raman spectroscopy was used in order to detect vibrations of possible amorphous species or crystalline phases, which might be hardly distinguished by XRD in presence of TCP. Fig. 12. shows Raman spectra of the precipitates washed with 100 mL of the solvent and annealed at 775 or 750 °C.

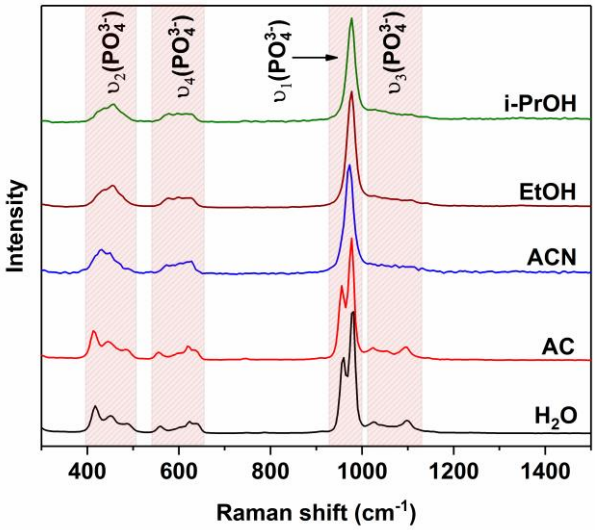


Fig. 12. Raman spectra of the precipitates washed with 100 mL of the solvent and annealed at 775 °C ($H_2O$ and AC) or 750 °C (ACN, EtOH and i-PrOH).

All Raman spectra contain peaks characteristic to the internal vibrations of phosphate groups in TCP. The spectroscopic differences between two groups of the samples corresponding to different TCP polymorphs are clearly seen. The spectra of the samples washed with $H_2O$ and AC are dominated by two distinctive sharp peaks located at around 955 and 977 $cm^{-1}$, which are attributed to the symmetric stretching ($\upsilon_1$) of P–O bonds in tetrahedron. Asymmetric stretching mode ($\upsilon_3$) of P–O bonds can be seen in spectra as less intense bands in the range of 1010-1130 $cm^{-1}$. Two other groups of the bands can be observed at lower wavenumbers from approximately 395 to 510 $cm^{-1}$

and from 540 to 660 $cm^{-1}$ and could be assigned to $\upsilon_2$ and $\upsilon_4$ O–P–O bending deformations of the phosphate tetrahedron, respectively [170, 171]. For the samples washed with ACN, EtOH and i-PrOH, the most intense bands specific of β-TCP are replaced by a single band at 965 $cm^{-1}$ attributed to $\upsilon_1$ vibration mode of phosphate groups of α-TCP. Other observed bands ($\upsilon_2$, $\upsilon_3$ and $\upsilon_4$) in the Raman spectra of these samples also have different shape in comparison to those of β-TCP, but positions stay nearly the same. However bands attributed to $\upsilon_3$ mode are quite week in the spectra of α-TCP [172].

The SEM micrographs of β- and α-TCP samples synthesized using $H_2O$, and ACN as washing solutions are given in Fig. 13.

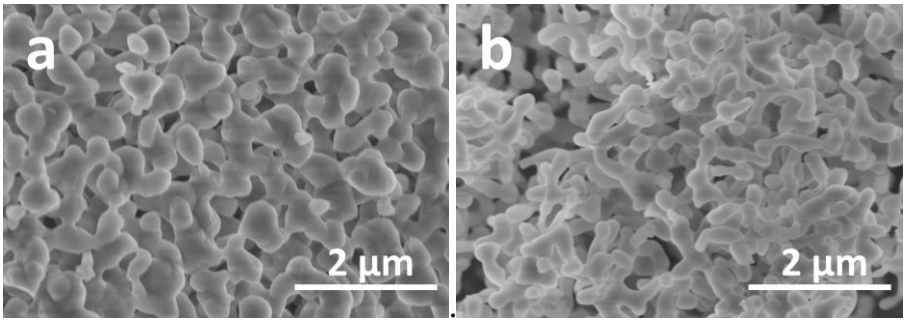


Fig. 13. SEM micrographs of the precipitates washed with 100 mL of $H_2O$ (a) and ACN (b) and annealed at 775 and 750 °C, respectively.

The SEM images demonstrate that synthesized TCP powders exhibit slightly different morphological features depending on their crystal structure. The samples washed only with $H_2O$ (Fig. 13a) consists of approximately 200-500 nm sized nearly spherical particles, which are necked to aggregates of irregular shape. The α-TCP sample synthesized after ACN treatment (Fig. 13b) consists of very uniform thinner particles with prolonged irregular shape. The thickness of the particles is about 300 nm. Powders synthesized with EtOH and i-PrOH in their turn showed very similar morphological features.

## 3.2. Effect of Mn doping on the low-temperature synthesis of TCP polymorphs

The as-prepared CP precipitates containing different amounts of Mn and dried at 50 °C were investigated by XRD and TG/DTG analysis (Fig. 14).

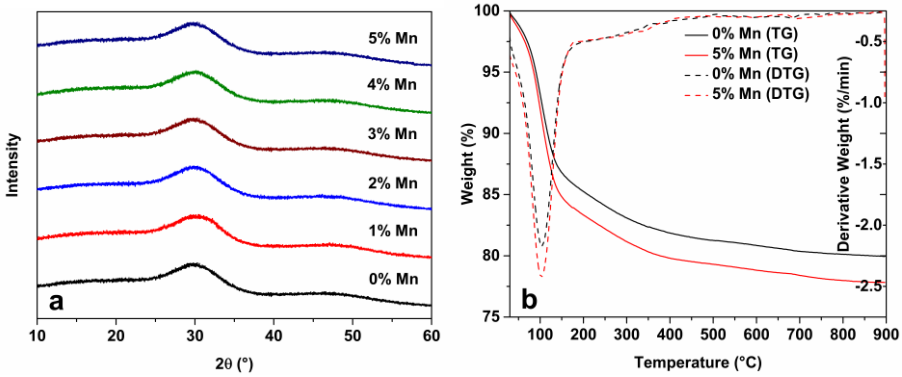


Fig. 14. XRD patterns of as-prepared CP precipitates with different amounts of Mn (a) and TG/DTG curves of CP precipitates with 0 and 5% of Mn (b).

The XRD patterns of as-prepared CP precipitates (Fig. 14a) evidently show the poorly crystalline nature of samples reflected in broad profile of the diffraction signals with a major signal centered around 30°. The obtained XRD patterns of both pristine and doped-samples indicated an amorphous nature of the powders and suggested that Mn content does not affect crystallinity of the samples. Non-crystalline CP was obtained for all samples regardless of the chemical composition.

TG/DTG curves of undoped and 5 mol% Mn-doped as-prepared CP precipitates are given in Fig. 14b as representative. It is clearly seen that behavior of TG curves is very similar for both samples, suggesting that presence of Mn ions does not affect thermal decomposition behavior of precursor powders. Decomposition occurs in few steps, during the first step a mass loss of about 15% is observed with its maximal rate at around 100 °C. This weight loss can be attributed to the removal of residual water from the samples. At higher temperatures, weight gradually decreases with a weight loss of about 5%, which is also attributed to the removal of water. Sample mass above 700 °C is nearly constant, no significant mass change above this temperature was observed.

The phase crystallinity and purity of all CP powders annealed at 700 °C for 5 h was studied by XRD analysis (Fig. 15), which showed the formation of different final products depending on the chemical composition of starting precipitates.

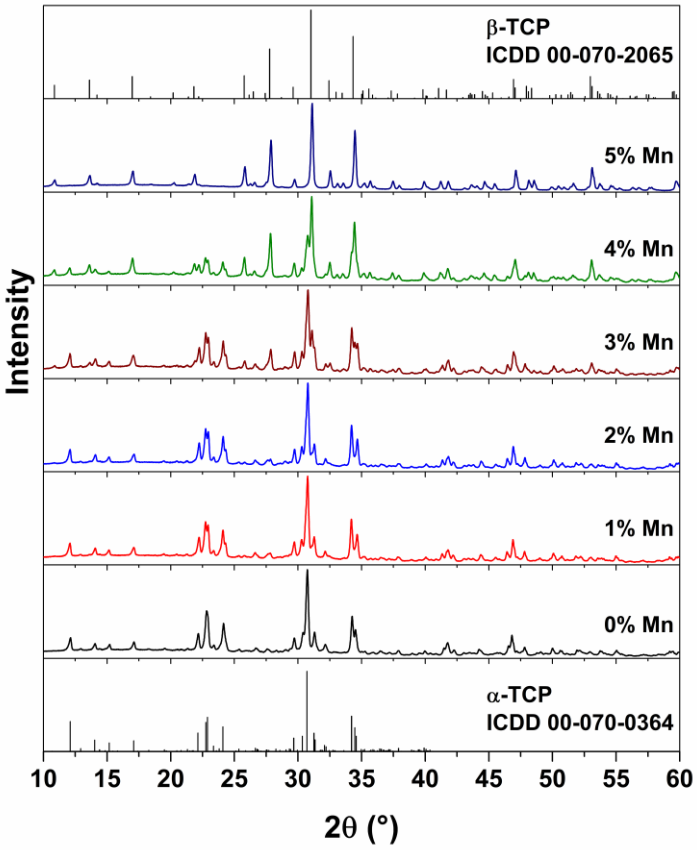


Fig. 15. XRD patterns of CP powders with different amounts of Mn annealed at 700 °C for 5 h.

The undoped sample crystallized to pure α-TCP phase with a monoclinic crystal structure. All diffraction peaks match very well the standard XRD data of α-$Ca_3(PO_4)_2$ (ICDD 00-070-0364). With addition of 1 mol% of Mn ions, monoclinic structure of the sample remained, however existence of minimal amount of β-TCP was detected. Moreover, some structural changes in α-TCP were observed. Diffraction peaks located at 22.8, 24.2, 34.3 and 46.8° noticeably split, which can be assumed as an evidence of incorporation of Mn ions into crystal lattice and structural changes of the latter. Increasing of Mn concentration to 2 mol% does not change a major phase of the sample, however, the presence β-TCP as a minor crystalline phase can be observed. For the samples with Mn content of 3 and 4 mol% a mixture of TCP polymorphs was formed in which the percentage of β-TCP increased with increasing Mn amount. Finally, when concentration of Mn reached 5 mol%, pure β-TCP phase was obtained. There are no XRD peaks arising from any

by-products and all signals correspond to rhombohedral crystal structure of $Ca_3(PO_4)_2$ (ICDD 00-070-2065). Thus, at the same temperature α- and β-TCP phases were obtained for undoped and 5% Mn-doped samples, respectively.

SEM images of pristine and 5 mol% Mn-doped CP precipitates annealed at 700 °C are given in Fig. 16. They reveal that undoped TCP sample consisted of mostly uniform sub-micro sized elongated dumbbell-shaped particles with some agglomerates (Fig. 16a) with axial grain size ranging between 120-150  m whereas length of the particles varied in the range of 300-700 nm. Substitution of Ca ions by 5 mol% of Mn slightly changed morphological features of the powders (Fig. 16b). Shape of the particles was found to be similar, however the dimensions were reduced possibly due to higher densification promoted by Mn doping.

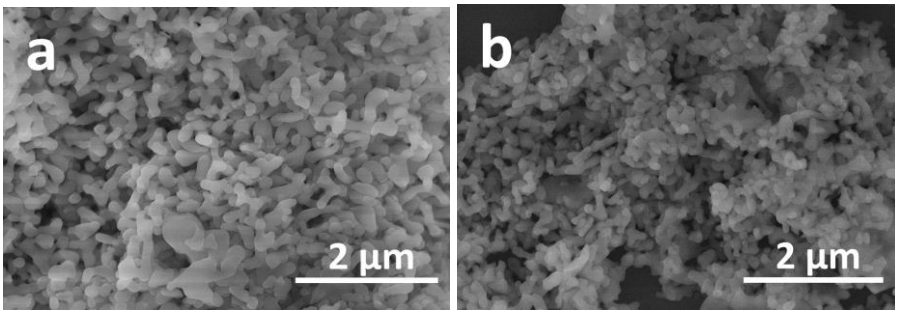


Fig. 16. SEM images of CP powders without Mn (a) and 5 mol% of Mn (b) annealed at 700 °C for 5 h.

All synthesized TCP samples were employed to screen their cytotoxicity profiles for different concentrations (25–100 µg/mL) with an incubation time of 48 h using colorimetric MTT assay. Results on the cell viability with different concentrations of the samples and incubation time of 48 h are depicted in Fig. 17.

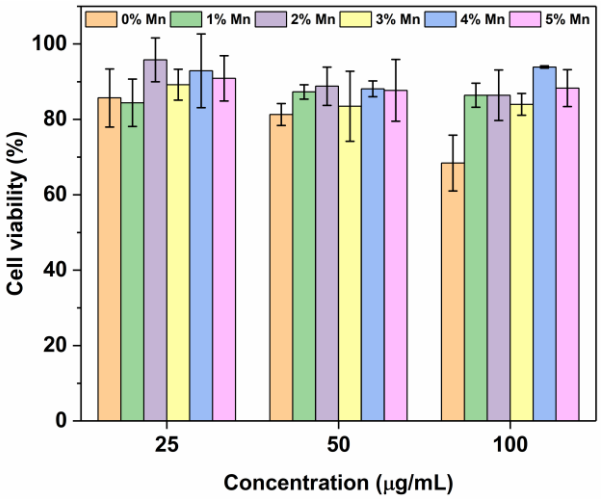


Fig. 17. Cell viability profile of cultured HEK293 cells after incubation for 48 h with the samples of TCP at different concentrations.

Two main regularities can be seen from the results. Firstly, the cell viability does not depend significantly on the concentration of the samples and for all concentrations it is determined to be above 80%, indicating biocompatible nature of the powders. Secondly, the cell viability does not depend on crystal structure of the samples and Mn content as well. The results have not revealed any toxic effects of Mn ions even with its highest concentration thus ruling out the leaching of $Mn^{2+}$ ions under physiological conditions. The only sample revealing a trend in an average cell viability was undoped α-TCP that surprisingly showed gradual decrease in cell viability from $85.7 \pm 7.7$ to $81.3 \pm 2.9$ and $73.8 \pm 6.2$% for concentration of 25, 50 and 100 μg/mL, respectively. However, it can be noticed, that introducing of 1 mol% of Mn improves cell viability profile of α-TCP and keeps it nearly constant for all sample concentrations although there are no changes in crystalline phase of the sample (see Fig. 15).

### 3.3. Effect of Mn doping on hydrolysis of low-temperature synthesized metastable α-TCP

The phase crystallinity and purity of α-TCP powders were investigated by XRD analysis. The XRD patterns of α-TCP samples containing different amounts of Mn ions and annealed at 700 °C are shown in Fig. 18.

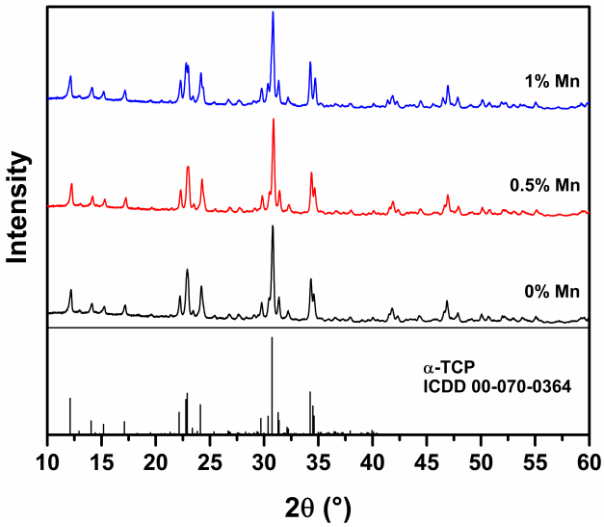


Fig. 18. XRD patterns of pristine and Mn-doped α-TCP powders annealed at 700 °C.

It is seen that all investigated samples after the thermal treatment crystallized to α-TCP regardless of the chemical composition. All diffraction peaks match very well standard XRD data of monoclinic $Ca_3(PO_4)_2$ (ICDD 00-070-0364) indicating that substitution of Ca by Mn ions on the level of 1 mol% does not lead to any phase transition or formation of secondary crystal phases. Visible splitting of some diffraction peaks located at around 23°, 24°, 34° and 47° can be assumed as an evidence of incorporation of Mn ions into α-TCP crystal structure, which led to some internal structural changes. Calculated cell parameters of pristine and Mn-doped α-TCP powders are given in Table 3. It can be seen, that substitution with Mn ions leads to the changes of cell parameters, which arise from the difference between ionic radii of $Ca^{2+}$ and $Mn^{2+}$ ions.

Table 3. Cell parameters of α-TCP powders.

| Sample | *a*, Å | *b*, Å | *c*, Å | *β*, ° |
|---|---|---|---|---|
| $Ca_3(PO_4)_2$ | 12.878(5) | 27.273(1) | 15.214(8) | 126.185(1) |
| $Ca_3(PO_4)_2$: 0.5% $Mn^{2+}$ | 12.869(8) | 27.285(8) | 15.209(6) | 126.209(8) |
| $Ca_3(PO_4)_2$: 1.0% $Mn^{2+}$ | 12.838(8) | 27.342(5) | 15.207(6) | 126.295(4) |

The morphology of pristine and 1 mol% Mn-doped α-TCP powders was investigated by taking SEM images, which are presented in Fig. 19.

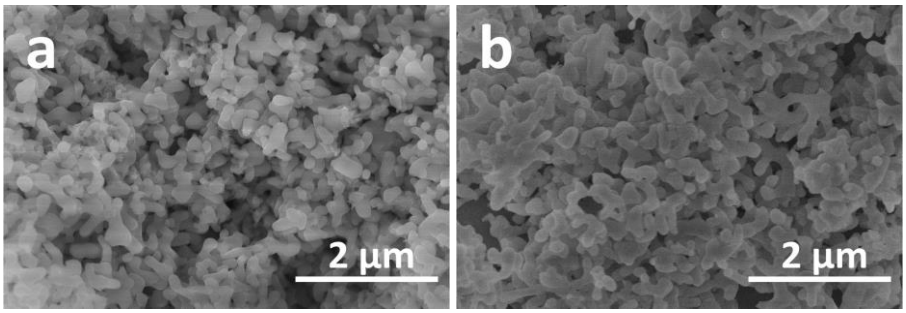

Fig. 19. SEM micrographs of pristine (a) and 1 mol% (b) Mn-doped α-TCP powders.

In both cases powders consisted of the agglomerates of nanodimensional mostly uniform elongated particles. Axial grain size of pristine α-TCP particles ranged approximately between 100 and 200 nm, whereas length of the particles varied in the range of 300-700 nm. Taking a closer look to both micrographs, a slight difference between them can be pointed out. Whereas doping with $Mn^{2+}$ ions did not result in perceptible changes of the shape, the size of Mn-doped α-TCP particles was found to be slightly enhanced compared to pristine species. Since the particles are elongated and of irregular shape, it is hard to estimate the size distribution by length, therefore size distribution by width was analyzed. For pristine α-TCP average size was estimated as (155±35) nm, whereas for 1 mol% Mn-doped sample this value was slightly higher, but still comparable – (176±31) nm. Except this minor difference, it could be stated that doping at 1 mol% level did not affect morphology of powders.

The XRD patterns of pristine and Mn-doped α-TCP powders after different times of soaking in deionized water are illustrated in Fig. 20.

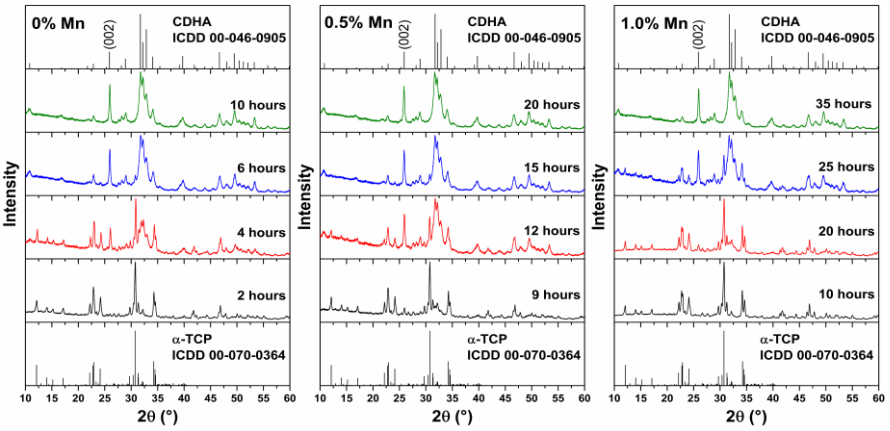


Fig. 20. XRD patterns of pristine and Mn-doped α-TCP powders after different times of hydrolysis.

It is seen that in all cases intensity of diffraction peaks corresponding to CDHA distinctly increase with an increase of soaking time, indicating gradual conversion of α-TCP to CDHA. Complete conversion of pristine, 0.5% and 1% Mn-doped α-TCP to CDHA was observed after 10, 20 and 35 hours, respectively. No signal originating from α-TCP was detected in the XRD pattern at these times. Evidently, Mn doping has an inhibiting effect on the hydrolysis rate of α-TCP, phase evolution observed for doped samples is the same as for pristine α-TCP, however transformation of doped samples occurred significantly slower compared to undoped powders. Possible explanation of this effect can be find in the mechanism of hydrolysis of α-TCP, which is based on dissolution-precipitation process. $Mn^{2+}$ ions are significantly smaller than $Ca^{2+}$, when released to surrounding media, they retard formation of CDHA. It is also evident for all fully hydrolyzed samples that diffraction peak located at 26° and corresponding to (002) crystal plane is more intense compared to standard XRD data. Such observation allows to make an assumption that crystal growth of CDHA occurs in a preferred direction along *c*-axis.

The FTIR spectra of pristine α-TCP powder after different times of soaking are given in Fig. 21a.

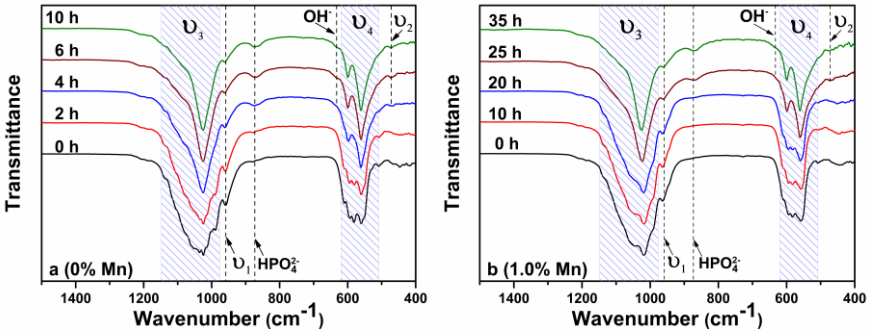


Fig. 21. FTIR spectra of pristine α-TCP (a) and α-TCP doped with 1 mol% of Mn (b) after different times of hydrolysis.

Spectra of untreated α-TCP and α-TCP after soaking for 2 h are very similar and can be characterized by several phosphate absorption bands located at 1160-970 ($\upsilon_3$), 958 ($\upsilon_1$), at 561, 582, 594 and 611 ($\upsilon_4$) and 450 $cm^{-1}$ ($\upsilon_2$). Such spectrum is characteristic of α-TCP polymorph [12] Noticeably different spectra were observed for samples after 4, 6 and 10 h of soaking. Absorption bands located at 1090, 1025 ($\upsilon_3$) and 960 $cm^{-1}$ ($\upsilon_1$) are assigned to the P–O stretching vibration mode and the bands at 600 and 560 $cm^{-1}$ ($\upsilon_4$) correspond to O–P–O bending mode of the phosphate group. Weak band located at 471 $cm^{-1}$ ($\upsilon_2$) is attributed to phosphate bending mode [173]. Remarkable feature of analyzed FTIR spectra is an absorption band located at 868 $cm^{-1}$ attributed to P–O(H) stretching mode of the $HPO_4^{2-}$ group, which is absent in α-TCP and present in CDHA structure. Evidently, intensity of this band gradually increases with an increase of soaking time, which caused by appearance of higher number of $HPO_4^{2-}$ groups in analyzed powders. Moreover, a weak band at 636 $cm^{-1}$, which appears only after 4 h of soaking, is also assigned to hydroxyl group [174]. The same trends were observed for Mn-doped α-TCP samples (Fig. 21b).

The SEM micrographs of CDHA powders obtained from pristine and 1 mol% Mn-doped α-TCP powders are represented in Fig. 22. It is seen that morphology of both samples after hydrolysis has changed considerably compared to untreated α-TCP powders. Hydrolyzed powders consist of flake-like particles, which form some larger agglomerates. Such morphological features are typical for CDHA crystals derived from α-TCP *via* hydrolysis process [175]. It is hard to estimate actual agglomerate size due to unclear border lines, but approximate size of clusters varied from 700 to 2000 nm. The size of CDHA particles derived from pristine α-TCP was observed to be smaller compared to that of CDHA derived from α-TCP doped with 1 mol% of Mn.

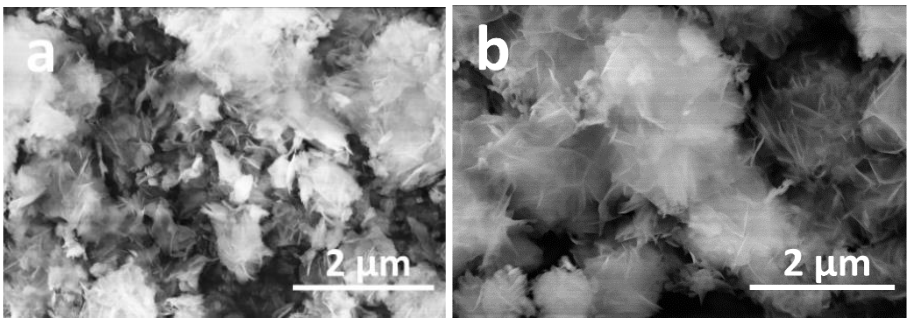

Fig. 22. SEM images of CDHA powders obtained from pristine α-TCP (a) and 1 mol% Mn-doped α-TCP (b) powders.

In order to determine actual composition of synthesized and fully hydrolyzed species, elemental analysis by means of ICP-OES was performed. The results of the analysis are summarized in Table 4.

Table 4. Results of the elemental analysis of the samples performed by ICP- OES.

| Sample | Before hydrolysis | | After hydrolysis | |
|---|---|---|---|---|
| | $\frac{n(Mn) \cdot 100\%}{n(Ca + Mn)}$ | $\frac{n(Mn) \cdot 100\%}{n(Ca + Mn)}$ | $\frac{n(Mn) \cdot 100\%}{n(Ca + Mn)}$ | $\frac{n(Mn) \cdot 100\%}{n(Ca + Mn)}$ |
| $Ca_3(PO_4)_2$ | - | 1.47 | - | 1.47 |
| $Ca_3(PO_4)_2$: 0.5% $Mn^{2+}$ | 0.518 | 1.49 | 0.520 | 1.49 |
| $Ca_3(PO_4)_2$: 1.0% $Mn^{2+}$ | 1.02 | 1.49 | 1.03 | 1.49 |

It is clearly seen that determined molar percentage of Mn in α-TCP samples is in good agreement with nominal values indicating successful synthesis of products with aspired substitution level. On the other hand, total metals to phosphorus ratio shows slightly lower values compared to theoretical. It is also notable, that chemical composition of powders did not change after hydrolysis process. These results indicate that there is no selective ion release during hydrolysis.

Fig. 23 shows the pH values of the aqueous solutions after soaking of α- TCP powders for various periods of time.

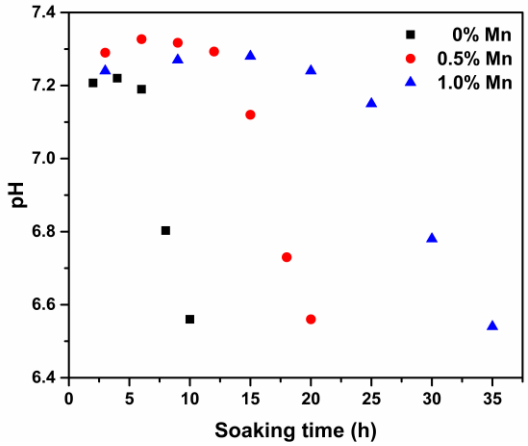

Fig. 23. Dependence of medium pH on soaking time.

The identical trend is clearly seen for all samples regardless of chemical composition of powders. On the early stage of hydrolysis pH is slightly basic and varies in the range from 7.2 to 7.3. The deviation from the pH value typically observed for deionized water after a contact with air is associated with dissolution of α-TCP, which leads to the appearance of $HPO_4^{2-}$ and $OH^-$ ions in surrounding media [176]. The initial pH is nearly constant until it starts to decrease at the particular stage of hydrolysis. The pH values start to decrease when CDHA becomes a major constituent of treated powders. The decrease of pH indicates precipitation of dissolved of $HPO_4^{2-}$ and $OH^-$ ions in the form of CDHA. Since $Mn^{2+}$ ions significantly inhibit hydrolysis process, the decrease of pH values for different samples is observed at different times with the shortest time for pristine α-TCP and the longest time for α-TCP doped with 1 mol% of Mn. The pH value at the point of complete transformation to CDHA was observed nearly equal for all samples and was determined at around 6.5.

### 3.4. Synthesis and luminescent properties of Mn-doped α-TCP

The phase crystallinity and purity of all synthesized α-TCP powders were investigated by means of XRD analysis. The XRD patterns of representative CPs precipitates doped with different amounts of $Mn^{2+}$ ions and annealed at 1250 °C are demonstrated in Fig. 24.

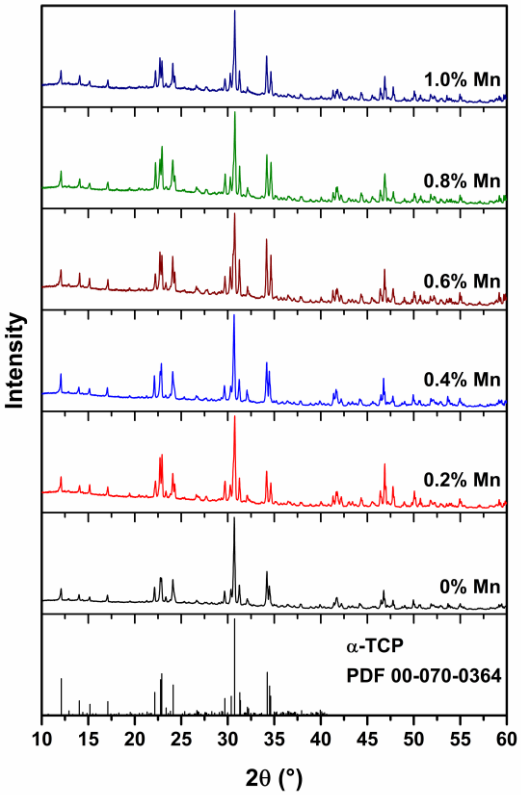


Fig. 24. XRD patterns of α-TCP doped with different amounts of Mn.

The obtained results clearly indicate that after the thermal treatment α-TCP crystal phase was formed regardless of chemical composition of the samples. All diffraction peaks can be attributed to monoclinic $Ca_3(PO_4)_2$ and match well the standard XRD data (ICDD 00-070-0364). Not even traces of β-TCP polymorph were detected, indicating complete transformation of initial CP precursor to α-TCP and successful prevention of reversible phase transition, which was achieved by a thermal quenching.

Fig. 25 illustrates PL excitation and emission spectra of Mn-doped α-TCP powders at room temperature.

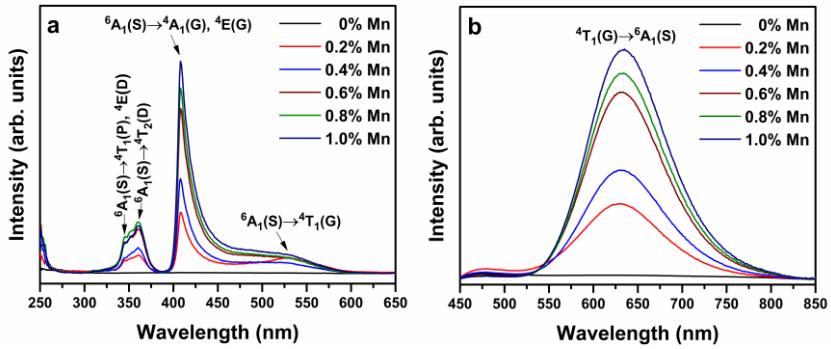


Fig. 25. Excitation (a) ($\lambda_{em}$ = 670 nm) and emission (b) ($\lambda_{ex}$ = 408 nm) spectra of Mn-doped α-TCP

Exploring the PL excitation spectra for 670 nm emission in the range from 250 to 650 nm (Fig. 25a), it is evident that undoped α-TCP sample is optically inactive. In the spectra of all Mn doped samples few excitation bands centered at around 345, 360, 408 and 529 nm were clearly observed. These bands correspond to the transitions from the $^6A_1(S)$ level to the [$^4T_1(P)$, $^4E(D)$], $^4T_2(D)$, [$^4A_1(G)$, $^4E(G)$] and $^4T_1(G)$ levels, respectively. There is also one intense band at around 250 nm, which is caused by the charge transfer state of $O^{2-}$–$Mn^{2+}$ transition [177-180]. The PL emission spectra of the samples excited by 408 nm radiation possess a single broadband emission in the range of around 525-825 nm and centered at about 630 nm (Fig. 25b). Such emission spectrum is characteristic of a 3d-3d emission band of $Mn^{2+}$ ions which is attributed to transition from exited $^4T_1(G)$ state to the fundamental $^6A_1(S)$ energy level [177, 181, 182]. All Mn-containing samples showed concentration-dependent behavior of both excitation and emission spectra. It is clearly seen that higher doping level results in stronger excitation and emission signals and the highest values were observed for α-TCP doped with 1 mol% of Mn ions.

Fig. 26 shows PL emission decay curves of Mn-doped α-TCP powders when specimens were excited at 408 nm and emission monitored at 670 nm.

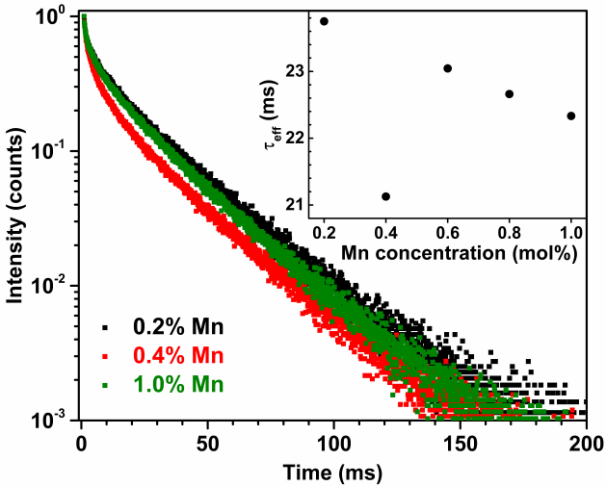


Fig. 26. PL decay ($\lambda_{ex}$ = 408 nm, $\lambda_{em}$ = 670 nm) curves of Mn-doped α-TCP at room temperature. Inset: calculated effective PL lifetime values.

As observed, the decay curves are very similar regardless of Mn content in the samples. It is obvious that with an increase of Mn concentration the effective PL lifetime values decrease. This dependence shows clearly linear behavior with an exception for the sample containing 0.4 mol% of Mn, which is clearly out of this trend. In order to correct this outlier, additionally 5 α-TCP samples doped with 0.4 mol% of Mn, samples were synthesized. However, all extra syntheses were reproducible and showed the same optical properties and $\tau_{eff}$ values. Therefore, the reason of such anomalous behavior is unclear. Unfortunately, the performed XPS analysis did not provide any information about the presence of other than $Mn^{2+}$ valence states because of lack of sensitivity, since concentrations of Mn are rather low. Possible occupancy of another crystallographic site is also hardly provable because of the same reason and large number of Ca sites (18 inequivalent Ca sites) in α-TCP structure.

### 3.5. Thermally induced crystallization and phase evolution of ACP substituted with divalent cations of different size

Four series of ACPs substituted with different amounts of $Mg^{2+}$, $Zn^{2+}$, $Sr^{2+}$ and $Ba^{2+}$ ions were prepared in order to investigate an influence of these substituents on crystallization behavior of ACP. The XRD patterns of the pristine ACP annealed at different temperatures are shown in Fig. 27.

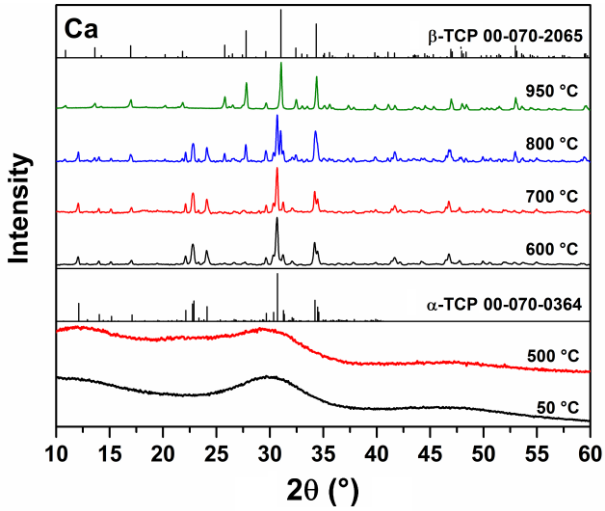


Fig. 27. XRD patterns of pristine ACP powders annealed at different temperatures.

The crystallization process starts at around 600 °C with a formation of α-TCP. At higher temperatures, gradual transformation to β-TCP occurs, with the coexistence of two polymorphs being the most obvious after annealing at 800 °C. The XRD pattern of the powders annealed at 900 °C is dominated by the reflections of β-TCP and only a negligible amount of α-TCP can be detected. Complete transformation to β-TCP was observed at around 950 °C.

The XRD patterns of the as-prepared ACP substituted with different amounts of Mg ions and annealed at 700 °C are represented in Fig. 28a. This temperature was selected as a representative temperature. The substitution level of 1 mol% already induces different crystallization behavior compared to the pristine ACP and promotes the formation of β-TCP. The coexistence of two polymorphs is clearly seen. When Mg content reaches 2.5 mol%, all diffraction peaks are associated with β-TCP and no signals arising from α-TCP can be observed. With further increase in the Mg content, no phase transitions were expectedly detected. Fig. 28b represents the phase evolution of ACP substituted with the maximal amount of Mg. As seen, after the heat treatment at 500 °C, the sample exists in amorphous form and after annealing at 600 °C crystallizes to β-TCP without an intermediate α-TCP phase. The temperature of the formation of β-TCP is significantly lower compared to that of the undoped ACP (see Fig. 27).

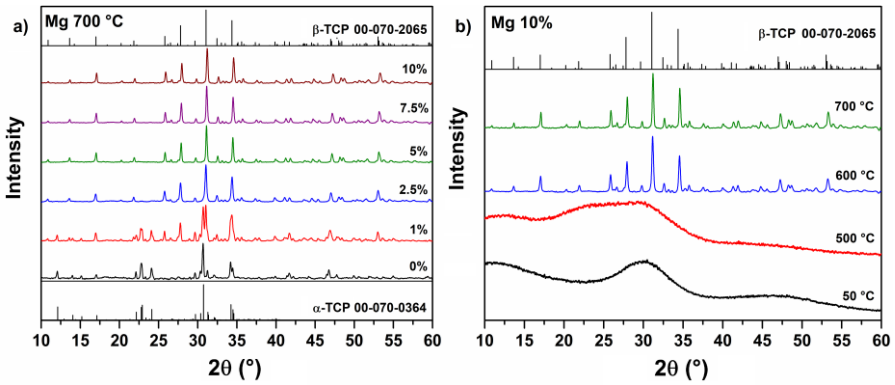


Fig. 28. XRD patterns of the ACP powders doped with different amounts of Mg and annealed at 700 °C (a); XRD patterns of ACP powders substituted with 10 mol% of Mg and annealed at different temperatures (b).

The XRD patterns of the as-prepared ACP substituted with different amounts of Zn ions and annealed at 700 °C are represented in Fig. 29a.

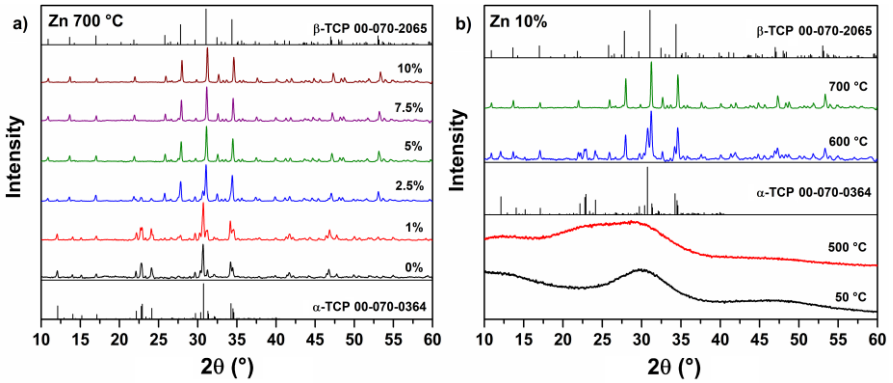


Fig. 29. XRD patterns of the ACP powders doped with different amounts of Zn and annealed at 700 °C (a); XRD patterns of ACP powders substituted with 10 mol% of Zn and annealed at different temperatures (b).

The trend in the obtained XRD patterns was similar to that of in the Mg-doped ACP case. The crystal phase transformation from α-TCP to β-TCP goes hand in hand with an increase in the concentration of Zn ions. However, in this case, the mentioned transition occurs slower in comparison with that in the case of Mg-doped ACP. The full transformation was observed at a higher substitution level, even for the sample containing 5 mol% of Zn ions, an insignificant amount of α-TCP can be detected. Most likely, the phase transition occurs at an intermediate concentration between 5 and 7.5 mol%. Moreover, there were

no secondary crystal phases detected even for a sample with the highest Zn content, indicating the formation of single-phase β-TCP.

The XRD patterns of the Sr-doped ACP annealed at 700 °C are displayed in Fig. 30a.

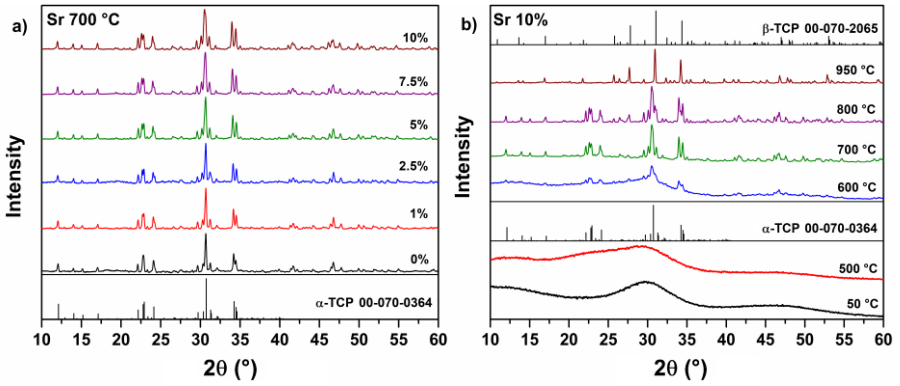


Fig. 30. XRD patterns of the ACP powders doped with different amounts of Sr and annealed at 700 °C (a); XRD patterns of ACP powders substituted with 10 mol% of Sr and annealed at different temperatures (b).

It can be seen that the substitution by $Sr^{2+}$ ions has a different effect in comparison with that induced by smaller ions. All samples were identified as α-TCP, and no β-TCP crystal phase was detected even at the highest substitution level of strontium. Fig. 30b illustrates the phase evolution of Sr-doped ACP with 10 mol% of Sr ions and annealed at different temperatures. A notable feature is that Sr ions at such concentration retard the crystallization process. It is seen that after annealing at 600 °C, poorly crystalline α-TCP was formed, since the obtained diffraction peaks are very broad and of low intensity. At higher temperatures (700 °C), the degree of crystallinity increases significantly and the phase-pure α-TCP was identified. Further increase in the annealing temperature resulted in a gradual phase transformation to β-TCP, which was obtained in its pure form at 950 °C. It can be concluded that the substitution by Sr ions does not lead to concentration-dependent phase transitions between TCP polymorphs. Moreover, it does not thermally stabilize α-TCP, with the phase transition to β-TCP occurring at the same temperature that was determined for pristine ACP (950 °C).

The XRD patterns of the Ba-doped ACP annealed at 700 °C are shown in Fig. 31a.

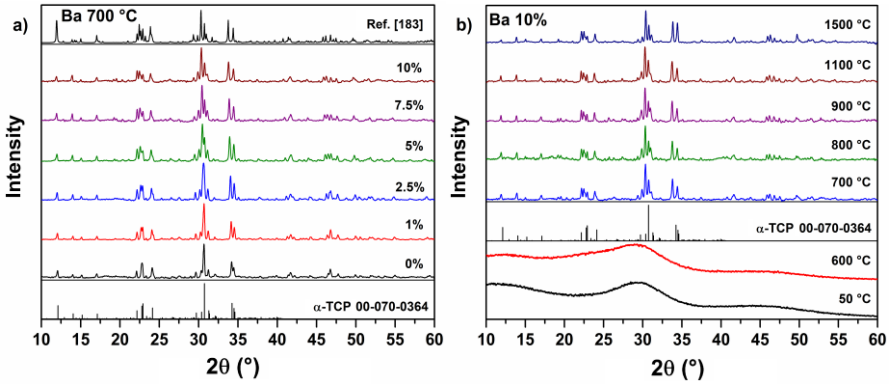


Fig. 31. XRD patterns of (a) the ACP powders doped with different amounts of Ba and annealed at 700 °C; (b) XRD patterns of ACP powders substituted with 10 mol % of Ba and annealed at different temperatures.

The observed trend is similar to that induced by Sr ions. For all substitution levels, the α-TCP crystal phase was identified, and β-TCP was not detected in any sample. At the same time, structural changes of α-TCP phase can be noticed. However, the evolution of the XRD patterns corresponds to the internal structural changes of α-TCP, but not to the formation of secondary crystal phases. For comparison, the XRD pattern of 10 mol% Ba-doped α- TCP reported by Yashima and Kawaike [183] was added. These authors performed a detailed study on the crystal structure and the site preference of the Ba-doped α-TCP through high-resolution synchrotron powder diffraction. It is seen that the XRD pattern of our synthesized sample matches very well the previously reported data. Fig. 31b shows the XRD patterns of Ba-doped ACP with 10 mol% Ba ions and annealed at different temperatures. Unlike in previous cases (see Figs. 28b, 29b, and 30b), after annealing at 600 °C, the synthesized powder was still amorphous and crystalline α-TCP was obtained only after annealing at 700 °C. Another distinctive feature is that the presence of Ba ions in such concentration stabilizes α-TCP and completely prevents the phase transformation to β-TCP. The obtained sample was annealed at different temperatures up to 1500 °C and no phase transition was detected.

### 3.6. Fe and Zn co-substituted β-TCP: Synthesis, structural, magnetic, mechanical and biological properties

The phase crystallinity and purity of annealed powders were characterized by XRD analysis. The XRD patterns and lattice parameters of β-TCP samples

containing different amounts of substituent ions and annealed at 800 °C are given in Fig. 32.

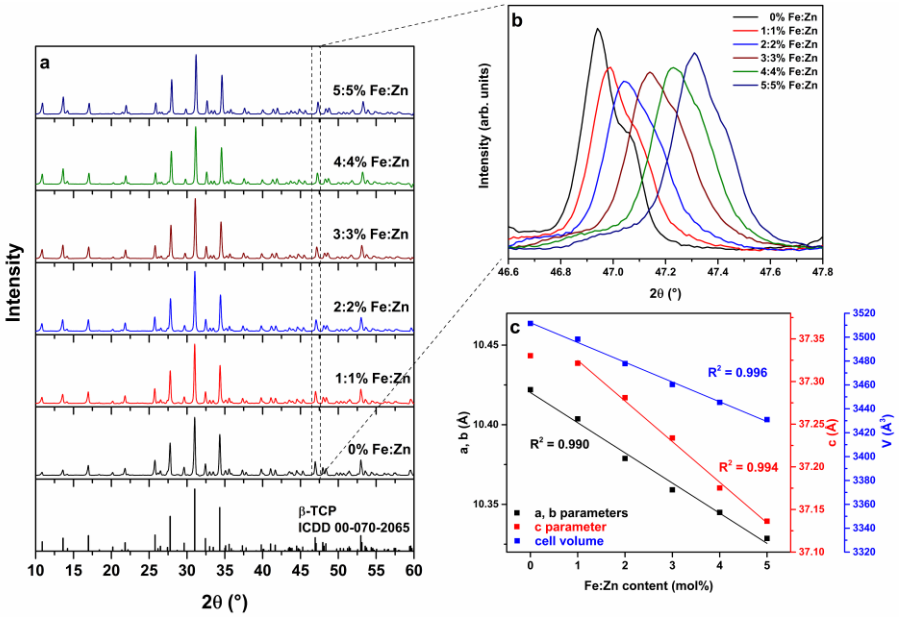


Fig. 32. XRD patterns of β-TCP powders (a, b) and lattice parameters of β-TCP powders (c) with different amounts of Fe and Zn.

Regardless of chemical composition all synthesized products crystallized to β-TCP phase. All diffraction peaks match very well standard XRD data of rhombohedral $Ca_3(PO_4)_2$ (ICDD 00-070-2065) and no reflections assigned to potential secondary crystal phases such as Fe or Zn phosphates were detected (Fig. 32a). Closer look at the diffraction patterns reveals gradual shift of diffraction peaks towards higher 2θ values (Fig. 32b). Such changes in the XRD patterns are explained by the mismatch in size between Ca and foreign ions and can be considered as an evidence of successful incorporation of smaller than $Ca^{2+}$ substituent ions into β-TCP crystal lattice. Dependence of calculated lattice parameters on substitution level in β-TCP powders is depicted in Fig. 32c. It is evident that lattice parameters *a* and *b* gradually decrease as substitution level increases. The decrease is linear, what is in line with $R^2$ values of linear fit of experimental data being close to unity. Slightly different behavior was observed for parameter *c*, which shows linear decrease only for samples with Fe and Zn content level ranged from 1 to 5 mol%, while parameter *c* of pristine β-TCP is out of this trend. This suggests that initially cell volume reduces mostly due to the changes of crystal lattice in *a* and *b*

directions. Rietveld refinement showed that foreign ions preferably occupy Ca(5) site in crystal lattice up to 4 mol% co-substitution level. Occupation of this site is in good agreement with previously reported theoretical and experimental studies on substituted β-TCP, which is characterized by low defect formation energies for small guest cations on octahedral Ca(5) site [38, 89, 184]. With the highest substitution level part of foreign ions also occupy Ca(4) site, which is also in good agreement with previously reported data for highly doped β-TCP [89, 151].

Vibrational spectroscopy was also employed to investigate the effect of substitution and check the presence of neighboring amorphous or crystalline materials, which are hardly detectable by XRD analysis in the presence of major β-TCP phase. Raman spectra of the synthesized β-TCP powders are depicted in Fig. 33.

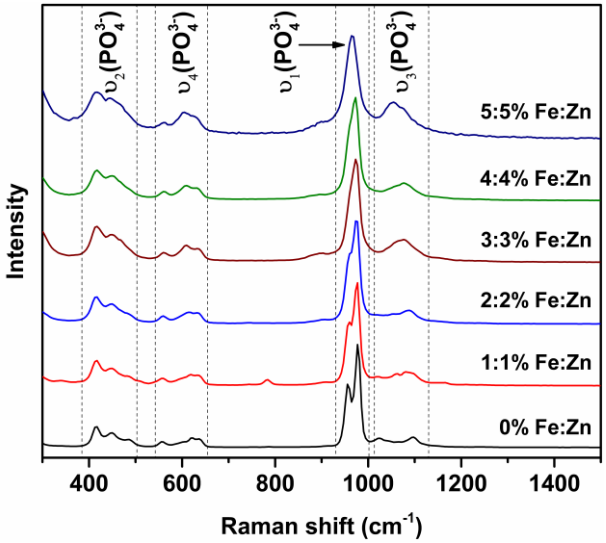


Fig. 33. Raman spectra of β-TCP powders with different amounts of Fe and Zn.

Four main groups of signals are clearly seen for all analyzed compounds. All obtained spectra are dominated by $\upsilon_1$ vibration mode located in the range of 930-1000 $cm^{-1}$. Other groups are seen in the range of approximately 385-500, 540-655 and 1015-1130 $cm^{-1}$ and attributed to $\upsilon_2$, $\upsilon_4$, and $\upsilon_3$ modes, respectively [185, 186]. It is obvious that shape of Raman spectra gradually changes as content of Fe and Zn ions increases. The split peak assigned to $\upsilon_1$ vibration mode for highly substituted samples is broadened and transformed into the single peak indicating lattice distortion induced by incorporation of foreign ions. Other signals with increase of substitution level also lose their

well-defined shape and became broadened. Week signal at around 785 $cm^{-1}$ is assigned to calcium pyrophosphate secondary phase, which is frequently found as an impurity in β-TCP powders prepared by precipitation method [187, 188].

Room temperature dependence of magnetization of β-TCP powders of all compositions on applied magnetic field strength is illustrated in Fig. 34.

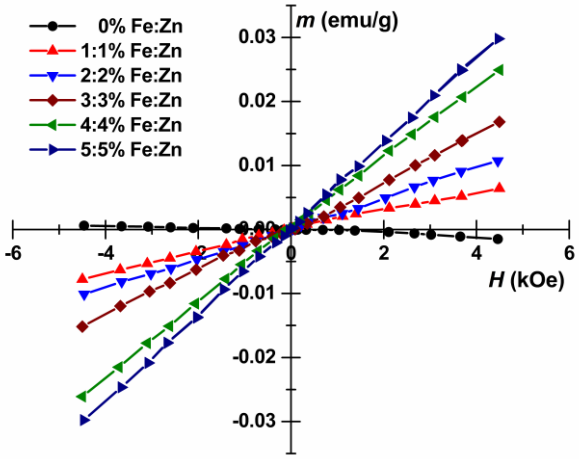


Fig. 34. Magnetization dependence on magnetic field strength for β-TCP powders with different amounts of Fe and Zn.

Different magnetic behavior of β-TCP samples depending on the presence of foreign ions is evident. Pristine sample shows weak diamagnetic properties. Different behavior is observed for Fe and Zn-containing powders, which clearly exhibit paramagnetic behavior. Magnetization values are linearly proportional to applied magnetic field strength, moreover magnetization obviously increases as Fe content in the samples increases. No saturation of magnetization was observed regardless of chemical composition of the samples in studied magnetic field range.

SEM was employed in order to investigate influence of foreign ions and their concentration on morphological features of β-TCP samples. SEM micrographs of pristine β-TCP powders and powders substituted with the highest amount of Fe and Zn are shown in Fig. 35.

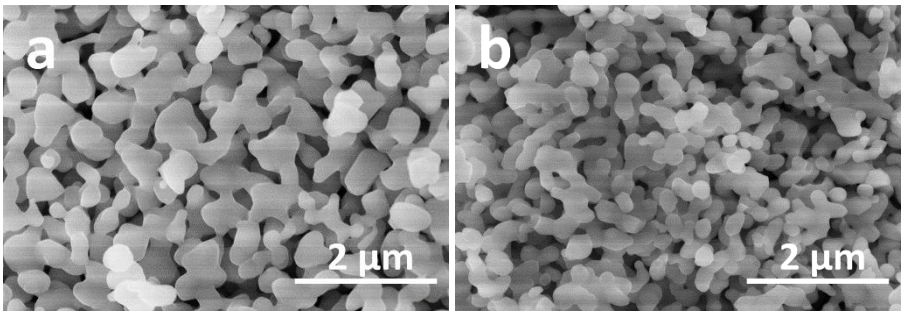


Fig. 35. SEM images of pristine β-TCP (a) and β-TCP powders co-substituted with 5 mol% of Fe and Zn (b).

It is seen that non-substituted β-TCP powders consist of mostly uniform particles of irregular shape, which are highly connected to each other and form porous aggregates. The grain size varies from approximately 200 to 500 nm. Substitution with Fe and Zn does not change porous nature of the aggregated powders, however it obviously affects the grain size, which was reduced significantly. The observed particles showed prolonged irregular shape with thickness of around 150–200 nm and length up to 1 µm.

In order to determine toxicity of the synthesized products, *in vivo* cytotoxicity assay was performed in solutions containing 1 wt% of β-TCP powders using zebrafish embryos. Digital photographs of zebrafish embryos taken at different time of presence in β-TCP-containing solutions are demonstrated in Fig. 36.

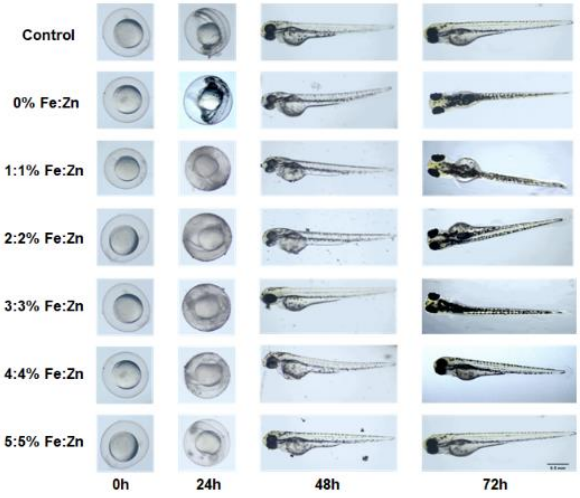


Fig. 36. Digital photographs of zebrafish embryos at different stages of growth in solutions containing β-TCP powders with different amount of Fe and Zn.

Evidently, embryos grown in different media visually do not differ from control zebrafish embryos, there are no visible hybridizations or anomalies caused by interaction with pristine or co-substituted β-TCP. Detailed data on hatching rate, survival rate and body length of zebrafish embryos grown in solutions with β-TCP powders for 72 h are summarized in Table 5.

Table 5. Hatching rate, survival rate and body length of zebrafish embryos grown in solutions containing β-TCP powders for 72 h ($N$=10).

| Sample | Hatching rate (%) | Survival rate (%) | Body length (mm) |
|---|---|---|---|
| E3 medium | 90 | 90 | 3.26 ± 0.21 |
| 0% Fe:Zn | 80 | 80 | 3.42 ± 0.24 |
| 1:1% Fe:Zn | 90 | 90 | 3.27 ± 0.42 |
| 2:2% Fe:Zn | 80 | 80 | 3.50 ± 0.27 |
| 3:3% Fe:Zn | 100 | 100 | 3.55 ± 0.24 |
| 4:4% Fe:Zn | 90 | 90 | 3.55 ± 0.13 |
| 5:5% Fe:Zn | 100 | 90 | 3.61 ± 0.17 |

It is seen that hatching and survival rate for all samples vary in the range of 80 to 100%, which is very close to the values obtained for control species, which are 90% for both parameters. Moreover, there are no trends, which could be associated with amount of Fe and Zn in investigated samples. On the other hand, there is a visible trend in the body length of the embryos. With the only exception for β-TCP with 1 mol% of Fe and Zn, mean values of the body length of the embryos monotonically increases as a concentration of foreign ions in β-TCP powders increases and exceeds body length of control embryos. Such behavior of zebrafish embryos in TCP-containing media together with an absence of visible anomalies indicate non-toxic nature of the synthesized powders.

All synthesized β-TCP powders were pressed into pellets and sintered in order to prepare ceramic bodies. Fig. 37 represents SEM images of polished and thermally etched surface of pristine β-TCP pellet and β-TCP pellet substituted with 5 mol% of Fe and Zn.

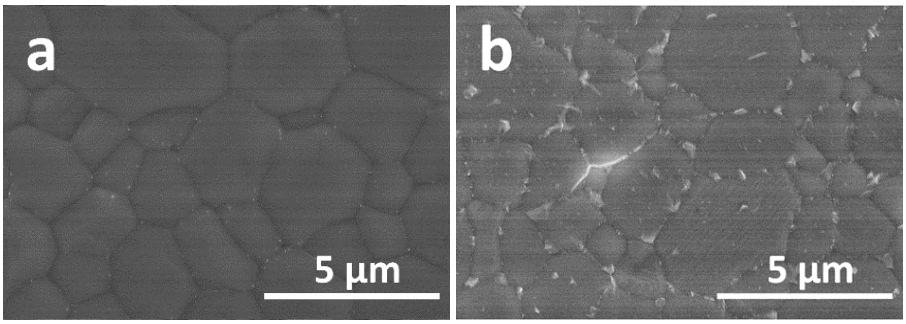


Fig. 37. SEM images of polished and thermally etched surface of pristine (a) β-TCP pellet and sample co-substituted with 5 mol% (b) of Fe and Zn and sintered at 1100 °C.

Surface of pure β-TCP pellet is composed of the grains varying in size in the range of approximately 1.5 to 7 µm. No cracks, holes or other clearly visible defects were observed. Substitution with foreign ions did not suppress or promote grain growth, which remained nearly the same in terms of size. Unfortunately, the highest substitution level resulted in formation of some visible cracks, moreover some deposits were observed in the grain boundaries.

Linear shrinkage , densities and Vickers hardness of sintered β-TCP pellets are given in Table 6.

Table 6. Linear shrinkage, density and Vickers hardness of β-TCP ceramics.

| Sample | Linear shrinkage (%) | Density (%) | Vickers hardness (GPa) |
|---|---|---|---|
| 0% Fe:Zn | 13 | 95 | 4.05 ± 0.27 |
| 1:1% Fe:Zn | 11 | 91 | 3.08 ± 0.18 |
| 2:2% Fe:Zn | 8 | 90 | 1.82 ± 0.05 |
| 3:3% Fe:Zn | 14 | 92 | 2.66 ± 0.06 |
| 4:4% Fe:Zn | 15 | 98 | 2.87 ± 0.11 |
| 5:5% Fe:Zn | 16 | 98 | 2.60 ± 0.06 |

It was observed, that linear shrinkage of the sintered pellets did not correlate with substitution level. Linear shrinkage was determined to be the highest for powders with 5 mol% of foreign ions and the lowest for powders with 2 mol% of Fe and Zn. Calculated relative densities of the sintered species also did not reveal any trends and varied in the range from 90 to 98% with the highest value for pellets with the highest substitution level. Vickers hardness measurements did not reveal improvement in mechanical properties of the prepared ceramics induced by substitution of Ca ions. Determined average

Vickers hardness ranged from 1.81 to 4.05 GPa, however the highest value was observed for pristine β-TCP ceramics and was in good agreement with previously reported values [98, 189-191]. The obtained results indicate, that partial substitution of Ca with Fe and Zn did not lead to superior mechanical properties.

# CONCLUSIONS

1. It was shown for the first time that phase-selective synthesis of TCP polymorphs can be achieved at almost the same temperature applying different kinds of liquids for the washing of as-prepared CP obtained by wet precipitation method. The nature and amount of washing agent determine amorphous or crystalline nature of the as-prepared species and the formation of TCP polymorphs after the thermal treatment. Washing of the as-prepared precipitates with water and AC and annealing at 775 °C led to the formation of β-TCP, while washing with ACN, EtOH and i- PrOH and annealing at 750 °C resulted in the crystallization of α-TCP.
2. Phase-selective preparation of α- and β-TCP polymorphs can be achieved at identical temperature (700 °C) through the doping with $Mn^{2+}$ ions. Increasing Mn content (5 mol%) resulted in the formation of β-TCP, while α-TCP was obtained without or with low Mn doping level (0–1 mol%). A mixture of two polymorphs was obtained for intermediate Mn concentrations. The obtained results are the first experimental work on the thermodynamic equilibrium between TCP polymorphs substituted with divalent cations.
3. It was demonstrated for the first time that the presence of $Mn^{2+}$ ions significantly retards hydrolysis of metastable α-TCP. Pristine, 0.5 and 1 mol% Mn-doped α-TCP fully hydrolyzed with the conversion to CDHA in 10, 20 and 35 h, respectively. The degree of crystallinity of starting TCP powders was comparable, indicating that inhibition process is associated not with the presence of amorphous phase, but with the formation of CDHA. Chemical composition of starting and fully hydrolyzed powders was identical, indicating that there is no selective ion release during the hydrolysis process.
4. Luminescent properties of Mn-doped α-TCP (doping level from 0.2 to 1 mol%) were studied for the first time. Mn-containing powders under excitation at 408 nm revealed a broadband emission in the range from 525 to 825 nm with a maximum centered at around 630 nm. Emission intensity was found to be dependent on Mn concentration and increased as Mn content increased. Photoluminescence lifetime values showed gradual decrease with an increase of Mn content.
5. Thermally induced crystallization and phase evolution of ACP partially substituted with smaller ($Mg^{2+}$, $Zn^{2+}$) and larger ($Sr^{2+}$, $Ba^{2+}$) divalent cations was investigated for the first time. Crystallization of ACP to TCP and further phase transformations between TCP polymorphs strongly depend on the size and concentration of substituents in ACP matrix.

Substitution with smaller ions does not affect crystallization temperature, however promotes the formation of β-TCP at significantly lower temperature compared to phase evolution of pristine ACP. Substitution with larger ions retards crystallization process, which was observed at elevated temperature. While substitution level of 10 mol% of Sr does not affect thermal stability of metastable α-TCP, the presence of 10 mol% of Ba stabilizes α-TCP crystal structure and totally prevents phase transition to β-TCP.

6. Wet precipitation method was successfully employed for the synthesis of β-TCP powders co-substituted with equal amounts of $Fe^{3+}$ and $Zn^{2+}$ ions in the range of 1-5 mol%. Structural analysis revealed gradual decrease in lattice parameters of the synthesized samples with an increase of substitution level. All substituted samples exhibited paramagnetic behavior, magnetization values were found to be proportional to $Fe^{3+}$ percentage in the synthesized powders. *In vivo* cytotoxicity assay did not reveal toxic behavior of the synthesized powders even with the highest content of foreign ions. Mechanical properties of sintered β-TCP pellets were not improved by substitution of $Ca^{2+}$ by foreign ions. Vickers hardness values were determined to be lower for substituted samples in comparison to those of undoped β-TCP.

# REFERENCES


[1] E. Jaul, J. Barron, *Front. Public Health*, 5 (2017) 335.
[2] R.W. Keen, *Curr. Osteoporos. Rep.*, 1 (2003) 66-70.
[3] I. Malkin, G. Bigman, R. Matias, L. Kalichman, M.J. Seibel, E. Kobyliansky, G. Livshits, *Arch. Osteoporos.*, 1 (2006) 59-68.
[4] E. Gomez-Barrena, P. Rosset, D. Lozano, J. Stanovici, C. Ermthaller, F. Gerbhard, *Bone*, 70 (2015) 93-101.
[5] J.R. Porter, T.T. Ruckh, K.C. Popat, *Biotechnol. Prog.*, (2009) 1539-1560.
[6] P.V. Giannoudis, J.J. Chris Arts, G. Schmidmaier, S. Larsson, *Injury*, 42 Suppl 2 (2011) S1-2.
[7] O. Faour, R. Dimitriou, C.A. Cousins, P.V. Giannoudis, *Injury*, 42 Suppl 2 (2011) S87-90.
[8] G. Fernandez de Grado, L. Keller, Y. Idoux-Gillet, Q. Wagner, A.M. Musset, N. Benkirane-Jessel, F. Bornert, D. Offner, *J. Tissue Eng.*, 9 (2018) 1-18.
[9] W. Habraken, P. Habibovic, M. Epple, M. Bohner, *Mater. Today*, 19 (2016) 69-87.
[10] E.A. Chudinova, M.A. Surmeneva, A.S. Timin, T.E. Karpov, A. Wittmar, M. Ulbricht, A. Ivanova, K. Loza, O. Prymak, A. Koptyug, M. Epple, R.A. Surmenev, *Colloids Surf. B Biointerfaces*, 176 (2019) 130-139.
[11] S.V. Dorozhkin, *Materials*, 6 (2013) 3840-3942.
[12] R.G. Carrodeguas, S. De Aza, *Acta Biomater.*, 7 (2011) 3536-3546.
[13] C. Tong, Y. Zhu, C. Xu, L. Yang, Y. Li, *Physica B: Condens. Matter.*, 521 (2017) 153-157.
[14] S. Tkachenko, M. Horynova, M. Casas-Luna, S. Diaz-de-la-Torre, K. Dvorak, L. Celko, J. Kaiser, E.B. Montufar, *J. Mech. Behav. Biomed. Mater.*, 81 (2018) 16-25.
[15] M. Motisuke, G. Mestres, C.O. Reno, R.G. Carrodeguas, C.A.C. Zavaglia, M.P. Ginebra, *Mater. Sci. Eng. C Mater. Biol. Appl.*, 75 (2017) 816-821.
[16] C. Qi, J. Lin, L.H. Fu, P. Huang, *Chem. Soc. Rev.*, 47 (2018) 357-403.
[17] J. da Costa Reis, M.T. Oliveira, Bone: Functions, Structure and Physiology, in: J. Belinha, M.-C. Manzanares-Céspedes, A.M.G. Completo (Eds.) The Computational Mechanics of Bone Tissue: Biological Behaviour, Remodelling Algorithms and Numerical Applications, Springer International Publishing, Cham, 2020, pp. 3-43.
[18] U.G. Wegst, H. Bai, E. Saiz, A.P. Tomsia, R.O. Ritchie, *Nat. Mater.*, 14 (2015) 23-36.
[19] S. Dorozhkin, *Materials*, 2 (2009) 399-498.
[20] A.L. Boskey, R. Coleman, *J. Dent. Res.*, 89 (2010) 1333-1348.
[21] E. Boanini, M. Gazzano, A. Bigi, *Acta Biomater.*, 6 (2010) 1882-1894.
[22] N. Eliaz, N. Metoki, *Materials*, 10 (2017).
[23] S.V. Dorozhkin, *J. Mater. Sci.*, 44 (2009) 2343-2387.

[24] Q. Liu, S. Huang, J.P. Matinlinna, Z. Chen, H. Pan, *Biomed Res. Int.*, 2013 (2013) 929748.
[25] A.L. Boskey, *Bonekey Rep.*, 2 (2013) 447.
[26] A. Laskus, J. Kolmas, *Int. J. Mol. Sci.*, 18 (2017).
[27] E. Landi, G. Celotti, G. Logroscino, A. Tampieri, *J. Eur. Ceram. Soc.*, 23 (2003) 2931-2937.
[28] M. Vallet-Regi, D.A.A. Navarrete, Biomimetic Nanoceramics in Clinical Use: From Materials to Applications, 1st ed., Royal Society of Chemistry, 2008.
[29] C. Combes, S. Cazalbou, C. Rey, *Minerals*, 6 (2016) 34.
[30] C.F. Arias, M.A. Herrero, L.F. Echeverri, G.E. Oleaga, J.M. Lopez, *PLoS One*, 13 (2018) 1-19.
[31] B. Clarke, *Clin. J. Am. Soc. Nephrol.*, 3 Suppl 3 (2008) S131-139.
[32] A.K. Garg, Implant Dentistry: A Practical Approach, 2 ed., Mosby Elsevier, 2009.
[33] J.C. Elliott, Structure and Chemistry of the Apatites and Other Calcium Orthophosphates, Elsevier Science, 1994.
[34] S.V. Dorozhkin, *J. Mater. Sci.*, 42 (2007) 1061-1095.
[35] S.V. Dorozhkin, *Morphologie*, 101 (2017) 125-142.
[36] S.V. Dorozhkin, Calcium Orthophosphate-Based Bioceramics and Biocomposites, Wiley-VCH, 2016.
[37] M. Mathew, L.W. Schroeder, B. Dickens, W.E. Brown, *Acta Crystallogr. B*, 33 (1977) 1325-1333.
[38] K. Matsunaga, T. Kubota, K. Toyoura, A. Nakamura, *Acta Biomater.*, 23 (2015) 329-337.
[39] X. Yin, M.J. Stott, A. Rubio, *Phys. Rev. B*, 68 (2003).
[40] B. Dickens, W.E. Brown, *Acta Crystallogr. B*, 28 (1972) 3056-3065.
[41] P. Ge, K. Sun, H. Li, F. Yang, *Optik*, 203 (2020) 164040.
[42] M. Sadat-Shojai, M.T. Khorasani, E. Dinpanah-Khoshdargi, A. Jamshidi, *Acta Biomater.*, 9 (2013) 7591-7621.
[43] C.L. Camire, S.J. S-Jean, S. Hansen, I. McCarthy, L. McCarthy, *J. Appl. Biomater. Biomech.*, 3 (2005) 106-111.
[44] B. Jokic, I. Jankovic-Castvan, D. Veljković, R. Petrović, S. Drmanic, D. Janaćković, *Key Eng. Mater.*, 309-311 (2006) 821-824.
[45] J. Marchi, A.C.S. Dantas, P. Greil, J.C. Bressiani, A.H.A. Bressiani, F.A. Müller, *Mater. Res. Bull.*, 42 (2007) 1040-1050.
[46] S. Pina, S.M. Olhero, S. Gheduzzi, A.W. Miles, J.M. Ferreira, *Acta Biomater.*, 5 (2009) 1233-1240.
[47] N. Döbelin, T.J. Brunner, W.J. Stark, M. Eggimann, M. Fisch, M. Bohner, *Key Eng. Mater.*, 396-398 (2008) 595-598.
[48] M. Bohner, T.J. Brunner, N. Doebelin, R. Tang, W.J. Stark, *J. Mater. Chem.*, 18 (2008) 4460.
[49] N. Döbelin, T.J. Brunner, W.J. Stark, M. Fisch, E. Conforto, M. Bohner, *J. Am. Ceram. Soc.*, 93 (2010) 3455-3463.
[50] S. Somrani, C. Rey, M. Jemal, *J. Mater. Chem.*, 13 (2003) 888-892.

[51] M. Kitamura, C. Ohtsuki, H. Iwasaki, S.-I. Ogata, M. Tanihara, *J. Mater. Sci. Mater. Med.*, 15 (2004) 1153-1158.
[52] M. Fathi, A. El Yacoubi, A. Massit, B.C.E. Idrissi, *Int. J. Eng. Res.*, 6 (2015) 139-143.
[53] H. Ji, Z. Huang, Z. Xia, M.S. Molokeev, M. Chen, V.V. Atuchin, M. Fang, Y.G. Liu, X. Wu, J.A. Varela, *J. Am. Ceram. Soc.*, 98 (2015) 3280-3284.
[54] J.T. Zhang, F. Tancret, J.M. Bouler, *Mater. Sci. Eng. C*, 31 (2011) 740-747.
[55] C. Combes, C. Rey, *Acta Biomater.*, 6 (2010) 3362-3378.
[56] R.A.V. Santen, *J. Phys. Chem. Lett.*, 88 (1984) 5768-5769.
[57] G. Cicek, E.A. Aksoy, C. Durucan, N. Hasirci, *J. Mater. Sci. Mater. Med.*, 22 (2011) 809-817.
[58] K. Hurle, J. Neubauer, F. Goetz-Neunhoeffer, W.C. Wei, *J. Am. Ceram. Soc.*, 99 (2016) 1055-1063.
[59] K. Hurle, J. Neubauer, M. Bohner, N. Doebelin, F. Goetz-Neunhoeffer, *Acta Biomater.*, 10 (2014) 3931-3941.
[60] M.P. Ginebra, E. Fernández, F.C.M. Driessens, J.A. Planell, *J. Am. Ceram. Soc.*, 82 (1999) 2808-2812.
[61] U. Gbureck, J.E. Barralet, L. Radu, H.G. Klinger, R. Thull, *Journal of the American Ceramic Society*, 87 (2004) 1126–1132
[62] M. Yashima, A. Sakai, *Chem. Phys. Lett.*, 372 (2003) 779-783.
[63] C.L. Camire, U. Gbureck, W. Hirsiger, M. Bohner, *Biomaterials*, 26 (2005) 2787-2794.
[64] C. Durucan, P.W. Brown, *J. Mater. Sci.*, 37 (2002) 963– 969.
[65] X. Wei, O. Ugurlu, M. Akinc, *J. Am. Ceram. Soc.*, 90 (2007) 2315-2321.
[66] J.C. Colpo, C. Pigatto, N. Brizuela, J. Aragón, L.A.L. dos Santos, *J. Mater. Sci.*, 53 (2018) 7112-7124.
[67] E.C.S. Rigo, L.A.D. Santos, L.C.O. Vercik, R.G. Carrodeguas, A.O. Boschi, *Lat. Am. Appl. Res.*, 37 (2007) 267-274.
[68] C.L. Camire, P. Nevsten, L. Lidgren, I. McCarthy, *J. Biomed. Mater. Res. B Appl. Biomater.*, 79 (2006) 159-165.
[69] L.A.D. Santos, L.C.D. Oliveira, E.C.S. Rigo, R.G. Carrodeguas, A.O. Boschi, A.C.F.D. Arruda, *Bone*, 25 (1999) 99S-102S.
[70] M. Bohner, J. LeMaitre, A.P. LeGrand, J.-B.D.E.d.l. Caillerie, P. Belgrand, *J. Mater. Sci. Mater. Med.*, 7 (1996) 457-463.
[71] R. Famery, N. Richard, P. Boch, *Ceram. Int.*, 20 (1994) 327-336.
[72] N.L. Vollmer, J.R. Spear, R.A. Ayers, *J. Mater. Sci. Mater. Med.*, 27 (2016) 104.
[73] R. Ayers, S. Nielsen-Preiss, V. Ferguson, G. Gotolli, J.J. Moore, H.-J. Kleebe, *Mater. Sci. Eng. C*, 26 (2006) 1333-1337.
[74] N. Vollmer, R. Ayers, *Int. J. Self Propag. High Temp. Synth.*, 21 (2013) 189-201.
[75] T.M. Volkmer, L.L. Bastos, V.C. Sousa, L.A. Santos, *Key Eng. Mater.*, 396-398 (2008) 591-594.

[76] S.V. Dorozhkin, *J. Funct. Biomater.*, 4 (2013) 209-311.
[77] M.B. Thürmer, C.E. Diehl, L.A.L. dos Santos, *Ceram. Int.*, 42 (2016) 18094-18099.
[78] A.F. Vasquez, S. Dominguez, L.A. Loureiro Dos Santos, *Mater. Sci. Eng. C Mater. Biol. Appl.*, 81 (2017) 148-155.
[79] M. Roozbahani, M. Alehosseini, M. Kharaziha, R. Emadi, *Mater. Sci. Eng. C Mater. Biol. Appl.*, 81 (2017) 532-541.
[80] A. Zima, J. Czechowska, D. Siek, R. Olkowski, M. Noga, M. Lewandowska-Szumiel, A. Slosarczyk, *J. Mater. Sci. Mater. Med.*, 28 (2017) 117.
[81] L.W.S. B. Dickens, W.E. Brown, *J. Solid State Chem.*, 10 (1974) 232-248.
[82] M. Yashima, A. Sakai, T. Kamiyama, A. Hoshikawa, *J. Solid State Chem.*, 175 (2003) 272-277.
[83] K. Spaeth, F. Goetz-Neunhoeffer, K. Hurle, *J. Solid State Chem.*, 285 (2020) 121225.
[84] G. Renaudin, S. Gomes, J.M. Nedelec, *Materials*, 10 (2017).
[85] M. Bohner, B.L.G. Santoni, N. Dobelin, *Acta Biomater.*, 113 (2020) 23-41.
[86] L. Liu, Y. Wu, C. Xu, S. Yu, X. Wu, H. Dai, *J. Nanomater.*, 2018 (2018) 1-7.
[87] V. Uskokovic, S. Markovic, L. Veselinovic, S. Skapin, N. Ignjatovic, D.P. Uskokovic, *Phys. Chem. Chem. Phys.*, 20 (2018) 29221-29235.
[88] R. Enderle, F. Gotz-Neunhoeffer, M. Gobbels, F.A. Muller, P. Greil, *Biomaterials*, 26 (2005) 3379-3384.
[89] A. Bigi, E. Foresti, M. Gandolfi, M. Gazzano, N. Roveri, *J. Inorg. Biochem.*, 66 (1997) 259-265.
[90] N. Jinlong, Z. Zhenxi, J. Dazong, *J. Mater. Synth. Process*, 9 (2002) 235-240.
[91] M. Bohner, J. Lemaître, T.A. Ring, *J. Colloid Interface Sci.*, 190 (1997) 37-48.
[92] C. Stahli, J. Thuring, L. Galea, S. Tadier, M. Bohner, N. Dobelin, *Acta Crystallogr. B Struct. Sci. Cryst. Eng. Mater.*, 72 (2016) 875-884.
[93] J. Tao, W. Jiang, H. Zhai, H. Pan, X. Xu, R. Tang, *Cryst. Growth Des.*, 8 (2008) 2227-2234.
[94] J. Tao, H. Pan, H. Zhai, J. Wang, L. Li, J. Wu, W. Jiang, X. Xu, R. Tang, *Cryst. Growth Des.*, 9 (2009) 3154–3160.
[95] L. Galea, M. Bohner, J. Thuering, N. Doebelin, C.G. Aneziris, T. Graule, *Biomaterials*, 34 (2013) 6388-6401.
[96] J.S. Bow, S.C. Liou, S.Y. Chen, *Biomaterials*, 25 (2004) 3155-3161.
[97] C. Makarov, I. Gotman, X. Jiang, S. Fuchs, C.J. Kirkpatrick, E.Y. Gutmanas, *J. Mater. Sci. Mater. Med.*, 21 (2010) 1771-1779.
[98] R. Ghosh, R. Sarkar, *Mater. Sci. Eng. C Mater. Biol. Appl.*, 67 (2016) 345-352.

[99] K.P. Sanosh, M.-C. Chu, A. Balakrishnan, T.N. Kim, S.-J. Cho, *Curr. Appl. Phys.*, 10 (2010) 68-71.
[100] D. Thomas, S. Su, J. Qiu, M.L. Pantoya, *Mater. Today Commun.*, 9 (2016) 47-53.
[101] S. Loher, W.J. Stark, M. Maciejewski, A. Baiker, S.E. Pratsinis, D. Reichardt, F. Maspero, F. Krumeich, D. Günther, *Chem. Mater.*, 17 (2005) 36-42.
[102] B. Liu, D.X. Lun, *Orthop. Surg.*, 4 (2012) 139-144.
[103] L. Witek, Y. Shi, J. Smay, *J. Adv. Ceram.*, 6 (2017) 157-164.
[104] P. Gao, H. Zhang, Y. Liu, B. Fan, X. Li, X. Xiao, P. Lan, M. Li, L. Geng, D. Liu, Y. Yuan, Q. Lian, J. Lu, Z. Guo, Z. Wang, *Sci. Rep.*, 6 (2016) 23367.
[105] J. Hu, Y. Hou, H. Park, M. Lee, *J. Biomed. Mater. Res. A*, 100 (2012) 1680-1686.
[106] J. Chou, T. Ito, M. Otsuka, B. Ben-Nissan, B. Milthorpe, *Adv. Healthc. Mater.*, 2 (2013) 678-681.
[107] T. Tanaka, Y. Kumagae, M. Chazono, H. Komaki, S. Kitasato, A. Kakuta, K. Marumo, *Open Biomed. Eng. J.*, 8 (2014) 52-59.
[108] S.V. Dorozhkin, *J. Mater. Sci. Mater. Med.*, 24 (2013) 1335-1363.
[109] C. Gungormus, A. Kilic, M.T. Akay, D. Kolankaya, *Environ. Toxicol. Pharmacol.*, 29 (2010) 111-116.
[110] S. V. Dorozhkin, *Int. J. Mater. Chem.*, 2 (2012) 19-46.
[111] F. Betts, A.S. Posner, *Mater. Res. Bull.*, 9 (1974) 353-360.
[112] M.W. Swift, C.G. Van de Walle, M.P.A. Fisher, *Phys. Chem. Chem. Phys.*, 20 (2018) 12373-12380.
[113] N. Kanzaki, G. Treboux, K. Onuma, S. Tsutsum, A. Ito, *Biomaterials*, 22 (2001) 2921-2929.
[114] G. Treboux, P. Layrolle, N. Kanzaki, K. Onuma, A. Ito, *J. Phys. Chem. Lett. A*, 104 (2000) 5111-5114.
[115] A.S. Posner, F. Betts, N.C. Blumenthal, *Prog. Cryst. Growth Charact. Mater.*, 3 (1980) 49-64.
[116] S. Kim, H.-S. Ryu, H.S. Jung, K.S. Hong, *Met. Mater. Int.*, 10 (2004) 171-175.
[117] Z.Z. Zyman, D.V. Rokhmistrov, V.I. Glushko, *J. Mater. Sci. Mater. Med.*, 21 (2010) 123-130.
[118] B. Szilágyi, N. Muntean, R. Barabás, O. Ponta, B.G. Lakatos, *Chem. Eng. Res. Des.*, 93 (2015) 278-286.
[119] R.D. Piazza, T.A.G. Pelizaro, J.E. Rodriguez-Chanfrau, A.A. La Serna, Y. Veranes-Pantoja, A.C. Guastaldi, *Mater. Chem. Phys.*, 239 (2020) 122004.
[120] X. Niu, L. Wang, F. Tian, L. Wang, P. Li, Q. Feng, Y. Fan, *J. Mech. Behav. Biomed. Mater.*, 54 (2016) 131-140.
[121] J.A. Stammeier, B. Purgstaller, D. Hippler, V. Mavromatis, M. Dietzel, *MethodsX*, 5 (2018) 1241-1250.
[122] K. Pakravanan, M. Rezaee Roknabadi, F. Farzanegan, A. Hashemzadeh, M. Darroudi, *Green Chem. Lett. Rev.*, 12 (2019) 278-285.

[123] D. Lee, P.N. Kumta, *Mater. Sci. Eng. C*, 30 (2010) 1313-1317.
[124] M. Schweikle, S.H. Bjornoy, A.T.J. van Helvoort, H.J. Haugen, P. Sikorski, H. Tiainen, *Acta Biomater.*, 90 (2019) 132-145.
[125] L.M. Grover, A.J. Wright, U. Gbureck, A. Bolarinwa, J. Song, Y. Liu, D.F. Farrar, G. Howling, J. Rose, J.E. Barralet, *Biomaterials*, 34 (2013) 6631-6637.
[126] X.M. Wang, Y. Yan, H.H. Ren, S.Y. Li, *J. Biomater. Appl.*, 34 (2019) 273-283.
[127] M. Luginina, R. Orru, G. Cao, D. Grossin, F. Brouillet, G. Chevallier, C. Thouron, C. Drouet, *J. Mater. Chem. B*, 8 (2020) 629-635.
[128] E. Lerner, R. Azoury, S. Sarig, *J. Cryst. Growth*, 97 (1989) 725-730.
[129] N. Ikawa, T. Kimura, Y. Oumi, T. Sano, *J. Mater. Chem.*, 19 (2009) 4906.
[130] A. Lebugle, E. Zahidi, G. Bonel, *React. Solid.*, 2 (1986) 151-161.
[131] Y. Li, W. Weng, *J. Mater. Sci. Mater. Med.*, 18 (2007) 2303-2308.
[132] Y. Li, W. Weng, K. Cheng, P. Du, G. Shen, J. Wang, G. Han, *J. Mater. Sci. Lett.*, 22 (2003) 1015-1016.
[133] J. Tao, H. Pan, H. Zhai, J. Wang, L. Li, J. Wu, W. Jiang, X. Xu, R. Tang, *Cryst. Growth Des.*, 9 (2009) 3154-3160.
[134] P. Layrolle, A. Lebugle, *Chem. Mater.*, 6 (1994) 1996-2004.
[135] B.H. Fellah, P. Layrolle, *Acta Biomater.*, 5 (2009) 735-742.
[136] P. Layrolle, A. Ito, T. Tateishi, *J. Am. Ceram. Soc.*, 81 (1988) 1421-1428.
[137] M. Ohta, T. Honma, M. Umesaki, A. Nakahira, *Key Eng. Mater.*, 309-311 (2006) 175-178.
[138] A.L. Anabelle Rodrigues, *Colloids Surf. A: Physicochem. and Eng. Asp.*, 145 (1998) 191-204.
[139] T. Yu, J. Ye, Y. Wang, *J. Biomed. Mater. Res. B Appl. Biomater.*, 90 (2009) 745-751.
[140] U. Gbureck, J.E. Barralet, L. Radu, H.G. Klinger, R. Thull, *J. Am. Ceram. Soc.*, 87 (2008) 1126-1132.
[141] U. Gbureck, *Biomaterials*, 24 (2003) 4123-4131.
[142] A. Tofighi, R. Palazzolo, *Key Eng. Mater.*, 284-286 (2005) 101-104.
[143] T.J. Brunner, M. Bohner, C. Dora, C. Gerber, W.J. Stark, *J. Biomed. Mater. Res. Part B Appl. Biomater.*, 83B (2007) 400-407.
[144] S. Le Grill, J. Soulie, Y. Coppel, P. Roblin, P. Lecante, O. Marsan, C. Charvillat, G. Bertrand, C. Rey, F. Brouillet, *J. Mater. Sci.*, 56 (2020) 1189-1202.
[145] R.A. Surmenev, M.A. Surmeneva, A.A. Ivanova, *Acta Biomater.*, 10 (2014) 557-579.
[146] N.M. Van den Vreken, I.Y. Pieters, H.A. Declercq, M.J. Cornelissen, R.M. Verbeeck, *Acta Biomater.*, 6 (2010) 617-625.
[147] K. Rubenis, S. Zemjane, J. Vecstaudza, J. Bitenieks, J. Locs, *J. Eur. Ceram. Soc.*, 41 (2021) 912-919.

[148] Y. Su, I. Cockerill, Y. Zheng, L. Tang, Y.X. Qin, D. Zhu, *Bioact. Mater.*, 4 (2019) 196-206.
[149] P.M. Torres, S.I. Vieira, A.R. Cerqueira, S. Pina, O.A. da Cruz Silva, J.C. Abrantes, J.M. Ferreira, *J. Inorg. Biochem.*, 136 (2014) 57-66.
[150] T. Wu, H. Shi, Y. Liang, T. Lu, Z. Lin, J. Ye, *Mater. Sci. Eng. C Mater. Biol. Appl.*, 109 (2020) 110481.
[151] R. Singh, M. Srivastava, N.K. Prasad, S. Awasthi, A. Kumar Dhayalan, S. Kannan, *New J. Chem.*, 41 (2017) 12879-12891.
[152] E. Balogh, G. Paragh, V. Jeney, *Pharmaceuticals*, 11 (2018).
[153] B.J. Kim, S.H. Ahn, S.J. Bae, E.H. Kim, S.H. Lee, H.K. Kim, J.W. Choe, J.M. Koh, G.S. Kim, *J. Bone Miner. Res.*, 27 (2012) 2279-2290.
[154] L. Toxqui, M.P. Vaquero, *Nutrients*, 7 (2015) 2324-2344.
[155] M. Yamaguchi, M.N. Weitzmann, *Mol. Cell. Biochem.*, 355 (2011) 179-186.
[156] E. O'Neill, G. Awale, L. Daneshmandi, O. Umerah, K.W. Lo, *Drug Discov. Today*, 23 (2018) 879-890.
[157] E.A. Ofudje, A.I. Adeogun, M.A. Idowu, S.O. Kareem, *Heliyon*, 5 (2019) e01716.
[158] A. Ito, H. Kawamura, M. Otsuka, M. Ikeuchi, H. Ohgushi, K. Ishikawa, K. Onuma, N. Kanzaki, Y. Sogo, N. Ichinose, *Mater. Sci. Eng. C*, 22 (2002) 21-25.
[159] J.T.B. Ratnayake, M. Mucalo, G.J. Dias, *J. Biomed. Mater. Res. B Appl. Biomater.*, 105 (2017) 1285-1299.
[160] E. Bonnelye, A. Chabadel, F. Saltel, P. Jurdic, *Bone*, 42 (2008) 129-138.
[161] Y. Hentrotin, A. Labasse, S.X. Zheng, P. Galais, Y. Tsouderos, J.M. Crilaard, J.Y. Reginster, *J. Bone Miner. Res.*, 16 (2001) 299-308.
[162] I. Fogelman, G.M. Blake, *BMJ*, 330 (2005) 1400-1401.
[163] D. Marx, A. Rahimnejad Yazdi, M. Papini, M. Towler, *Bone Rep.*, 12 (2020) 100273.
[164] J. Kravchenko, T.H. Darrah, R.K. Miller, H.K. Lyerly, A. Vengosh, *Environ. Geochem. Health*, 36 (2014) 797-814.
[165] M. Kikuchi, Astsushi Yamazaki, M. Akao, H. Aoki, *Biomed. Mater. Eng.*, 6 (1996) 405-413.
[166] Z. Xiu, M. Lü, S. Liu, G. Zhou, B. Su, H. Zhang, *Mater. Res. Bull.*, 40 (2005) 1617-1622.
[167] A. Yasukawa, M. Nakajima, K. Kandori, T. Ishikawa, *J. Colloid Interface Sci.*, 212 (1999) 220-227.
[168] Y. Zhang, L. Chen, J. Zeng, K. Zhou, D. Zhang, *Mater. Sci. Eng. C Mater. Biol. Appl.*, 39 (2014) 143-149.
[169] F.R. Baxter, I.G. Turner, C.R. Bowen, J.P. Gittings, J.B. Chaudhuri, *J. Mater. Sci. Mater. Med.*, 20 (2009) 1697-1708.
[170] R. Meenambal, P. Poojar, S. Geethanath, K. Sanjeevi, *J. Am. Ceram. Soc.*, 100 (2017) 1831-1841.
[171] N.K. P, J.M.F. Ferreira, K. S, *J. Eur. Ceram. Soc.*, 37 (2017) 2953-2963.

[172] M. Lasgorceix, L. Grenho, M.H. Fernandes, C. Ott, L. Boilet, A. Leriche, F. Monteiro, F. Cambier, S. Hocquet, *J. Eur. Ceram. Soc.*, 38 (2018) 5545-5553.
[173] S. Koutsopoulos, *J. Biomed. Mater. Res.*, 62 (2002) 600-612.
[174] A. Siddharthan, S.K. Seshadri, T.S.S. Kumar, *J. Mater. Sci.: Mater. Med.*, 15 (2004) 1279-1284.
[175] C. Durucan, P.W. Brown, *J. Mater. Sci. Mater. Med.*, 11 (2000) 365-371.
[176] K. Tsuru, Ruslin, M. Maruta, S. Matsuya, K. Ishikawa, *J. Mater. Sci. Mater. Med.*, 26 (2015) 244.
[177] G. Blasse, B.C. Grabmaier, A General Introduction to Luminescent Materials. In: Luminescent Materials., Springer, 1994.
[178] L. Wu, B. Wang, Y. Zhang, L. Li, H.R. Wang, H. Yi, Y.F. Kong, J.J. Xu, *Dalton Trans.*, 43 (2014) 13845-13851.
[179] L. Lin, M. Yin, C. Shi, W. Zhang, *J. Alloys Compd*, 455 (2008) 327-330.
[180] R. Cao, W. Wang, J. Zhang, Y. Ye, T. Chen, S. Guo, F. Xiao, Z. Luo, *Opt. Mater.*, 79 (2018) 223-226.
[181] Q. Zhou, L. Dolgov, A.M. Srivastava, L. Zhou, Z. Wang, J. Shi, M.D. Dramićanin, M.G. Brik, M. Wu, *J. Mater. Chem. C*, 6 (2018) 2652-2671.
[182] A. Lecointre, R. Ait Benhamou, A. Bessiére, G. Wallez, M. Elaatmani, B. Viana, *Opt. Mater.*, 34 (2011) 376-380.
[183] M. Yashima, Y. Kawaike, *Chem. Mater.*, 19 (2007) 3973-3979.
[184] R.K. Singh, M. Srivastava, N.K. Prasad, S. Awasthi, A. Dhayalan, S. Kannan, *Mater. Sci. Eng. C Mater. Biol. Appl.*, 78 (2017) 715-726.
[185] A. Jillavenkatesa, R.A. Condrate, *Spectrosc. Lett.*, 31 (2006) 1619-1634.
[186] P.N.d. Aza, C. Santos, A. Pazo, S.d. Aza, R. Cusco, L. Artus, *Chem. Mater.*, 9 (1997) 912-915.
[187] P.M.C. Torres, J.C.C. Abrantes, A. Kaushal, S. Pina, N. Döbelin, M. Bohner, J.M.F. Ferreira, *J. Eur. Ceram. Soc.*, 36 (2016) 817-827.
[188] L. Sinusaite, I. Grigoraviciute-Puroniene, A. Popov, K. Ishikawa, A. Kareiva, A. Zarkov, *Ceram. Int.*, 45 (2019) 12423-12428.
[189] C. Shuai, P. Feng, L. Zhang, C. Gao, H. Hu, S. Peng, A. Min, *Sci. Technol. Adv. Mater.*, 14 (2013) 055002.
[190] M. Trabelsi, I. AlShahrani, H. Algarni, F. Ben Ayed, E.S. Yousef, *Mater. Sci. Eng. C Mater. Biol. Appl.*, 96 (2019) 716-729.
[191] A. Tricoteaux, E. Rguiti, D. Chicot, L. Boilet, M. Descamps, A. Leriche, J. Lesage, *J. Eur. Ceram. Soc.*, 31 (2011) 1361-1369.

# CURRICULUM VITAE

## PERSONAL INFORMATION

| | |
|---|---|
| Name, Surname | Lauryna Kavaliauskienė |
| Date of Birth | 1992-04-22 |
| E-mail | lauryna.sinusaite@gmail.com |

## ACADEMIC EDUCATION

| | |
|---|---|
| 2011 – 2015 | Bachelor of Science in Chemistry, Vilnius University |
| 2015 – 2017 | Master of Science in Chemistry, Vilnius University |
| 2017 – 2021 | Doctoral studies, Chemistry, Vilnius University |

## WORK EXPERIENCE

| | |
|---|---|
| 2015 August – 2018 May | Senior Specialist at Institute of Chemistry, Vilnius University |
| 2018 June – 2018 September | Chemist at Nature Research Centre |
| 2019 September – 2019 October<br>2020 August – 2020 December | Junior Researcher at Institute of Chemistry, Vilnius University |

## OTHER ACTIVITIES

| | |
|---|---|
| 2019 June – 2019 August | Erasmus+ exchange programme student at Institute of Solid State Physics, University of Latvia. |
| 2019 September – 2019 October<br>2020 August – 2020 December | Participant of the project „Novel Bulk and Nano Composite Materials - A Way Towards Superior Multiferroic Properties“ financed by Research Council of Lithuania |

# SANTRAUKA

Yra žinoma, kad žmonių gyvenimo trukmė ilgėja, senyvo amžiaus žmonių skaičius didėja dėl sparčiai besivystančios medicinos bei gerėjančių gyvenimo sąlygų. Vyresnio amžiaus žmonės vis dažniau susiduria su kaulų ligomis, tokiomis kaip kaulų vėžys ar osteoporozė. Kadangi vyresnių žmonių organizmuose pakinta biocheminiai procesai, dėl kurių sumažėja kaulų tankis, kaulų lūžių rizika ženkliai išauga. Statistika rodo, kad 1990 metais pasaulyje buvo 1,6 mln. žmonių, kurie patyrė klubo kaulo lūžius. Yra manoma, kad šis skaičius iki 2050 metų padidės iki 6 mln. Dėl šių priežasčių valstybė sveikatos išlaidoms turi atitinkamai skirti didesnį finansavimą.

Dažniausiai kaulai po nestiprių lūžių geba sugyti patys, tačiau kaule esant didelėms ertmėms, kurios susiformuoja dėl sudėtingesnių lūžių, infekcijų ar kaulų vėžio, kaulas pilnai pats sugyti negali. Savaime negyjantys kaulai yra gydomi paimant ir persodinant žmogaus kaulinį audinį, kitais atvejais yra naudojami dirbtiniai kaulo pakaitalai. Šie pakaitalai turėtų būti biosuderinami, bioirūs, struktūriškai suderinami su žmogaus kaulu, mechaniškai tvirti, netoksiški ir nebrangūs.

Šiomis dienomis sintetiniais kaulo pakaitalais yra naudojamos tokios medžiagos kaip: biostiklas, kalcio sulfatas, kalcio fosfato keramika arba cementas bei polimeriniai kompozitai. Žmogaus kaulas yra sudarytas iš karbonizuoto kalcio hidroksiapatito, todėl dažnai kaulų defektų gydymui yra naudojamas kalcio fosfatas, kuris puikiai atitinka kaulo pakaitalams keliamus reikalavimus. Kalcio fosfatais galima dengti metalinius implantus siekiant pagerinti kaulo ir impalnto fiksaciją, taip pat gali būti užpildomos kaulo lūžio vietos paruošta pasta arba gaminami kaulo pakaitalų karkasai.

Egzistuoja du kambario temperatūroje stabilūs trikalcio fosfato (TCP) polimorfai: α- ir β-TCP. Abu polimorfai turi vienodą cheminę sudėtį, tačiau dėl skirtingos kristalinės struktūros pasižymi skirtingomis savybėmis, pavyzdžiui, tankiu ir tirpumu. Dėl šių skirtumų, tirpesnis α-TCP polimorfas yra naudojamas kaip kalcio fosfatų cementų sudedamoji dalis, o mažiau tirpus β-TCP yra naudojamas kaulo karkasų bei keramikų gamybai. Sintezės sąlygos turi didelę įtaką galutinio produkto formavimuisi ir grynumui. Dalinis kalcio jonų pakeitimas kalcio fosfatuose kitais bioaktyviais jonais modifikuoja jų fizikochemines, mechanines, morfologines savybes, tirpumą, gali suteikti antibakterinių savybių. Taip pat pagerina kalcio fosfato biosuderinamumą bei pritaikomumą kaulų regeneracijai.

Šios daktaro disertacijos tikslas buvo ištirti pasirinktų metalų jonų ir sintezės sąlygų įtaką faziškai selektyviai TCP polimorfų sintezei ir jų savybėms. Šiam tikslui pasiekti buvo iškelti šie uždaviniai:

• įvertinti sintezės sąlygų poveikį faziškai selektyviai TCP polimorfų sintezei nusodinimo metodu;

• ištirti legiravimo Mn jonais įtaką faziškai selektyviai TCP polimorfų sintezei;

• ištirti legiravimo Mn jonais įtaką žemoje temperatūroje susintetinto metastabilaus α-TCP hidrolizės greičiui;

• ištirti aukštoje temperatūroje susintetinto Mn jonais legiruoto α-TCP liuminescencines savybes;

• ištirti skirtingo dydžio dvivalenčių katijonų (Mg, Zn, Sr ir Ba) įtaką termiškai indukuotai ACP kristalizacijai ir faziniams virsmams;

• ištirti Fe ir Zn jonais pakeitimo poveikį struktūrinėms, magnetinėms, mechaninėms ir biologinėms β-TCP savybėms.

Gauti tyrimų rezultatai yra aprašyti disertacijos „Rezultatai ir jų aptarimas“ dalyje.

3.1. skyriuje aptarta skirtingų praplovimo skysčių (dejonizuoto vandens, acetono, acetonitrilo, etanolio ir izopropanolio) ir kaitinimo temperatūros įtaka TCP polimorfų sintezei nusodinimo metodu;

3.2. skyriuje aprašyta legiravimo Mn jonais įtaka selektyviai TCP polymorfų sintezei nusodinimo metodu. Aprašyta kokią įtaką Mn jonai turi susintetintų junginių citotoksiškumui bei morfologijai;

3.3. skyriuje aptarta Mn jonų įtaka metastabilaus α-TCP hidrolizės greičiui. Parodyta α-TCP hidrolizės greičio priklausomybė nuo Mn jonų koncentracijos, Mn jonų įtaka susiformavusių CDHA miltelių morfologijai;

3.4. skyriuje aprašytos Mn jonais legiruoto α-TCP liuminescencinės savybės. Parodytos optinių savybių priklausomybės nuo Mn koncentracijos ir temperatūros;

3.5. skyriuje aprašyta skirtingo dydžio dvivalenčių katijonų įtaka termiškai indukuotai ACP kristalizacijai. Parodyta kristalizacijos ir fazinių virsmų priklausomybė nuo priemaišinio jono dydžio ir koncentracijos;

3.6. skyriuje aptartos β-TCP legiruoto Fe ir Zn jonais sintezė ir savybės. Aprašytos Fe jonų suteiktos magnetinės savybės bei įvertintas medžiagų citotoksiškumas. Tai pat aptartos paruoštų keramikų mechaninės savybės.

# IŠVADOS

1. Pirmą kartą buvo parodyta, kad faziškai selektyvi TCP polimorfų sintezė gali būti atlikta beveik toje pačioje temperatūroje, naudojant cheminio nusodinimo metodu susintetinto kalcio fosfato nuosėdoms plauti skirtingo tipo skysčius. Praplovimo skysčio prigimtis ir kiekis lemia amorfinių arba kristalinių nuosėdų susidarymą, kurias iškaitinus susidaro skirtingi TCP polimorfai. β-TCP susidaro nuosėdas plaunant vandeniu arba AC ir kaitinant 775 °C temperatūroje. Nuosėdų plovimas ACN, EtOH ir i-PrOH ir atkaitinimas 750 °C temperatūroje lemia α-TCP kristalizaciją.
2. Faziškai selektyvus α- ir β-TCP polimorfų susidarymas gali būti pasiektas toje pačioje temperatūroje (700 °C) dalį $Ca^{2+}$ jonų pakeičiant $Mn^{2+}$ jonais. Esant didesniam Mn jonų kiekiui (5 mol%) susidaro β-TCP, o esant mažesniam Mn jonų kiekiui (0–1 mol%) susiformuoja α-TCP. Mėginiai su tarpinėms Mn koncentracijoms buvo sudaryti iš dviejų polimorfų mišinio. Atliktas tyrimas yra pirmasis eksperimentinis darbas, parodantis termodinaminę pusiausvyrą tarp TCP polimorfų, pakeistų dvivalenčiais katijonais.
3. Pirmą kartą buvo parodyta, kad $Mn^{2+}$ jonų buvimas α-TCP kristalinėje gardelėje žymiai sulėtina jo hidrolizę. Grynas α-TCP ir α-TCP legiruotas su 0,5 ir 1 mol% Mn jonų pilnai hidrolizuojamas, pereinant į CDHA, atitinkamai per 10, 20 ir 35 valandas. Pradinių TCP miltelių kristališkumo laipsnis buvo panašus, tai rodo, kad hidrolizės slopinimo procesas yra susijęs ne su amorfinės fazės buvimu, o su CDHA susidarymu. Pradinių ir visiškai hidrolizuotų miltelių cheminė sudėtis buvo identiška, kas rodo, kad hidrolizės proceso metu nėra selektyvaus jonų išsiskyrimo.
4. Pirmą kartą buvo ištirtos $Mn^{2+}$ jonais legiruoto α-TCP liuminescencinės savybės (Mn koncentracija nuo 0,2 iki 1 mol%). Mn turintys milteliai, sužadinanti 408 nm bangos ilgio spinduliuote, parodė plačią emisiją spektro intervale nuo 525 iki 825 nm, emisijos maksimumas buvo užfiksuotas ties 630 nm. Nustatyta, kad emisijos intensyvumas priklauso nuo Mn koncentracijos ir didėja didėjant Mn kiekiui. Gesimo trukmės palaipsniui mažėjo didėjant Mn kiekiui milteliuose.
5. Pirmą kartą buvo ištirta ACP, kuriame dalis $Ca^{2+}$ jonų pakeista mažesniais ($Mg^{2+}$, $Zn^{2+}$) ir didesniais ($Sr^{2+}$, $Ba^{2+}$) dvivalenčiais katijonais, termiškai indukuota kristalizacija ir faziniai virsmai. Buvo parodyta, kad ACP kristalizacija į TCP ir tolesnės fazinės transformacijos tarp TCP polimorfų labai priklauso nuo pakaitų dydžio ir koncentracijos ACP matricoje. Pakeitimas mažesniais jonais neturi įtakos kristalizacijos temperatūrai, tačiau skatina β-TCP susidarymą žymiai žemesnėje temperatūroje,

lyginant su grynu ACP. Pakeitimas didesniais jonais stabdo kristalizacijos procesą, kuris buvo pastebėtas aukštesnėje temperatūroje. Nustatyta, kad pakeitimas Sr jonais (10 mol%) neturi įtakos metastabilus α-TCP terminiam stabilumui, o pakeitimas Ba jonais (10 mol%) stabilizuoja α-TCP struktūrą ir visiškai užblokuoja fazinį virsmą iš α-TCP į β-TCP.

6. Nusodinimo metodas buvo sėkmingai pritaikytas β-TCP miltelių, pakeistų vienodu $Fe^{3+}$ ir $Zn^{2+}$ jonų kiekiu intervale 1-5 mol%, sintezei. Struktūrinė analizė atskleidė laipsnišką susintetintų mėginių gardelės parametrų mažėjimą, didėjant pakaitų koncentracijai. Visiems $Fe^{3+}$ jonų turintiems mėginiams būdingas paramagnetinis elgesys, nustatyta, kad įmagnetėjimo vertės yra proporcingos $Fe^{3+}$ kiekiui milteliuose. Citotoksiškumo tyrimas neparodė sintetinių miltelių toksinio poveikio, net turint didžiausią priemaišinių jonų kiekį. Pagamintų β-TCP keramikų mechaninės savybės nebuvo pagerintos pakeitus $Ca^{2+}$ kitais jonais. Nustatyta, kad keramikų iš pakeistų mėginių Vickerso kietumo vertės yra mažesnės, lyginant su nelegiruoto β-TCP keramikos vertėmis.

# ACKNOWLEDGEMENTS

First of all, I would like to express my deep gratitude to my research advisor Assist. Prof. Dr. Aleksej Žarkov for endless patience, numerous disscusions and support. The help and support I have received from him during years of study were essential to keep me going further with my research.

Also, I would like to thank my research consultant Prof. Dr. Stasys Tautkus for guidance, advices and encouragement throughout my years of study.

I am very grateful for all people that were involved in my research. Your collaborations, insights, remarks and contributions allowed me to improve scientific quality of this research.

Finally, I would like to thank my friends and family for support.

# LIST OF PUBLICATIONS

**Articles in journals indexed in Clarivate Analytics Web of Science database**

1. **L. Sinusaite**, I. Grigoraviciute-Puroniene, A. Popov, K. Ishikawa, A. Kareiva, A. Zarkov, Controllable synthesis of tricalcium phosphate (TCP) polymorphs by wet precipitation: Effect of washing procedure, *Ceramics International*, 45 **(2019)** 12423-12428.
2. **L. Sinusaite**, A.M. Renner, M.B. Schutz, A. Antuzevics, U. Rogulis, I. Grigoraviciute-Puroniene, S. Mathur, A. Zarkov, Effect of Mn doping on the low-temperature synthesis of tricalcium phosphate (TCP) polymorphs, *Journal of the European Ceramic Society*, 39 **(2019)** 3257-3263.
3. **L. Sinusaite**, A. Popov, A. Antuzevics, K. Mazeika, D. Baltrunas, J.- C. Yang, J.L. Horng, S. Shi, T. Sekino, K. Ishikawa, A. Kareiva, A. Zarkov, Fe and Zn co-substituted beta-tricalcium phosphate (β-TCP): Synthesis, structural, magnetic, mechanical and biological properties, *Materials Science and Engineering: C*, 112 **(2020)** 110918.
4. **L. Sinusaite**, A. Antuzevics, A.I. Popov, U. Rogulis, M. Misevicius, A. Katelnikovas, A. Kareiva, A. Zarkov, Synthesis and luminescent properties of Mn-doped alpha-tricalcium phosphate, *Ceramics International*, 47(4) **(2021)** 5335-5340.
5. **L. Sinusaite**, A. Popov, E. Raudonyte-Svirbutaviciene, J.-C. Yang, A. Kareiva, A. Zarkov, Effect of Mn doping on hydrolysis of low-temperature synthesized metastable alpha-tricalcium phosphate, *Ceramics International*, 47(9) **(2021)** 12078-12083.
6. **L. Sinusaite**, A. Kareiva, A. Zarkov, Thermally induced crystallization and phase evolution of amorphous calcium phosphate substituted with divalent cations having different sizes, *Crystal Growth & Design*, 21(2) **(2021)** 1242-1248.

**Articles not included in this thesis**

1. I. Mikalauskaite, G. Pleckaityte, **L. Sinusaite**, V. Plausinaitiene, A. Katelnikovas, A. Beganskiene, Temperature induced emission enhancement and investigation of $Nd^{3+}\rightarrow Yb^{3+}$ energy transfer efficiency in $NaGdF_4:Nd^{3+}$, $Yb^{3+}$, $Er^{3+}$ upconverting nanoparticles, *Journal of Luminescence*, 223 **(2020)** 117237.
2. D. Griesiute, **L. Sinusaite**, A. Kizalaite, A. Antuzevics, K. Mazeika, D. Baltrunas, T. Goto, T. Sekino, A. Kareiva, A. Zarkov, The influence of

$Fe^{3+}$ doping on thermally induced crystallization and phase evolution of amorphous calcium phosphate, *CrystEngComm*, 23, **(2021)** 4627-4637.

**Published contributions to academic conferences**

1. A. Antuzevics, U. Rogulis, A.I. Popov, A. Zarkov, **L. Sinusaite**, A. Kareiva. Luminescence and Electron Paramagnetic Resonance Investigation of Manganese Doped Tricalcium Phosphate. 34th Scientific Conference, Riga, Latvia 20-22 February 2018, p. 53.
2. **L. Sinusaite**, A. Antuzevics, I. Grigoraviciute-Puroniene, A.I. Popov, U. Rogulis, A. Katelnikovas, A. Kareiva, A. Zarkov. Phase Evolution, Structural and Luminescent Properties of Mn-doped Calcium Hydroxyapatite, alpha- and beta-Tricalcium Phosphates Advanced materials and technologies, Palanga, Lithuania, 27-31 August 2018, p. 104.
3. **L. Sinusaite**, I. Grigoraviciute-Puroniene, A. Antuzevics, A. Kareiva, A. Zarkov. Effect of Manganese Doping on the Low Temperature Synthesis of Tricalcium Phosphate Polymorphs, EcoBalt 2018, Vilnius, Lithuania, 25-27 October 2018, p. 84.
4. A. Kizalaite, **L. Sinusaite**, A. Kareiva, A. Zarkov. Effect of Mn Doping on Hydrolysis Rate and Dissolution of Alpha tricalcium Phosphate, Open Readings 2019, Vilnius, Lithuania, 19-22 March 2019, p. 80.
5. **L. Sinusaite**, I. Grigoraviciutė-Puroniene, A. Popov, A. Kareiva, A. Zarkov. Controllable Synthesis of Tricalcium Phosphate (TCP) Polymorphs by Wet Precipitation: Effect of Washing Procedure, Chemistry and Chemical Technology 2019, Vilnius, Lithuania, 16 May 2019, p. 117.
6. **L. Sinusaite**, I. Grigoraviciute-Puroniene, A. Popov, A. Zarkov. Low Temperature Precipitation Synthesis of Tricalcium Phosphate Polymorphs: Effects of Doping and Washing Procedure, Euromat 2019, Stockholm, Sweden, 1-5 September 2019, p. 2251.
7. A. Kizalaite, **L. Sinusaite**, D. Griesiute, A. Popov, A. Antuzevics, K. Mazeika, D. Baltrunas, J.-C. Yang, A. Kareiva, A. Zarkov. Fe and Zn co-substituted beta-tricalcium phosphate: synthesis, structural, magnetic, mechanical and biological properties. Open Readings 2020, Vilnius, Lithuania, 17-20 March 2020, p. 122.
8. **L. Sinusaite**, D. Griesiute, A. Antuzevics, A. Katelnikovas, A. Zarkov. High-temperature synthesis, structural and luminescent properties of Mn-doped α-tricalcium phosphate. Open Readings 2020, Vilnius, Lithuania, 17-20 March 2020, p. 225.

9. **L. Sinusaite**, A. Zarkov. Investigation of Crystallization of Amorphous Calcium Phosphate Substituted with Smaller ($Mg^{2+}$, $Zn^{2+}$) and Larger ($Sr^{2+}$, $Ba^{2+}$) Divalent Ions. Advanced materials and technologies, Palanga, Lithuania, 24-28 August 2020, p. 115.
10. A. Zarkov, **L. Sinusaite**, A. Kizalaite, D. Griesiute, A. Popov, A. Antuzevics, K. Mazeika, D. Baltrunas, A. Kareiva. Synthesis and Characterization of Dual Substituted beta-Tricalcium Phosphate. Advanced materials and technologies, Palanga, Lithuania, 24-28 August 2020, p. 116.
11. A. Kareiva, **L. Sinusaite**, D. Griesiute, A. Kizalaite, A. Popov, A. Zarkov. Synthesis and characterization of Fe and Zn co-substituted beta-tricalcium phosphate. Chemistry, physics and technology of surface, Kyiv, Ukraine, 21-22 October 2020, p. 84.
12. **L. Sinusaite**, A. Kareiva, A. Zarkov. Effect of Mn doping on hydrolysis of low-tempertaure synthesized metastable alpha-tricalcium phosphate. Nanostructured Bioceramic Materials 2020, Vilnius, Lithuania, 1-3 December 2020, p. 70.

Article I

**Controllable synthesis of tricalcium phosphate (TCP) polymorphs by wet precipitation: Effect of washing procedure**

L. Sinusaite, I. Grigoraviciute-Puroniene, A. Popov, K. Ishikawa, A. Kareiva, A. Zarkov

*Ceramics International*, 45 (2019) 12423-12428

Ceramics International 45 (2019) 12423–12428

Contents lists available at ScienceDirect

Ceramics International

journal homepage: www.elsevier.com/locate/ceramint

# Controllable synthesis of tricalcium phosphate (TCP) polymorphs by wet precipitation: Effect of washing procedure

Lauryna Sinusaite[a], Inga Grigoraviciute-Puroniene[a], Anton Popov[a,b], Kunio Ishikawa[c], Aivaras Kareiva[a], Aleksej Zarkov[a,*]

[a] Institute of Chemistry, Vilnius University, Naugarduko 24, LT-03225 Vilnius, Lithuania
[b] Department of Immunology, State Research Institute Centre for Innovative Medicine, Santariskiu 5, LT-08406 Vilnius, Lithuania
[c] Department of Biomaterials, Faculty of Dental Science, Kyushu University, 3-1-1, Maidashi, Higashi-ku, Fukuoka 812-8532, Japan

ARTICLE INFO

*Keywords:*
Tricalcium phosphate
TCP
Processing conditions
Polymorphs
Washing procedure

ABSTRACT

In the present work, effect of processing conditions on the synthesis of tricalcium phosphate (TCP) polymorphs was investigated. Pure α- and β-TCP polymorphs were prepared by wet precipitation method at almost identical thermal conditions. It was shown that formation of the compound with desired crystalline structure can be achieved by applying a washing procedure with a certain solvent to as-prepared calcium phosphate precipitates. Effect of water, acetone, acetonitrile, ethanol and isopropanol on the crystallinity and crystal structure of the as-prepared and annealed powders was studied. It was demonstrated that type of the washing liquid strongly affects crystalline or amorphous nature of the as-prepared precipitates and formation of different TCP polymorphs after thermal treatment. Washing of the as-prepared precipitates with water and acetone leads to the formation of β-TCP, while washing with acetonitrile and alcohols leads to the crystallization of α-TCP. The thermal behavior of dried precipitates was investigated by thermogravimetric analysis (TGA). The crystallinity, crystal structure and structural changes were evaluated by X-ray powder diffraction (XRD), Fourier-transform infrared (FTIR) and Raman spectroscopy. Scanning electron microscopy (SEM) was used for the characterization of morphological features of the synthesized products.

## 1. Introduction

Nowadays calcium phosphate (CP) biomaterials attract huge attention in the field of regenerative medicine. Due to the compositional similarity to the mineral phase of bones and excellent biocompatibility, different synthetic CPs have been widely used as biomaterials for bone repair [1]. Moreover, CPs have attracted significant interest in simultaneous use as bone substitute and drug delivery vehicle, adding a new dimension to their applications [2,3]. Among synthetic CPs currently used as biomaterials, the most popular are calcium hydroxyapatite ($Ca_{10}(PO_4)_6(OH)_2$, HA), calcium-deficient HA ($Ca_{10-x}(PO_4)_{6-x}(HPO_4)_x(OH)_{2-x}$, CDHA) and tricalcium phosphate ($Ca_3(PO_4)_2$, TCP) [4–6]. Some of these materials under certain conditions are able to transform from one to another [7–10].

TCP has 3 polymorphs, however only 2 of them can be stabilized at room temperature – α- and β-TCP. α-TCP crystallizes in the monoclinic crystal system with the space group $P2_1/a$, while β-TCP crystallizes in the rhombohedral crystal system with the space group R3c [11]. β-TCP has denser structure and its theoretical density is 3.066 $g/cm^{-3}$ against 2.866 $g/cm^{-3}$ of α-TCP. Both TCP polymorphs are used for medical purposes, however, due to the different physicochemical properties these materials are used for different applications. In aqueous media α-TCP hydrolyzes with transformation to CDHA and due to this high reactivity it is often used in bone cements as a major powder component [12,13]. β-TCP in its turn is widely used for the fabrication of mono- or biphasic (as a rule comprise β-TCP and HA mixture) bioceramics [14,15].

Most frequently β-TCP is synthesized by solid state reaction or wet precipitation methods at temperatures about 800 °C and higher [16,17]. α-TCP in its turn is usually prepared by annealing Ca and P precursor mixture at temperatures above 1125 °C, which is the temperature of the phase transition from β-TCP to α-TCP [18,19]. Additional difficulties to high-temperature treatment disadvantages causes the nature of this phase transition, which is reversible and very sensitive to impurities and processing conditions [9,10,20]. Thermal quenching is commonly used in order to stabilize metastable α-TCP polymorph [21,22]. However, it was shown that α-TCP can be also obtained at such low temperatures as 600–700 °C with further transformation to β-TCP at around

* Corresponding author.
*E-mail address:* aleksej.zarkov@chf.vu.lt (A. Zarkov).

https://doi.org/10.1016/j.ceramint.2019.03.174
Received 1 February 2019; Received in revised form 21 March 2019; Accepted 22 March 2019
Available online 25 March 2019

800 °C [23]. Thereby α-TCP can be synthesized at both high and low temperatures having β-TCP polymorph at intermediate temperatures.

It is well known that processing conditions can drastically affect structure, morphology and physicochemical properties of materials [24–29]. Previously, investigation of the formation of various CPs from calcium propionate and triethyl phosphate was reported by Kjellin et al. [30]. It was shown that different materials such as β-TCP, CDHA, monetite or amorphous calcium phosphate (ACP) can be obtained depending on water content in a reaction mixture. Duncan et al. investigated the role of the chemical composition of monetite on the synthesis and properties of α-TCP [31]. It was concluded that the ratio of α- and β-TCP polymorphs prepared by solid state reaction synthesis method depends on purity of starting materials, and properties of phase pure α-TCP may be indirectly affected by purity of the chemicals. Lau et al. proposed a phase-tunable synthesis of CPs by hydrothermal/solvothermal method [32]. Utilization of water, methanol and ethanol as reaction solvent resulted in a formation of HA, β-TCP or anhydrous dicalcium phosphate, respectively. Recently, effect of reaction solvents such as distilled water, tetrahydrofuran and N,N-dimethylformamide on sol-gel derived HA powders was studied [33]. Chemical structure and morphology of the obtained products were found to be strongly dependent on the dielectric constant and polarity of the solvent. Li et al. studied the influence of polyethylene glycol addition to the reaction mixture on the synthesis of β-TCP [34]. The results showed that the polyethylene glycol played an important role in improving the purity and dispersity of β-TCP powders.

In the present work we report on the effect of washing procedure of the as-prepared CP precipitates on the synthesis of TCP polymorphs. While majority of studies are focused on the effect of different solvents during chemical reaction, we present the influence of different solvents already after precipitation reaction. Water, acetone, acetonitrile, ethanol and isopropanol were chosen to investigate the influence of the washing liquids on the thermal behavior, structure, composition and morphology of initial precipitates and final materials. It was shown that synthesis of desired pure TCP polymorph can be easily controlled by washing of the as-precipitated species with particular solvent.

## 2. Materials and methods

### 2.1. Synthesis

All compounds were synthesized by wet precipitation method using calcium nitrate tetrahydrate ($Ca(NO_3)_2{\cdot}4H_2O$, ≥99%, Roth) and diammonium hydrogen phosphate ($(NH_4)_2HPO_4$, ≥98%, Roth) as starting materials. For all experiments Ca to P ratio was kept 1.50 and amount of taken precursors was calculated for preparation of 1.5 g of final TCP product. For the synthesis an appropriate amount of $Ca(NO_3)_2{\cdot}4H_2O$ was dissolved in deionized water resulting in 0.75 M solution. Next, concentrated ammonia solution ($NH_4OH$, 25%) was added to the above solution in order to adjust pH to 10. In parallel 0.5 M $(NH_4)_2HPO_4$ solution in deionized water was prepared. Next, under constant stirring on magnetic stirrer, the prepared solutions were mixed together resulting in the instant formation of white precipitates. The obtained precipitates were stirred in the reaction mixture for 10 min, afterwards vacuum filtered and washed with a certain solvent. First, all precipitated species were always washed with 100 mL of deionized water following by washing with different volumes (20, 40, 60, 80 and 100 mL) of deionized water, acetone (AC, ≥99.8%, Roth), acetonitrile (ACN, ≥99.5%, Roth), ethanol (EtOH, 96%, Roth) or isopropanol (i-PrOH, ≥99.5%, Roth). Additional washing with deionized water was performed in order to ensure the same sum volume and washing time for all solvents. All synthesis and washing procedures were performed under identical conditions using the same Buchner funnel and cellulose filters (55 mm in diameter, retention range – 5–13 μm). After washing the precipitates were dried at 50 °C overnight in the oven. Finally, dry powders were ground in agate mortar and annealed in the furnace for 5 h in air.

### 2.2. Characterization

Powder X-ray diffraction data were collected using Ni-filtered Cu Kα radiation on Rigaku MiniFlex II diffractometer working in Bragg-Brentano (θ/2θ) geometry. The data were collected within 2θ angle range from 10 to 60° at a step width of 0.01° and speed of 2°/min. Lattice parameters were refined by the Rietveld method using the FullProf suite in the profile matching mode. The average crystallite size (τ) was calculated by Scherrer equation:

$$\tau = \frac{0.9\lambda}{B\cos\theta} \quad (1)$$

where λ is the X-ray wavelength, B is the full width at half maximum (FWHM) of a diffraction peak and θ is the Bragg angle. The thermal decomposition of the as-prepared precipitates was analyzed through thermogravimetric (TG) analysis using Perkin Elmer STA 6000 Simultaneous Thermal Analyzer. Samples of about 5–10 mg were heated from 25 to 900 °C at a heating rate of 10 °C/min in a dry flowing air (20 mL/min). Infrared (FTIR) spectra were recorded in the range of $3000-400\ cm^{-1}$ employing Bruker ALPHA ATR spectrometer. Raman spectroscopy measurements were performed at room temperature using combined Raman and scanning near field optical microscope (SNOM) WiTec Alpha 300 R equipped with 532 nm excitation laser source. Morphology of the synthesized powders was characterized by scanning electron microscopy performed with a Hitachi SU-70 field-emission scanning electron microscope (FE-SEM). Elemental analysis of the synthesized samples was performed by inductively coupled plasma optical emission spectrometry (ICP-OES) using Perkin-Elmer Optima 7000DV spectrometer. The samples were dissolved in 5% nitric acid ($HNO_3$, Rotipuran® Supra 69%, Carl Roth) and diluted to an appropriate volume. Calibration solutions were prepared by an appropriate dilution of the stock standard solutions (single-element ICP standards 1000 mg/L, Carl Roth).

## 3. Results and discussion

Washing of as-prepared precipitates is a commonly used procedure performing synthesis of inorganic materials by precipitation method. It is usually applied in order to remove remained dissolved ions from the reaction liquid phase and adsorbed ions from the surface of obtained precipitates. Deionized water is the most frequently used for these purposes. In the present work in addition to deionized water we took into consideration four other solvents (acetone, acetonitrile, ethanol and isopropanol). All these solvents are miscible with water. The polarities of AC, ACN, EtOH and i-PrOH are 0.355, 0.460, 0.654 and 0.546, respectively. Effect of the washing agent after drying procedure was visible even to the naked eye. The precipitates washed with $H_2O$ and AC were compact in volume and densely agglomerated into few hard pieces, it was quite difficult to grind them in an agate mortar. Visual appearance and mechanical properties of the precipitates washed with ACN, EtOH and i-PrOH were found to be strongly dependent on utilized amount of the solvent. The precipitates washed with higher amount of these liquids were voluminous and soft.

The XRD patterns of the as-prepared precipitates washed with 100 mL of different solvents and dried at 50 °C are given in Fig. 1. Phase composition analysis revealed that using $H_2O$ and AC as washing agents, crystalline phase corresponding to CDHA was obtained. Crystal phase composition was found to be independent of the used amount of $H_2O$ and AC. In the case of ACN, EtOH and i-PrOH different situation was observed. No sharp diffraction peaks were detected in the XRD patterns of these samples, only very broad peak at about 30°, which is characteristic for ACP [35]. It should be noticed that amorphous powders were obtained only using 100 mL and higher volume of the solvent, while CDHA was formed with lower amount of the solvent. The

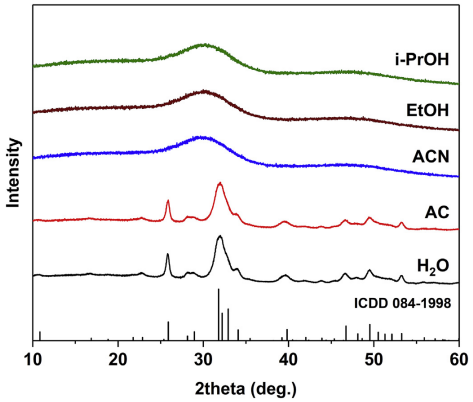


**Fig. 1.** XRD patterns of the as-prepared precipitates washed with 100 mL of the solvent and dried at 50 °C.

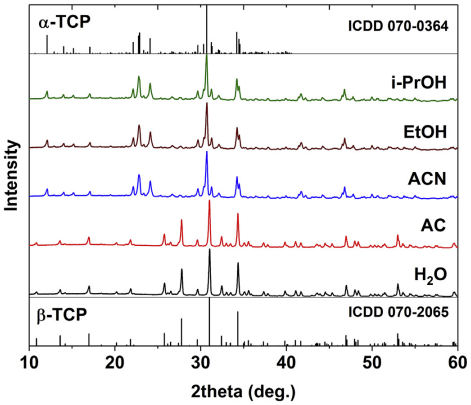


**Fig. 3.** XRD patterns of the precipitates washed with 100 mL of different solvent and annealed at 775 °C ($H_2O$ and AC) or 750 °C (ACN, EtOH and i-PrOH).

XRD patterns of the as-prepared powders washed with different amounts of solvent (20–100 mL) are shown in Fig. S1. The XRD results clearly illustrate the degradation of CDHA phase with increasing volumes of ACN, EtOH and i-PrOH.

Thermal decomposition behavior of the precipitated species washed with 100 mL of the solvent and dried at 50 °C is depicted in Fig. 2. It is obvious, that thermal behavior of the precipitates depends on the nature of the used washing agent and can be divided into 2 groups. The precipitates washed with $H_2O$ and AC, which reveal CDHA crystal phase, are combined in the first group. The TG curves of these samples are almost identical, only with the difference in a total weight loss. Initial mass loss up to 180 °C is associated with a removal of adsorbed solvents from the surface of the precipitates. This process further gradually continues by removal of crystallized water at higher temperatures. The last weight loss at 765 °C is associated with final removal of water molecules from CDHA crystal lattice. With further temperature increase the sample mass becomes constant. Total mass loss for $H_2O$- and AC-washed precipitates was only 7.3 and 9.5%, respectively, which is noticeably lower than for three other samples. The precipitates washed with ACN, EtOH and i-PrOH also exhibited very similar thermal

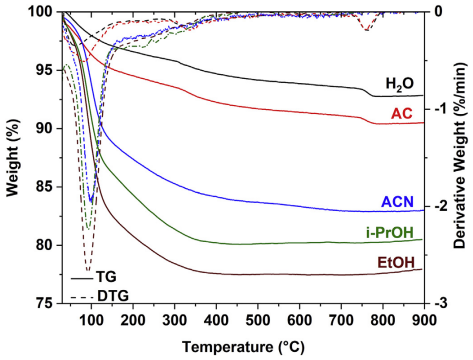


**Fig. 2.** TG/DTG curves of the as-prepared precipitates washed with 100 mL of the solvent and dried at 50 °C.

behavior. The mass of the EtOH- and i-PrOH-washed precipitates did not change already starting from 400 °C. For ACN-washed sample thermal stability temperature is higher, however, weight loss above 400 °C is insignificant in comparison to the determined below this temperature. Total weight loss was 17.1, 22.5 and 19.7% for ACN-, EtOH- and i-PrOH-washed samples, respectively. This difference can be associated with amount of residual water removed from the samples at an initial stage of heating (below 160 °C). These results coincide with previously published work by Rodrigues and Lebugle [36]. The authors showed that as-prepared CPs synthesized in alcoholic medium contain almost 3 times higher amount of $H_2O$ in comparison to those synthesized in aqueous medium.

The XRD patterns of the precipitates washed with 100 mL of the solvent and annealed at 775 or 750 °C, are shown in Fig. 3. It is seen that in the case of $H_2O$ and AC, the powders after annealing at 775 °C crystallize to β-TCP phase. All diffraction peaks match very well the standard XRD data of rhombohedral $Ca_3(PO_4)_2$ (ICDD 00-070-2065). And in the case of treatment with ACN, EtOH and i-PrOH the samples after annealing at 750 °C crystallize to α-TCP polymorph. The XRD patterns of these samples match the standard XRD data of monoclinic $Ca_3(PO_4)_2$ (ICDD 00-070-0364). The lattice parameters and crystallite size of the synthesized TCP polymorphs are summarized in Table 1. It is seen that the lattice parameters are very similar for each group of the polymorphs. Average crystallite size was found to be smaller for α-TCP samples and larger for β-TCP samples. Crystal structure of the final product was found to be independent of the volumes of $H_2O$ and AC used for washing procedure. The β-TCP phase was obtained after annealing in all cases. Oppositely, in the case of ACN, EtOH and i-PrOH crystal structure of the annealed products was found to be strongly dependent on the used amount of the solvent. The evolution of crystal phases depending on the amount of solvent used in the synthesis

**Table 1**
Lattice parameters and crystallite size of the synthesized TCP samples.

| Sample | a, Å | b, Å | c, Å | V, Å$^3$ | Crystallite size, nm |
|---|---|---|---|---|---|
| TCP – $H_2O$ | 10.423 | 10.423 | 37.336 | 3512 | 59.7 |
| TCP – AC | 10.426 | 10.426 | 37.336 | 3514 | 62.9 |
| TCP – ACN | 12.857 | 27.222 | 15.187 | 4290 | 46.0 |
| TCP – EtOH | 12.860 | 27.227 | 15.191 | 4293 | 45.4 |
| TCP – i-PrOH | 12.861 | 27.226 | 15.190 | 4293 | 49.7 |

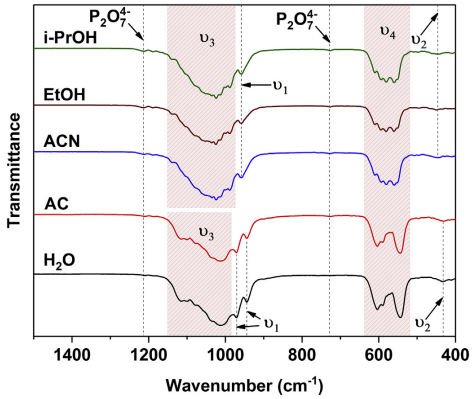


**Fig. 4.** FTIR spectra of the precipitates washed with 100 mL of the solvent and annealed at 775 °C ($H_2O$ and AC) or 750 °C (ACN, EtOH and i-PrOH).

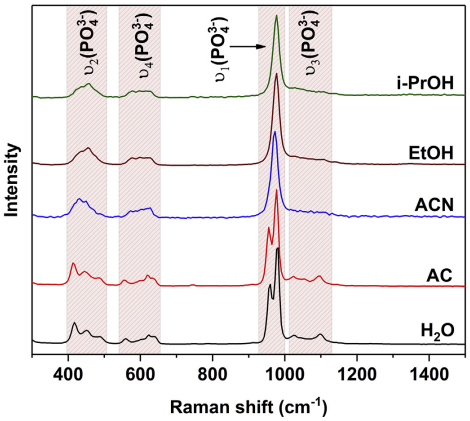


**Fig. 5.** Raman spectra of the precipitates washed with 100 mL of the solvent and annealed at 775 °C ($H_2O$ and AC) or 750 °C (ACN, EtOH and i-PrOH).

processing is illustrated in Fig. S2.

The initial idea of this study was to compare the products synthesized at exactly the same thermal conditions, however, it was not possible to do due to the formation of polymorphs mixtures. α-TCP was found to be monophasic only at ≤750 °C, while at higher temperatures small amount of β-TCP phase was observed. On the other hand, the single-phase β-TCP polymorph was not obtained at 750 °C, since its CDHA precursor does not decompose completely at this temperature. Therefore, in order to prepare pure polymorphs, slightly different annealing temperatures were selected. In principal, identical temperature regime would not change the situation. The XRD patterns of the representative precipitates washed with $H_2O$ and EtOH and both annealed at 750 and 775 °C are shown in Fig. S3.

Vibrational spectroscopy was used for the characterization of the synthesized products in order to detect vibrations of possible amorphous species or crystalline phases, which might be hardly distinguished by XRD in presence of TCP. Fig. 4 shows FTIR spectra of the precipitates washed with 100 mL of the solvent and annealed at 775 or 750 °C. To demonstrate the vibrational modes characteristic of the phosphate group the wavenumber range of 1500–400 $cm^{-1}$ was selected. The FTIR spectra of the samples washed with $H_2O$ and AC and annealed at 775 °C reveal the presence of characteristic phosphate absorption bands observed at 1150–990 ($\nu_3$), 971 and 944 ($\nu_1$), at 605, 590 and 544 ($\nu_4$), and at 433 $cm^{-1}$ ($\nu_2$). The obtained results confirm the formation of β-TCP as the main crystalline phase. For the samples treated with 100 mL of ACN, EtOH and i-PrOH and annealed at 750 °C absorption bands located at 1145 − 975 ($\nu_3$), 957 ($\nu_1$), at 550, 561, 582, 595 and 611 ($\nu_4$), and 452 $cm^{-1}$ ($\nu_2$) can be observed in FTIR spectra, which clearly demonstrate formation of α-TCP polymorph [11]. These observations are consistent very well with the XRD results. There are also week absorption bands at 1213 $cm^{-1}$ and 729 $cm^{-1}$ which could be attributed to the presence of negligible amount of $P_2O_7^{4-}$ groups in the synthesis products [37]. Formation of calcium pyrophosphate as a by-product is quite frequently observed for TCP powders synthesized by precipitation method [16,38]. The FTIR spectra obtained for the precipitates washed with 20–80 mL of ACN, EtOH and i-PrOH and annealed at 750 °C additionally to phosphate bands have an additional well resolved band at 877 $cm^{-1}$ (see Fig. S4). This band corresponds to P−O(H) stretching in monohydrogenophosphate ions ($HPO_4^{2-}$) [39]. It is also noteworthy that after washing with 100 mL the characteristic $HPO_4^{2-}$ absorption band disappears from FTIR spectrum. Contrary, the intensity of the absorption band attributed to pyrophosphate group increases.

Fig. 5 presents Raman spectra in a wavenumber region from 300 to 1500 $cm^{-1}$ for the precipitates washed with 100 mL of the solvent and annealed at 775 or 750 °C. These spectra confirm the results obtained by XRD and FTIR measurements. All Raman spectra contain peaks characteristic to the internal vibrations of phosphate groups in TCP. On the other hand, the spectroscopic differences between two groups of the samples corresponding to different TCP polymorphs are clearly seen. The spectra of the samples washed with $H_2O$ and AC are dominated by two distinctive sharp peaks located at around 955 and 977 $cm^{-1}$, which are attributed to the symmetric stretching ($\nu_1$) of P−O bonds in tetrahedron. Asymmetric stretching mode ($\nu_3$) of P−O bonds can be seen in spectra as less intense bands in the range of 1010–1130 $cm^{-1}$. Two other groups of the bands can be observed at lower wavenumbers from approximately 395 to 510 $cm^{-1}$ and from 540 to 660 $cm^{-1}$ and could be assigned to $\nu_2$ and $\nu_4$ O−P−O bending deformations of the phosphate tetrahedron, respectively [40,41]. For the samples washed with ACN, EtOH and i-PrOH, the most intense bands specific of β-TCP are replaced by a single band at 965 $cm^{-1}$ attributed to $\nu_1$ vibration mode of phosphate groups of α-TCP. Other observed bands ($\nu_2$, $\nu_3$ and $\nu_4$) in the Raman spectra of these samples also have different shape in comparison to those of β-TCP, but positions stay nearly the same. However bands attributed to $\nu_3$ mode are quite week in the spectra of α-TCP [42,43].

The SEM micrographs of β- and α-TCP samples, synthesized using $H_2O$ and ACN, respectively, are given in Fig. 6 as representative. The SEM images demonstrate that synthesized TCP powders exhibit slightly different morphological features depending on their crystal structure. The sample washed only with $H_2O$ (Fig. 6a) consist of approximately 200–500 nm sized nearly spherical particles, which are necked to aggregates of irregular shape. In the case of AC (Fig. S5a) morphology of the powders is similar, particles have comparable size, but more polydispersive and show higher coalescence in comparison to $H_2O$-washed. The α-TCP sample synthesized after ACN treatment (Fig. 6b) consists of very uniform thinner particles with prolonged irregular shape. The thickness of the particles is about 300 nm. Powders synthesized with EtOH and i-PrOH in their turn show very similar morphological features (Fig. S5b,c). However, it can be seen that EtOH-washed powders are slightly larger in size.

Elemental analysis of the synthesized products was performed in order to check possible selective removal of calcium or phosphate ions from the precipitates by certain liquid during washing procedure. The

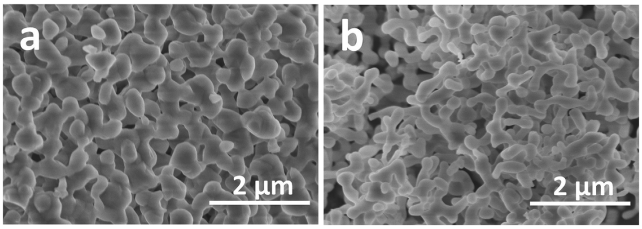


**Fig. 6.** SEM micrographs of the precipitates washed with 100 mL of $H_2O$ (a) and ACN (b) and annealed at 775 and 750 °C, respectively.

**Table 2**
Results of elemental analysis of the synthesized products.

| Sample | Ca to P ratio |
|---|---|
| TCP – $H_2O$ | 1.48 |
| TCP – AC | 1.46 |
| TCP – ACN | 1.46 |
| TCP – EtOH | 1.47 |
| TCP – i-PrOH | 1.45 |

results of the determination of Ca and P by ICP-OES in the samples washed with 100 mL of the solvents are summarized in Table 2. As seen from Table 2, the determined Ca to P ratio for all samples was slightly lower than nominal one. However, the results obtained for different solvents were very close to each other. As a rule, authors do not report on the chemical composition of TCP powders in their works, therefore it is difficult to compare the obtained results with literature data. However, previously Torres et al. [38] reported on the chemical composition of synthesized Mn-doped β-TCP. The ratio of metals to P in this study was determined to be in the range from 1.494 to 1.482, which is also lower than theoretical for TCP. Stahli et al. determined Ca/P ratio 1.44 in hydrogen-substituted β-TCP synthesized in organic media [44]. The same tendency caused by the same reason could be expected for our synthesized samples. Moreover, the results presented in Table 2 correlate with the results documented in previous paragraphs, which confirm the presence of $Ca_2P_2O_7$ as a minor phase in the synthesized TCP specimens. Ca to P ratio in this by-product is 1 to 1, which slightly distorts elemental ratio in bulk material. The results of elemental analysis show that formation of the crystalline or amorphous as-prepared precipitates is not induced by the difference in chemical composition.

It can be concluded that after the heat treatment at nearly identical conditions the precipitated CDHA and ACP precursors crystallize to β-TCP and α-TCP, respectively. Thereby, the reason of the formation of different polymorphs of TCP probably lies in the initial stage of the synthesis, i.e. in the formation of CDHA or ACP after washing and drying procedures. Possible explanation may be found in the interaction of $H_2O$ molecules with as-precipitated species. During the precipitation of CP, an amorphous material built up of clusters forms first. These clusters are composed of CPs in which ions are highly solvated, interacting and forming a gel [45]. The presence of $H_2O$ in the reaction medium leads to the formation of hydration layer around CP particles, strong interaction between $H_2O$ molecules and phosphates, and, subsequently, formation of denser CDHA structure. Bonding of ACN, EtOH and i-PrOH to $H_2O$ molecules modifies water interaction with phosphates, and CP clusters become partly isolated from each other. Consequently, the process of agglomeration of clusters is interrupted and the level of hydrolysis is reduced. Taking into account that transformation of ACP to CDHA occurs by a dissolution/reprecipitation process [46], the effect of the solvents can be attributed to the fact that ACN, EtOH and i-PrOH decrease solubility and dissolution rate of ACP, resulting in the decrease of CDHA formation. Moreover, ACN, EtOH and i-PrOH in the filtered wet solid expedite the drying process and slow the transformation of ACP [45–48]. However, to obtain single-phase β-TCP and α-TCP, the temperature of final heat-treatment should be also adjusted. Finally, the developed environmentally benign synthetic approach for α- and β-TCP could be successfully applied for modification of surface of bone implants through wet chemistry approach [49,50].

## 4. Conclusions

In the present work effects of processing conditions on the synthesis of TCP polymorphs were investigated. α- and β-TCP polymorphs were prepared by the same wet precipitation procedure at very close thermal conditions. Formation of the desired TCP polymorph can be controlled by applying a washing procedure to as-prepared calcium phosphate precipitates. It was shown that the nature and amount of washing agent determine amorphous or crystalline nature of the as-precipitated species and the formation of TCP polymorphs during the thermal treatment. Washing of the as-prepared precipitates with water and acetone led to the formation of β-TCP, while washing with acetonitrile, ethanol and isopropanol led to the crystallization of α-TCP. Maximal temperature for the synthesis of pure α-TCP under chosen synthesis conditions was determined to be 750 °C with the following formation of minor β-TCP phase at higher temperatures. On the contrary, minimal temperature for the synthesis of pure β-TCP was determined to be only 775 °C. The SEM images demonstrated that synthesized TCP powders exhibited slightly different morphological features depending on their crystal structure.

## Acknowledgements

AK would like to express sincere gratitude for Fellowship administrated by The Japan Society for the Promotion of Science (JSPS). Fellow's ID No.: L12546. Rokas Vargalis (Vilnius University) is acknowledged for assistance with SEM measurements.

## Appendix A. Supplementary data

Supplementary data to this article can be found online at https://doi.org/10.1016/j.ceramint.2019.03.174.

## References

[1] J.M. Bouler, P. Pilet, O. Gauthier, E. Verron, Biphasic calcium phosphate ceramics for bone reconstruction: a review of biological response, Acta Biomater. 53 (2017) 1–12.
[2] D. Pastorino, C. Canal, M.-P. Ginebra, Drug delivery from injectable calcium phosphate foams by tailoring the macroporosity–drug interaction, Acta Biomater. 12 (2015) 250–259.
[3] S. Bose, S. Tarafder, Calcium phosphate ceramic systems in growth factor and drug delivery for bone tissue engineering: a review, Acta Biomater. 8 (2012) 1401–1421.
[4] J. Lu, H. Yu, C. Chen, Biological properties of calcium phosphate biomaterials for bone repair: a review, RSC Adv. 8 (2018) 2015–2033.
[5] W. Habraken, P. Habibovic, M. Epple, M. Bohner, Calcium phosphates in

biomedical applications: materials for the future? Mater. Today 19 (2016) 69–87.
[6] L. Sundarabharathi, M. Chinnaswamy, D. Ponnamma, H. Parangusan, M.A.A. Al-Maadeed, Investigation of antimicrobial properties and in-vitro bioactivity of $Ce^{3+}$-$Sr^{2+}$ dual-substituted nano hydroxyapatites, J. Am. Ceram. Soc. 102 (2019) 144–157.
[7] M. Motisuke, G. Mestres, C.O. Renó, R.G. Carrodeguas, C.A.C. Zavaglia, M.-P. Ginebra, Influence of Si substitution on the reactivity of α-tricalcium phosphate, Mater. Sci. Eng. C 75 (2017) 816–821.
[8] I. Grigoraviciute-Puroniene, K. Tsuru, E. Garskaite, Z. Stankeviciute, A. Beganskiene, K. Ishikawa, A. Kareiva, A novel wet polymeric precipitation synthesis method for monophasic beta-TCP, Adv. Powder Technol. 28 (2017) 2325–2331.
[9] M. Frasnelli, V.M. Sglavo, Effect of $Mg^{2+}$ doping on beta-alpha phase transition in tricalcium phosphate (TCP) bioceramics, Acta Biomater. 33 (2016) 283–289.
[10] D. Brazete, P.M.C. Torres, J.C.C. Abrantes, J.M.F. Ferreira, Influence of the Ca/P ratio and cooling rate on the allotropic α↔β-tricalcium phosphate phase transformations, Ceram. Int. 44 (2018) 8249–8256.
[11] R.G. Carrodeguas, S. De Aza, α-Tricalcium phosphate: synthesis, properties and biomedical applications, Acta Biomater. 7 (2011) 3536–3546.
[12] T. Yu, S. Zeng, X. Liu, H. Shi, J. Ye, C. Zhou, Application of Sr-doped octacalcium phosphate as a novel Sr carrier in the α-tricalcium phosphate bone cement, Ceram. Int. 43 (2017) 12579–12587.
[13] H. Shi, S. Zeng, X. Liu, T. Yu, C. Zhou, Effects of strontium doping on the degradation and Sr ion release behaviors of α-tricalcium phosphate bone cement, J. Am. Ceram. Soc. 101 (2018) 502–508.
[14] M. Ebrahimi, M.G. Botelho, S.V. Dorozhkin, Biphasic calcium phosphates bioceramics (HA/TCP): concept, physicochemical properties and the impact of standardization of study protocols in biomaterials research, Mater. Sci. Eng. C 71 (2017) 1293–1312.
[15] H. Zhang, X. Li, J. Wen, C. Zhao, Preparation and characterisation of HA/TCP biphasic porous ceramic scaffolds with pore-oriented structure, Ceram. Int. 43 (2017) 11780–11785.
[16] J. Wang, J. Qian, W. Xu, Y. Wang, G. Hou, T. Sun, L. Luo, Effects of $Sr^{2+}$/$Zn^{2+}$ co-substitution on crystal structure and properties of nano-β-tricalcium phosphate, Ceram. Int. 44 (2018) 6096–6103.
[17] S. Feng, F. He, J. Ye, Fabrication and characterization of honeycomb β-tricalcium phosphate scaffolds through an extrusion technique, Ceram. Int. 43 (2017) 6778–6785.
[18] H. Shi, W. Zhang, X. Liu, S. Zeng, T. Yu, C. Zhou, Synergistic effects of citric acid - sodium alginate on physicochemical properties of α-tricalcium phosphate bone cement, Ceram. Int. 45 (2019) 2146–2152.
[19] D. Siek, A. Ślósarczyk, A. Przekora, A. Belcarz, A. Zima, G. Ginalska, J. Czechowska, Evaluation of antibacterial activity and cytocompatibility of α-TCP based bone cements with silver-doped hydroxyapatite and $CaCO_3$, Ceram. Int. 43 (2017) 13997–14007.
[20] P.M.C. Torres, J.C.C. Abrantes, A. Kaushal, S. Pina, N. Döbelin, M. Bohner, J.M.F. Ferreira, Influence of Mg-doping, calcium pyrophosphate impurities and cooling rate on the allotropic α↔β-tricalcium phosphate phase transformations, J. Eur. Ceram. Soc. 36 (2016) 817–827.
[21] J.T. Zhang, F. Tancret, J.M. Bouler, Fabrication and mechanical properties of calcium phosphate cements (CPC) for bone substitution, Mater. Sci. Eng. C 31 (2011) 740–747.
[22] H. Ji, Z. Huang, Z. Xia, M.S. Molokeev, M. Chen, V.V. Atuchin, M. Fang, Y.g. Liu, X. Wu, Phase transformation in $Ca_3(PO_4)_2$:$Eu^{2+}$ via the controlled quenching and increased $Eu^{2+}$ content: identification of new cyan-emitting α-$Ca_3(PO_4)_2$:$Eu^{2+}$ phosphor, J. Am. Ceram. Soc. 98 (2015) 3280–3284.
[23] N. Döbelin, T.J. Brunner, W.J. Stark, M. Fisch, E. Conforto, M. Bohner, Thermal treatment of flame-synthesized amorphous tricalcium phosphate nanoparticles, J. Am. Ceram. Soc. 93 (2010) 3455–3463.
[24] R. Faridi-Majidi, N. Nezafati, M. Pazouki, S. Hesaraki, The effect of synthesis parameters on morphology and diameter of electrospun hydroxyapatite nanofibers, J. Australas. Ceram. Soc. 53 (2017) 225–233.
[25] S.C. Cox, P. Jamshidi, R.L. Williams, L.M. Grover, K.K. Mallick, The importance of processing conditions on the biological response to apatites, Powder Technol. 284 (2015) 195–203.
[26] L. Stipniece, I. Narkevica, K. Salma-Ancane, Low-temperature synthesis of nano-crystalline hydroxyapatite: effect of Mg and Sr content, J. Am. Ceram. Soc. 100 (2017) 1697–1706.
[27] N. Vandecandelaere, F. Bosc, C. Rey, C. Drouet, Peroxide-doped apatites: preparation and effect of synthesis parameters, Powder Technol. 255 (2014) 3–9.
[28] W.P.S.L. Wijesinghe, M.M.M.G.P.G. Mantilaka, E.V.A. Premalal, H.M.T.U. Herath, S. Mahalingam, M. Edirisinghe, R.P.V.J. Rajapakse, R.M.G. Rajapakse, Facile synthesis of both needle-like and spherical hydroxyapatite nanoparticles: effect of synthetic temperature and calcination on morphology, crystallite size and crystallinity, Mater. Sci. Eng. C 42 (2014) 83–90.
[29] G.S. Kumar, G. Karunakaran, E.K. Girija, E. Kolesnikov, N.V. Minh, M.V. Gorshenkov, D. Kuznetsov, Size and morphology-controlled synthesis of mesoporous hydroxyapatite nanocrystals by microwave-assisted hydrothermal method, Ceram. Int. 44 (2018) 11257–11264.
[30] P. Kjellin, A.K. Rajasekharan, F. Currie, P. Handa, Investigation of calcium phosphate formation from calcium propionate and triethyl phosphate, Ceram. Int. 42 (2016) 14061–14065.
[31] J. Duncan, J.F. MacDonald, J.V. Hanna, Y. Shirosaki, S. Hayakawa, A. Osaka, J.M.S. Skakle, I.R. Gibson, The role of the chemical composition of monetite on the synthesis and properties of α-tricalcium phosphate, Mater. Sci. Eng. C 34 (2014) 123–129.
[32] C. Ching Lau, P.J.T. Reardon, J. Campbell Knowles, J. Tang, Phase-tunable calcium phosphate biomaterials synthesis and application in protein delivery, ACS Biomater. Sci. Eng. 1 (2015) 947–954.
[33] M.A. Nazeer, E. Yilgor, M.B. Yagci, U. Unal, I. Yilgor, Effect of reaction solvent on hydroxyapatite synthesis in sol–gel process, Royal Soc. Open Sci. 4 (2017).
[34] H. Li, F. Xue, X. Wan, H. Liu, J. Bai, C. Chu, Polyethylene glycol-assisted preparation of beta-tricalcium phosphate by direct precipitation method, Powder Technol. 301 (2016) 255–260.
[35] E. Garskaite, K.A. Gross, S.W. Yang, T.C.K. Yang, J.C. Yang, A. Kareiva, Effect of processing conditions on the crystallinity and structure of carbonated calcium hydroxyapatite (CHAp), CrystEngComm 16 (2014) 3950–3959.
[36] A. Rodrigues, A. Lebugle, Influence of ethanol in the precipitation medium on the composition, structure and reactivity of tricalcium phosphate, Colloids Surf. A Physicochem. Eng. Asp. 145 (1998) 191–204.
[37] W.I. Abdel-Fattah, F.M. Reicha, T.A. Elkhooly, Nano-beta-tricalcium phosphates synthesis and biodegradation: 1. Effect of microwave and $SO_4^{2-}$ ions on β-TCP synthesis and its characterization, Biomed. Mater. 3 (2008) 034121.
[38] P.M.C. Torres, S.I. Vieira, A.R. Cerqueira, S. Pina, O.A.B. da Cruz Silva, J.C.C. Abrantes, J.M.F. Ferreira, Effects of Mn-doping on the structure and biological properties of β-tricalcium phosphate, J. Inorg. Biochem. 136 (2014) 57–66.
[39] K.P. Sanosh, M.-C. Chu, A. Balakrishnan, T.N. Kim, S.-J. Cho, Sol–gel synthesis of pure nano sized β-tricalcium phosphate crystalline powders, Curr. Appl. Phys. 10 (2010) 68–71.
[40] R. Meenambal, P. Poojar, S. Geethanath, K. Sanjeevi, Structural insights in $Dy^{3+}$-doped β-Tricalcium phosphate and its multimodal imaging characteristics, J. Am. Ceram. Soc. 100 (2017) 1831–1841.
[41] P.N. Kumar, J.M.F. Ferreira, S. Kannan, Phase transition mechanisms involved in the formation of structurally stable β-$Ca_3(PO_4)_2$-α-$Al_2O_3$ composites, J. Eur. Ceram. Soc. 37 (2017) 2953–2963.
[42] M. Lasgorceix, L. Grenho, M.H. Fernandes, C. Ott, L. Boilet, A. Leriche, F. Monteiro, F. Cambier, S. Hocquet, Femtosecond laser impact on calcium phosphate bioceramics assessed by micro-Raman spectroscopy and osteoblastic behaviour, J. Eur. Ceram. Soc. 38 (2018) 5545–5553.
[43] A.F. Vásquez, S. Domínguez, L.A. Loureiro dos Santos, α-TCP cements prepared by syringe-foaming: influence of $Na_2HPO_4$ and surfactant concentration, Mater. Sci. Eng. C 81 (2017) 148–155.
[44] C. Stahli, J. Thuring, L. Galea, S. Tadier, M. Bohner, N. Dobelin, Hydrogen-substituted β-tricalcium phosphate synthesized in organic media, Acta Crystallogr. B 72 (2016) 875–884.
[45] E. Babaie, H. Zhou, B. Lin, S.B. Bhaduri, Influence of ethanol content in the precipitation medium on the composition, structure and reactivity of magnesium–calcium phosphate, Mater. Sci. Eng. C 53 (2015) 204–211.
[46] M.S. Tung, T.J. O'Farrell, Effect of ethanol on the formation of calcium phosphates, Colloids Surf. A Physicochem. Eng. Asp. 110 (1996) 191–198.
[47] L. Vecbiskena, K.A. Gross, U. Riekstina, T.C.-K. Yang, Crystallized nano-sized alpha-tricalcium phosphate from amorphous calcium phosphate: microstructure, cementation and cell response, Biomed. Mater. 10 (2015) 025009.
[48] Z. Zyman, D. Rokhmistrov, V. Glushko, Structural changes in precipitates and cell model for the conversion of amorphous calcium phosphate to hydroxyapatite during the initial stage of precipitation, J. Cryst. Growth 353 (2012) 5–11.
[49] K. Duan, R. Wang, Surface modifications of bone implants through wet chemistry, J. Mater. Chem. 16 (2006) 2309–2321.
[50] G. Ciobanu, M. Harja, Cerium-doped hydroxyapatite/collagen coatings on titanium for bone implants, Ceram. Int. 45 (2019) 2852–2857.

Article II

**Effect of Mn doping on the low-temperature synthesis of tricalcium phosphate (TCP) polymorphs**

L. Sinusaite, A.M. Renner, M.B. Schutz, A. Antuzevics, U. Rogulis, I. Grigoraviciute-Puroniene, S. Mathur, A. Zarkov

*Journal of the European Ceramic Society,* 39 (2019) 3257-3263

Journal of the European Ceramic Society 39 (2019) 3257–3263

Contents lists available at ScienceDirect

Journal of the European Ceramic Society

journal homepage: www.elsevier.com/locate/jeurceramsoc

# Effect of Mn doping on the low-temperature synthesis of tricalcium phosphate (TCP) polymorphs

Lauryna Sinusaite[a], Alexander M. Renner[b], Markus B. Schütz[b], Andris Antuzevics[c], Uldis Rogulis[c], Inga Grigoraviciute-Puroniene[a], Sanjay Mathur[b], Aleksej Zarkov[a,*]

[a] Institute of Chemistry, Vilnius University, Naugarduko 24, LT-03225, Vilnius, Lithuania
[b] Institute of Inorganic Chemistry, University of Cologne, Greinstrasse 6, 50939, Cologne, Germany
[c] Institute of Solid State Physics, University of Latvia, Kengaraga 8, LV-1063, Riga, Latvia

ARTICLE INFO

*Keywords:*
Tricalcium phosphate
$Ca_3(PO_4)_2$
Polymorphism
Alpha-TCP
Beta-TCP
Mn doping

ABSTRACT

Effect of Mn doping on the low-temperature synthesis of tricalcium phosphate (TCP) polymorphs was demonstrated in α- and β-TCP polymorphs prepared by wet precipitation method under identical conditions and annealed at 700 °C. Calcium phosphates with Mn doping level in the range from 1 to 5 mol% were studied and the formation of desired polymorph was controlled by varying Mn content in as-prepared precipitates. It was found that increasing Mn content resulted in the formation of β-TCP, while α-TCP was obtained with low Mn doping level, whereas a mixture of two polymorphs was obtained for intermediate Mn concentrations. Moreover, doping with Mn ions allowed the synthesis of β-TCP at relatively low temperature (700 °C). Synthesized compounds were characterized by X-ray diffraction (XRD) analysis, electron paramagnetic resonance (EPR), Fourier-transform infrared spectroscopy (FTIR), scanning electron microscopy (SEM), inductively coupled plasma optical emission spectrometry (ICP-OES) and colorimetric MTT assay.

## 1. Introduction

Calcium phosphates (CPs) are the main constituents of bones and teeth and play an essential role in human life. Due to the similarity to the mineral phase of bones and excellent biocompatibility, different synthetic CPs have been widely applied as biomaterials for bone repair [1]. These materials are used in biomedical applications in different forms varying from thin coatings on metallic implants to sintered bioceramics [2]. Tricalcium phosphate ($Ca_3(PO_4)_2$, TCP) is one of the representative biomaterials, which finds an application in bone cements and bone implants due to its excellent resorbability and osteoconductivity [3].

There are three known polymorphs of TCP: the low-temperature β-TCP and the high-temperature forms α- and α'-TCP. The last one is not suitable for practical applications, because it exists only at temperatures above 1430 °C and transforms to α-TCP on cooling below the transition temperature. In contrast, β-TCP is stable at room temperature and transforms at about 1125 °C to α-TCP phase, which can be retained during the cooling to room temperature [4]. However, thermal quenching is often required for the synthesis of pure α-TCP without β-TCP secondary phase, which forms during the cooling of the sample, since phase transition from β- to α-TCP is reversible [5–7]. Commonly, the synthesis of both α- and β-TCP polymorphs is performed by thermal treatment of a precursor with appropriate Ca to P molar ratio (1.5:1). Usually β-TCP powders are synthesized by solid-state reaction or wet precipitation method at temperatures about 800 °C or higher [8–11]. The most common approach to the synthesis of α-TCP is thermal transformation of crystalline β-TCP at temperatures above 1125 °C [12]. However, α-TCP can be also synthesized from amorphous CP at such low temperatures as 600–700 °C with further transformation to β-TCP at about 900 °C [13]. Thereby, α-TCP can be obtained at low and high temperatures – below the temperature of formation of β-TCP and above the temperature of transition of β-TCP to α-TCP.

α- and β-TCP crystallize in the monoclinic and rhombohedral crystal systems, respectively. Theoretical densities are 2.866 g $cm^{-3}$ for α-TCP and 3.066 g $cm^{-3}$ for β-TCP. These structural differences between α- and β-polymorphs are responsible for their different chemical and biological properties, such as solubility and biodegradability [4]. The solubility of α-TCP is higher [14], moreover it is much more reactive in aqueous solutions than β-TCP and easily hydrolyzes with a formation of calcium deficient hydroxyapatite ($Ca_{10-x}(PO_4)_{6-x}(HPO_4)_x(OH)_{2-x}$, CDHA), which is similar to bone hydroxyapatite ($Ca_{10}(PO_4)_6(OH)_2$, HA) [15]. These differences in chemical properties of TCP polymorphs define their different practical applications. α-TCP is widely used as a

* Corresponding author.
*E-mail address:* aleksej.zarkov@chf.vu.lt (A. Zarkov).

https://doi.org/10.1016/j.jeurceramsoc.2019.03.057
Received 22 February 2019; Received in revised form 23 March 2019; Accepted 31 March 2019
Available online 01 April 2019

major powder component of various bone cements [16–18], whereas β-TCP is an important component of mono- or biphasic bioceramics and composites [19–21]. Both of these materials promote bone growth where implanted and support the proliferation of fibroblasts, osteoblasts and other bone cells [22].

It is well known that doping at even very low levels can drastically affect physical and morphological properties of different materials, including TCP [23,24]. At the same time surface properties such as microporosity, grain size and specific surface area have been shown to play a determinant role in the process of osteoinduction of biomaterials [2]. Therefore, partial substitution of $Ca^{2+}$ ions in CP matrix by biologically active inorganic ions is a promising strategy to improve bone defect healing. For example, improved biological performance of Mn and Sr co-doped β-TCP was shown by Torres *et al.* [8], and small amount of $Fe^{3+}$ ions was found to have a positive impact on the biomedical properties of HA [25]. Number of previous studies on synthetic CPs have explained the role of substitution with biocompatible ions, such as $Mg^{2+}$, $Zn^{2+}$, $Sr^{2+}$, $Si^{4+}$ etc. [26–31].

Mn is known to be a doping element that plays an important role in bone metabolism by controlling the cellular activity of osteoblasts and osteoclasts [32]. Recently, HA doped and co-doped with $Mg^{2+}$, $Mn^{2+}$ and $Sr^{2+}$ ions was synthesized by Moreira et al. by wet precipitation method [33]. Biocompatibility of Mn-doped HA and β-TCP was studied that revealed the toxicity of these compounds to be negligible [34,35]. Miola et al. performed in vitro study of Mn-doped bioactive glasses for bone regeneration and demonstrated that Mn-doping can promote the expression of alkaline phosphatase and some other bone morphogenetic proteins [36]. Improved bioactivity of electrodeposited $Sr^{2+}$ and $Mn^{2+}$ co-doped HA films on Ti implant was shown by Huang et al. [37]. Moreover, doping of CPs with paramagnetic ions such as $Gd^{3+}$ or $Mn^{2+}$ makes it possible to use these materials for magnetic resonance imaging application [38,39].

In the present work, we report on the influence of Mn doping on the low-temperature synthesis of both α- and β-TCP polymorphs and demonstrate a phase-selective preparation of different crystalline phases, induced by the concentration of dopants, under identical processing conditions. To the best of our knowledge, Mn-doped α-TCP was synthesized for the first time in this study. Moreover, it was demonstrated that Mn doping lowers the temperature of phase transition from α- to β-TCP.

## 2. Material and methods

### 2.1. Synthesis

Calcium nitrate tetrahydrate ($Ca(NO_3)_2 \cdot 4H_2O$, ≥99%, Roth), manganese(II) nitrate tetrahydrate ($Mn(NO_3)_2 \cdot 4H_2O$, 98%, Alfa Aesar) and diammonium hydrogen phosphate ($(NH_4)_2HPO_4$, ≥98%, Roth) were used as starting materials for the synthesis. Firstly, an appropriate amount of $(NH_4)_2HPO_4$ was dissolved in deionized water to obtain a 0.5 M solution, to which concentrated ammonia solution ($NH_4OH$, 25%, Roth) was added under constant mixing in order to adjust the pH to 10. Following this, a solution containing Ca and Mn nitrates dissolved in deionized water (total metal ions concentration was 0.75 M) was rapidly added to the above mixture resulting in the instantaneous formation of precipitates. Total metal ions to phosphorous ratio was kept 1.50 for all synthesized compounds. The obtained precipitates were mixed in the reaction mixture for 10 min, afterwards filtered, washed with deionized water and ethanol and dried at 50 °C overnight in the oven. Finally, dry powders were ground in agate mortar and annealed in the furnace at 700 °C temperature for 5 h in air atmosphere with a heating rate of 5 °C/min.

### 2.2. Characterization

Powder X-ray diffraction data were collected using Ni-filtered Cu Kα radiation on Rigaku MiniFlex II diffractometer working in Bragg-Brentano (θ/2θ) geometry. The data were collected within 2θ angle range from 10° to 60° at a step width of 0.01° and speed of 1°/min. The thermal decomposition of the as-prepared precipitates was analyzed through thermogravimetric (TG) analysis using Perkin Elmer STA 6000 Simultaneous Thermal Analyzer. Samples of about 5–10 mg were heated from 25 to 900 °C at a heating rate of 10 °C/min in a dry flowing air (20 mL/min). Morphology of the synthesized powders was characterized by scanning electron microscopy performed with a Hitachi SU-70 field-emission scanning electron microscope (FE-SEM). Infrared (FTIR) spectra were obtained in the range of 4000–400 $cm^{-1}$ employing Bruker ALPHA ATR spectrometer. Electron paramagnetic resonance (EPR) spectra were recorded using a conventional X-band (microwave frequency ≈ 9.18 GHz) RE 13-06 spectrometer with 100 kHz field modulation at room temperature. The magnetic field was calibrated with a DPPH reference sample with g = 2.0036 ± 0.0002. Elemental analysis of the synthesized products was performed by means of inductively coupled plasma optical emission spectrometry (ICP-OES) using Agilent 5110 ICP-OES spectrometer. The samples prior to analysis were dissolved in 5% nitric acid ($HNO_3$, Rotipuran® Supra 69%, Roth) and diluted to an appropriate volume with deionized water. Calibration solutions were prepared by an appropriate dilution of the stock standard solutions (single-element ICP standards 1000 mg/L, Roth). The cytotoxicity of the synthesized samples was evaluated by means of MTT assay using HEK 293 cells. HEK 293 cells (150 µL of $7.5 \times 10^4$ cells/mL) were cultured in a 96-well plate at 37 °C, 5% $CO_2$ for 24 h. The samples with different concentrations of TCP powders (25, 50 and 100 µg/mL dispersed in sterile cell medium) were added (200 µL) to 96-well plate and incubated over a period of 6, 24 and 48 h at 37 °C. HEK 293 cells treated only with culture media were fixed as a positive control. To each well, MTT (5 mg/mL) was added for 2 h incubation at 37 °C. Afterwards, the supernatant was removed, and 150 µL of DMSO/well were added to resolve the formazan crystals. The absorbance was measured at 630 nm using Elisa reader multiplate (ELX 800, BioTek Instruments).

## 3. Results and discussion

The XRD patterns of as-prepared CP precipitates with different amount of Mn (Fig. 1a) evidently show the poorly crystalline nature of samples reflected in broad profile of the diffraction signals with a major signal centered around 30°. The obtained XRD patterns of both pristine and doped-samples indicated an amorphous nature of the powders and suggested that Mn content does not affect crystallinity of the samples. Non-crystalline CP was obtained for all samples regardless of the chemical composition. XRD patterns of similar shape for amorphous CP were previously reported by Vecstaudza et al. [40].

FTIR spectra of the as-prepared CP powders are demonstrated in Fig. 1b. The wavenumber range of 4000–400 $cm^{-1}$ was selected to demonstrate the representative functional groups of synthesized materials. In all cases, the most dominant resonance of the analyzed samples are the phosphate $\nu_3$ mode, centered at 1024 $cm^{-1}$, and the phosphate $\nu_4$ domain, discerned at 562 $cm^{-1}$ [41]. A weak shoulder of the absorption band at 1024 $cm^{-1}$ can be seen at around 951 $cm^{-1}$, which is attributed to $\nu_1(PO_4^{3-})$ resonance and a week band at 870 $cm^{-1}$ is assigned to the stretching mode of protonated phosphate group [41,42]. Therefore, the FTIR spectra indicated the presence of phosphate ions in the as-prepared samples. It is also noteworthy that broad and non-split shape of the mentioned bands implies amorphous character of the as-prepared materials, previously confirmed by XRD results. Additionally, broad absorption bands centered at 3250 $cm^{-1}$ and 1660 $cm^{-1}$are assignable to O—H stretching and H—O—H bending mode of residual water [41].

Room temperature EPR spectra of the CP precipitates dried at 50 °C are illustrated in Fig. 1c. In general, $Mn^{2+}$ EPR spectra are sufficiently complex, especially in low symmetry polycrystalline systems, as the

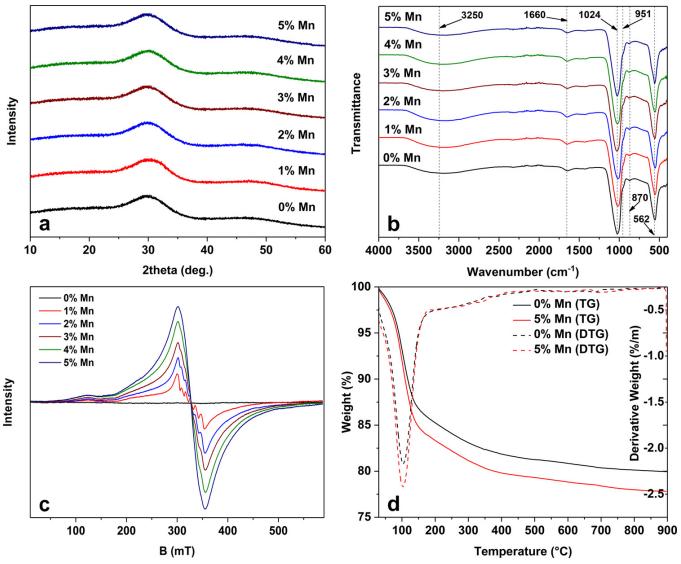


**Fig. 1.** XRD patterns (a), FTIR spectra (b), EPR spectra (c) of CP precipitates with different amount of Mn dried at 50 °C and TG/DTG curves of dried CP precipitates with 0 and 5% of Mn (d).

averaging across all possible single crystal orientations and the overlap of signals from multiple possible sites lead to broadening of the spectra. The obtained spectra showed typical $Mn^{2+}$ EPR spectral features – zero field splitting (ZFS) of the $^6S_{5/2}$ ground state electron spin $S = 5/2$ and hyperfine (HF) coupling to the 100% abundant $^{55}Mn$ nuclear spin $I = 5/2$. As expected, no resonance signals were observed in the undoped sample. The increase of Mn content has two effects – first, EPR spectra intensities were found to increase with increasing concentration of dopants. The intensity of peaks reflected the number of spins in the system and can, in principle, be applied for analyzing $Mn^{2+}$ content in the sample [43]. The second effect observed upon increasing the dopant content, was the spin-spin interaction promoted line broadening, therefore, EPR spectra were better resolved at lower Mn concentrations. For the interpretation of the $Mn^{2+}$ EPR spectra the following spin-Hamiltonian (SH) was used [44]:

$$H = g\beta BS + D[S_z^2 - S(S+1)/3] + E(S_x^2 - S_y^2) + ASI \quad (1)$$

where $g$ is the $g$-factor, $\beta$ is the Bohr magneton and $S_{x,y,z}$ are the projections of the spin operator $S$. The HF coupling tensor $A$ quantifies the interaction between the nuclear and electron spins. For $S$-state ions such as $Mn^{2+}$ $g$ and A values are typically isotropic. The effect of ZFS is reflected in the SH parameters $D$ and $E$. In the EPR spectra of the as-prepared precipitates (Fig. 1c) the $2I+1 = 6$ component HF structure of the central $M_S = +1/2 \rightarrow -1/2$ transition can be clearly resolved for $Mn^{2+}$ concentration below 3 mol%. The estimated SH parameters $g \approx 2.00$ and $A \approx 260$ MHz are in a good agreement with the reported values for $Mn^{2+}$ defects substituting the Ca lattice sites of HA [43,45].

TG/DTG curves of undoped and 5 mol% Mn-doped as-prepared CP precipitates are given in Fig. 1d as representative. It is clearly seen that behavior of TG curves is very similar for both samples, suggesting that presence of Mn ions does not affect thermal decomposition behavior of precursor powders. Decomposition occurs in few steps, during the first step a mass loss of about 15% is observed with its maximal rate at around 100 °C. This weight loss can be attributed to the removal of residual water from the samples. At higher temperatures weight gradually decreases with a weight loss of about 5%, which is also attributed to the removal of water. Sample mass above 700 °C is nearly constant indicating no significant mass change above this temperature.

The phase crystallinity and purity of all CP powders annealed at 700 °C for 5 h was characterized by XRD analysis (Fig. 2) that showed the formation of different final products depending on the chemical composition of starting precipitates. The undoped sample crystallized to pure α-TCP phase with a monoclinic crystal structure. All the diffraction peaks match very well the standard XRD data of α-$Ca_3(PO_4)_2$ (ICDD 00-070-0364). With addition of 1 mol% of Mn ions, monoclinic structure of the sample remained, however existence of minimal amount of β-TCP was detected. Moreover, some structural changes in α-TCP were observed. Diffraction peaks located at 22.8, 24.2, 34.3 and 46.8° noticeably split, which can be assumed as an evidence of incorporation of Mn ions into crystal lattice and structural changes of the latter. Detailed study on the influence of Mn doping on the structural properties of α-TCP will be published elsewhere. Increasing of Mn concentration to 2 mol% does not change a major phase of the sample, however presence β-TCP as a minor crystalline phase can be observed. For the samples with Mn content of 3 and 4 mol% a mixture of TCP polymorphs was formed in which the percentage of β-TCP increased with increasing Mn amount. Finally, when concentration of Mn reached 5 mol%, pure β-TCP phase was obtained. There are no XRD peaks arising from any by-products and all signals correspond to rhombohedral crystal structure of $Ca_3(PO_4)_2$ (ICDD 00-070-2065). Thus, at the same temperature α- and β-TCP phases were obtained for undoped and 5% Mn-doped samples, respectively. Stabilization of β-TCP structure can be associated with thermodynamic stability of doped α- and β-TCP. Previously, first-principal calculations of divalent substitution of $Ca^{2+}$ ions in TCP polymorphs were reported by Matsunaga *et al.* [46]. It was shown that α-TCP can easily incorporate smaller sized cations ($Mg^{2+}$ and $Zn^{2+}$) only at the limited number of Ca sites in its crystal lattice. On

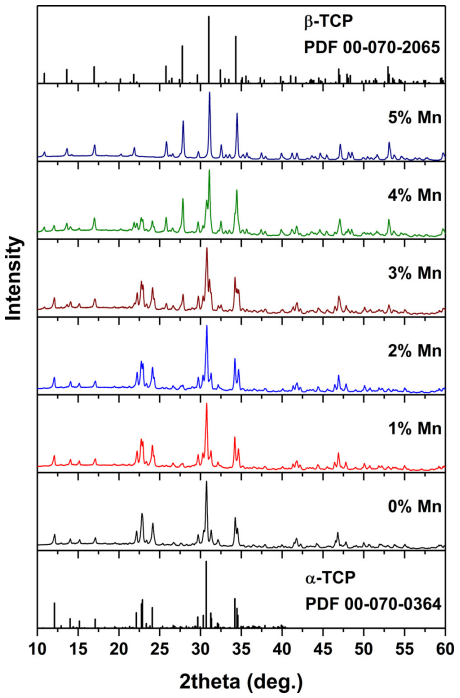


**Fig. 2.** XRD patterns of CP powders with different amount of Mn annealed at 700 °C for 5 h.

the other hand, β-TCP structure shows low defect formation energy of small substitutional cations on Ca-5 sites, therefore divalent cations are more stable in β-TCP, as compared to those in α-TCP. Considering the temperature of the formation of β-TCP, previously Dobelin et al. reported on the complete transformation of flame-synthesized undoped α-TCP powders to β-TCP only at 950 °C temperature [13]. Somrani et al. observed this phase transition at 900 °C, whereas at 800 °C dominant α-TCP phase with a small amount of β-TCP was obtained [47]. Therefore, it can be concluded that presence of Mn ions in a crystal structure of TCP lowers α- to β-TCP phase transition temperature significantly.

The FTIR spectra (1500–500 $cm^{-1}$) of the samples annealed at 700 °C for 5 h are depicted in Fig. 3. Given the different phase composition in CP samples consisting of α- and β-TCP polymorphs, the structural differences in these materials resulted in different characteristic bands of phosphate ions [48]. In all the analyzed samples several distinct bands observed at around 1200–990 $cm^{-1}$ correspond to the phosphate $\nu_3$ stretching mode [49]. Some differences among the spectra representing different polymorphs appear on the lower wavenumber side of the $\nu_3$ mode. For the undoped sample the single resonance at 960 $cm^{-1}$ and for the sample doped with 5 mol% of Mn two distinct bands at 986 and 946 $cm^{-1}$ can be seen. These bands correspond well to $\nu_1$ mode of α and β-TCP phases, respectively [4]. In the case of undoped sample, a broad absorbance band centered at around 570 $cm^{-1}$ is assigned to the $\nu_4$ bending mode of the phosphate group. However, it is evident that with an increase of Mn content it gradually becomes resolved into two distinct peaks, which is characteristic for β-TCP phase [4]. Thereby, the FTIR spectra indicate the presence of

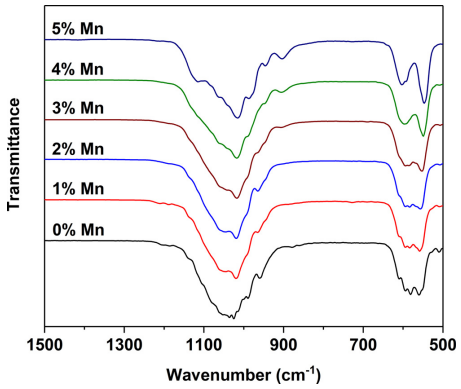


**Fig. 3.** FTIR spectra of CP powders with different amount of Mn annealed at 700 °C for 5 h.

phosphate ions in the annealed samples, confirming formation of two different TCP polymorphs. It is also noteworthy that FTIR spectrum of pure β-TCP phase, which actually is 5 mol% Mn-doped sample, has a well distinguished but unknown band at 905 $cm^{-1}$. This band was also detected in TCP samples by Torres et al. however it was not interpreted [50]. The samples with 3 and 4 mol% of Mn also possess the same peak, the intensity of this band increases with increasing of Mn content.

The EPR spectra of CP precipitates annealed at 700 °C are shown in Fig. 4. Similarly, to the precipitates dried at 50 °C, the HF structure is resolved only for Mn doping level of 1 and 2 mol% and its estimated magnitude is $A \approx 260$ MHz. The value of A correlates with the electronegativity of the surrounding ligands [51], which suggests that the nature of $Mn^{2+}$ bonding to the neighboring ligands is similar in the as-prepared precipitates and α-TCP structures. On the other hand, the broad fine structure curves caused by local crystal field effects at defect sites, are different depending on Mn concentration. Signal at $B \approx 260$ and 440 mT appear when Mn doping exceeds 2 mol%. According to the XRD data (see Fig. 2), the products formed at intermediate doping concentrations are not single phase, therefore, the observed EPR spectrum most likely is a superposition of several $Mn^{2+}$ signals. The

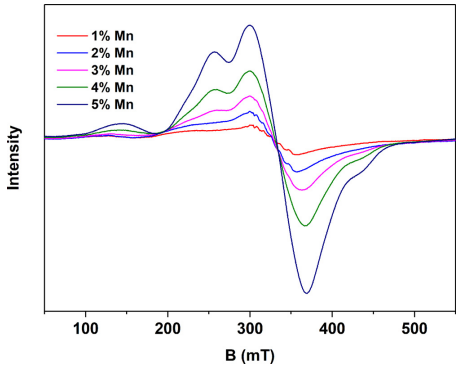


**Fig. 4.** Room temperature EPR spectra of CP precipitates with different amount of Mn annealed at 700 °C.

**Table 1**
Results of the elemental analysis of the samples performed by ICP-OES.

| Sample | Mn/(Mn + Ca), % | (Mn + Ca)/P |
|---|---|---|
| $Ca_3(PO_4)_2$ | – | 1.46 |
| $Ca_3(PO_4)_2$ : 1% Mn | 1.02 | 1.47 |
| $Ca_3(PO_4)_2$ : 2% Mn | 2.07 | 1.47 |
| $Ca_3(PO_4)_2$ : 3% Mn | 3.06 | 1.47 |
| $Ca_3(PO_4)_2$ : 4% Mn | 4.05 | 1.46 |
| $Ca_3(PO_4)_2$ : 5% Mn | 5.14 | 1.48 |

evaluated ZFS parameter $D \approx 1350$ MHz of the additional structure is in a good agreement with the determined value for $Mn^{2+}$ substituting the Ca-5 site of β-TCP [52]. Thus EPR spectra corroborate the results of XRD – at doping level above 3 mol% the samples annealed at 700 °C contain β-TCP phase.

In order to confirm chemical composition of the synthesized compounds, elemental analysis was performed by means of ICP-OES. Results of the analysis are summarized in Table 1.

Based on the experimental data on Mn to Ca ratio that are in a good agreement with nominal chemical composition, it can be concluded that precipitation of Mn and Ca occurs with a similar rate and this synthesis method is suitable for the preparation of Mn-doped TCP powders with controllable chemical composition. However, metals to P ratio was determined to be slightly lower than nominal one for TCP and varied in the range from 1.46 to 1.48 probably due to the presence of small amount of neighboring phases such as calcium pyrophosphate ($Ca_2P_2O_7$) with lower Ca to P ratio. Formation of $Ca_2P_2O_7$ during the synthesis of TCP by precipitation method was also observed by other groups [8,50]. Another possible reason of this mismatch is a formation of hydrogen-substituted TCP, which was previously reported for β-TCP synthesized in organic media [53].

SEM images of CP precipitates with 0 and 5 mol% of Mn annealed at 700 °C reveal (Fig. 5) that undoped TCP sample consisted of mostly uniform sub-micro sized elongated dumbbell-shaped particles with some agglomerates (Fig. 5a) with axial grain size ranging between 120–150 nm whereas length of the particles varied in the range of 300–700 nm. Substitution of Ca ions by 5 mol% of Mn slightly changed morphological features of the powders (Fig. 5b). Shape of the particles was found to be similar, however the dimensions were reduced possibly due to higher densification promoted by Mn doping. SEM images of the samples with intermediate Mn content are given in Fig. S1.

All synthesized TCP samples were employed to screen their cytotoxicity profiles for different concentrations (25–100 μg/mL) with an incubation time of 6, 24, and 48 h using colorimetric MTT assay. Cell viability was calculated according to the control sample, which did not contain synthesized TCP powders. Results on the cell viability with different concentrations of the samples and incubation time of 48 h are depicted in Fig. 6. Two main regularities can be seen from the results. Firstly, the cell viability does not depend significantly on the concentration of the samples and for all concentrations it is determined to be above 80%, indicating biocompatible nature of the powders. Secondly, the cell viability does not depend on crystal structure of the samples and Mn content as well. The results have not revealed any toxic effects of Mn ions even with its highest concentration thus ruling out the leaching of $Mn^{2+}$ ions under physiological conditions. The only sample revealing a trend in an average cell viability was undoped α-TCP that surprisingly showed gradual decrease in cell viability from 85.7 ± 7.7 to 81.3 ± 2.9 and 73.8 ± 6.2% for concentration of 25, 50 and 100 μg/mL, respectively. However, it can be noticed, that introducing of 1 mol% of Mn improves cell viability profile of α-TCP and keeps it nearly constant for all sample concentrations although there are no changes in crystalline phase of the sample (see Fig. 2).

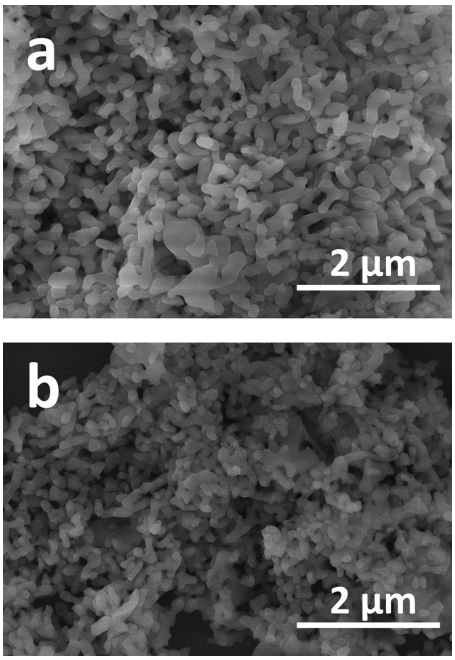


**Fig. 5.** SEM images of CP powders without Mn (a) and 5 mol% of Mn (b) annealed at 700 °C for 5 h.

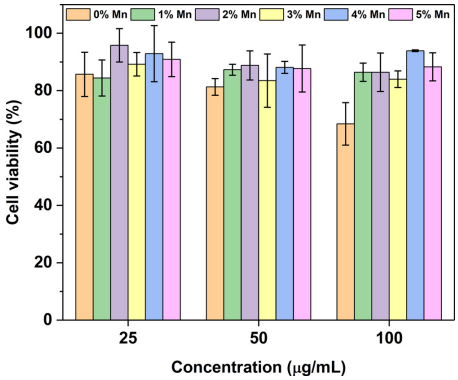


**Fig. 6.** Cell viability profile of cultured HEK 293 cells after incubation for 48 h with the samples of TCP at different concentrations.

## 4. Conclusions

Both α- and β-TCP polymorphs were prepared by wet precipitation method under identical processing conditions after annealing at 700 °C. The phase-selective preparation of different crystalline phases was achieved through a doping with Mn ions. Although Mn content did not

affect structure of the as-prepared precipitates, it was found that increasing Mn content resulted in the formation of β-TCP, while α-TCP was obtained with low Mn doping level, whereas a mixture of two polymorphs was obtained for intermediate Mn concentrations. To the best of our knowledge Mn-doped α-TCP was synthesized for the first time in this study. It was demonstrated that partial substitution of Ca by Mn ions leads to the structural changes in α-TCP crystal lattice. Moreover, doping with Mn ions allowed the synthesis of β-TCP at relatively low temperature – 700 °C. Cytotoxicity test have not revealed any toxic effects of Mn ions even for the samples with the highest Mn concentration, on the contrary, introducing of 1 mol% of Mn to α-TCP resulted in higher cell viability values.

## Notes

The authors declare no competing financial interest.

## Acknowledgements

This research was funded by the European Social Fund under the No. 09.3.3- LMT-K-712 “Development of Competences of Scientists, other Researchers and Students through Practical Research Activities” measure (grant No. 09.3.3-LMT-K-712-07-0056). Authors are thankful to the University of Cologne for infrastructural and financial support. JSC “Interlux” is acknowledged for providing equipment for elemental analysis. Authors are grateful to R. Vargalis (Vilnius University) for taking SEM images.

## Appendix A. Supplementary data

Supplementary material related to this article can be found, in the online version, at doi:https://doi.org/10.1016/j.jeurceramsoc.2019.03.057.

## References

[1] J.M. Bouler, P. Pilet, O. Gauthier, E. Verron, Biphasic calcium phosphate ceramics for bone reconstruction: a review of biological response, Acta Biomater. 53 (2017) 1–12.
[2] W. Habraken, P. Habibovic, M. Epple, M. Bohner, Calcium phosphates in biomedical applications: materials for the future? Mater. Today 19 (2016) 69–87.
[3] S.V. Dorozhkin, Calcium orthophosphates, J. Mater. Sci. 42 (2007) 1061–1095.
[4] R.G. Carrodeguas, S. De Aza, α-Tricalcium phosphate: synthesis, properties and biomedical applications, Acta Biomater. 7 (2011) 3536–3546.
[5] J. Duncan, J.F. MacDonald, J.V. Hanna, Y. Shirosaki, S. Hayakawa, A. Osaka, J.M.S. Skakle, I.R. Gibson, The role of the chemical composition of monetite on the synthesis and properties of α-tricalcium phosphate, Mater. Sci. Eng. C 34 (2014) 123–129.
[6] G. Cicek, E.A. Aksoy, C. Durucan, N. Hasirci, Alpha-tricalcium phosphate (α-TCP): solid state synthesis from different calcium precursors and the hydraulic reactivity, J. Mater. Sci. Mater. Med. 22 (2011) 809–817.
[7] D. Brazete, P.M.C. Torres, J.C.C. Abrantes, J.M.F. Ferreira, Influence of the Ca/P ratio and cooling rate on the allotropic α↔β-tricalcium phosphate phase transformations, Ceram. Int. 44 (2018) 8249–8256.
[8] P.M.C. Torres, A. Marote, A.R. Cerqueira, A.J. Calado, J.C.C. Abrantes, S. Olhero, O.A.B. da Cruz e Silva, S.I. Vieira, J.M.F. Ferreira, Injectable MnSr-doped brushite bone cements with improved biological performance, J. Mater. Chem. B Mater. Biol. Med. 5 (2017) 2775–2787.
[9] P.M.C. Torres, J.C.C. Abrantes, A. Kaushal, S. Pina, N. Döbelin, M. Bohner, J.M.F. Ferreira, Influence of Mg-doping, calcium pyrophosphate impurities and cooling rate on the allotropic α↔β-tricalcium phosphate phase transformations, J. Eur. Ceram. Soc. 36 (2016) 817–827.
[10] P. Nandha Kumar, J.M.F. Ferreira, S. Kannan, Phase transition mechanisms involved in the formation of structurally stable β-$Ca_3(PO_4)_2$-α-$Al_2O_3$ composites, J. Eur. Ceram. Soc. 37 (2017) 2953–2963.
[11] M. Lasgorceix, L. Grenho, M.H. Fernandes, C. Ott, L. Boilet, A. Leriche, F. Monteiro, F. Cambier, S. Hocquet, Femtosecond laser impact on calcium phosphate bioceramics assessed by micro-Raman spectroscopy and osteoblastic behaviour, J. Eur. Ceram. Soc. 38 (2018) 5545–5553.
[12] L. Carbajal, S. Serena, M.A. Sainz, A. Caballero, Phase and melting relationships of β, α and α′-$Ca_3(PO_4)_2$ polymorphs in the $Ca_3(PO_4)_2$-$Zn_3(PO_4)_2$ system, J. Eur. Ceram. Soc. 37 (2017) 2277–2283.
[13] N. Döbelin, T.J. Brunner, W.J. Stark, M. Fisch, E. Conforto, M. Bohner, Thermal treatment of flame-synthesized amorphous tricalcium phosphate nanoparticles, J. Am. Ceram. Soc. 93 (2010) 3455–3463.
[14] S.V. Dorozhkin, M. Epple, Biological and medical significance of calcium phosphates, Angew. Chem. Int. Ed. 41 (2002) 3130–3146.
[15] E. Boanini, M. Gazzano, A. Bigi, Ionic substitutions in calcium phosphates synthesized at low temperature, Acta Biomater. 6 (2010) 1882–1894.
[16] A. Zima, J. Czechowska, D. Siek, R. Olkowski, M. Noga, M. Lewandowska-Szumieł, A. Ślósarczyk, How calcite and modified hydroxyapatite influence physicochemical properties and cytocompatibility of alpha-TCP based bone cements, J. Mater. Sci. Mater. Med. 28 (2017) 117.
[17] A.F. Vásquez, S. Domínguez, L.A. Loureiro dos Santos, α-TCP cements prepared by syringe-foaming: influence of $Na_2HPO_4$ and surfactant concentration, Mater. Sci. Eng. C 81 (2017) 148–155.
[18] M. Roozbahani, M. Alehosseini, M. Kharaziha, R. Emadi, Nano-calcium phosphate bone cement based on Si-stabilized α-tricalcium phosphate with improved mechanical properties, Mater. Sci. Eng. C 81 (2017) 532–541.
[19] R. Taktak, A. Elghazel, J. Bouaziz, S. Charfi, H. Keskes, Tricalcium phosphate-fluorapatite as bone tissue engineering: evaluation of bioactivity and biocompatibility, Mater. Sci. Eng. C 86 (2018) 121–128.
[20] K. Maji, S. Dasgupta, K. Pramanik, A. Bissoyi, Preparation and characterization of gelatin-chitosan-nanoβ-TCP based scaffold for orthopaedic application, Mater. Sci. Eng. C 86 (2018) 83–94.
[21] M. Ebrahimi, M.G. Botelho, S.V. Dorozhkin, Biphasic calcium phosphates bioceramics (HA/TCP): concept, physicochemical properties and the impact of standardization of study protocols in biomaterials research, Mater. Sci. Eng. C 71 (2017) 1293–1312.
[22] M.B. Thürmer, C.E. Diehl, L.A.L. dos Santos, Calcium phosphate cements based on alpha-tricalcium phosphate obtained by wet method: synthesis and milling effects, Ceram. Int. 42 (2016) 18094–18099.
[23] S. Tkachenko, M. Horynová, M. Casas-Luna, S. Diaz-de-la-Torre, K. Dvořák, L. Celko, J. Kaiser, E.B. Montufar, Strength and fracture mechanism of iron reinforced tricalcium phosphate cermet fabricated by spark plasma sintering, J. Mech. Behav. Biomed. Mater. 81 (2018) 16–25.
[24] M. Motisuke, G. Mestres, C.O. Renó, R.G. Carrodeguas, C.A.C. Zavaglia, M.-P. Ginebra, Influence of Si substitution on the reactivity of α-tricalcium phosphate, Mater. Sci. Eng. C 75 (2017) 816–821.
[25] J. Lu, H. Yu, C. Chen, Biological properties of calcium phosphate biomaterials for bone repair: a review, RSC Adv. 8 (2018) 2015–2033.
[26] M. Šupová, Substituted hydroxyapatites for biomedical applications: a review, Ceram. Int. 41 (2015) 9203–9231.
[27] M. Frasnelli, V.M. Sglavo, Effect of $Mg^{2+}$ doping on beta-alpha phase transition in tricalcium phosphate (TCP) bioceramics, Acta Biomater. 33 (2016) 283–289.
[28] G. Dong, Y.X. Zheng, L.Y. He, G. Wu, C.L. Deng, The effect of silicon doping on the transformation of amorphous calcium phosphate to silicon-substituted alpha-tricalcium phosphate by heat treatment, Ceram. Int. 42 (2016) 883–890.
[29] Ž. Radovanović, B. Jokić, D. Veljović, S. Dimitrijević, V. Kojić, R. Petrović, D. Janaćković, Antimicrobial activity and biocompatibility of $Ag^{+}$- and $Cu^{2+}$-doped biphasic hydroxyapatite/α-tricalcium phosphate obtained from hydrothermally synthesized $Ag^{+}$- and $Cu^{2+}$-doped hydroxyapatite, Appl. Surf. Sci. 307 (2014) 513–519.
[30] X. Li, Y. Sogo, A. Ito, H. Mutsuzaki, N. Ochiai, T. Kobayashi, S. Nakamura, K. Yamashita, R.Z. LeGeros, The optimum zinc content in set calcium phosphate cement for promoting bone formation in vivo, Mater. Sci. Eng. C 29 (2009) 969–975.
[31] M.E. Zilm, L. Yu, W.A. Hines, M. Wei, Magnetic properties and cytocompatibility of transition-metal-incorporated hydroxyapatite, Mater. Sci. Eng. C 87 (2018) 112–119.
[32] B. Bracci, P. Torricelli, S. Panzavolta, E. Boanini, R. Giardino, A. Bigi, Effect of $Mg^{2+}$, $Sr^{2+}$, and $Mn^{2+}$ on the chemico-physical and in vitro biological properties of calcium phosphate biomimetic coatings, J. Inorg. Biochem. 103 (2009) 1666–1674.
[33] M.P. Moreira, G.D. de Almeida Soares, J. Dentzer, K. Anselme, L.Á. de Sena, A. Kuznetsov, E.Ad. Santos, Synthesis of magnesium- and manganese-doped hydroxyapatite structures assisted by the simultaneous incorporation of strontium, Mater. Sci. Eng. C 61 (2016) 736–743.
[34] S. Lala, M. Ghosh, P.K. Das, T. Kar, S.K. Pradhan, Mechanical preparation of nanocrystalline biocompatible single-phase Mn-doped A-type carbonated hydroxyapatite (A-cHAp): effect of Mn doping on microstructure, Dalton Trans. 44 (2015) 20087–20097.
[35] R. Singh, M. Srivastava, N.K. Prasad, S. Awasthi, A. Kumar Dhayalan, S. Kannan, Structural analysis and magnetic induced hyperthermia of $Fe^{3+}$ and $Mn^{2+}$ substituted β-$Ca_3(PO_4)_2$, New J. Chem. 41 (2017) 12879–12891.
[36] M. Miola, C.V. Brovarone, G. Maina, F. Rossi, L. Bergandi, D. Ghigo, S. Saracino, M. Maggiora, R.A. Canuto, G. Muzio, E. Vernè, In vitro study of manganese-doped bioactive glasses for bone regeneration, Mater. Sci. Eng. C 38 (2014) 107–118.
[37] Y. Huang, H. Qiao, X. Nian, X. Zhang, X. Zhang, G. Song, Z. Xu, H. Zhang, S. Han, Improving the bioactivity and corrosion resistance properties of electrodeposited hydroxyapatite coating by dual doping of bivalent strontium and manganese ion, Surf. Coat. Technol. 291 (2016) 205–215.
[38] R. Meenambal, P. Poojar, S. Geethanath, S. Kannan, Substitutional limit of gadolinium in β-tricalcium phosphate and its magnetic resonance imaging characteristics, J. Biomed. Mater. Res. B: Appl. Biomater. 105 (2017) 2545–2552.
[39] S.S. Syamchand, G. Sony, Multifunctional hydroxyapatite nanoparticles for drug delivery and multimodal molecular imaging, Microchim. Acta 182 (2015) 1567–1589.
[40] J. Vecstaudza, M. Gasik, J. Locs, Amorphous calcium phosphate materials: formation, structure and thermal behaviour, J. Eur. Ceram. Soc. 39 (2019) 1642–1649.
[41] C. Combes, C. Rey, Amorphous calcium phosphates: synthesis, properties and uses in biomaterials, Acta Biomater. 6 (2010) 3362–3378.

[42] C.J.S. Ibsen, D. Chernyshov, H. Birkedal, Apatite formation from amorphous calcium phosphate and mixed amorphous calcium phosphate/amorphous calcium carbonate, Chem. Eur. J. 22 (2016) 12347–12357.
[43] F. Murzakhanov, B. Gabbasov, K. Iskhakova, A. Voloshin, G. Mamin, V. Putlyaev, E. Klimashina, I. Fadeeva, A. Fomin, S. Barinov, T. Biktagirov, S. Orlinskii, M. Gafurov, Conventional electron paramagnetic resonance for studying synthetic calcium phosphates with metal impurities ($Mn^{2+}$, $Cu^{2+}$, $Fe^{3+}$), Magn. Reson. Solids 19 (2017) 10.
[44] S.A. Altshulter, B.I. Kozyrev, Electron Paramagnetic Resonance in Compounds of Transition Elements, Wiley, New York, 1974.
[45] B. Sutter, T. Wasowicz, T. Howard, L.R. Hossner, D.W. Ming, Characterization of iron, manganese, and copper synthetic hydroxyapatites by electron paramagnetic resonance spectroscopy, Soil Sci. Soc. Am. J. 66 (2002) 1359–1366.
[46] K. Matsunaga, T. Kubota, K. Toyoura, A. Nakamura, First-principles calculations of divalent substitution of $Ca^{2+}$ in tricalcium phosphates, Acta Biomater. 23 (2015) 329–337.
[47] S. Somrani, C. Rey, M. Jemal, Thermal evolution of amorphous tricalcium phosphate, J. Mater. Chem. 13 (2003) 888–892.
[48] J. Chen, Y. Wang, X. Chen, L. Ren, C. Lai, W. He, Q. Zhang, A simple sol-gel technique for synthesis of nanostructured hydroxyapatite, tricalcium phosphate and biphasic powders, Mater. Lett. 65 (2011) 1923–1926.
[49] W.I. Abdel-Fattah, F.M. Reicha, T.A. Elkhooly, Nano-beta-tricalcium phosphates synthesis and biodegradation: 1. Effect of microwave and $SO_4^{2-}$ ions on β-TCP synthesis and its characterization, Biomed. Mater. 3 (2008) 034121.
[50] P.M.C. Torres, S.I. Vieira, A.R. Cerqueira, S. Pina, O.A.B. da Cruz Silva, J.C.C. Abrantes, J.M.F. Ferreira, Effects of Mn-doping on the structure and biological properties of β-tricalcium phosphate, J. Inorg. Biochem. 136 (2014) 57–66.
[51] F.J. Owens, Paramagnetic resonance of divalent manganese in thallous azide, J. Chem. Phys. 57 (1972) 2349–2354.
[52] I. Mayer, S. Cohen, S. Gdalya, O. Burghaus, D. Reinen, Crystal structure and EPR study of Mn-doped beta-tricalcium phosphate, Mater. Res. Bull. 43 (2008) 447–452.
[53] C. Stahli, J. Thuring, L. Galea, S. Tadier, M. Bohner, N. Dobelin, Hydrogen-substituted β-tricalcium phosphate synthesized in organic media, Acta Crystallogr. Sect. B 72 (2016) 875–884.

Article III

**Effect of Mn doping on hydrolysis of low-temperature synthesized metastable alpha-tricalcium phosphate**

L. Sinusaite, A. Popov, E. Raudonyte-Svirbutaviciene, J.-C. Yang, A. Kareiva, A. Zarkov

*Ceramics International,* 47(9) (2021) 12078-12083

Ceramics International 47 (2021) 12078–12083

Contents lists available at ScienceDirect

Ceramics International

journal homepage: www.elsevier.com/locate/ceramint

# Effect of Mn doping on hydrolysis of low-temperature synthesized metastable alpha-tricalcium phosphate

Lauryna Sinusaite [a], Anton Popov [a,b], Eva Raudonyte-Svirbutaviciene [c], Jen-Chang Yang [d], Aivaras Kareiva [a], Aleksej Zarkov [a,*]

[a] Institute of Chemistry, Vilnius University, Naugarduko 24, LT-03225, Vilnius, Lithuania
[b] Department of Immunology, State Research Institute Centre for Innovative Medicine, Santariskiu 5, LT-08406, Vilnius, Lithuania
[c] SRI Nature Research Centre, Institute of Geology and Geography, Akademijos 2, LT-08412, Vilnius, Lithuania
[d] Graduate Institute of Nanomedicine and Medical Engineering, College of Biomedical Engineering, Taipei Medical University, 250 Wu-Hsing St, Taipei, 11052, Taiwan

ARTICLE INFO

*Keywords:*
α-tricalcium phosphate
TCP
Precipitation
Hydrolysis
Mn doping
Hydroxyapatite

ABSTRACT

In the present work, effect of Mn doping on hydrolysis rate of low-temperature synthesized metastable α-tricalcium phosphate (α-TCP) was investigated. α-TCP powders containing different amount of $Mn^{2+}$ ions (0, 0.5 and 1 mol%) were synthesized by wet co-precipitation process, followed by annealing and crystallization of as-precipitated amorphous calcium phosphate at 700 °C. It was demonstrated that the presence of $Mn^{2+}$ ions significantly retards hydrolysis rate of α-TCP. While pristine α-TCP fully hydrolyzed with a conversion to calcium-deficient hydroxyapatite in 10 h, complete hydrolysis of α-TCP doped with 0.5 and 1 mol% of Mn occurred only after 20 and 35 h, respectively. Initial and final products were characterized by X-ray diffraction (XRD) analysis, infrared (FTIR) spectroscopy and scanning electron microscopy (SEM). Chemical composition of starting and fully hydrolyzed α-TCP powders was determined by inductively coupled plasma optical emission spectrometry (ICP-OES).

## 1. Introduction

Synthetic calcium phosphates (CPs) are widely used in medicine as biomaterials due to the compositional similarities to inorganic part of natural bone [1]. Alpha-tricalcium phosphate (α-TCP, $Ca_3(PO_4)_2$) is a member of CPs family commonly used for regenerative medicine purposes. Due to its physico-chemical properties it is utilized as a main inorganic part in most commercial calcium based cement formulations [2]. Under reaction with water α-TCP hydrolyzes and converts to calcium-deficient hydroxyapatite (CDHA, $Ca_{10-x}(PO_4)_{6-x}(HPO_4)_x(OH)_{2-x}$) according to Eq. (1).

$$3\alpha\text{-}Ca_3(PO_4)_2 + H_2O \rightarrow Ca_9(HPO_4)(PO_4)_5(OH) \quad (1)$$

Conventional way of preparation of α-TCP employs an annealing procedure of Ca and P containing precursors at temperatures above 1125 °C, which is the point of phase transformation of β-TCP to α-TCP [3]. High annealing temperatures lead to significant grain growth and sintering of material, which considerably lowers specific surface area of powders. In order to reduce the size of the particles additional procedures such as ball milling are required. Another way to prepare α-TCP is preparation of metastable α-TCP from amorphous calcium phosphate (ACP) with Ca to P ratio of 1.5:1. Despite the fact that β-TCP is assumed to be a low-temperature polymorph, upon heating ACP first crystallizes to α-TCP. This process is in agreement with Ostwald step rule, according to which crystallization often occurs in such a way that thermodynamically less stable phase is obtained first, followed by thermodynamically more stable [4,5]. Such crystallization behavior of ACP was previously experimentally proven in a number of studies [6–9].

Effect of doping on hydrolysis kinetics of α-TCP is rather poorly investigated topic. Only few studies are reported investigating an effect of Ca substitution by other divalent ions. Effect of Sr on the reactivity of α-TCP was investigated by Boanini et al. [10]. It was demonstrated that presence of Sr ions in α-TCP crystal lattice at the level of 5% and higher delays the conversion of α-TCP to CDHA. The results obtained by Hurle et al. confirms previous findings and also revealed that hydrolysis rate of α-TCP is retarded significantly by doping with Sr [11]. Investigation of the effect of cations smaller than Ca is even more challenging due to the difficulties in preparation of α-TCP substituted with smaller ions. The reason is a specific crystal structure of α-TCP, characterized by a high

* Corresponding author.
*E-mail address:* aleksej.zarkov@chf.vu.lt (A. Zarkov).

https://doi.org/10.1016/j.ceramint.2021.01.052
Received 18 October 2020; Received in revised form 11 December 2020; Accepted 7 January 2021
Available online 11 January 2021

defect energy for substitution of Ca ions by small divalent cations, which shift thermodynamic equilibrium towards another polymorph – β-TCP [12]. Moreover, previous studies reporting on hydrolysis of α-TCP investigate hydrolysis of high-temperature α-TCP [13–17]. Synthesis of this material at temperatures as low as 700 °C leads to the formation smaller particles with lower degree of crystallinity and enhanced surface area compared to high-temperature synthesis, which could result in higher reactivity and shorter setting times of cement pastes.

Manganese is an essential element in human body, it is involved in many biological processes related to the growth and metabolism of bone tissues, moreover Mn is a minor constituent of bones and teeth [18,19]. Biological properties of Mn-containing biomaterials were reported in some previous studies. Torres et al. [20] investigated *in vitro* proliferation and differentiation of osteoblast-like cells in the presence of Mn-doped β-TCP powders, which significantly induced pre-osteoblastic proliferation, however biological benefits were found to be limited to lower Mn substitution levels. Wu et al. reported on the improvement of osteogenesis of CP bone cement achieved by incorporation of Mn-doped β-TCP [21], noting an increased adsorption of proteins and positive role of released $Mn^{2+}$ ions. Recent study by Rau et al. [22] demonstrated that doping of β-TCP with $Mn^{2+}$ ions significantly inhibited the growth of some bacterial species whereas did not affect negatively the viability of adipose-derived mesenchymal stem cells. Moreover, $Mn^{2+}$ is known to be optically active and paramagnetic ion, which can be used for bio-imaging application [23,24] and potentially make possible *in vivo* monitoring of biodegradation of α-TCP and its hydrolysis product.

In the present work, we report on the investigation of hydrolysis process of low-temperature synthesized metastable α-TCP. Undoped powders and α-TCP samples containing 0.5 and 1 mol% of $Mn^{2+}$ ions were synthesized by wet co-precipitation process, followed by annealing and crystallization of as-precipitated amorphous calcium phosphate at 700 °C. The influence of doping on hydrolysis process and final products was studied.

## 2. Experimental

### 2.1. Synthesis

Pristine and $Mn^{2+}$-doped α-TCP powders (0.5 and 1 mol%) were prepared by wet precipitation method at room temperature according to previously reported procedure [25,26]. Briefly, the appropriate amounts of calcium nitrate tetrahydrate ($Ca(NO_3)_2 \cdot 4H_2O$, ≥99%, Roth) and manganese(II) nitrate tetrahydrate ($Mn(NO_3)_2 \cdot 4H_2O$, 98%, Alfa Aesar) were dissolved in deionized water to obtain 0.75 M total metal ions solution. Diammonium hydrogen phosphate ($(NH_4)_2HPO_4$, ≥98%, Roth) was separately dissolved in deionized water resulting in 0.5 M solution, to which concentrated ammonia solution ($NH_4OH$, 25%, Roth) was added in order to adjust pH to 10. Next, $Ca^{2+}$ and $Mn^{2+}$ nitrates solution was rapidly added to $(NH_4)_2HPO_4$ solution under constant mixing on magnetic stirrer, the pH value of the final solution was 10. Instantly formed precipitates were stirred in the reaction mixture at 400 rpm, the maturation time was 10 min, afterwards the precipitates were vacuum filtered and washed with deionized water and isopropanol (≥99.5%, Roth). After washing, the obtained precipitates were dried at 50 °C overnight in the oven. Finally, dry powders were ground in agate mortar and annealed in the furnace at 700 °C for 5 h in air. Maximal substitution level was chosen as 1 mol% on the basis of our previous work, which indicated that higher amount of $Mn^{2+}$ ions leads to the formation of biphasic products consisting of two different TCP polymorphs [25]. Hydrolysis of α-TCP powders was carried out in deionized water at 37 °C. For this purpose, 400 mg of α-TCP powders were soaked in 15 mL of deionized water and stored for different periods of time. Then the products were filtered, rinsed with deionized water and dried. All samples were investigated in triplicate.

### 2.2. Characterization

Powder X-ray diffraction (XRD) data were collected using Ni-filtered Cu Kα radiation on Rigaku MiniFlex II diffractometer working in Bragg-Brentano (θ/2θ) geometry. The data were collected within 2θ angle range from 10 to 60° at a step width of 0.02° and speed of 2°/min. Lattice parameters were refined by the Rietveld method using the Full-Prof suite. Degree of crystallinity of the obtained powders was calculated using Match! software (version 3.10.1.1.169). Infrared (FTIR) spectra were obtained in the range of 4000−400 $cm^{-1}$ employing Bruker ATR spectrometer with 4 $cm^{-1}$ resolution. Morphology of the synthesized products was analyzed with a Hitachi SU-70 field-emission scanning electron microscope (FE-SEM). Particle size distribution was estimated from SEM micrographs using ImageJ software. Elemental analysis of the synthesized samples was performed by inductively coupled plasma optical emission spectrometry (ICP-OES) using Perkin Elmer Optima 7000DV spectrometer. The samples were dissolved in 5% nitric acid ($HNO_3$, Rotipuran® Supra 69%, Roth) and diluted to an appropriate volume with deionized water. Calibration solutions were prepared by dilution of the stock standard solutions (single-element ICP standards 1000 mg/L, Roth). The $N_2$ adsorption and desorption isotherms of samples were obtained at −196 °C by using Brunauer–Emmett–Teller (BET) analyzer TriStar II 3020, Micromeritics. Prior to the gas sorption measurements, all the samples were outgassed in $N_2$ atmosphere at 100 °C for 2 h.

## 3. Results and discussion

The phase crystallinity and purity of as-prepared and annealed powders were investigated by XRD analysis. The as-prepared powders were determined to be amorphous, no sharp diffraction peaks arising from crystalline materials were observed. The XRD patterns of α-TCP samples containing different amount of $Mn^{2+}$ ions and annealed at 700 °C are shown in Fig. 1. It is seen that all investigated samples after a thermal treatment crystallized to α-TCP regardless of the chemical composition. All diffraction peaks match very well standard XRD data of monoclinic $Ca_3(PO_4)_2$ (ICDD #00-070-0364) indicating that substitution of Ca by Mn ions on the level of 1 mol% does not lead to any phase transition or formation of secondary crystal phases. Visible splitting of some diffraction peaks located at around 23°, 24°, 34° and 47° can be assumed as an evidence of incorporation of $Mn^{2+}$ ions into α-TCP crystal structure, which led to some internal structural changes. Calculated cell

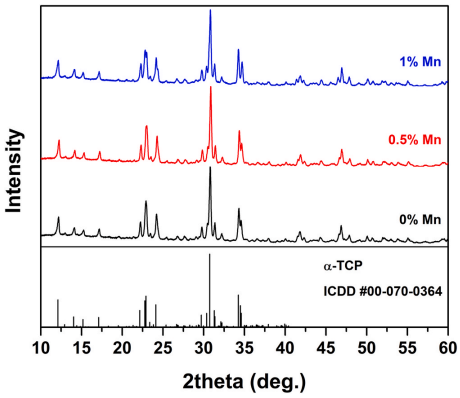


**Fig. 1.** XRD patterns of pristine and Mn-doped α-TCP powders annealed at 700 °C.

parameters of pristine and Mn-doped α-TCP powders are given in Table 1. It can be seen, that substitution with Mn ions leads to the changes of cell parameters, which arise from the difference between ionic radii of $Ca^{2+}$ and $Mn^{2+}$ ions [27]. Degree of crystallinity of the obtained powders was calculated in order to quantify the effect of doping on the presence of amorphous component of powders. The degree of crystallinity of powders was calculated as 68.9, 79.5 and 80.5% for undoped, 0.5 mol% doped and 1 mol% doped α-TCP, respectively. These results suggest, that the presence of Mn ions increases degree of crystallinity and lowers amount of amorphous phase, however this effect is limited, since the difference between doped samples was found to be negligible.

The morphology of pristine and 1 mol% Mn-doped α-TCP powders was investigated by taking SEM images, which are presented in Fig. 2.

In both cases powders consisted of the agglomerates of nanodimensional mostly uniform elongated particles. Axial grain size of pristine α-TCP particles ranged approximately between 100 and 200 nm, whereas length of the particles varied in the range of 300–700 nm. Taking a closer look to both micrographs, a slight difference between them can be pointed out. Whereas doping with $Mn^{2+}$ ions did not result in perceptible changes of the shape, the size of Mn-doped α-TCP particles was found to be slightly enhanced compared to pristine species. Since the particles are elongated and of irregular shape, it is hard to estimate the size distribution by length, therefore size distribution by width was analyzed. For pristine α-TCP average size was estimated as 155 ± 35 nm, whereas for doped samples this values were slightly higher, but still comparable – 168 ± 37 and 176 ± 31 nm for 0.5 and 1 mol% Mn-doped powders, respectively. Except this minor difference it could be stated that doping did not affect morphology of powders. Overall, it is evident that particles with nanodimensions were synthesized, which is hardly achievable performing α-TCP synthesis in conventional high-temperature way.

Taking into account that hydrolysis rate of α-TCP can be strongly affected by the surface area of investigated powders, BET analysis was performed in order to estimate the influence of Mn doping on specific surface area of synthesized α-TCP powders. Nitrogen adsorption-desorption isotherms of samples are depicted in Fig. S1 and the values of BET surface area are summarized in Table 2. Despite the fact that determined values are slightly lower for the sample with 0.5 mol% of Mn, we consider such difference as insignificant, all samples possess very similar values. Moreover, there is no correlation between BET surface area and Mn content in powders.

The XRD patterns of pristine and Mn-doped α-TCP powders after different times of soaking in deionized water are illustrated in Fig. 3.

It is seen that in all cases intensity of diffraction peaks corresponding to CDHA distinctly increases with an increase of soaking time, indicating gradual conversion of α-TCP to CDHA. Complete conversion of pristine α-TCP to CDHA was observed after 10 h, no signal originating from α-TCP was detected in the XRD pattern. As was mentioned above, previous works investigating hydrolysis process of α-TCP consider high-temperature synthesized α-TCP. It was shown that α-TCP prepared at 1250 °C did not fully converted to CDHA in water at room temperature even after soaking for 1 month [13]. Durucan and Brown demonstrated that α-TCP synthesized by solid-state reaction at 1150 °C fully converted to CDHA in deionized water at 37 °C in 18 h [14]. It was also reported that hydrolysis rate increases with an increase of water temperature. Another study revealed that high-temperature synthesized α-TCP fully converted to CDHA in deionized water at 37.4 °C in 21 h [15]. These and some other [10,16,17] results indicate that in our case complete transformation of α-TCP to CDHA occurred in significantly faster way, the required time was approximately 2 times shorter. The reason of such a difference can be found in processing conditions of initial α-TCP powders, low annealing temperature resulted in particles of lower dimensions, higher surface area and lower degree of crystallinity.

Evidently, Mn doping has an inhibiting effect on the hydrolysis rate of α-TCP, phase evolution observed for doped samples is the same as for pristine α-TCP, however transformation of doped samples occurred significantly slower compared to undoped powders. After 10 h of soaking no signals of CDHA can be seen from the XRD patter of 1 mol% Mn-doped α-TCP. Full transformation of α-TCP doped with 0.5 and 1 mol % of Mn was observed after 20 and 35 h, respectively. Thus, it can be concluded that substitution of Ca by Mn ions on the level of 1 mol% leads to more than 3-fold decrease in hydrolysis rate. Since BET analysis did not reveal any considerable difference in surface area between starting α-TCP powders (see Table 2), this factor is not considered as defining the retardation of hydrolysis. On the other hand, it was calculated that amount of amorphous phase in pristine α-TCP is higher compared to doped samples. This fact could result in faster hydrolysis rate of undoped powders. However, degree of crystallinity of both Mn-doped samples was very close, but hydrolysis rate was significantly slower for α-TCP doped with 1 mol% of Mn. Possible explanation of this retardation effect can be find in the mechanism of hydrolysis of α-TCP, which is based on dissolution-precipitation process [17,28–30]. $Mn^{2+}$ ions are significantly smaller than $Ca^{2+}$ [27], when released to surrounding media, they retard formation of CDHA. Similar effect was observed for Zn-doped α-TCP by Sogo et al. [31]. The authors demonstrated that hydrolysis inhibition strongly depends on the content of Zn in starting TCP powders. α-TCP with Zn content of 0.11 wt% and undoped α-TCP were hydrolyzed to CDHA at nearly the same reaction rate, whereas Zn content of more than 0.26 wt% significantly retarded phase transformation. It is also evident for all fully hydrolyzed samples that diffraction peak located at 26° and corresponding to (002) crystal plane is more intense compared to standard XRD data. Such observation allows to make an assumption that crystal growth of CDHA occurs in a preferred direction along c-axis. Anisotropic growth of CDHA crystals during the hydrolysis of α-TCP was also observed in other studies [32, 33].

FTIR spectroscopy was employed for additional investigation of the evolution of crystal structure during hydrolysis of α-TCP samples. The FTIR spectra of pristine α-TCP powder after different times of soaking are given in Fig. 4a.

Obvious evolution of the spectrum shape confirms the results obtained by XRD analysis. Spectra of untreated α-TCP and α-TCP after soaking for 2 h are very similar and can be characterized by several phosphate absorption bands located at 1160–970 ($\nu_3$), 958 ($\nu_1$), at 561, 582, 594 and 611 ($\nu_4$) and 450 $cm^{-1}$ ($\nu_2$). Such spectrum is characteristic of α-TCP polymorph [3]. It should be noticed that very week absorption bands were detected at 728 and 1187 $cm^{-1}$. These bands indicate the presence of negligible amount of neighboring calcium pyrophosphate [20], however the intensity of these bands was found to be the same in the FTIR spectra of all starting TCP powders. Noticeably different spectra were observed for samples after 4, 6 and 10 h of soaking. Absorption bands located at 1090, 1025 ($\nu_3$) and 960 $cm^{-1}$ ($\nu_1$) are assigned to the P–O stretching vibration mode and the bands at 600 and 560 $cm^{-1}$ ($\nu_4$) correspond to O–P–O bending mode of the phosphate group. Weak band located at 471 $cm^{-1}$ ($\nu_2$) is attributed to phosphate bending mode [34]. Remarkable feature of analyzed FTIR spectra is an absorption band located at 868 $cm^{-1}$ attributed to P–O(H) stretching mode of the $HPO_4^{2-}$ group, which is absent in α-TCP and present in CDHA structure. Evidently, intensity of this band gradually increases with an increase of soaking time, which caused by appearance of higher number of $HPO_4^{2-}$ groups in analyzed powders. Moreover, a weak band at 636 $cm^{-1}$, which appears only after 4 h of soaking is also assigned to hydroxyl group [35]. The same trends were observed for Mn-doped

**Table 1**
Cell parameters of α-TCP powders.

| Sample | a, Å | b, Å | c, Å | β, deg. |
|---|---|---|---|---|
| $Ca_3(PO_4)_2$ | 12.878(5) | 27.273(1) | 15.214(8) | 126.185(1) |
| $Ca_3(PO_4)_2$: 0.5% $Mn^{2+}$ | 12.869(8) | 27.285(8) | 15.209(6) | 126.209(8) |
| $Ca_3(PO_4)_2$: 1.0% $Mn^{2+}$ | 12.838(8) | 27.342(5) | 15.207(6) | 126.295(4) |

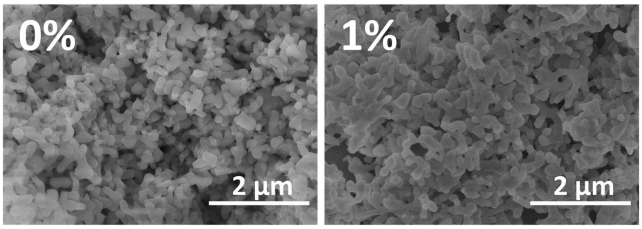


**Fig. 2.** SEM micrographs of pristine and 1 mol% Mn-doped α-TCP powders.

**Table 2**
BET surface area of α-TCP powders.

| Sample | BET surface area, $m^2/g$ |
|---|---|
| $Ca_3(PO_4)_2$ | 10.31 ± 0.22 |
| $Ca_3(PO_4)_2$: 0.5% $Mn^{2+}$ | 9.79 ± 0.19 |
| $Ca_3(PO_4)_2$: 1.0% $Mn^{2+}$ | 10.54 ± 0.17 |

α-TCP samples (Fig. 4b).

The SEM micrographs of CDHA powders obtained from pristine and 1 mol% Mn-doped α-TCP powders are represented in Fig. 5.

It is seen that morphology of both samples after hydrolysis has changed considerably compared to untreated α-TCP powders. Hydrolyzed powders consist of flake-like particles, which form some larger agglomerates. Such morphological features are typical for CDHA crystals derived from α-TCP *via* hydrolysis process [14,15,17,28,31]. It is hard to estimate actual agglomerate size due to unclear border lines, but approximate size of clusters varied from 700 to 2000 nm. The size of CDHA particles derived from pristine α-TCP was observed to be smaller compared to that of CDHA derived from α-TCP doped with 1 mol% of Mn. The flake-like morphology of CDHA is in good agreement with the preferred orientation observed in the XRD patterns of hydrolyzed powders (Fig. 3).

BET analysis of fully hydrolyzed powders derived from α-TCP samples with different amount of Mn was performed and results are given in Fig. S2 and Table 3. It is seen that hydrolysis reaction led to approximately 5 and 4-fold increase of BET surface area of pristine and Mn-doped samples, respectively (see Table 2).

Precise control of chemical composition is a well-known problem in preparation of multicomponent products by co-precipitation synthesis method. In order to determine actual composition of synthesized and fully hydrolyzed species, elemental analysis by means of ICP-OES was performed. The results of the analysis are summarized in Table 4. It is clearly seen that determined molar percentage of $Mn^{2+}$ in α-TCP samples is in good agreement with nominal values indicating successful synthesis of products with aspired substitution level. On the other hand, total metals to phosphorus ratio shows slightly lower values compared to theoretical. It is also notable, that chemical composition of powders did not change after hydrolysis process. These results indicate that there is no selective ion release during hydrolysis.

Fig. 6 shows the pH values of the aqueous solutions after soaking of α-TCP powders for various periods of time.

The identical trend is clearly seen for all samples regardless of chemical composition of powders. On the early stage of hydrolysis pH is slightly basic and varies in the range from 7.2 to 7.3. The deviation from the pH value typically observed for deionized water after a contact with

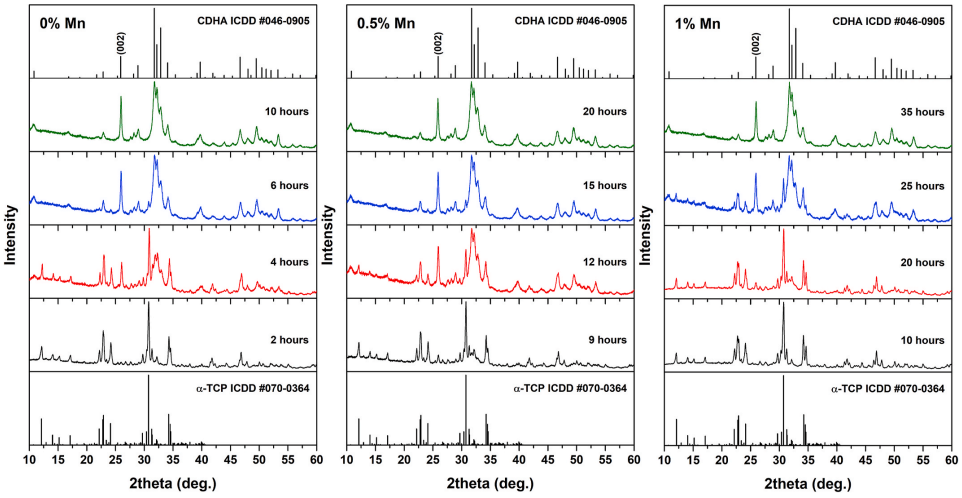


**Fig. 3.** XRD patterns of pristine and Mn-doped α-TCP powders after different times of hydrolysis.

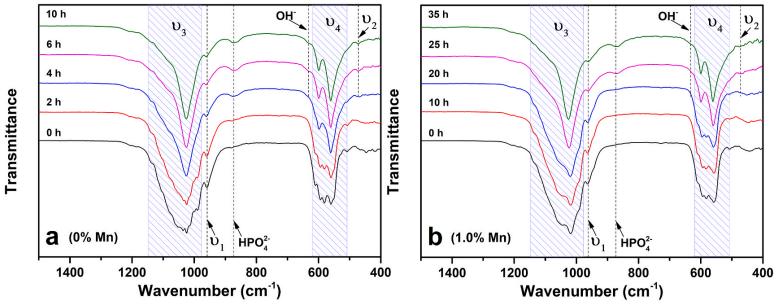


**Fig. 4.** FTIR spectra of pristine α-TCP (a) and α-TCP doped with 1 mol% of Mn (b) after different times of hydrolysis.

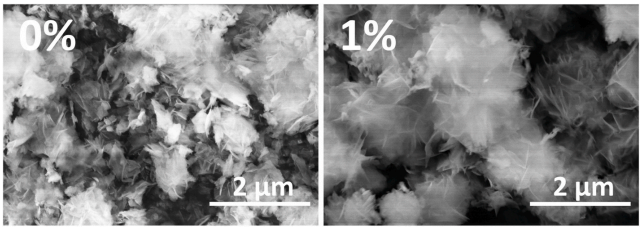


**Fig. 5.** SEM micrographs of CDHA powders obtained from pristine and 1 mol% Mn-doped α-TCP powders.

**Table 3**
BET surface area of resulted CDHA powders.

| Sample | BET surface area, $m^2/g$ |
|---|---|
| CDHA | 47.61 ± 0.13 |
| CDHA: 0.5% $Mn^{2+}$ | 39.29 ± 0.16 |
| CDHA: 1.0% $Mn^{2+}$ | 39.61 ± 0.13 |

**Table 4**
Results of the elemental analysis of the samples performed by ICP-OES.

| Sample | Before hydrolysis | | After hydrolysis | |
|---|---|---|---|---|
| | $\frac{n(Mn)\cdot 100\%}{n(Ca+Mn)}$ | $\frac{n(Ca+Mn)}{n(P)}$ | $\frac{n(Mn)\cdot 100\%}{n(Ca+Mn)}$ | $\frac{n(Ca+Mn)}{n(P)}$ |
| $Ca_3(PO_4)_2$ | – | 1.47 | – | 1.47 |
| $Ca_3(PO_4)_2$: 0.5% $Mn^{2+}$ | 0.518 | 1.49 | 0.520 | 1.49 |
| $Ca_3(PO_4)_2$: 1.0% $Mn^{2+}$ | 1.02 | 1.49 | 1.03 | 1.49 |

air is associated with dissolution of α-TCP, which leads to the appearance of $HPO_4^{2-}$ and $OH^-$ ions in surrounding media [13,17]. The initial pH is nearly constant until it starts to decrease at the particular stage of hydrolysis. These results go hand in hand with the data of XRD and FTIR analysis, the pH values start to decrease when CDHA becomes a major constituent of treated powders. The decrease of pH indicates precipitation of dissolved $HPO_4^{2-}$ and $OH^-$ ions in the form of CDHA. Since $Mn^{2+}$ ions significantly inhibit hydrolysis process, the decrease of pH values for different samples is observed at different times with the shortest time for pristine α-TCP and the longest time for α-TCP doped with 1 mol% of Mn. The pH value at the point of complete transformation to CDHA was observed nearly equal for all samples and was determined at around 6.5.

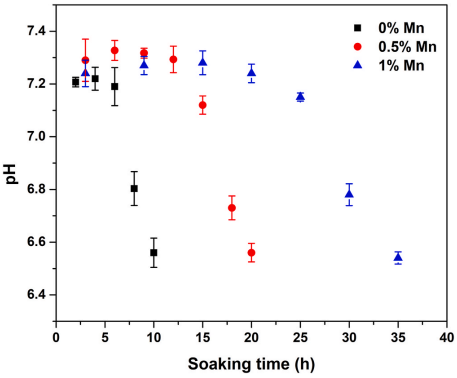


**Fig. 6.** Dependence of medium pH on soaking time.

Such behavior of pH values agrees well with previous studies on hydrolysis of α-TCP [10,28,33].

## 4. Conclusions

In this study, effect of $Mn^{2+}$ doping on hydrolysis rate of low-temperature synthesized metastable α-TCP was investigated. Undoped α-TCP and α-TCP powders containing 0.5 and 1 mol% of $Mn^{2+}$ ions were successfully synthesized by wet co-precipitation process with high phase purity and controlled chemical composition. It was demonstrated that

the presence of $Mn^{2+}$ ions significantly retards hydrolysis of α-TCP. While pristine α-TCP fully hydrolyzed with a conversion to calcium-deficient hydroxyapatite in 10 h, complete hydrolysis of α-TCP doped with 0.5 and 1 mol% of Mn occurred only after 20 and 35 h, respectively. The results of elemental analysis confirmed that chemical composition of starting and fully hydrolyzed powders was identical, indicating that there is no selective ion release during hydrolysis process.

## Notes

The authors declare no competing financial interest.

## Declaration of competing interest

The authors declare that they have no known competing financial interests or personal relationships that could have appeared to influence the work reported in this paper.

## Acknowledgements

This project has received funding from European Social Fund (project No 09.3.3-LMT-K-712-19-0069) under grant agreement with the Research Council of Lithuania (LMTLT). Dr. J. Gaidukevic and Dr. R. Skaudzius (Vilnius University) are highly acknowledged for their help and assistance.

## Appendix A. Supplementary data

Supplementary data to this article can be found online at https://doi.org/10.1016/j.ceramint.2021.01.052.

## References

[1] W. Habraken, P. Habibovic, M. Epple, M. Bohner, Calcium phosphates in biomedical applications: materials for the future? Mater. Today 19 (2) (2016) 69–87.
[2] L. Schröter, F. Kaiser, S. Stein, U. Gbureck, A. Ignatius, Biological and mechanical performance and degradation characteristics of calcium phosphate cements in large animals and humans, Acta Biomater. 117 (2020) 1–20.
[3] R.G. Carrodeguas, S. De Aza, α-Tricalcium phosphate: synthesis, properties and biomedical applications, Acta Biomater. 7 (10) (2011) 3536–3546.
[4] R.A. Van Santen, The Ostwald step rule, J. Phys. Chem. 88 (24) (1984) 5768–5769.
[5] C. Combes, C. Rey, Amorphous calcium phosphates: synthesis, properties and uses in biomaterials, Acta Biomater. 6 (9) (2010) 3362–3378.
[6] V. Uskoković, S. Marković, L. Veselinović, S. Škapin, N. Ignjatović, D.P. Uskoković, Insights into the kinetics of thermally induced crystallization of amorphous calcium phosphate, Phys. Chem. Chem. Phys. 20 (46) (2018) 29221–29235.
[7] S. Somrani, C. Rey, M. Jemal, Thermal evolution of amorphous tricalcium phosphate, J. Mater. Chem. 13 (4) (2003) 888–892.
[8] D. Nicola, T.J. Brunner, W.J. Stark, F. Martin, C. Egle, B. Marc, Thermal treatment of flame-synthesized amorphous tricalcium phosphate nanoparticles, J. Am. Ceram. Soc. 93 (10) (2010) 3455–3463.
[9] M. Maciejewski, T.J. Brunner, S.F. Loher, W.J. Stark, A. Baiker, Phase transitions in amorphous calcium phosphates with different Ca/P ratios, Thermochim. Acta 468 (1) (2008) 75–80.
[10] E. Boanini, S. Panzavolta, K. Rubini, M. Gandolfi, A. Bigi, Effect of strontium and gelatin on the reactivity of α-tricalcium phosphate, Acta Biomater. 6 (3) (2010) 936–942.
[11] K. Hurle, J. Neubauer, F. Goetz-Neunhoeffer, Influence of $Sr^{2+}$ on calcium-deficient hydroxyapatite formation kinetics and morphology in partially amorphized α-TCP, J. Am. Ceram. Soc. 99 (3) (2016) 1055–1063.
[12] K. Matsunaga, T. Kubota, K. Toyoura, A. Nakamura, First-principles calculations of divalent substitution of $Ca^{2+}$ in tricalcium phosphates, Acta Biomater. 23 (2015) 329–337.
[13] L. Yubao, Z. Xingdong, K. de Groot, Hydrolysis and phase transition of alpha-tricalcium phosphate, Biomaterials 18 (10) (1997) 737–741.
[14] C. Durucan, P.W. Brown, α-Tricalcium phosphate hydrolysis to hydroxyapatite at and near physiological temperature, J. Mater. Sci. Mater. Med. 11 (6) (2000) 365–371.
[15] K.S. TenHuisen, P.W. Brown, Formation of calcium-deficient hydroxyapatite from α-tricalcium phosphate, Biomaterials 19 (23) (1998) 2209–2217.
[16] S.Y. Yoon, Y.M. Park, S.S. Park, R. Stevens, H.C. Park, Synthesis of hydroxyapatite whiskers by hydrolysis of α-tricalcium phosphate using microwave heating, Mater. Chem. Phys. 91 (1) (2005) 48–53.
[17] K. Tsuru, Ruslin, M. Maruta, S. Matsuya, K. Ishikawa, Effects of the method of apatite seed crystals addition on setting reaction of alpha-tricalcium phosphate based apatite cement, J. Mater. Sci. Mater. Med. 26 (10) (2015) 244.
[18] J. Aaseth, G. Boivin, O. Andersen, Osteoporosis and trace elements – an overview, J. Trace Elem. Med. Biol. 26 (2) (2012) 149–152.
[19] E. Boanini, M. Gazzano, A. Bigi, Ionic substitutions in calcium phosphates synthesized at low temperature, Acta Biomater. 6 (6) (2010) 1882–1894.
[20] P.M.C. Torres, S.I. Vieira, A.R. Cerqueira, S. Pina, O.A.B. da Cruz Silva, J.C. C. Abrantes, J.M.F. Ferreira, Effects of Mn-doping on the structure and biological properties of β-tricalcium phosphate, J. Inorg. Biochem. 136 (2014) 57–66.
[21] T. Wu, H. Shi, Y. Liang, T. Lu, Z. Lin, J. Ye, Improving osteogenesis of calcium phosphate bone cement by incorporating with manganese doped β-tricalcium phosphate, Mater. Sci. Eng. C 109 (2020), 110481.
[22] J.V. Rau, I.V. Fadeeva, A.S. Fomin, K. Barbaro, E. Galvano, A.P. Ryzhov, F. Murzakhanov, M. Gafurov, S. Orlinskii, I. Antoniac, V. Uskoković, Sic parvis magna: manganese-substituted tricalcium phosphate and its biophysical properties, ACS Biomater. Sci. Eng. 5 (12) (2019) 6632–6644.
[23] V. Dahanayake, C. Ponnrungroj, M. Pablico-Lansigan, W.J. Hickling, T. Lyons, D. Lah, Y. Lee, E. Parasido, J.A. Bertke, C. Albanese, O. Rodriguez, E. Van Keuren, S.L. Stoll, Paramagnetic clusters of $Mn_3(O_2CCH_3)_6(bpy)_2$ in polyacrylamide nanobeads as a new design approach to a $T_1$–$T_2$ multimodal magnetic resonance imaging contrast agent, ACS Appl. Mater. Interfaces 11 (20) (2019) 18153–18164.
[24] C. Qi, J. Lin, L.-H. Fu, P. Huang, Calcium-based biomaterials for diagnosis, treatment, and theranostics, Chem. Soc. Rev. 47 (2) (2018) 357–403.
[25] L. Sinusaite, A.M. Renner, M.B. Schuetz, A. Antuzevics, U. Rogulis, I. Grigoraviciute-Puroniene, S. Mathur, A. Zarkov, Effect of Mn doping on the low-temperature synthesis of tricalcium phosphate (TCP) polymorphs, J. Eur. Ceram. Soc. 39 (10) (2019) 3257–3263.
[26] L. Sinusaite, I. Grigoraviciute-Puroniene, A. Popov, K. Ishikawa, A. Kareiva, A. Zarkov, Controllable synthesis of tricalcium phosphate (TCP) polymorphs by wet precipitation: effect of washing procedure, Ceram. Int. 45 (9) (2019) 12423–12428.
[27] R.D. Shannon, Revised effective ionic radii and systematic studies of interatomic distances in halides and chalcogenides, Acta Crystallogr. A 32 (5) (1976) 751–767.
[28] H. Shi, S. Zeng, X. Liu, T. Yu, C. Zhou, Effects of strontium doping on the degradation and Sr ion release behaviors of α-tricalcium phosphate bone cement, J. Am. Ceram. Soc. 101 (2) (2018) 502–508.
[29] Z.X. Li Yubao, K. de Groot, Hydrolysis and phase transition of alpha-tricalcium phosphate, Biomaterials 18 (10) (1997) 737–741.
[30] H. Monma, T. Kanazawa, The hydration of alpha-tricalcium phosphate, Journal of the Ceramic Association, Japan 84 (968) (1976) 209–213.
[31] Y. Sogo, A. Ito, M. Kamo, T. Sakurai, K. Onuma, N. Ichinose, M. Otsuka, R. Z. LeGeros, Hydrolysis and cytocompatibility of zinc-containing α-tricalcium phosphate powder, Mater. Sci. Eng. C 24 (6) (2004) 709–715.
[32] T. Goto, I.Y. Kim, K. Kikuta, C. Ohtsuki, Hydroxyapatite formation by solvothermal treatment of α-tricalcium phosphate with water–ethanol solution, Ceram. Int. 38 (2) (2012) 1003–1010.
[33] T. Goto, I.Y. Kim, K. Kikuta, C. Ohtsuki, Comparative study of hydroxyapatite formation from alpha- and beta-tricalcium phosphates under hydrothermal conditions, J. Ceram. Soc. Japan 120 (1400) (2012) 131–137.
[34] S. Koutsopoulos, Synthesis and characterization of hydroxyapatite crystals: a review study on the analytical methods, J. Biomed. Mater. Res. 62 (4) (2002) 600–612.
[35] A. Siddharthan, S.K. Seshadri, T.S.S. Kumar, Microwave accelerated synthesis of nanosized calcium deficient hydroxyapatite, J. Mater. Sci. Mater. Med. 15 (12) (2004) 1279–1284.

Article IV

**Synthesis and luminescent properties of Mn-doped alpha-tricalcium phosphate**

L. Sinusaite, A. Antuzevics, A.I. Popov, U. Rogulis, M. Misevicius, A. Katelnikovas, A. Kareiva, A. Zarkov

*Ceramics International,* 47(4) (2021) 5335-5340

Ceramics International 47 (2021) 5335–5340

Contents lists available at ScienceDirect

Ceramics International

journal homepage: www.elsevier.com/locate/ceramint

# Synthesis and luminescent properties of Mn-doped alpha-tricalcium phosphate

Lauryna Sinusaite [a], Andris Antuzevics [b], Anatoli I. Popov [b], Uldis Rogulis [b], Martynas Misevicius [a], Arturas Katelnikovas [a], Aivaras Kareiva [a], Aleksej Zarkov [a,*]

[a] Institute of Chemistry, Vilnius University, Naugarduko 24, LT-03225, Vilnius, Lithuania
[b] Institute of Solid State Physics, University of Latvia, Kengaraga 8, LV-1063, Riga, Latvia

ARTICLE INFO

*Keywords:*
Tricalcium phosphate
α-TCP
Mn doping
Photoluminescence

ABSTRACT

In this work, a series of $Mn^{2+}$-doped α-tricalcium phosphate (α-TCP) powders was synthesized by wet co-precipitation method followed by high-temperature annealing and thermal quenching. It was shown that $Mn^{2+}$-doped α-TCP polymorph can be successfully synthesized with a doping level up to 1 mol%. All Mn-doped samples exhibited a broadband emission in the range from 525 to 825 nm with a maximum centered at around 630 nm. The highest emission intensity was observed for the sample with the highest content of Mn. The crystal structure and purity were evaluated by powder X-ray diffraction (XRD), Fourier-transform infrared (FTIR) and electron paramagnetic resonance (EPR) spectroscopies. Scanning electron microscopy (SEM) was used to investigate the morphological features of the synthesized products. Optical properties were investigated by means of photoluminescence measurements. Excitation spectra, emission spectra and decay curves of the samples were studied. Temperature-dependent photoluminescence measurements were performed as well.

## 1. Introduction

Synthetic calcium phosphates (CPs) are widely used for regenerative medicine purposes due to their biological properties and compositional similarity to natural human bone [1]. One of the most popular and frequently used CP is tricalcium phosphate (TCP, $Ca_3(PO_4)_2$). It has two polymorphs, which can be stabilized at room temperature, and both of them are used for biomedical applications as injectable bone fillers or ceramic substitutes [2,3]. β-TCP is characterized by rhombohedral structure with the space group *R3c* (#161) and 5 inequivalent Ca sites, α-TCP crystallizes in the monoclinic crystal system with $P2_1/a$ space group (#14) and has 18 inequivalent Ca sites [4,5]. α-TCP is assumed to be a high-temperature polymorph, which is usually synthesized by annealing of CP precursor mixture with Ca to P ratio 1.5:1 at temperatures above 1125 °C, which is the phase transition temperature for transformation from β- to α-TCP [6]. It is well known, that this phase transition is reversible and highly sensitive to the presence of impurities, most of smaller cations retard this transformation and stabilize β-TCP crystal phase [7–10]. Moreover, thermal quenching is frequently used to avoid undesired reversible transition and obtain single-phase α-TCP [11, 12].

Partial substitution of Ca ions by other biologically active cations is assumed to be a promising tool to superior biological properties of synthetic CPs [13–16]. It is also known that presence of foreign ions in CP matrix can modify significantly physicochemical, mechanical and anti-bacterial properties of materials, to promote changes in morphology, solubility and ion release kinetics [17]. Additionally, doping elements open new possibilities for applications of CPs as multifunctional materials. Optically active lanthanide ions and paramagnetic ions, such as $Gd^{3+}$ or $Mn^{2+}$, make it possible to use these materials for bioimaging applications including fluorescence, magnetic resonance or multimodal imaging [18–21]. Due to complicated preparation of doped α-TCP, most of the works are focused on the synthesis and investigation of substituted β-TCP [22,23] and very limited number on α-TCP [24–27]. Just recently, Luo et al. [28] suggested to use Eu doping for optical *in vivo* monitoring of biodegradation of α-TCP. Besides, α-TCP is considered as a promising host matrix for the synthesis of luminescent materials. Zhou et al. reported on cyan-emitting $Eu^{2+}$-doped α-TCP for potential application in white light emitting diodes (LEDs) [29]. Ji et al. [12] and Tong et al. [30] investigated luminescent properties of both TCP polymorphs partially substituted with $Eu^{2+}$ ions and found that $Eu^{2+}$ emission shifts from 416 nm (blue range) to 480 nm

* Corresponding author.
*E-mail address:* aleksej.zarkov@chf.vu.lt (A. Zarkov).

https://doi.org/10.1016/j.ceramint.2020.10.114
Received 14 September 2020; Received in revised form 13 October 2020; Accepted 15 October 2020
Available online 15 October 2020

(cyan range) if β-TCP transforms to α-TCP.

Manganese is an essential element in human organism that plays an important role in bone development. It acts as a cofactor of several enzymes like glycosyltransferases which are involved in formation of bone and cartilage matrix [31,32]. Furthermore, $Mn^{2+}$ enhances the ligand binding affinity of integrin and activates osteoblast adhesion [33,34]. Previous studies revealed that doping with $Mn^{2+}$ ions resulted in improvements of bioactivity of calcium hydroxyapatite (HAp) coatings [35] and osteogenesis of CP-based cements [32]. Number of works on Mn-doped TCP were published, however, all of them report on Mn-doped β-TCP [31,32,34,36–38]. To the best of our knowledge, there are no papers studying Mn-doped α-TCP. The only report that briefly describes low-temperature metastable Mn-doped α-TCP is focused on thermodynamic stability and phase transition of TCP polymorphs [39].

At the same time Mn is also known for its optical properties and previously was incorporated into different hosts for the preparation of luminescent materials [40]. The electronic structure of $Mn^{2+}$ ions allows shifting of their broadband emission from green to red depending on the crystal field strength of the host material [41]. Luminescent properties of $Mn^{2+}$-doped HAp and β-TCP were previously investigated by Lecointre et al. [42]. It was demonstrated that emission wavelength depends on the host material, orange emission peaked at 581 nm and red emission peaked at 645 nm were observed for HAp and β-TCP, respectively.

The main aim of this study was to investigate feasibility of the synthesis of Mn-doped α-TCP and to study its structural and luminescent properties. In order to do that, a series of α-TCP powders doped with different amounts of $Mn^{2+}$ ions ranging from 0.2 to 1.0 mol% was synthesized by wet co-precipitation method followed by high-temperature thermal treatment. The crystal structure and purity were evaluated by powder X-ray diffraction, electron paramagnetic resonance and Fourier-transform infrared spectroscopies. Optical properties were investigated by means of photoluminescence measurements.

## 2. Materials and methods

### 2.1. Synthesis

Mn-doped α-TCP powders were synthesized by wet co-precipitation method. Calcium nitrate tetrahydrate ($Ca(NO_3)_2{\cdot}4H_2O$, ≥99%, Roth), manganese (II) nitrate tetrahydrate ($Mn(NO_3)_2{\cdot}4H_2O$, 98%, Alfa Aesar) and diammonium hydrogen phosphate ($(NH_4)_2HPO_4$, ≥98%, Roth) were used as starting materials. Total metal ions to phosphorus ratio was kept 1.5:1 for all samples. Firstly, 0.75 M $Ca^{2+}$ and $Mn^{2+}$ nitrate solution was prepared by dissolving metal salts in deionized water. Secondly, an appropriate amount of $(NH_4)_2HPO_4$ was separately dissolved in deionized water to obtain 0.5 M solution, to which concentrated ammonia solution ($NH_4OH$, 25%, Roth) was added in order to adjust pH value to 10. Next, metal ions solution was rapidly added to $(NH_4)_2HPO_4$ solution under constant stirring resulting in the instantaneous formation of precipitates. The reaction mixture was stirred for 10 min, afterwards precipitates were separated by vacuum filtering, washed with deionized water and ethanol. The obtained precipitates were dried at 50 °C overnight in the oven and ground in agate mortar. In order to obtain α-TCP phase, the precipitates were transferred to alumina crucible, annealed at 1250 °C for 12 h and rapidly cooled down by pouring the powder on a metal plate.

### 2.2. Characterization

Powder X-ray diffraction (XRD) data were obtained using Ni-filtered Cu Kα radiation on a Bruker D8 Advance diffractometer with Bragg-Brentano focusing geometry and position sensitive LynxEYE detector. The data were collected within 2θ angle range from 10 to 110° (step width 0.01° and integration time 1.5 s). Fourier-transform infrared (FTIR) spectra were recorded in the range of 4000−400 $cm^{-1}$ employing Bruker ALPHA ATR spectrometer with 4 $cm^{-1}$ resolution. Morphology of the synthesized samples was investigated with a Hitachi SU-70 field-emission scanning electron microscope (FE-SEM). Elemental analysis of powders was carried out by inductively coupled plasma optical emission spectrometry (ICP-OES) using PerkinElmer Optima 7000DV spectrometer. The samples were dissolved in 5% nitric acid ($HNO_3$, Rotipuran® Supra 69%, Roth) and diluted to an appropriate volume. Calibration solutions were prepared by dilution of the stock standard solutions (single-element ICP standards 1000 mg/L, Roth). Room temperature electron paramagnetic resonance (EPR) measurements were performed on Bruker ELEXSYS-II E500 CW-EPR system at X (9.5 GHz; 2 mW) and Q (33.9 GHz; 2 mW) microwave frequency bands. Magnetic field modulation amplitude was 0.2 mT. Spectra intensities for X-band EPR measurements were normalized to sample mass. Excitation and emission spectra were measured on the Edinburgh Instruments FLS980 spectrometer equipped with double excitation and emission monochromators, 450 W Xe arc lamp, a cooled (−20 °C) single-photon counting photomultiplier (Hamamatsu R928), and mirror optics for powder samples. The photoluminescence (PL) emission spectra were corrected by a correction file obtained from a tungsten incandescent lamp certified by NPL (National Physics Laboratory, UK). When measuring excitation spectra ($\lambda_{em}$ = 670 nm), excitation and emission bandwidths were set to 1.60 and 5.00 nm, respectively. When measuring emission spectra ($\lambda_{ex}$ = 408 nm), excitation and emission bandwidths were set to 4.00 and 1.60 nm, respectively. For both measurements, step width was 1.00 nm and integration time was 0.2 s. The PL decay kinetics were measured on the same Edinburgh Instruments FLS980 spectrometer. Xe μ-flash lamp μF920 was used as an excitation source. Excitation wavelength was 408 nm while emission was monitored at 670 nm. For temperature-dependent excitation and emission measurements, a cryostat MicrostatN from the Oxford Instruments had been applied to the present spectrometer. Liquid nitrogen was used as a cooling agent. The measurements were performed at 77 K and at 100–500 K in 50 K intervals. Temperature stabilization time was 90 s and temperature tolerance was set to ±5 K. During the measurements dried nitrogen was flushed over the cryostat window to avoid the condensation of water at low temperatures on the surface of the window.

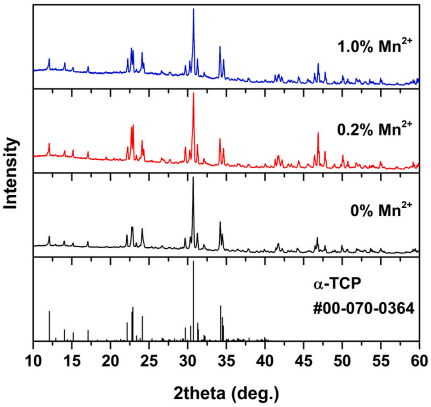


**Fig. 1.** XRD patterns of α-TCP powders doped with different amount of $Mn^{2+}$.

## 3. Results and discussion

The phase crystallinity and purity of all synthesized α-TCP powders were investigated by means of XRD analysis. The XRD patterns of

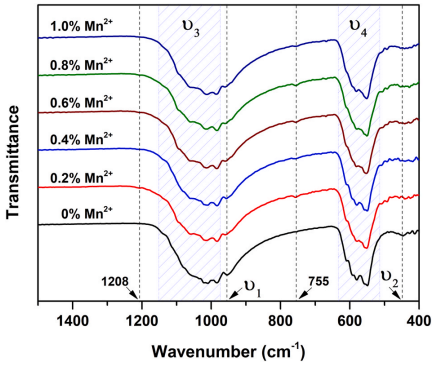


**Fig. 2.** FTIR spectra of α-TCP powders doped with different amount of $Mn^{2+}$.

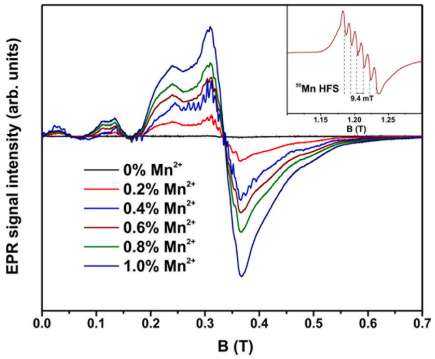


**Fig. 3.** Experimental X-band EPR spectra detected at room temperature. Inset: Q-band EPR spectrum of α-TCP sample with 0.6 mol% of $Mn^{2+}$.

**Table 1**
Results of the elemental analysis of the samples performed by ICP-OES.

| Sample | Mn/(Mn + Ca), mol% | (Mn + Ca)/P |
|---|---|---|
| $Ca_3(PO_4)_2$ | – | 1.46 |
| $Ca_3(PO_4)_2$ : 0.2% $Mn^{2+}$ | 0.21 | 1.47 |
| $Ca_3(PO_4)_2$ : 0.4% $Mn^{2+}$ | 0.42 | 1.47 |
| $Ca_3(PO_4)_2$ : 0.6% $Mn^{2+}$ | 0.62 | 1.47 |
| $Ca_3(PO_4)_2$ : 0.8% $Mn^{2+}$ | 0.82 | 1.47 |
| $Ca_3(PO_4)_2$ : 1.0% $Mn^{2+}$ | 1.01 | 1.50 |

representative CPs precipitates doped with minimal and maximal amounts of $Mn^{2+}$ ions and annealed at 1250 °C are demonstrated in Fig. 1. The obtained results clearly indicate that after the thermal treatment α-TCP crystal phase was formed regardless of chemical composition of the samples. All diffraction peaks can be attributed to monoclinic $Ca_3(PO_4)_2$ and match well the standard XRD data (ICDD #00-070-0364). Not even traces of β-TCP polymorph were detected, indicating complete transformation of initial CP precursor to α-TCP and successful prevention of reversible phase transition, which was achieved by a thermal quenching. It should be noted, that attempts to synthesize α-TCP powders with higher content of Mn were unsuccessful and resulted in biphasic products containing certain amount of secondary β-TCP phase. Similar β-TCP stabilizing effect was previously reported for other smaller ions such as Mg and Zn [7,43]. Moreover, during preparation of α-TCP containing 2 mol% of Mn, the annealed powder has melted, probably due to formation of eutectic mixture.

FTIR spectroscopy was employed to further characterize the synthesized products and identify potential neighboring phases, which could be hardly detectable by XRD in the presence of major α-TCP phase. The FTIR spectra of $Mn^{2+}$ doped α-TCP in the range from 1500 to 400 $cm^{-1}$ are given in Fig. 2. It is seen that all the obtained FTIR spectra are very similar and can be characterized by absorption bands characteristic of phosphate ions. The spectra are dominated by broad absorption bands located at 1150-970 $cm^{-1}$ ($\nu_3$), 550, 560, 582, 596 and 611 $cm^{-1}$ ($\nu_4$), 955 $cm^{-1}$ ($\nu_1$) and less intense band centered at 450 $cm^{-1}$ ($\nu_2$) [6]. The results confirm the formation of targeted α-TCP structure and shape of the spectra is very similar with that of previously reported FTIR spectra of α-TCP [6]. Nevertheless, additional very weak absorption bands, which do not correspond to α-TCP, were observed at 1208 and 755 $cm^{-1}$. These signals indicate the presence of negligible amount of calcium pyrophosphate ($Ca_2P_2O_7$) by-phase [44], which is quite often observed in TCP powders synthesized by precipitation method [31,45,46].

**Table 2**
Normalized DI values of EPR signal intensities for the investigated samples.

| Sample | DI, arb. units |
|---|---|
| $Ca_3(PO_4)_2$ | 0.00 |
| $Ca_3(PO_4)_2$ : 0.2% $Mn^{2+}$ | 0.19 |
| $Ca_3(PO_4)_2$ : 0.4% $Mn^{2+}$ | 0.37 |
| $Ca_3(PO_4)_2$ : 0.6% $Mn^{2+}$ | 0.57 |
| $Ca_3(PO_4)_2$ : 0.8% $Mn^{2+}$ | 0.72 |
| $Ca_3(PO_4)_2$ : 1.0% $Mn^{2+}$ | 1.00 |

One of the most important steps in characterization of materials is to determine chemical composition of synthesized products. Moreover, it is known that in some cases the control of stoichiometry in mixed-cation compounds synthesized by co-precipitation method can be challenging. In order to confirm stoichiometric co-precipitation of both metal ions, elemental analysis by means of ICP-OES was performed. The results of the analysis are summarized in Table 1.

It is obvious that determined Mn content is very close to theoretical values, which demonstrates that employed synthetic approach allows to prepare materials with controllable chemical composition. Total metals to phosphorus ratio shows slightly lower values than nominal 1.5:1. The possible explanation of insignificant deviation from theoretical values can be in the presence of minor $Ca_2P_2O_7$ phase, which was detected by FTIR spectroscopy.

X-band EPR spectra of the investigated samples are shown in Fig. 3 and representative Q-band EPR spectrum of α-TCP sample with 0.6 mol % of $Mn^{2+}$ is presented in the inset of Fig. 3. EPR signals associated with $Mn^{2+}$ are typical in the family of Mn-doped CPs [36,39,42,47–53]. $Mn^{2+}$ is an electron spin $S = 5/2$ paramagnetic system, which interacts with the 100% abundant $^{55}Mn$ isotope with nuclear spin $I = 5/2$. Zero field splitting (ZFS) of the ground state leads to five allowed transitions in the presence of external field $B$, which are further split into $2I+1 = 6$ hyperfine structure (HFS) components each. In powdered systems HFS is usually resolved for the central $m_S = -1/2 \leftrightarrow m_S = +1/2$ transition only, as the outer transitions are more sensitive to variations of ZFS parameter values induced by structural disorder effects. High field EPR can be used to simplify the spectra of high spin systems with a large magnitude of ZFS [36,51], therefore, measurements at Q-band were carried out. The additional spectra allowed to determine the average separation of 9.4 mT between the HFS components, which is close to the values reported for HAp and β-TCP [36,39,47–52]. Thus, it can be concluded that the coupling of $Mn^{2+}$ electron and nuclear spins is similar for all these CPs.

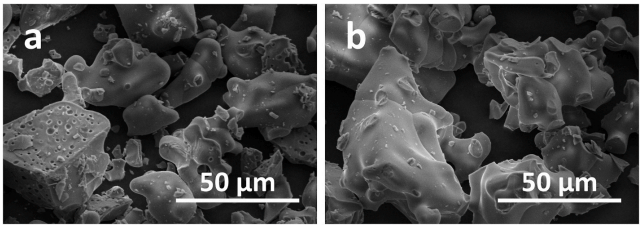


**Fig. 4.** SEM images of pristine (a) and 1 mol% $Mn^{2+}$-doped α-TCP (b) powders.

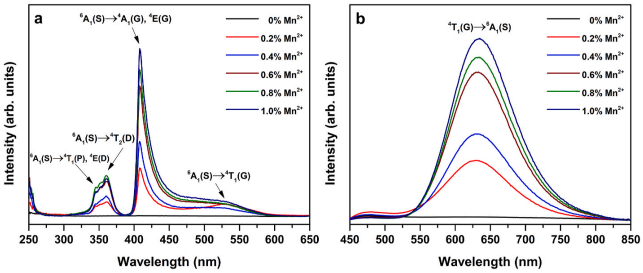


**Fig. 5.** Excitation ($\lambda_{em}$ = 670 nm) and emission ($\lambda_{ex}$ = 408 nm) spectra of $Mn^{2+}$-doped α-TCP.

The most apparent feature in X-band EPR spectra is the correlation of EPR signal intensities with the level of Mn doping. The double integral (DI) of EPR signal intensity is proportional to the number of spins in the sample and can be used for a quantitative analysis of $Mn^{2+}$ content [51, 53]. An estimation of EPR spectra DI values normalized to the 1.0 mol% $Mn^{2+}$ sample is given in Table 2. There is a reasonable correlation with the results of elemental analysis (see Table 1), which is a strong indication that Mn is predominantly in the 2+ oxidation state.

Apart from the broadening effect with an increase of $Mn^{2+}$ concentration [36,39,42,51–53], the shape of EPR spectra remains unchanged, which implies that ions occupy the same positions in the lattice up to 1.0 mol% substitution level. A notable exception is the α-TCP sample with 0.4 mol% of $Mn^{2+}$, for which sharp lines are overlaying the spectrum. The additional signal exhibits HFS characteristic to $^{55}Mn$, therefore it must be originating from another Mn-related paramagnetic center. $Mn^{2+}$ ions occupying other crystallographic sites of *α*-TCP structure or minor crystalline phases as well as Mn ions occurring in other oxidation states could be offered as possible explanations, however, additional studies are required to establish the nature of this phenomenon.

Fig. 4 shows SEM images of pristine and 1 mol% $Mn^{2+}$-doped α-TCP powders as representatives. As it might be expected after annealing at high temperature and grinding in agate mortar, both samples consisted of the polydisperse monoliths of irregular shape. The size of the particles varied from approximately 5 to 80 µm. No clearly visible grains and grain boundaries were observed. Some pores can be seen on the interior surface of the crushed monoliths. Overall, there is no significant difference between pristine and doped samples indicating that in investigated doping level the presence of $Mn^{2+}$ ions does not have perceptible effect on morphology of α-TCP specimens.

Fig. 5 illustrates PL excitation and emission spectra of $Mn^{2+}$-doped α-TCP powders at room temperature. Exploring the PL excitation spectra for 670 nm emission in the range from 250 to 650 nm (Fig. 5a), it is evident that undoped α-TCP sample is optically inactive. In the spectra of all Mn-doped samples few excitation bands centered at around 345,

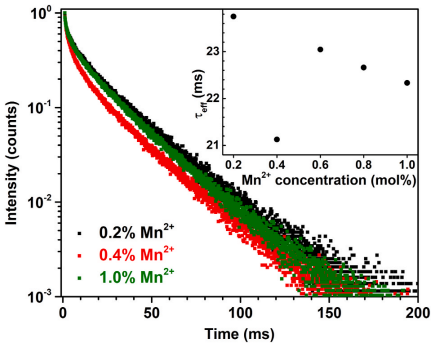


**Fig. 6.** PL decay ($\lambda_{ex}$ = 408 nm, $\lambda_{em}$ = 670 nm) curves of $Mn^{2+}$-doped α-TCP at room temperature. Inset: calculated effective PL lifetime values.

360, 408 and 529 nm were clearly observed. These bands correspond to the transitions from the $^6A_1(S)$ level to the [$^4T_1(P)$, $^4E(D)$], $^4T_2(D)$, [$^4A_1(G)$, $^4E(G)$] and $^4T_1(G)$ levels, respectively. There is also one intense band at around 250 nm, which is caused by the charge transfer state of $O^{2-}$–$Mn^{2+}$ transition [41,54–56]. The shape of the excitation spectra is similar to that of previously reported for $Mn^{2+}$-doped β-TCP [42]. The PL emission spectra of the samples excited by 408 nm radiation possess a single broadband emission in the range of around 525–825 nm and centered at about 630 nm. Such emission spectrum is characteristic of a 3d-3d emission band of $Mn^{2+}$ ions which is attributed to transition from excited $^4T_1(G)$ state to $^6A_1(S)$ ground level [40–42]. All Mn-containing samples showed concentration-dependent behavior of both excitation

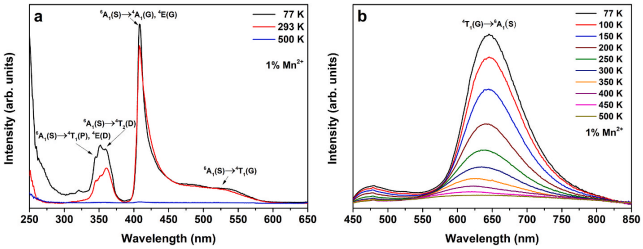


**Fig. 7.** Temperature-dependent excitation ($\lambda_{em}$ = 670 nm) and emission ($\lambda_{ex}$ = 408 nm) spectra of α-TCP doped with 1 mol% of $Mn^{2+}$.

and emission spectra. It is clearly seen that higher doping level results in stronger excitation and emission signals, i.e., the highest values were observed for α-TCP doped with 1 mol% of $Mn^{2+}$ ions. However, as was mentioned above, we were not able to prepare α-TCP powders with higher Mn content in order to obtain higher emission intensity. The observed emission maximum is slightly blue-shifted in comparison to that of Mn-doped β-TCP and red-shifted compared to that of Mn-doped HAp, which were shown to be centered at 645 and 581 nm, respectively [42]. At the same time for X-ray excited Mn-doped β-TCP emission maximum was detected at 660 nm [38].

Fig. 6 shows PL emission decay curves of $Mn^{2+}$-doped α-TCP powders when specimens were excited at 408 nm and emission monitored at 670 nm. As observed, the decay curves are very similar regardless of Mn content in the samples. In order to calculate the effective PL lifetime values, the following equation was employed [57]:

$$\tau_{eff} = \frac{\int_0^\infty I(t)tdt}{\int_0^\infty I(t)dt} \quad (1)$$

where $I(t)$ is the PL emission intensity at a time $t$ after the cutoff of excitation light. The calculated effective PL lifetime values ($\tau_{eff}$) as a function of $Mn^{2+}$ concentration are given in the inset of Fig. 6. It is obvious that with an increase of Mn content the effective PL lifetime values decrease. This dependence shows clearly linear behavior with an exception for the sample containing 0.4 mol% of $Mn^{2+}$, which is clearly out of this trend. In order to correct this outlier, which we initially thought originates from a potential mistake in preparation of this particular sample, we additionally synthesized 5 separate α-TCP samples doped with 0.4 mol% of Mn. However, all extra syntheses were reproducible and showed the same optical properties and $\tau_{eff}$ values. Moreover, it goes hand in hand with additional signals in EPR spectra. Therefore, the reason of such anomalous behavior is unclear. Unfortunately, the performed XPS analysis did not provide any information about the presence of other than $Mn^{2+}$ valence states because of lack of sensitivity, since concentrations of Mn are rather low. Possible occupancy of another crystallographic site is also hardly provable because of the same reason and large number of Ca sites (18 inequivalent Ca sites) in α-TCP structure.

The excitation and emission spectra as a function of temperature for α-TCP doped with 1 mol% $Mn^{2+}$ are depicted in Fig. 7. Evidently, the excitation spectrum changes significantly depending on the temperature (see Fig. 7a). The comparison of the spectra recorded at room temperature and at 77 K shows that at lower temperature the intensity of excitation band corresponding to the charge transfer state of $O^{2-}$–$Mn^{2+}$ transition, located at ca. 250 nm, increases drastically. The intensity of the other bands in UV region also increases significantly; however, at a longer wavelength region this increase is not so substantial. The intensity of excitation bands at 500 K is negligible compared to that at room temperature. It is also seen that emission intensity monotonically increases as temperature decreases (Fig. 7b). Moreover, a red shift was observed in the emission peak with decreasing temperature. It was found that emission peak gradually shifts from 620 nm at 500 K to 645 nm at 77 K. Another observed temperature-induced effect – emission peak broadening. It was determined that emission peak broadens significantly at elevated temperatures. This could be explained by the fact that at higher temperatures lattice vibrations increase leading to the changes in local surrounding of $Mn^{2+}$ ions.

## 4. Conclusions

A series of $Mn^{2+}$-doped α-TCP powders with a doping level ranging from 0.2 to 1 mol% were successfully synthesized by co-precipitation method followed by high-temperature annealing and thermal quenching. The results of XRD, FTIR and elemental analysis confirmed that proposed synthetic approach is suitable for the synthesis of $Mn^{2+}$-doped α-TCP with a good phase purity and controllable chemical composition. Optical properties of the synthesized specimens were investigated in terms of PL. It was demonstrated that Mn-containing powders under excitation at 408 nm revealed a broadband emission in the range from 525 to 825 nm with a maximum centered at around 630 nm. Emission intensity was found to be Mn concentration dependent and increased as Mn content increased. On the contrary, PL lifetime values showed gradual decrease with an increase of Mn content. Temperature-dependent PL measurements exhibited a gradual and significant increase of emission intensity at lower temperatures.

## Declaration of competing interest

The authors declare that they have no known competing financial interests or personal relationships that could have appeared to influence the work reported in this paper.

## Acknowledgements

This project has received funding from European Social Fund (project No 09.3.3-LMT-K-712-19-0069) under grant agreement with the Research Council of Lithuania (LMTLT).

## References

[1] W. Habraken, P. Habibovic, M. Epple, M. Bohner, Calcium phosphates in biomedical applications: materials for the future?, Mater, Today Off. 19 (2) (2016) 69–87.
[2] S.V. Dorozhkin, Calcium orthophosphates in nature, biology and medicine, Materials 2 (2) (2009) 399–498.
[3] S.V. Dorozhkin, Functionalized calcium orthophosphates ($CaPO_4$) and their biomedical applications, J. Mater. Chem. B 7 (47) (2019) 7471–7489.
[4] M. Mathew, L.W. Schroeder, B. Dickens, W.E. Brown, The crystal structure of alpha-$Ca_3(PO_4)_2$, Acta Crystallogr. B 33 (5) (1977) 1325–1333.
[5] B. Dickens, L.W. Schroeder, W.E. Brown, Crystallographic studies of the role of Mg as a stabilizing impurity in β-$Ca_3(PO_4)_2$. The crystal structure of pure β-$Ca_3(PO_4)_2$, J. Solid State Chem. 10 (3) (1974) 232–248.

[6] R.G. Carrodeguas, S. De Aza, α-Tricalcium phosphate: synthesis, properties and biomedical applications, Acta Biomater. 7 (10) (2011) 3536–3546.

[7] M. Frasnelli, V.M. Sglavo, Effect of $Mg^{2+}$ doping on beta-alpha phase transition in tricalcium phosphate (TCP) bioceramics, Acta Biomater. 33 (2016) 283–289.

[8] E. Boanini, M. Gazzano, A. Bigi, Ionic substitutions in calcium phosphates synthesized at low temperature, Acta Biomater. 6 (6) (2010) 1882–1894.

[9] P.M.C. Torres, J.C.C. Abrantes, A. Kaushal, S. Pina, N. Döbelin, M. Bohner, J.M. F. Ferreira, Influence of Mg-doping, calcium pyrophosphate impurities and cooling rate on the allotropic α↔β-tricalcium phosphate phase transformations, J. Eur. Ceram. Soc. 36 (3) (2016) 817–827.

[10] D. Brazete, P.M.C. Torres, J.C.C. Abrantes, J.M.F. Ferreira, Influence of the Ca/P ratio and cooling rate on the allotropic α↔β-tricalcium phosphate phase transformations, Ceram. Int. 44 (7) (2018) 8249–8256.

[11] J.T. Zhang, F. Tancret, J.M. Bouler, Fabrication and mechanical properties of calcium phosphate cements (CPC) for bone substitution, Mater. Sci. Eng. C 31 (4) (2011) 740–747.

[12] H. Ji, Z. Huang, Z. Xia, M.S. Molokeev, M. Chen, V.V. Atuchin, M. Fang, Y.g. Liu, X. Wu, Phase transformation in $Ca_3(PO_4)_2$:$Eu^{2+}$ via the controlled quenching and increased $Eu^{2+}$ content: identification of new cyan-emitting α-$Ca_3(PO_4)_2$:$Eu^{2+}$ phosphor, J. Am. Ceram. Soc. 98 (10) (2015) 3280–3284.

[13] A. Bigi, E. Boanini, M. Gazzano, 7-Ion substitution in biological and synthetic apatites, in: C. Aparicio, M.-P. Ginebra (Eds.), Biomineralization and Biomaterials, Woodhead Publishing, Boston, 2016, pp. 235–266.

[14] J.T.B. Ratnayake, M. Mucalo, G.J. Dias, Substituted hydroxyapatites for bone regeneration: a review of current trends, J. Biomed. Mater. Res. B Appl. Biomater. 105 (5) (2017) 1285–1299.

[15] T. Tite, A.-C. Popa, L.M. Balescu, I.M. Bogdan, I. Pasuk, J.M.F. Ferreira, G.E. Stan, Cationic substitutions in hydroxyapatite: current status of the derived biofunctional effects and their, In Vitro Interrogation Methods, Materials 11 (11) (2018) 2081.

[16] M. Šupová, Substituted hydroxyapatites for biomedical applications: a review, Ceram, Bar Int. 41 (8) (2015) 9203–9231.

[17] B. Yilmaz, A.Z. Alshemary, Z. Evis, Co-doped hydroxyapatites as potential materials for biomedical applications, Microchem. J. 144 (2019) 443–453.

[18] R. Meenambal, P. Poojar, S. Geethanath, S. Kannan, Substitutional limit of gadolinium in β-tricalcium phosphate and its magnetic resonance imaging characteristics, J. Biomed. Mater. Res. B Appl. Biomater. 105 (8) (2017) 2545–2552.

[19] S.S. Syamchand, G. Sony, Multifunctional hydroxyapatite nanoparticles for drug delivery and multimodal molecular imaging, Microchim, Acta 182 (9) (2015) 1567–1589.

[20] C. Qi, J. Lin, L.-H. Fu, P. Huang, Calcium-based biomaterials for diagnosis, treatment, and theranostics, Chem. Soc. Rev. 47 (2) (2018) 357–403.

[21] P. Mi, D. Kokuryo, H. Cabral, H. Wu, Y. Terada, T. Saga, I. Aoki, N. Nishiyama, K. Kataoka, A pH-activatable nanoparticle with signal-amplification capabilities for non-invasive imaging of tumour malignancy, Nat, Nanotechnology 11 (8) (2016) 724–730.

[22] L. Sinusaite, A. Popov, A. Antuzevics, K. Mazeika, D. Baltrunas, J.-C. Yang, J. L. Horng, S. Shi, T. Sekino, K. Ishikawa, A. Kareiva, A. Zarkov, Fe and Zn co-substituted beta-tricalcium phosphate (β-TCP): synthesis, structural, magnetic, mechanical and biological properties, Mater. Sci. Eng. C 112 (2020) 110918.

[23] M. Gallo, B. Le Gars Santoni, T. Douillard, F. Zhang, L. Gremillard, S. Dolder, W. Hofstetter, S. Meille, M. Bohner, J. Chevalier, S. Tadier, Effect of grain orientation and magnesium doping on β-tricalcium phosphate resorption behavior, Acta Biomater. 89 (2019) 391–402.

[24] Y. Sogo, A. Ito, M. Kamo, T. Sakurai, K. Onuma, N. Ichinose, M. Otsuka, R. Z. LeGeros, Hydrolysis and cytocompatibility of zinc-containing α-tricalcium phosphate powder, Mater. Sci. Eng. C 24 (6) (2004) 709–715.

[25] E. Boanini, S. Panzavolta, K. Rubini, M. Gandolfi, A. Bigi, Effect of strontium and gelatin on the reactivity of α-tricalcium phosphate, Acta Biomater. 6 (3) (2010) 936–942.

[26] K. Hurle, J. Neubauer, F. Goetz-Neunhoeffer, Influence of $Sr^{2+}$ on calcium-deficient hydroxyapatite formation kinetics and morphology in partially amorphized α-TCP, J. Am. Ceram. Soc. 99 (3) (2016) 1055–1063.

[27] S.J. Saint-Jean, C.L. Camiré, P. Nevsten, S. Hansen, M.P. Ginebra, Study of the reactivity and in vitro bioactivity of Sr-substituted α-TCP cements, J. Mater. Sci. Mater. Med. 16 (11) (2005) 993.

[28] D. Luo, C. Tong, Y. Zhu, C. Xu, Y. Li, Color tracing in the hydration process of α-$Ca_3(PO_4)_2$:Eu, J. Lumin. 219 (2020) 116863.

[29] W. Zhou, J. Han, X. Zhang, Z. Qiu, Q. Xie, H. Liang, S. Lian, J. Wang, Synthesis and photoluminescence properties of a cyan-emitting phosphor $Ca_3(PO_4)_2$:$Eu^{2+}$ for white light-emitting diodes, Opt. Mater. 39 (2015) 173–177.

[30] C. Tong, Y. Zhu, C. Xu, L. Yang, Y. Li, Luminescence properties and color identification of Eu doped $Ca_3(PO_4)_2$ phosphors calcined in air, Physica B Condens, Matter 521 (2017) 153–157.

[31] P.M.C. Torres, S.I. Vieira, A.R. Cerqueira, S. Pina, O.A.B. da Cruz Silva, J.C. C. Abrantes, J.M.F. Ferreira, Effects of Mn-doping on the structure and biological properties of β-tricalcium phosphate, J. Inorg. Biochem. 136 (2014) 57–66.

[32] T. Wu, H. Shi, Y. Liang, T. Lu, Z. Lin, J. Ye, Improving osteogenesis of calcium phosphate bone cement by incorporating with manganese doped β-tricalcium phosphate, Mater. Sci. Eng. C 109 (2020) 110481.

[33] E. György, P. Toricelli, G. Socol, M. Iliescu, I. Mayer, I.N. Mihailescu, A. Bigi, J. Werckman, Biocompatible $Mn^{2+}$-doped carbonated hydroxyapatite thin films grown by pulsed laser deposition, J. Biomed. Mater. Res. 71A (2) (2004) 353–358.

[34] R. Singh, M. Srivastava, N.K. Prasad, S. Awasthi, A. Kumar Dhayalan, S. Kannan, Structural analysis and magnetic induced hyperthermia of $Fe^{3+}$ and $Mn^{2+}$ substituted β-$Ca_3(PO_4)_2$, New J. Chem. 41 (21) (2017) 12879–12891.

[35] Y. Huang, H. Qiao, X. Nian, X. Zhang, X. Zhang, G. Song, Z. Xu, H. Zhang, S. Han, Improving the bioactivity and corrosion resistance properties of electrodeposited hydroxyapatite coating by dual doping of bivalent strontium and manganese ion, Surf. Coating. Technol. 291 (2016) 205–215.

[36] J.V. Rau, I.V. Fadeeva, A.S. Fomin, K. Barbaro, E. Galvano, A.P. Ryzhov, F. Murzakhanov, M. Gafurov, S. Orlinskii, I. Antoniac, V. Uskoković, Sic parvis magna: manganese-substituted tricalcium phosphate and its biophysical properties, ACS biomater, Sci. Eng 5 (12) (2019) 6632–6644.

[37] Y.-j Zhang, Z.-y Mao, D.-J. Wang, J. Zhao, Synchronous red and blue emitting $Ca_3(PO_4)_2$:$Eu^{2+}$, $Mn^{2+}$ phosphors applicable for plant-lighting, Mater. Res. Bull. 67 (2015) 1–4.

[38] A. Bessière, A. Lecointre, R.A. Benhamou, E. Suard, G. Wallez, B. Viana, How to induce red persistent luminescence in biocompatible $Ca_3(PO_4)_2$, J. Mater. Chem. C 1 (6) (2013) 1252–1259.

[39] L. Sinusaite, A.M. Renner, M.B. Schuetz, A. Antuzevics, U. Rogulis, I. Grigoraviciute-Puroniene, S. Mathur, A. Zarkov, Effect of Mn doping on the low-temperature synthesis of tricalcium phosphate (TCP) polymorphs, J. Eur. Ceram. Soc. 39 (10) (2019) 3257–3263.

[40] Q. Zhou, L. Dolgov, A.M. Srivastava, L. Zhou, Z. Wang, J. Shi, M.D. Dramićanin, M. G. Brik, M. Wu, $Mn^{2+}$ and $Mn^{4+}$ red phosphors: synthesis, luminescence and applications in WLEDs, A review, J. Mater. Chem. C 6 (11) (2018) 2652–2671.

[41] G. Blasse, B.C. Grabmaier, A General Introduction to Luminescent Materials, Luminescent Materials, Springer Berlin Heidelberg, Berlin, Heidelberg, 1994, pp. 1–9.

[42] A. Lecointre, R. Ait Benhamou, A. Bessière, G. Wallez, M. Elaatmani, B. Viana, Red long-lasting phosphorescence (LLP) in β-TCP type $Ca_{9.5}Mn(PO_4)_7$ compounds, Opt. Mater. 34 (2) (2011) 376–380.

[43] L. Carbajal, A. Caballero, M.A. Sainz, Design and processing of ZnO doped tricalcium phosphate based materials: influence of β/α polymorph phase assemblage on microstructural evolution, J. Eur. Ceram. Soc. 32 (3) (2012) 569–577.

[44] B.C. Cornilsen, R.A. Condrate, The vibratonal spectra of β-$Ca_2P_2O_7$ and γ-$Ca_2P_2O_7$, J. Inorg. Nucl. Chem. 41 (4) (1979) 602–605.

[45] L. Sinusaite, I. Grigoraviciute-Puroniene, A. Popov, K. Ishikawa, A. Kareiva, A. Zarkov, Controllable synthesis of tricalcium phosphate (TCP) polymorphs by wet precipitation: effect of washing procedure, Ceram. Int. 45 (9) (2019) 12423–12428.

[46] A. Destainville, E. Champion, D. Bernache-Assollant, E. Laborde, Synthesis, characterization and thermal behavior of apatitic tricalcium phosphate, Mater. Chem. Phys. 80 (1) (2003) 269–277.

[47] I. Mayer, H. Diab, D. Reinen, C. Albrecht, Manganese in apatites, chemical, ligand-field and electron paramagnetic resonance spectroscopy studies, J. Mater. Sci. 28 (9) (1993) 2428–2432.

[48] I. Mayer, F.J.G. Cuisinier, I. Popov, Y. Schleich, S. Gdalya, O. Burghaus, D. Reinen, Phase relations between β-tricalcium phosphate and hydroxyapatite with manganese(II): structural and spectroscopic properties, Eur. J. Inorg. Chem. 2006 (7) (2006) 1460–1465.

[49] I. Mayer, S. Cohen, S. Gdalya, O. Burghaus, D. Reinen, Crystal structure and EPR study of Mn-doped beta-tricalcium phosphate, Mater. Res. Bull. 43 (2) (2008) 447–452.

[50] I. Matković, N. Maltar-Strmečki, V. Babić-Ivančić, M. Dutour Sikirić, V. Noethig-Laslo, Characterisation of β-tricalcium phosphate-based bone substitute materials by electron paramagnetic resonance spectroscopy, Radiat. Phys. Chem. 81 (10) (2012) 1621–1628.

[51] F. Murzakhanov, G. Mamin, A. Voloshin, E. Klimashina, V. Putlyaev, V. Doronin, S. Bakhteev, R. Yusupov, M. Gafurov, S. Orlinskii, Conventional electron paramagnetic resonance of $Mn^{2+}$ in synthetic hydroxyapatite at different concentrations of the doped manganese, IOP Conf, Ser. Earth Environ. Sci. 155 (2018), 012006.

[52] B. Sutter, T. Wasowicz, T. Howard, L.R. Hossner, D.W. Ming, Characterization of iron, manganese, and copper synthetic hydroxyapatites by electron paramagnetic resonance spectroscopy, Soil Sci. Soc. Am. J. 66 (4) (2002) 1359–1366.

[53] B. Gabbasov, M. Gafurov, A. Starshova, D. Shurtakova, F. Murzakhanov, G. Mamin, S. Orlinskii, Conventional, pulsed and high-field electron paramagnetic resonance for studying metal impurities in calcium phosphates of biogenic and synthetic origins, J. Magn. Magn Mater. 470 (2019) 109–117.

[54] L. Wu, B. Wang, Y. Zhang, L. Li, H.R. Wang, H. Yi, Y.F. Kong, J.J. Xu, Structure and photoluminescence properties of a rare-earth free red-emitting $Mn^{2+}$-activated $KMgBO_3$, Dalton Trans. 43 (37) (2014) 13845–13851.

[55] L. Lin, M. Yin, C. Shi, W. Zhang, Luminescence properties of a new red long-lasting phosphor: $Mg_2SiO_4$:$Dy^{3+}$, $Mn^{2+}$, J. Alloys Compd. 455 (1) (2008) 327–330.

[56] R. Cao, W. Wang, J. Zhang, Y. Ye, T. Chen, S. Guo, F. Xiao, Z. Luo, Luminescence properties of $Sr_2Mg_3P_4O_{15}$:$Mn^{2+}$ phosphor and the improvement by co-doping $Bi^{3+}$, Opt. Mater. 79 (2018) 223–226.

[57] F. Lahoz, I.R. Martín, J. Mendez-Ramos, P. Nunez, Dopant distribution in a $Tm^{3+}$–$Yb^{3+}$ codoped silica based glass ceramic: an infrared-laser induced upconversion study, J. Chem. Phys. 120 (13) (2004) 6180–6190.

Article V

**Thermally induced crystallization and phase evolution of amorphous calcium phosphate substituted with divalent cations having different sizes**

L. Sinusaite, A. Kareiva, A. Zarkov

*Crystal Growth & Design,* 21(2) (2021) 1242-1248

CRYSTAL GROWTH & DESIGN

pubs.acs.org/crystal

Article

# Thermally Induced Crystallization and Phase Evolution of Amorphous Calcium Phosphate Substituted with Divalent Cations Having Different Sizes

Lauryna Sinusaite, Aivaras Kareiva, and Aleksej Zarkov*

Cite This: *Cryst. Growth Des.* 2021, 21, 1242−1248

Read Online

ACCESS | Metrics & More | Article Recommendations | Supporting Information

**ABSTRACT:** The present work investigates the crystallization and phase evolution of amorphous calcium phosphate (ACP) partially substituted with smaller ($Mg^{2+}$, $Zn^{2+}$) and larger ($Sr^{2+}$, $Ba^{2+}$) divalent ions in the range from 1 to 10 mol % (M/P = 1.5:1). It has been demonstrated that the crystallization of ACP to tricalcium phosphate (TCP) and subsequent phase transformations between TCP polymorphs strongly depend on the nature and concentration of the substituents in the ACP matrix. Two different effects induced by the presence of foreign ions were observed. Substitution with smaller ions did not affect the crystallization temperature but promoted the formation of $\beta$-TCP at a significantly lower temperature compared to the phase evolution of pristine ACP. Moreover, the effect of Mg was found to be more significant than that of Zn in the transformation of metastable $\alpha$-TCP to $\beta$-TCP. On the other hand, substitution with larger ions retarded the crystallization process, which was observed at elevated temperatures. While the substitution level of 10 mol % of Sr did not affect the thermal stability of metastable $\alpha$-TCP, the presence of 10 mol % of Ba stabilized $\alpha$-TCP crystal structure and totally prevented the phase transition to $\beta$-TCP.

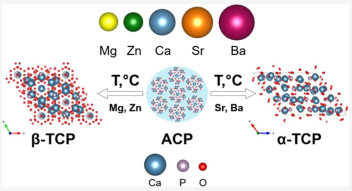


## 1. INTRODUCTION

Synthetic calcium phosphates (CPs) are widely used in medicine as bone substitutes due to their excellent biocompatibility, osteoconductivity, and chemical composition similar to those of natural bone.[1] Most frequently, crystalline solids such as calcium hydroxyapatite (HAp, $Ca_{10}(PO_4)_6(OH)_2$), tricalcium phosphate (TCP, $Ca_3(PO_4)_2$), or octacalcium phosphate (OCP, $Ca_8H_2(PO_4)_6{\cdot}5H_2O$) are used for biomedical applications.[2] On the other hand, amorphous calcium phosphates (ACPs) also attract considerable attention in the field of biomaterials science and bone regenerative medicine due to their metastability, which can result in superior biochemical reactivity.[3] For biomedical applications, ACPs can be prepared in different forms such as coatings on metal implants, ceramics, and CP-based cement.[4−7] Additionally, synthetic ACPs can be used as a precursor for the synthesis of other phosphate crystalline materials.[8−10] The crystallization of ACPs is of fundamental importance because transformation between amorphous and crystalline apatite affects some vitally important processes including biomineralization, where ACP has been reported as the transient phase in both *in vivo* and *in vitro* studies. Understanding the mechanism of these phase transitions can potentially lead to controllable formation and dissolution of hard tissues *in vivo* and allow to design new synthetic biomaterials. Moreover, unraveling the mechanism of the formation of crystalline CPs could contribute essentially to understanding the diseases caused by pathological mineralization.[11−15]

CPs can be characterized by different Ca-to-P ratios, which is usually fixed for crystalline materials with an exception for calcium-deficient hydroxyapatite (CDHA, $Ca_{10-x}(PO_4)_{6-x}(HPO_4)_x(OH)_{2-x}$), where this ratio can vary. Unlike crystalline solids, synthetic ACPs can be prepared as a substance with different Ca-to-P ratios ranging from 1.2 to 2.2.[16] This ratio strongly depends on the formation conditions such as synthesis media, pH, and presence of foreign ions.[17] In this study, we investigate the crystallization behavior of substituted ACP with a total metal ion-to-P ratio of 1.5:1. Such an elemental ratio is most commonly found in amorphous precipitates obtained in alkaline media. The crystalline analogue of an ACP with that chemical composition is TCP. This orthophosphate has two polymorphs, which can be stabilized at room temperature. The low-temperature $\beta$-TCP crystallizes in the rhombohedral crystal system with the space group $R3c$ and the high-temperature $\alpha$-TCP is characterized by a monoclinic crystal structure with the space group $P2_1/a$.[18] Due to the different physicochemical

Received: November 12, 2020
Revised: January 6, 2021
Published: January 20, 2021

properties, most frequently, these polymorphs are used for different applications. $\beta$-TCP is usually employed in the fabrication of bioceramics, while $\alpha$-TCP is used for the preparation of CP-based cement. The phase transition from $\beta$-TCP to $\alpha$-TCP occurs at around 1125 °C.[19] This transformation is known to be reversible and sensitive to impurities and the cooling process. A number of works have been published on the investigation of the influence of foreign ions on the reversibility and temperature of this phase transition.[20−30] Moreover, different substitution effects were reported depending on the nature of foreign ions. For instance, Mg stabilizes $\beta$-TCP and increases $\beta$- to $\alpha$-TCP transition temperature to 1540 °C at a substitution level of 8 mol %.[31] On the other hand, doping with Si inhibited reversion of $\alpha$- to $\beta$-TCP on cooling, however, transformation temperature from $\beta$-TCP to $\alpha$-TCP on heating was not affected by the presence of Si.[30] Overall, previous studies were focused on high-temperature transformations of TCP polymorphs.

At the same time, metastable $\alpha$-TCP can be also synthesized from ACP at low temperature (around 600 °C) with a further transformation to $\beta$-TCP at around 950 °C. This low-temperature phase transition from $\alpha$- to $\beta$-TCP is quite a poorly investigated topic. A number of reports have been published on the crystallization and phase evolution of ACP;[12,32−34] however, only undoped ACP has been studied so far. To the best of our knowledge, there are no studies on the effect of foreign ions on the crystallization behavior and phase evolution of ACP. Recently, we demonstrated that phase-pure TCP polymorphs can be prepared from ACP at identical temperatures by the partial substitution of Ca by a certain amount of $Mn^{2+}$ ions.[35] It was shown that the presence of $Mn^{2+}$ ions promotes the formation of $\beta$-TCP, while pristine ACP crystallizes to $\alpha$-TCP. In the present work, we report a comprehensive investigation of the crystallization of ACPs substituted with smaller and larger divalent ions. Moreover, this study provides information on the effect of foreign ions on the relationship between TCP polymorphs at low temperatures (600−900 °C). Partially, this work is aimed to confirm experimentally a previous theoretical study by Matsunaga et al. on the thermodynamic stability of TCP polymorphs substituted with smaller and larger divalent ions.[36]

## 2. EXPERIMENTAL SECTION

**2.1. Synthesis.** Calcium nitrate tetrahydrate ($Ca(NO_3)_2{\cdot}4H_2O$, ≥99%, Roth), magnesium nitrate hexahydrate ($Mg(NO_3)_2{\cdot}6H_2O$, 99%, Chempur), zinc nitrate hexahydrate ($Zn(NO_3)_2{\cdot}6H_2O$, 99%, Chempur), strontium nitrate ($Sr(NO_3)_2$, ≥99%, Roth), barium nitrate ($Ba(NO_3)_2$, ≥99%, Roth), and diammonium hydrogen phosphate ($(NH_4)_2HPO_4$, ≥98%, Roth) were used as starting materials. Synthesis of pristine and substituted CPs with substitution levels of 1, 2.5, 5, 7.5, and 10 mol % was performed by a slightly modified procedure reported previously.[35,37] Substitution level is given here with respect to Ca ions. Ten mol percent corresponds to the nominal composition of $(Ca_{2.7}M_{0.3}(PO_4)_2)$. Briefly, an appropriate amount of $(NH_4)_2HPO_4$ was dissolved in deionized water to obtain a 0.5 M solution, to which concentrated ammonia solution ($NH_4OH$, 25%, Roth) was added under constant mixing to adjust pH value to 10 (in the case of Zn-substituted ACP pH was adjusted to 9). Next, a solution containing an appropriate ratio of metal nitrates dissolved in deionized water (total metal ions concentration was 0.75 M) was rapidly added to the above mixture, resulting in the instantaneous formation of precipitates. The molar ratio of the total metal ions to phosphorous was kept at 1.50. The obtained precipitates were mixed in the reaction mixture for 10 min, filtered, washed with deionized water and isopropanol, and dried at 50 °C overnight. Dry powders were ground in an agate mortar and annealed in a muffle furnace at different temperatures for 5 h with a heating rate of 5 °C/min.

**2.2. Characterization.** Powder X-ray diffraction (XRD) data were collected using Ni-filtered Cu K$\alpha$ radiation on a Rigaku MiniFlex II diffractometer working in the Bragg−Brentano ($\theta/2\theta$) geometry. The data were collected within a $2\theta$ angle range from 10 to 60°, with a step width of 0.02° and a scanning speed of 1°/min. Elemental analysis of the synthesized products was performed by means of inductively coupled plasma optical emission spectrometry (ICP-OES) using a Perkin Elmer Optima 7000 DV spectrometer. The samples prior to analysis were dissolved in 5% nitric acid ($HNO_3$, Rotipuran Supra 69%, Roth) and diluted to an appropriate volume with deionized water. Calibration solutions were prepared by dilution of the stock standard solutions (single-element ICP standards 1000 mg/L, Roth).

## 3. RESULTS AND DISCUSSION

Four series of ACPs substituted with different amounts of $Mg^{2+}$, $Zn^{2+}$, $Sr^{2+}$, and $Ba^{2+}$ ions were prepared to investigate the influence of these substituents on the crystallization behavior of ACP. Hereafter, the synthesized powders will be indicated in the text as Mg-ACP, Zn-ACP, Sr-ACP, and Ba-ACP depending on the introduced foreign ion. Substitution level ranging from 1 to 10 mol % was chosen for all substituents based on the ability of the TCP structure to accept different amounts of these ions depending on their ionic radius. It was demonstrated in previous works that $Mg^{2+}$ and $Zn^{2+}$ can substitute calcium in the $\beta$-TCP structure up to approximately 14 and 20 mol %, respectively. On the other hand, the threshold limit value for $Sr^{2+}$ is greatly higher at 80 mol %.[31,38,39] Therefore, for this study, the same substitution level, which is lower than the maximal value, was chosen for all elements. The visual representation of ionic radii of the selected divalent cations is illustrated in Figure 1.[40]

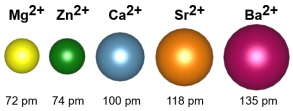


**Figure 1.** Ionic radii of the selected divalent cations in a sixfold coordination.

As an initial step, the elemental analysis of the as-prepared ACPs was performed by means of ICP-OES to confirm their chemical composition and ensure that different substitution-induced effects are caused exceptionally by the nature of foreign ions but not by their unequal actual amounts in the ACP matrix. The results of the elemental analysis of Mg-ACP, Zn-ACP, Sr-ACP, and Ba-ACP specimens are summarized in Table 1.

As seen, the determined ratios of metal ions and Ca are in good agreement with nominal substitution values for all

**Table 1. Results of the Elemental Analysis of the Samples Performed by ICP-OES**

| theoretical $M^{2+}$ amount, mol % | $\frac{n(Mg)\cdot 100\,\%}{n(Ca+Mg)}$ | $\frac{n(Zn)\cdot 100\,\%}{n(Ca+Zn)}$ | $\frac{n(Sr)\cdot 100\,\%}{n(Ca+Sr)}$ | $\frac{n(Ba)\cdot 100\,\%}{n(Ca+Ba)}$ |
|---|---|---|---|---|
| 1 | 0.987 | 0.975 | 0.968 | 1.01 |
| 2.5 | 2.38 | 2.33 | 2.63 | 2.53 |
| 5 | 4.74 | 4.66 | 4.75 | 5.14 |
| 7.5 | 7.33 | 7.27 | 7.35 | 7.58 |
| 10 | 9.67 | 9.76 | 9.39 | 10.1 |


https://dx.doi.org/10.1021/acs.cgd.0c01534
Cryst. Growth Des. 2021, 21, 1242−1248

synthesized samples. In all cases, the discrepancies between the target and the actual molar ratio do not exceed 10%. Taking into account a substitution step chosen for this study, we consider such a mismatch as insignificant. To avoid any confusion, hereafter, all ACPs are indicated by a nominal substitution level.

The XRD patterns of the pristine ACP annealed at different temperatures are shown in Figure 2. Evidently, the

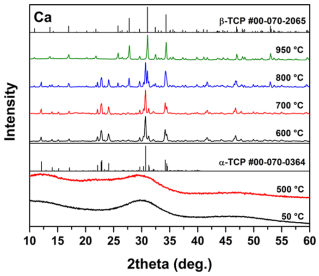


**Figure 2.** XRD patterns of pristine ACP powders annealed at different temperatures.

crystallization process starts at around 600 °C with a formation of $\alpha$-TCP. At higher temperatures, gradual transformation to $\beta$-TCP occurs, with the coexistence of two polymorphs being the most obvious after annealing at 800 °C. The XRD pattern of the powders annealed at 900 °C is dominated by the reflections of $\beta$-TCP and only a negligible amount of $\alpha$-TCP can be detected. Complete transformation to $\beta$-TCP was observed at around 950 °C. These results are in good agreement with the previously published results by Döbelin et al.[34] They reported the start of crystallization process at 525 °C and full transformation of $\alpha$- to $\beta$-TCP at 950 °C, while an insignificant amount of $\alpha$-TCP was still present after annealing at 900 °C. Somrani et al.[33] reported on the phase-pure $\beta$-TCP after annealing at 900 °C; however, a closer look at the provided XRD pattern reveals a minor amount of neighboring $\alpha$-TCP. The work by Maciejewski et al.[41] reports on the transformation of TCP polymorphs in the 870−950 °C temperature range. On the other hand, some contradictions compared to the literature data were also found. Uskoković et al.[12] obtained a mixture of TCP polymorphs even after the heat treatment of ACP at 1000 °C.

The XRD patterns of the as-prepared ACP substituted with different amounts of Mg ions are represented in Figure S1. The exclusively amorphous phase was obtained in all samples regardless of the Mg content in the as-prepared precipitates, there were no visible sharp diffraction peaks corresponding to any crystalline material. Figure 3 depicts the XRD patterns of Mg-ACP annealed at 700 °C, which was selected as a representative temperature. Obviously, the substitution level of 1 mol % already induces different crystallization behavior compared to the pristine ACP and promotes the formation of $\beta$-TCP. The coexistence of two polymorphs is clearly seen. When Mg content reaches 2.5 mol %, all diffraction peaks are associated with $\beta$-TCP and no signals arising from $\alpha$-TCP can be observed. With further increase in the Mg content, no phase transitions were expectedly detected; however, a gradual shift of the position of reflection peaks toward higher angles was

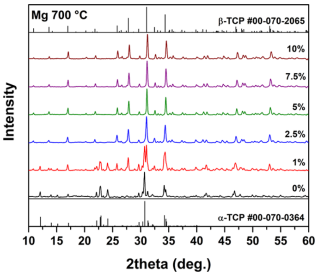


**Figure 3.** XRD patterns of the Mg-ACP powders having different amounts of Mg and annealed at 700 °C.

observed. Such a trend can be interpreted as evidence of the incorporation of Mg ions into the crystal lattice of $\beta$-TCP. This shift is explained by a mismatch in the ionic radii between $Ca^{2+}$ and $Mg^{2+}$ ions. In a sixfold coordination, the $Ca^{2+}$ has an ionic radius of 100 pm, which is significantly higher than that of the $Mg^{2+}$ in the same coordination at 72 pm.[40]

Figure 4 represents the phase evolution of Mg-ACP substituted with the maximal amount of Mg. As seen, after

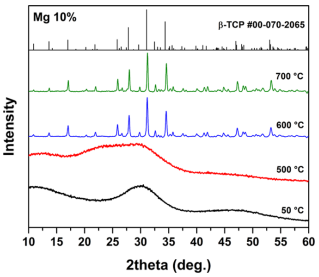


**Figure 4.** XRD patterns of ACP powders substituted with 10 mol % of Mg and annealed at different temperatures.

the heat treatment at 500 °C, the sample exists in amorphous form and after annealing at 600 °C crystallizes to $\beta$-TCP without an intermediate $\alpha$-TCP phase. The temperature of the formation of $\beta$-TCP is significantly lower compared to that of the undoped ACP (see Figure 2). A similar phenomenon was previously reported for the Mn-doped ACP, it was demonstrated that the Mn substitution level of 5 mol % also lowers the temperature of formation of $\beta$-TCP, which was obtained at 700 °C.[35] The crystallization of $\beta$-TCP from CDHA also was shown to occur at a noticeably higher temperature of 775 °C.[37] The XRD patterns of Mg-ACP after thermal treatment at 600 °C are shown in Figure S2 for comparison. It can be seen that complete transformation of $\alpha$- to $\beta$-TCP occurs even with a lower amount of Mg ions; $\beta$-TCP with a negligible amount of neighboring $\alpha$-TCP was formed already at the doping level of 2.5 mol %.

All of the as-prepared Zn-containing ACPs were confirmed to be amorphous by means of XRD analysis since no diffraction peaks were observed (see Figure S3). The XRD patterns of Zn-ACP annealed at 700 °C are illustrated in Figure 5. The trend in the obtained XRD patterns was similar


https://dx.doi.org/10.1021/acs.cgd.0c01534
Cryst. Growth Des. 2021, 21, 1242−1248

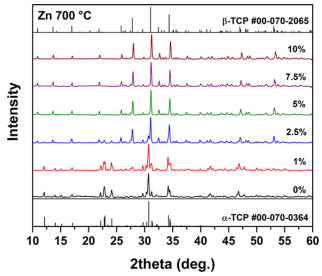


**Figure 5.** XRD patterns of the Zn-ACP powders having different amounts of Zn and annealed at 700 °C.

to that of in the Mg-ACP case. The crystal phase transformation from $\alpha$-TCP to $\beta$-TCP goes hand in hand with an increase in the concentration of Zn ions. However, in this case, the mentioned transition occurs slower in comparison with that in the case of Mg-ACP. The full transformation was observed at a higher substitution level, even for the sample containing 5 mol % of Zn ions, an insignificant amount of $\alpha$-TCP can be detected. Most likely, the phase transition occurs at an intermediate concentration between 5 and 7.5 mol %. However, the principal goal of this study was to investigate the main trends and regularities and not to determine an exact concentration leading to the phase transition; therefore, more precise experiments were not performed. Moreover, this concentration could vary significantly depending on the annealing temperature. The progressive shift of the position of the XRD peaks to higher angles can be also seen for Zn-substituted samples. Moreover, there were no secondary crystal phases detected even for a sample with the highest Zn content, indicating the formation of single-phase $\beta$-TCP.

Figure 6 represents the phase evolution of Zn-ACP substituted with the maximal amount of Zn. Similarly, like in

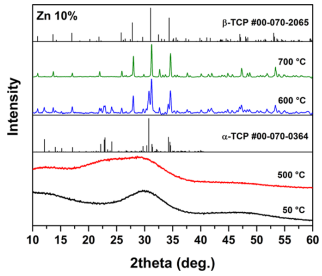


**Figure 6.** XRD patterns of the ACP powders substituted with 10 mol % of Zn and annealed at different temperatures.

the Mg-ACP case (see Figure 4), after the heat treatment at 500 °C, the specimen remains amorphous; however, after annealing at 600 °C, the obtained powders consist of a mixture of two polymorphs. Single-phase $\beta$-TCP is obtained only after annealing at 700 °C. The XRD patterns of Zn-ACP after the thermal treatment at 600 °C are shown in Figure S4 for comparison. It is seen that contrary to Mg-ACP, even the highest Zn substitution level (10 mol %) does not result in the crystallization of the phase-pure $\beta$-TCP, with a significant amount of $\alpha$-TCP is still present after the heat treatment at such temperature.

To summarize the effect of smaller ions, it can be concluded that neither Mg nor Zn lowers the crystallization temperature of ACP. On the other hand, the presence of both Mg and Zn ions promotes the transformation of $\alpha$-TCP and ACP to $\beta$-TCP; however, the effect of these ions is not identical. A smaller amount of Mg ions (compared to the amount of Zn ions) is required to cause the same level of changes in the crystalline phase composition and to shift the thermodynamic equilibrium to $\beta$-TCP. The phase transition from $\alpha$-TCP to $\beta$-TCP can be explained by the difference in the ionic radii between Ca and foreign ions. According to the study performed by Matsunaga et al.,[36] very limited amount of Ca sites in the $\alpha$-TCP crystal structure is suitable for substitution by smaller ions. On the other hand, in the crystal structure of $\beta$-TCP, the Ca(5) site is distinctive for a low defect formation energy of substitutional smaller divalent cations. For this reason, the formation of $\beta$-TCP is more thermodynamically preferable. The possible explanation of the difference in the crystallization of Mg- and Zn-ACP could be related to the size of these ions, which are slightly smaller for Mg. In sixfold coordination, the ionic radii of $Mg^{2+}$ and $Zn^{2+}$ ions are 72 and 74 pm, respectively.[40]

Similarly as for Mg- and Zn-ACP, all of the as-synthesized Sr-ACP were determined to be amorphous independently of the Sr substitution level (see Figure S5). The XRD patterns of the Sr-substituted ACP annealed at 700 °C are displayed in Figure 7. It can be seen that the substitution by $Sr^{2+}$ ions has a

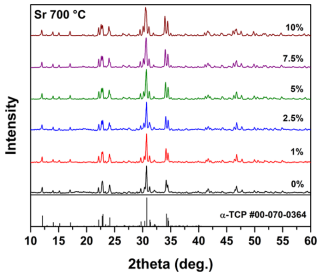


**Figure 7.** XRD patterns of the Sr-ACP powders having different amounts of Sr and annealed at 700 °C.

different effect in comparison with that induced by smaller ions. All samples were identified as $\alpha$-TCP, and no $\beta$-TCP crystal phase was detected even at the highest substitution level of strontium. All diffraction peaks match very well the standard XRD data for monoclinic $Ca_3(PO_4)_2$ (ICDD #00-070-0364). On the other hand, some changes in the XRD patterns induced by the presence of $Sr^{2+}$ ions in the crystal structure can be observed. The width of the most intense reflection peaks monotonically increased with increasing the substitution level. Moreover, the distance between the diffraction peaks located at around 34° gradually increases along with their intensity. A gradual shift of the peaks to lower angles with an increase of the Sr content is caused by a mismatch in the size between Ca and Sr ions.


https://dx.doi.org/10.1021/acs.cgd.0c01534
Cryst. Growth Des. 2021, 21, 1242−1248

Figure 8 illustrates the phase evolution of Sr-ACP substituted with 10 mol % of Sr ions and annealed at different

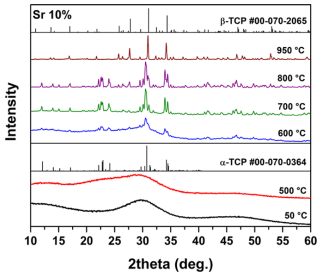


**Figure 8.** XRD patterns of the ACP powders substituted with 10 mol % of Sr and annealed at different temperatures.

temperatures. A notable feature is that Sr ions at such concentration obviously retard the crystallization process. It is seen that after annealing at 600 °C, poorly crystalline $\alpha$-TCP was formed, since the obtained diffraction peaks are very broad and of low intensity. At higher temperatures (700 °C), the degree of crystallinity increases significantly and the phase-pure $\alpha$-TCP was identified. Further increase in the annealing temperature resulted in a gradual phase transformation to $\beta$-TCP, which was obtained in its pure form at 950 °C. It can be concluded that the substitution by Sr ions does not lead to concentration-dependent phase transitions between TCP polymorphs. Moreover, it does not thermally stabilize $\alpha$-TCP, with the phase transition to $\beta$-TCP occurring at the same temperature that was determined for pristine ACP.

The as-prepared ACP substituted with different amounts of Ba ions revealed the same amorphous nature as ACP with other substituents (Figure S5). The XRD patterns of the Ba-substituted CP annealed at 700 °C are displayed in Figure 9.

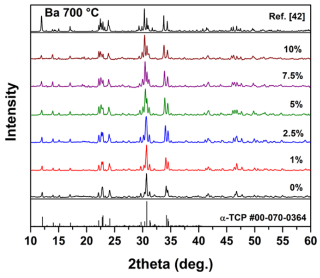


**Figure 9.** XRD patterns of the Ba-ACP powders having different amounts of Ba and annealed at 700 °C.

The observed trend is similar to that induced by Sr ions. For all substitution levels, the $\alpha$-TCP crystal phase was identified, and $\beta$-TCP was not detected in any sample. At the same time, structural changes of $\alpha$-TCP phase can be noticed. However, the evolution of the XRD patterns corresponds to the internal structural changes of $\alpha$-TCP, but not to the formation of secondary crystal phases. For comparison, the XRD pattern of 10 mol % Ba-doped $\alpha$-TCP reported by Yashima and Kawaike[42] was added. These authors performed a detailed study on the crystal structure and the site preference of the Ba-doped $\alpha$-TCP through high-resolution synchrotron powder diffraction. It is seen that the XRD pattern of our synthesized sample matches very well the previously reported data.

Figure 10 shows the XRD patterns of Ba-ACP substituted with 10 mol % Ba ions and annealed at different temperatures.

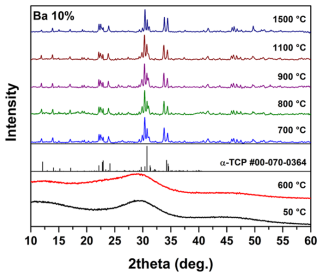


**Figure 10.** XRD patterns of ACP powders substituted with 10 mol % of Ba and annealed at different temperatures.

Unlike in previous cases (see Figures 4, 6, and 8), after annealing at 600 °C, the synthesized powder was still amorphous and crystalline $\alpha$-TCP was obtained only after annealing at 700 °C. Another distinctive feature is that the presence of Ba ions in such concentration stabilizes $\alpha$-TCP and completely prevents the phase transformation to $\beta$-TCP. The obtained sample was annealed at different temperatures up to 1500 °C and no phase transition was detected.

Summarizing the obtained results, it can be concluded that larger ions differently affect crystallization and phase evolution of ACP compared to the effect induced by doping with smaller ions. Both larger ions retard crystallization of ACP and this phenomenon is more obvious for Ba ions (135 pm), which significantly surpass Ca (100 pm) and Sr (118 pm) in size.[40] Moreover, neither Sr nor Ba ions promote the phase transformation to $\beta$-TCP. Contrary, Ba acts as a stabilizer of $\alpha$-TCP; however, the stabilization effect was not observed for Sr ions in the studied concentration range. According to Matsunaga et al.,[36] there are low defect formation energies of substitutional larger cations in the Ca(5) site of the $\alpha$-TCP structure; however, the calculated defect formation energies in the Ca(4) site of $\beta$-TCP are even lower, but the difference is not so significant as in the case of smaller cations. Moreover, there is a large number of Ca sites in $\alpha$-TCP with relatively lower defect formation energies compared to $\beta$-TCP. On the other hand, these calculations do not completely go hand in hand with the experimental data on the Ba-substituted $\alpha$-TCP,[42] since the highest occupancy factors of Ba ions were determined for Ca(17), Ca(11), and Ca(5) sites.

Overall, it can be concluded that the thermally induced crystallization of ACP is strongly influenced by the presence of foreign ions. This effect is dependent both on the nature of substituent ions and substitution level. The key factor determining the formation of a distinct crystalline phase is the ionic radius of the substituents. Due to the peculiarities of the crystal structure of TCP polymorphs, foreign ions having smaller radius shift the thermodynamic equilibrium toward the formation of $\beta$-TCP, while the presence of larger ions leads to


https://dx.doi.org/10.1021/acs.cgd.0c01534
Cryst. Growth Des. 2021, 21, 1242−1248

the formation of $\alpha$-TCP. Our obtained experimental results are in good agreement and confirm the previously performed theoretical calculations.[36] Comparing these data with other reports on the crystallization of amorphous materials in the presence of foreign ions, some similarities and differences can be found. It was demonstrated by Alberic et al. that the presence of Mg ions in amorphous calcium carbonate retards the crystallization process, whereas an increase in the water content accelerates the transformation.[43] On the other hand, like in our case, the presence of Ba ions was shown to inhibit the crystallization of amorphous calcium barium carbonate.[44] Crystallization temperature increased with increasing barium content in the amorphous precursor. The work by Sugiura et al. investigated the influence of alkali metal ions having different sizes on the formation of octacalcium phosphate layered structure.[45] It was found that the nature of the interaction of metal ions with octacalcium phosphate strongly depends on the ionic radius; particularly, large ions exhibited an inhibiting effect on the formation of octacalcium phosphate.

## 4. CONCLUSIONS

This work presented the experimental investigations of crystallization and phase evolution of ACP partially substituted with smaller ($Mg^{2+}$, $Zn^{2+}$) and larger ($Sr^{2+}$, $Ba^{2+}$) divalent cations (M/P = 1.5:1). Crystallization of ACP to TCP and further phase transformations between TCP polymorphs strongly depended on the size and concentration of substituents in the ACP matrix. Two different effects induced by the presence of foreign ions have been outlined. Substitution with smaller ions did not affect the crystallization temperature but promoted the formation of $\beta$-TCP at significantly lower temperatures compared to the phase evolution of pristine ACP. Moreover, the effect of Mg was found to be more significant than that of Zn in the transformation of metastable $\alpha$-TCP to $\beta$-TCP. Substitution with larger ions retarded the crystallization process, which was observed at elevated temperatures. While the substitution level of 10 mol % of Sr did not affect the thermal stability of the metastable $\alpha$-TCP, the presence of 10 mol % of Ba stabilized the $\alpha$-TCP crystal structure and totally prevented the phase transition to $\beta$-TCP.

## ■ ASSOCIATED CONTENT

### Supporting Information

The Supporting Information is available free of charge at https://pubs.acs.org/doi/10.1021/acs.cgd.0c01534.

XRD patterns of the as-prepared ACPs and ACPs annealed at 600 °C (S1–S6). Thermogravimetry-differential scanning calorimetry (TG-DSC) curves of the as-prepared ACP powders (S7) (PDF)

## ■ AUTHOR INFORMATION


### Corresponding Author

**Aleksej Zarkov** – *Institute of Chemistry, Vilnius University, LT-03225 Vilnius, Lithuania;* orcid.org/0000-0002-3574-2296; Email: aleksej.zarkov@chf.vu.lt

### Authors

**Lauryna Sinusaite** – *Institute of Chemistry, Vilnius University, LT-03225 Vilnius, Lithuania*

**Aivaras Kareiva** – *Institute of Chemistry, Vilnius University, LT-03225 Vilnius, Lithuania*

Complete contact information is available at: https://pubs.acs.org/10.1021/acs.cgd.0c01534


### Notes

The authors declare no competing financial interest.

## ■ ACKNOWLEDGMENTS

This project has received funding from the European Social Fund (project No 09.3.3-LMT-K-712-19-0069) under grant agreement with the Research Council of Lithuania (LMTLT).

## ■ REFERENCES


(1) Habraken, W.; Habibovic, P.; Epple, M.; Bohner, M. Calcium phosphates in biomedical applications: materials for the future? *Mater. Today* **2016**, *19*, 69–87.

(2) Eliaz, N.; Metoki, N. Calcium Phosphate Bioceramics: A Review of Their History, Structure, Properties, Coating Technologies and Biomedical Applications. *Materials* **2017**, *10*, 334.

(3) Mayen, L.; Jensen, N. D.; Laurencin, D.; Marsan, O.; Bonhomme, C.; Gervais, C.; Smith, M. E.; Coelho, C.; Laurent, G.; Trebosc, J.; Gan, Z.; Chen, K.; Rey, C.; Combes, C.; Soulié, J. A soft-chemistry approach to the synthesis of amorphous calcium ortho/pyrophosphate biomaterials of tunable composition. *Acta Biomater.* **2020**, *103*, 333–345.

(4) Luginina, M.; Orru, R.; Cao, G.; Grossin, D.; Brouillet, F.; Chevallier, G.; Thouron, C.; Drouet, C. First successful stabilization of consolidated amorphous calcium phosphate (ACP) by cold sintering: toward highly-resorbable reactive bioceramics. *J. Mater. Chem. B* **2020**, *8*, 629–635.

(5) Surmenev, R. A.; Surmeneva, M. A.; Ivanova, A. A. Significance of calcium phosphate coatings for the enhancement of new bone osteogenesis – A review. *Acta Biomater.* **2014**, *10*, 557–579.

(6) Van den Vreken, N. M. F.; Pieters, I. Y.; Declercq, H. A.; Cornelissen, M. J.; Verbeeck, R. M. H. Characterization of calcium phosphate cements modified by addition of amorphous calcium phosphate. *Acta Biomater.* **2010**, *6*, 617–625.

(7) Rubenis, K.; Zemjane, S.; Vecstaudza, J.; Bitenieks, J.; Locs, J. Densification of amorphous calcium phosphate using principles of the cold sintering process. *J. Eur. Ceram. Soc.* **2021**, *41*, 912–919.

(8) Montes-Hernandez, G.; Renard, F. Nucleation of Brushite and Hydroxyapatite from Amorphous Calcium Phosphate Phases Revealed by Dynamic In Situ Raman Spectroscopy. *J. Phys. Chem. C* **2020**, *124*, 15302–15311.

(9) Iijima, M.; Onuma, K. Roles of Fluoride on Octacalcium Phosphate and Apatite Formation on Amorphous Calcium Phosphate Substrate. *Cryst. Growth Des.* **2018**, *18*, 2279–2288.

(10) Niu, X.; Chen, S.; Tian, F.; Wang, L.; Feng, Q.; Fan, Y. Hydrolytic conversion of amorphous calcium phosphate into apatite accompanied by sustained calcium and orthophosphate ions release. *Mater. Sci. Eng. C* **2017**, *70*, 1120–1124.

(11) Wang, X.; Yang, J.; Andrei, C. M.; Soleymani, L.; Grandfield, K. Biomineralization of calcium phosphate revealed by in situ liquid-phase electron microscopy. *Commun. Chem.* **2018**, *1*, No. 80.

(12) Uskoković, V.; Marković, S.; Veselinović, L.; Škapin, S.; Ignjatović, N.; Uskoković, D. P. Insights into the kinetics of thermally induced crystallization of amorphous calcium phosphate. *Phys. Chem. Chem. Phys.* **2018**, *20*, 29221–29235.

(13) Ucar, S.; Bjørnøy, S. H.; Bassett, D. C.; Strand, B. L.; Sikorski, P.; Andreassen, J.-P. Formation of Hydroxyapatite via Transformation of Amorphous Calcium Phosphate in the Presence of Alginate Additives. *Cryst. Growth Des.* **2019**, *19*, 7077–7087.

(14) Yu, M.; Wang, L.; Zhang, W.; Ganss, B. An Evolutionarily Conserved Subdomain in Amelotin Promotes Amorphous Calcium Phosphate-to-Hydroxyapatite Phase Transition. *Cryst. Growth Des.* **2019**, *19*, 2104–2113.

(15) Lotsari, A.; Rajasekharan, A. K.; Halvarsson, M.; Andersson, M. Transformation of amorphous calcium phosphate to bone-like apatite. *Nat. Commun.* **2018**, *9*, No. 4170.

(16) Dorozhkin, S. V.; Epple, M. Biological and medical significance of calcium phosphates. *Angew. Chem., Int. Ed.* **2002**, *41*, 3130−3146.
(17) Combes, C.; Rey, C. Amorphous calcium phosphates: Synthesis, properties and uses in biomaterials. *Acta Biomater.* **2010**, *6*, 3362−3378.
(18) Carrodeguas, R. G.; De Aza, S. α-Tricalcium phosphate: Synthesis, properties and biomedical applications. *Acta Biomater.* **2011**, *7*, 3536−3546.
(19) Mathew, M.; Schroeder, L. W.; Dickens, B.; Brown, W. E. The crystal structure of alpha-$Ca_3(PO_4)_2$. *Acta Crystallogr., Sect. B: Struct. Crystallogr. Cryst. Chem.* **1977**, *33*, 1325−1333.
(20) Frasnelli, M.; Sglavo, V. M. Effect of $Mg^{2+}$ doping on beta-alpha phase transition in tricalcium phosphate (TCP) bioceramics. *Acta Biomater.* **2016**, *33*, 283−289.
(21) Sasidharan Pillai, R.; Sglavo, V. M. Effect of MgO addition on solid state synthesis and thermal behavior of beta-tricalcium phosphate. *Ceram. Int.* **2015**, *41*, 2512−2518.
(22) Brazete, D.; Torres, P. M. C.; Abrantes, J. C. C.; Ferreira, J. M. F. Influence of the Ca/P ratio and cooling rate on the allotropic α↔β-tricalcium phosphate phase transformations. *Ceram. Int.* **2018**, *44*, 8249−8256.
(23) Torres, P. M. C.; Abrantes, J. C. C.; Kaushal, A.; Pina, S.; Döbelin, N.; Bohner, M.; Ferreira, J. M. F. Influence of Mg-doping, calcium pyrophosphate impurities and cooling rate on the allotropic α↔β-tricalcium phosphate phase transformations. *J. Eur. Ceram. Soc.* **2016**, *36*, 817−827.
(24) Qiu, C.; Lu, T.; He, F.; Feng, S.; Fang, X.; Zuo, F.; Jiang, Q.; Deng, X.; Ye, J. Influences of gallium substitution on the phase stability, mechanical strength and cellular response of β-tricalcium phosphate bioceramics. *Ceram. Int.* **2020**, *46*, 16364−16371.
(25) Carbajal, L.; Caballero, A.; Sainz, M. A. Design and processing of ZnO doped tricalcium phosphate based materials: Influence of β/α polymorph phase assemblage on microstructural evolution. *J. Eur. Ceram. Soc.* **2012**, *32*, 569−577.
(26) Carbajal, L.; Serena, S.; Caballero, A.; Saínz, M. A.; Detsch, R.; Boccaccini, A. R. Role of ZnO additions on the β/α phase relation in TCP based materials: Phase stability, properties, dissolution and biological response. *J. Eur. Ceram. Soc.* **2014**, *34*, 1375−1385.
(27) Carbajal, L.; Serena, S.; Sainz, M. A.; Caballero, A. Phase and melting relationships of β, α and α′-$Ca_3(PO_4)_2$ polymorphs in the $Ca_3(PO_4)_2$-$Zn_3(PO_4)_2$ system. *J. Eur. Ceram. Soc.* **2017**, *37*, 2277−2283.
(28) Bandyopadhyay, A.; Petersen, J.; Fielding, G.; Banerjee, S.; Bose, S. ZnO, $SiO_2$, and SrO doping in resorbable tricalcium phosphates: Influence on strength degradation, mechanical properties, and in vitro bone−cell material interactions. *J. Biomed. Mater. Res., Part B* **2012**, *100B*, 2203−2212.
(29) Carrodeguas, R. G.; De Aza, A. H.; Turrillas, X.; Pena, P.; De Aza, S. New Approach to the β→α Polymorphic Transformation in Magnesium-Substituted Tricalcium Phosphate and its Practical Implications. *J. Am. Ceram. Soc.* **2008**, *91*, 1281−1286.
(30) Mestres, G.; Le Van, C.; Ginebra, M.-P. Silicon-stabilized α-tricalcium phosphate and its use in a calcium phosphate cement: Characterization and cell response. *Acta Biomater.* **2012**, *8*, 1169−1179.
(31) Enderle, R.; Götz-Neunhoeffer, F.; Göbbels, M.; Müller, F. A.; Greil, P. Influence of magnesium doping on the phase transformation temperature of β-TCP ceramics examined by Rietveld refinement. *Biomaterials* **2005**, *26*, 3379−3384.
(32) Uskoković, V. Disordering the Disorder as the Route to a Higher Order: Incoherent Crystallization of Calcium Phosphate through Amorphous Precursors. *Cryst. Growth Des.* **2019**, *19*, 4340−4357.
(33) Somrani, S.; Rey, C.; Jemal, M. Thermal evolution of amorphous tricalcium phosphate. *J. Mater. Chem.* **2003**, *13*, 888−892.
(34) Döbelin, N.; Brunner, T. J.; Stark, W. J.; Fisch, M.; Conforto, E.; Bohner, M. Thermal treatment of flame-synthesized amorphous tricalcium phosphate nanoparticles. *J. Am. Ceram. Soc.* **2010**, *93*, 3455−3463.
(35) Sinusaite, L.; Renner, A. M.; Schuetz, M. B.; Antuzevics, A.; Rogulis, U.; Grigoraviciute-Puroniene, I.; Mathur, S.; Zarkov, A. Effect of Mn doping on the low-temperature synthesis of tricalcium phosphate (TCP) polymorphs. *J. Eur. Ceram. Soc.* **2019**, *39*, 3257−3263.
(36) Matsunaga, K.; Kubota, T.; Toyoura, K.; Nakamura, A. First-principles calculations of divalent substitution of $Ca^{2+}$ in tricalcium phosphates. *Acta Biomater.* **2015**, *23*, 329−337.
(37) Sinusaite, L.; Grigoraviciute-Puroniene, I.; Popov, A.; Ishikawa, K.; Kareiva, A.; Zarkov, A. Controllable synthesis of tricalcium phosphate (TCP) polymorphs by wet precipitation: Effect of washing procedure. *Ceram. Int.* **2019**, *45*, 12423−12428.
(38) Bigi, A.; Foresti, E.; Gandolfi, M.; Gazzano, M.; Roveri, N. Isomorphous substitutions in β-tricalcium phosphate: The different effects of zinc and strontium. *J. Inorg. Biochem.* **1997**, *66*, 259−265.
(39) Araújo, J. C.; Sader, M. S.; Moreira, E. L.; Moraes, V. C. A.; LeGeros, R. Z.; Soares, G. A. Maximum substitution of magnesium for calcium sites in Mg-β-TCP structure determined by X-ray powder diffraction with the Rietveld refinement. *Mater. Chem. Phys.* **2009**, *118*, 337−340.
(40) Shannon, R. D. Revised effective ionic radii and systematic studies of interatomic distances in halides and chalcogenides. *Acta Crystallogr., Sect. A* **1976**, *32*, 751−767.
(41) Maciejewski, M.; Brunner, T. J.; Loher, S. F.; Stark, W. J.; Baiker, A. Phase transitions in amorphous calcium phosphates with different Ca/P ratios. *Thermochim. Acta* **2008**, *468*, 75−80.
(42) Yashima, M.; Kawaike, Y. Crystal Structure and Site Preference of Ba-Doped α-Tricalcium Phosphate $(Ca_{1-x}Ba_x)_3(PO_4)_2$ through High-Resolution Synchrotron Powder Diffraction (x = 0.05 to 0.15). *Chem. Mater.* **2007**, *19*, 3973−3979.
(43) Albéric, M.; Bertinetti, L.; Zou, Z.; Fratzl, P.; Habraken, W.; Politi, Y. The Crystallization of Amorphous Calcium Carbonate is Kinetically Governed by Ion Impurities and Water. *Adv. Sci.* **2018**, *5*, No. 1701000.
(44) Whittaker, M. L.; Sun, W.; DeRocher, K. A.; Jayaraman, S.; Ceder, G.; Joester, D. Structural Basis for Metastability in Amorphous Calcium Barium Carbonate (ACBC). *Adv. Funct. Mater.* **2018**, *28*, No. 1704202.
(45) Sugiura, Y.; Saito, Y.; Endo, T.; Makita, Y. Effect of the Ionic Radius of Alkali Metal Ions on Octacalcium Phosphate Formation via Different Substitution Modes. *Cryst. Growth Des.* **2019**, *19*, 4162−4171.

Article VI

**Fe and Zn co-substituted beta-tricalcium phosphate (β-TCP): Synthesis, structural, magnetic, mechanical and biological properties**

L. Sinusaite, A. Popov, A. Antuzevics, K. Mazeika, D. Baltrunas, J.- C. Yang, J.L. Horng, S. Shi, T. Sekino, K. Ishikawa, A. Kareiva, A. Zarkov

*Materials Science and Engineering: C,* 112 (2020) 110918

Materials Science & Engineering C 112 (2020) 110918

Contents lists available at ScienceDirect

Materials Science & Engineering C

journal homepage: www.elsevier.com/locate/msec

# Fe and Zn co-substituted beta-tricalcium phosphate (β-TCP): Synthesis, structural, magnetic, mechanical and biological properties

Lauryna Sinusaite[a], Anton Popov[a,b], Andris Antuzevics[c], Kestutis Mazeika[d], Dalis Baltrunas[d], Jen-Chang Yang[e], Jiun Lin Horng[f], Shengfang Shi[g], Tohru Sekino[g], Kunio Ishikawa[h], Aivaras Kareiva[a], Aleksej Zarkov[a,g,*]

[a] Institute of Chemistry, Vilnius University, Naugarduko 24, LT-03225 Vilnius, Lithuania
[b] Department of Immunology, State Research Institute Centre for Innovative Medicine, Santariskiu 5, LT-08406 Vilnius, Lithuania
[c] Institute of Solid State Physics, University of Latvia, Kengaraga 8, LV-1063 Riga, Latvia
[d] State Research Institute Center for Physical Sciences and Technology, Vilnius LT-02300, Lithuania
[e] Graduate Institute of Nanomedicine and Medical Engineering, College of Biomedical Engineering, Taipei Medical University, 250 Wu-Hsing St, Taipei 11052, Taiwan
[f] Department of Anatomy and Cell Biology, Taipei Medical University, 250 Wu-Hsing St, Taipei 11052, Taiwan
[g] The Institute of Scientific and Industrial Research, Osaka University, 8–1 Mihogaoka, Ibaraki, Osaka 567–0047, Japan
[h] Department of Biomaterials, Faculty of Dental Science, Kyushu University, Maidashi, Higashi-Ku, Fukuoka, Japan

ARTICLE INFO

*Keywords:*
Beta-tricalcium phosphate
$Fe^{3+}$ and $Zn^{2+}$ co-substitution
Structural analysis
Magnetic properties
Cytotoxicity

ABSTRACT

In the present work, $Fe^{3+}$ and $Zn^{2+}$ co-substituted β-tricalcium phosphate (β-TCP) has been synthesized by wet co-precipitation method. Co-substitution level in the range from 1 to 5 mol% has been studied. Thermal decomposition of as-prepared precipitates was shown to be affected by introducing of foreign ions, decreasing the decomposition temperature of precursor. It was determined that partial substitution of $Ca^{2+}$ by $Fe^{3+}$ and $Zn^{2+}$ ions leads to the change in lattice parameters, which gradually decrease as doping level increases. Lattice distortion was also confirmed by means of Raman spectroscopy, which showed gradual change of the peaks shape in the Raman spectra. Rietveld refinement and electron paramagnetic resonance study confirmed that $Fe^{3+}$ ions occupy only one Ca crystallographic site until $Fe^{3+}$ and $Zn^{2+}$ substitution level reaches 5 mol%. All co-substituted samples revealed paramagnetic behavior, magnetization of powders was determined to be linearly dependent on concentration of $Fe^{3+}$ ions. Cytotoxicity of the synthesized species was estimated by *in vivo* assay using zebrafish (*Danio rerio*) and revealed non-toxic nature of the samples. Preparation of ceramic bodies from the powders was performed, however the results obtained on Vickers hardness of the ceramics did not show improvement in mechanical properties induced by co-substitution.

## 1. Introduction

Calcium phosphates (CPs) are the main inorganic part of biological hard tissues such as bones or teeth and play an essential role in human life. This reason makes synthetic CPs widely used in medicine for repair and reconstruction of diseased or damaged parts of bone. For these purposes CPs can be used in different forms varying from thin coatings on metallic implants, used to aid implant fixation into bone, to sintered bioceramics, to be used as synthetic bone graft substitutes [1–3]. Despite the fact that inorganic part of bones mainly consists of calcium hydroxyapatite (HAp, $Ca_{10}(PO_4)_6(OH)_2$), other CPs are also widely used for biomedical purposes. One of the CPs most frequently used for the fabrication of bioceramics is tricalcium phosphate (TCP, $Ca_3(PO_4)_2$), which attracts practical interest due to several reasons such as excellent biocompatibility, osteoconductivity and chemical composition similar to natural bone [4]. Low-temperature β-TCP polymorph crystallizes in the rhombohedral crystal system with the space group R3c [5]. For the fabrication of biodegradable bioceramics it is usually used in its pure form or as a mixture with HAp, resulting in biphasic calcium phosphate bioceramics [6].

Partial substitution of Ca by other biologically active ions has been proposed as a promising tool to the superior biological performance of CP-based materials [7]. Chemical modification can drastically affect physicochemical, mechanical and anti-bacterial properties of materials, to cause changes in morphology, density, solubility and ion release kinetics [8]. Importance of this approach has been underlined in a

* Corresponding author at: Institute of Chemistry, Vilnius University, Naugarduko 24, LT-03225 Vilnius, Lithuania.
*E-mail address:* aleksej.zarkov@chf.vu.lt (A. Zarkov).

https://doi.org/10.1016/j.msec.2020.110918
Received 3 December 2019; Received in revised form 14 March 2020; Accepted 31 March 2020
Available online 03 April 2020

number of recent reviews [9–11]. Substitution-induced properties allow to combine biocompatibility of CPs with newly obtained properties resulting in application of these materials in new areas such as various imaging modalities including fluorescence, magnetic resonance or multimodal imaging, as well as for various therapeutic approaches including chemotherapy, gene therapy, hyperthermia or combination therapy [12].

Despite the fact that different CPs have been reported to be substituted with a huge variety of ions, co-doping of CPs still remains relatively new approach. Since substitution with single ions opens so many horizons for new applications, it makes sense to use multielement substitution for the synergistic effect or multifunctioning of CP-based materials [12,13]. The synthesized nanocrystalline CP phases co-substituted with different cations exhibited osteogenic and antibacterial ability and demonstrated enhanced biological effects [14–16]. The obtained results suggested potential future applications as new smart biomaterials integrating a significant boosting of bone regeneration with adequate protection against bacteria.

In the present work, $Fe^{3+}$ and $Zn^{2+}$ were chosen due to the significant performance enhancement that these elements can deliver. Fe is an essential element for human and animals. It can be found in the structure of many enzymes, which are involved in oxygen transport, electron transport, oxidation-reduction and other biological processes in human body [17]. Moreover, as a trace element Fe is also present in natural bones and teeth [18]. Additional interest Fe causes because of its magnetic properties. Previous studies demonstrated that partial substitution of Ca by Fe ions in synthetic CPs can result in materials with multifunctional properties. Superparamagnetic Fe-doped CPs were successfully utilized *in vivo* as imaging agents for magnetic resonance and nuclear imaging [19]. Moreover, feasibility of application of $Fe^{3+}$-doped HAp and Fe oxide nanoparticles coated with amorphous CP for the intracellular hyperthermia of cancers of bone and brain has been shown [20]. Another work demonstrated that Fe-doped HAp could be used as functional nano-carriers for the magnetically assisted delivery of bioactive molecules [21]. Zinc in its turn is the second most abundant trace element in the human body, which is required for the functioning of many enzymes [22]. Zn-containing CPs have shown enhanced bioactivity and promotion of growth of adipose-derived mesenchymal stem cells [23]. Moreover, antibacterial properties of Zn-substituted CPs were reported in a number of previous works showing inhibitory effect towards pathogenic microorganisms [24–26].

The successful incorporation of $Sr^{2+}$ together with $Zn^{2+}$ ions into the HAp structure was demonstrated in [27,28]. $Ag^{+}$ and $Zn^{2+}$ ions were co-doped with beta-tricalcium phosphate (AgZn-TCP) [29]. Cu/Zn ions co-substituted biphasic calcium phosphate scaffolds showed improved angiogenesis and osteogenesis properties [30]. Similar biological behavior and physical properties showed $Sr^{2+}$ and $Fe^{3+}$ co-substituted HAp [31,32]. Additionally, these nanoparticles demonstrated high blood compatibility with high *in vitro* bioactivity performance. The substitution effects of Fe and Mn into the HAp and TCP has been investigated by several authors [33–35]. Haemolytic and cytotoxicity tests confirmed the biocompatibility of the synthesized specimens. Next, the fabricated Ce-HAp-$Fe_3O_4$ nanocomposites exhibited the excellent pathogen inhibition towards *Escherichia coli* [36]. The multifunctional properties of synthesized co-substituted CPs and HAp nanoparticles make them a potential candidate for various biomedical applications, including bone grafting and guided bone regeneration, targeted drug delivery, magnetic resonance imaging, and hyperthermia based cancer treatment.

However, the dual substitution using only two $Zn^{2+}$ and $Fe^{3+}$ ions in β-TCP was not investigated yet. The main goal of the present work was to develop synthetic approach and comprehensively characterize β-TCP bioceramics with magnetic and biological properties. Due to these reasons β-TCP partially substituted with $Fe^{3+}$ and $Zn^{2+}$ ions was chosen and series of products with different substitution level was investigated in detail.

## 2. Materials and methods

### 2.1. Synthesis

β-TCP powders substituted with equal amounts of $Fe^{3+}$ and $Zn^{2+}$ ions were synthesized by simple co-precipitation method. Series of compounds containing $Fe^{3+}$ and $Zn^{2+}$ ions in the range from 0 to 5 mol % with a step of 1 mol% were studied in the present work. For the synthesis calcium nitrate tetrahydrate ($Ca(NO_3)_2 \cdot 4H_2O$, ≥99%, Roth), iron(III) nitrate nonahydrate ($Fe(NO_3)_3 \cdot 9H_2O$, ≥98%, Alfa Aesar), zinc(II) nitrate hexahydrate ($Zn(NO_3)_2 \cdot 6H_2O$, ≥98%, Chempur) and diammonium hydrogen phosphate ($(NH_4)_2HPO_4$, ≥98%, Roth) were used as starting materials. Firstly, an appropriate amount of $(NH_4)_2HPO_4$ was dissolved in deionized water to obtain a 0.5 M solution, to which concentrated ammonia solution ($NH_4OH$, 25%, Roth) was added under constant stirring, pH of the obtained solution was adjusted to 9. Next, an aqueous solution containing appropriate amounts of Ca, Fe and Zn nitrates (total metal ions concentration was 0.75 M) was rapidly added to the above mixture resulting in the instantaneous formation of precipitates. The obtained precipitates were stirred in the reaction mixture for 10 min, afterwards filtered, washed with deionized water and dried at 50 °C overnight in the oven. Finally, dry powders were ground in agate mortar and annealed in a furnace at 800 °C temperature for 5 h in air atmosphere with a heating rate of 5 °C/min. For the preparation of β-TCP ceramics polyvinyl alcohol was used as a binder. Powders were uniaxially pressed in 15 mm die using cold isostatic pressing at 200 MPa and sintered at 1100 °C for 5 h in air atmosphere.

### 2.2. Characterization

Thermal decomposition of the as-prepared precipitates was analyzed through thermogravimetric (TG) analysis using Perkin Elmer STA 6000 Simultaneous Thermal Analyzer. Dried samples of about 10 mg were heated from 25 to 900 °C with a heating rate of 10 °C/min in a dry flowing air (20 mL/min). Powder X-ray diffraction analysis was performed using Ni-filtered Cu Kα radiation on Rigaku MiniFlex II diffractometer working in Bragg-Brentano (θ/2θ) geometry. The data were collected within 2θ range from 10 to 110° at a step width of 0.01° and speed of 1°/min. Lattice parameters were refined by the Rietveld method using the FullProf suite in the profile matching mode. Fourier transform infrared spectra (FTIR) were taken in the range of 4000–400 $cm^{-1}$ with Bruker ALPHA ATR spectrometer with 4 $cm^{-1}$ resolution. Raman spectra were recorded at room temperature using combined Raman and scanning near field optical microscope (SNOM) WiTec Alpha 300 R equipped with 532 nm excitation laser source. Morphological features of the synthesized products were analyzed with a Hitachi SU-70 field-emission scanning electron microscope (FE-SEM). Quantitative elemental analysis of the samples using Perkin Elmer Optima 7000DV inductively coupled plasma optical emission spectrometer (ICP-OES). The analyzed powders were dissolved in nitric acid ($HNO_3$, Rotipuran® Supra 69%, Carl Roth) and diluted with deionized water. Ion release experiment was carried out by soaking 0.2 g of β-TCP powders at 37 °C in 10 mL of simulated body fluid (SBF) prepared according to Kokubo et al. [37]. Concentrations of ions in SBF ($Na^{+}$ – 142, $K^{+}$ – 5.0, $Ca^{2+}$ – 2.5, $Mg^{2+}$ – 1.5, $Cl^{-}$ – 148.8, $HPO_4^{-}$ – 1.0, $HCO_3^{2-}$ – 4.2, $SO_4^{2-}$ – 0.5 mM, pH = 7.3) were nearly equivalent to those of human blood plasma. The amount of Fe and Zn ions released from β-TCP samples was determined by ICP-OES, every sample was analyzed in triplicate. Room temperature electron paramagnetic resonance (EPR) spectra were measured with Bruker ELEXSYS-II E500 CW-EPR spectrometer. Power of 9.46 GHz microwaves was set at 0.6325 mW. The magnetic field was modulated at 100 kHz with 0.4 mT modulation amplitude. EPR signal intensities have been normalized to the sample mass. Dependence of magnetization of samples on the strength of magnetic field were recorded using magnetometer

consisting of the lock-in amplifier SR510 (Stanford Research Systems), the gauss/teslameter FH-54 (Magnet Physics) and the laboratory magnet supplied by the power source SM 330-AR-22 (Delta Elektronika). Mössbauer spectra were measured in transmission geometry using $^{57}$Co(Rh) source and Mössbauer spectrometer (Wissenschaftliche Elektronik GmbH) at room temperature and low temperature (> 10 K) applying closed cycle He cryostat (Advanced Research Systems). Density of the sintered pellets was measured by Archimedes' method in water. Vickers hardness of the prepared β-TCP ceramics was measured using Future-Tech Vickers hardness tester FV-310e. Ten indentations of a single load of 1 kg (9.8 N) and holding time of 15 s were used for the pellets of each composition.

### 2.3. Zebrafish embryo toxicity assay

No license is required if the zebrafish embryos used < 5 days old under the European Union, Directive 2010/63/EU (revised from Directive 86/609/EEC) [38]. To evaluate acute toxicity and developmental defects of specimens, zebrafish embryos were exposed to solutions containing 1 wt% of various Fe:Zn co-substituted β-TCP powders under temperature of 28 °C, while E3 medium (5 mM NaCl, 0.17 mM KCl, 0.33 mM $CaCl_2$, and 0.33 mM $MgSO_4$) was used for the control group. Fertilized wild-type zebrafish (*Danio rerio*) eggs 1 h post fertilization (1 hpf) were pipetted into polystyrene Petri dishes (35 mm × 10 mm, sterile, stackable, Fisher Scientific) with 10 embryos per plate ($N$ = 10) and the data were recorded at representative stages (24, 48, and 72 hpf). The survivability and conditions of the embryos were captured under a light microscope (Olympus SZX16, Shinjuku-ku, Tyoko, Japan) and a digital camera (Canon EOS 550D, Ohta-ku, Tokyo, Japan) under 40× and 100× magnifications. Percentage survival of the embryos was evaluated and scored for lethal or teratogenic effects.

## 3. Results and discussion

Thermogravimetric analysis (TG/DTG) of pristine and Fe-Zn co-substituted as-prepared precipitates was performed in order to investigate thermal behavior of precursor powders and estimate minimal required annealing temperature. TG/DTG curves corresponding to non-substituted sample and co-substituted sample with the highest content of Fe and Zn ions are shown in Fig. 1 as representative. It is seen that for both samples thermal decomposition occurs in a very similar way, however it is obvious that presence of foreign ions reduces final decomposition temperature of precursors. For pristine precipitates residual mass is constant at above 775 °C, whereas for substituted sample

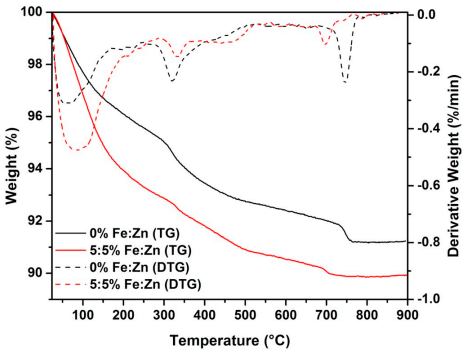


**Fig. 1.** TG/DTG curves of dried as-prepared precipitates with 0 and 5:5 mol% of Fe and Zn.

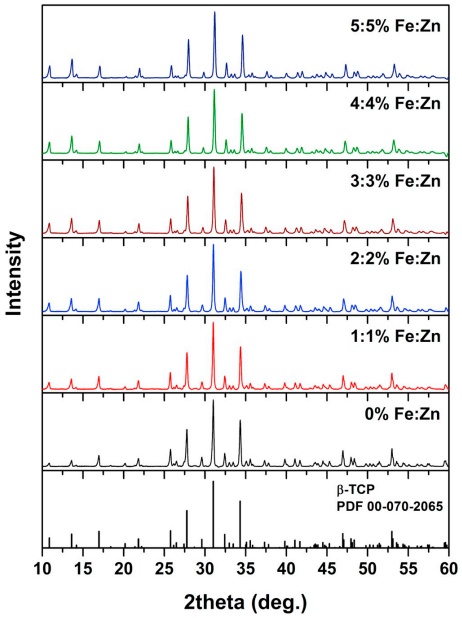


**Fig. 2.** XRD patterns of TCP powders with different amounts of Fe and Zn.

this temperature is lowered by approximately 50 °C, which is clearly seen from DTG curves. Total weight loss, attributed to the removal of adsorbed and crystalline water and possible residuals of ammonium nitrate, was determined to be 8.8 and 10% for pure and substituted precipitates, respectively. Based on the results of thermal analysis an identical annealing temperature of 800 °C was chosen for all samples.

The phase crystallinity and purity of annealed powders were characterized by XRD analysis. The XRD patterns of β-TCP samples containing different amounts of substituent ions and annealed at 800 °C are given in Fig. 2. Regardless of chemical composition all synthesized products crystallized to β-TCP phase. All diffraction peaks match very well standard XRD data of rhombohedral $Ca_3(PO_4)_2$ (ICDD 00-070-2065) and no reflections assigned to potential secondary crystal phases such as Fe or Zn phosphates were detected. Closer look at the diffraction patterns reveals gradual shift of diffraction peaks towards higher 2θ values. Displacement of the particular peak is illustrated in Fig. S1 as representative. Such changes in the XRD patterns are explained by the mismatch in size between Ca and foreign ions and can be considered as an evidence of successful incorporation of substituent ions into β-TCP crystal lattice. Ionic radius of $Ca^{2+}$ in six-fold coordination is 100 pm, and ionic radii of both $Fe^{3+}$ and $Zn^{2+}$ ions are significantly smaller – 65 and 74 pm, respectively [39]. Dependence of calculated lattice parameters on substitution level in β-TCP powders is depicted in Fig. 3. It is evident that lattice parameters a and b gradually decrease as substitution level increases. The decrease is linear, what is in line with $R^2$ values of linear fit of experimental data being close to unity. Slightly different behavior was observed for parameter c, which shows linear decrease only for samples with Fe and Zn content level ranged from 1 to 5 mol%, while parameter c of pristine β-TCP is out of this trend. This suggests that initially cell volume reduces mostly due to the changes of crystal lattice in a and b directions. Similar change in lattice parameter c was

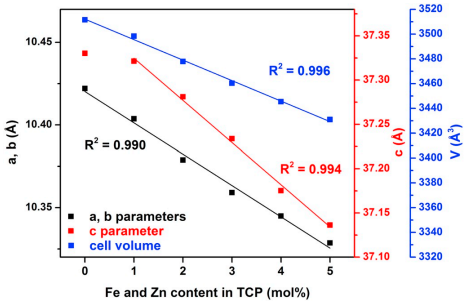


**Fig. 3.** Lattice parameters of TCP powders with different amounts of Fe and Zn.

previously reported by Mellier et al. for Ga-substituted β-TCP [40]. Rietveld refinement showed that foreign ions preferably occupy Ca(5) site in crystal lattice up to 4 mol% co-substitution level. Occupation of this site is in good agreement with previously reported theoretical and experimental studies on substituted β-TCP, which is characterized by low defect formation energies for small guest cations on octahedral Ca (5) site [41–43]. With the highest substitution level part of foreign ions also occupy Ca(4) site, which is also in good agreement with previously reported data for highly doped β-TCP [35,44].

Vibrational spectroscopy was also employed to investigate the effect of substitution and check the presence of neighboring amorphous or crystalline materials, which are hardly detectable by XRD analysis in the presence of major β-TCP phase. Raman spectra of the synthesized β-TCP powders are depicted in Fig. 4. Four main groups of signals are clearly seen for all analyzed compounds. All obtained spectra are dominated by $\nu_1$ vibration mode located in the range of 930–1000 $cm^{-1}$. Other groups are seen in the range of approximately 385–500, 540–655 and 1015–1130 $cm^{-1}$ and attributed to $\nu_2$, $\nu_4$, and $\nu_3$ modes, respectively [45,46]. It is obvious that shape of Raman spectra gradually changes as content of Fe and Zn ions increases. The splitted peak assigned to $\nu_1$ vibration mode for highly substituted samples is broadened and transformed into the single peak indicating lattice distortion induced by incorporation of foreign ions. Other signals with increase of substitution level also lose their well-defined shape and

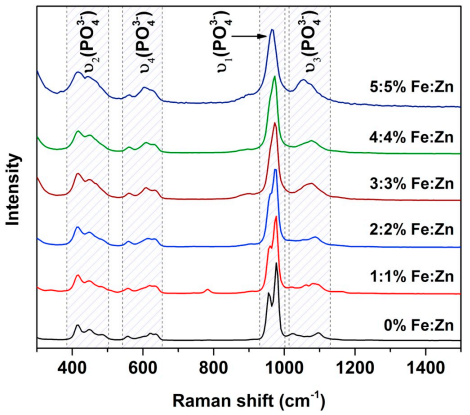


**Fig. 4.** Raman spectra of TCP powders with different amounts of Fe and Zn.

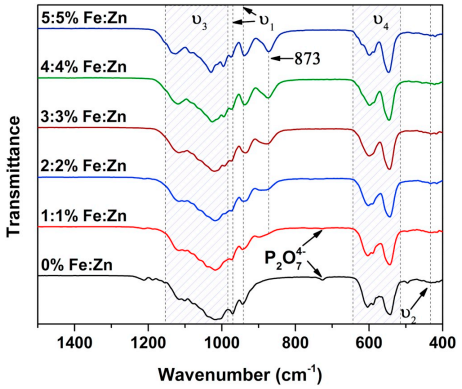


**Fig. 5.** FTIR spectra of TCP powders with different amounts of Fe and Zn.

became broadened. Week signal at around 785 $cm^{-1}$ is assigned to calcium pyrophosphate secondary phase, which is frequently found as an impurity in β-TCP powders prepared by precipitation method [47,48].

Fig. 5 shows FTIR spectra of the synthesized powders. The wavenumber range of 1500–400 $cm^{-1}$ was selected to demonstrate the absorption bands of representative functional groups. All FTIR spectra show vibrational modes characteristic to phosphate groups in β-TCP crystal structure. Four groups of absorption bands are clearly visible and distinguishable. Broad bands located at 1150–990 and 645–515 $cm^{-1}$ are assigned to phosphate $\nu_3$ stretching mode and $\nu_4$ bending mode, respectively. Two absorption bands located at 970 and 940 $cm^{-1}$ are ascribed to $\nu_1$ mode and weak absorption band centered at around 432 $cm^{-1}$ corresponds to $\nu_2$ mode [45]. Additional weak absorption band located at 729 $cm^{-1}$ was observed in FTIR spectra of pristine β-TCP and β-TCP substituted with 1 mol% of foreign ions, however it is not seen in FTIR spectra of the samples with higher substitution level. This band corresponds to $P_2O_7^{4-}$ group and confirms the presence of negligible amount of calcium pyrophosphate [49]. Another clearly visible band can be seen at 873 $cm^{-1}$. Appearance of this signal is obviously caused by substitution of Ca by foreign ions, since intensity of this band monotonically increases as substitution level increases. Similar absorption band was previously observed in FTIR spectra of other substituted β-TCP powders [40,43,50]. In order to figure out which particularly foreign ion is responsible for the appearance of this band, TCP powders substituted with single $Fe^{3+}$ and $Zn^{2+}$ ions were synthesized. The above-mentioned absorption band was absent in FTIR spectrum of 10 mol% Zn-substituted β-TCP, however it was clearly visible for Fe-substituted sample (see Fig. S2). These observations allow to conclude that this absorption band is induced by presence of $Fe^{3+}$ ions. According to previous studies it could be attributed to $HPO_4^{2-}$ group [51].

Deviation of the actual chemical composition of final products from the target stoichiometry is a well-known issue for the synthesis of multicomponent compounds by co-precipitation method. In order to confirm chemical composition of the synthesized powders, elemental analysis by means of ICP-OES was performed. The results of the analysis are summarized in Table 1.

Determined molar percentage of the substituents is in good agreement with nominal values and monotonically increases as theoretical substitution level increases. On the other hand, there is a notable trend that for all samples amount Fe is regularly lower than theoretical, however, this mismatch is not significant and does not exceed 10%. In

**Table 1**
Results of the elemental analysis of the samples performed by ICP-OES.

| Sample | $\frac{n(Zn) \cdot 100\,\%}{n(Ca + Zn + Fe)}$ | $\frac{n(Fe) \cdot 100\,\%}{n(Ca + Zn + Fe)}$ |
|---|---|---|
| 1:1% Fe:Zn | 1.03 | 0.966 |
| 2:2% Fe:Zn | 1.93 | 1.81 |
| 3:3% Fe:Zn | 3.27 | 2.86 |
| 4:4% Fe:Zn | 4.01 | 3.71 |
| 5:5% Fe:Zn | 5.26 | 4.68 |

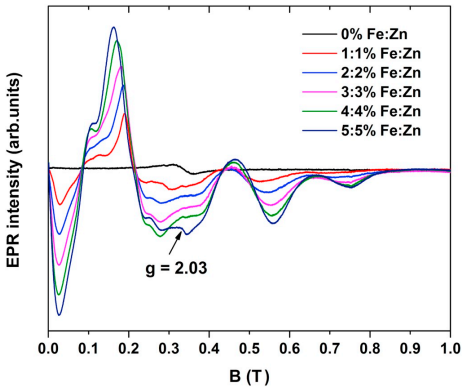


**Fig. 6.** EPR spectra of TCP powders with different amounts of Fe and Zn.

combination with XRD, Raman and FTIR data, elemental analysis indicates that suggested synthetic approach is suitable for the preparation of Fe and Zn co-substituted β-TCP powders with good phase purity and controllable composition.

Room temperature EPR spectra of the investigated samples are depicted in Fig. 6. A relatively low intensity Lorentzian-shape signal with peak-to-peak linewidth of around 50 mT centered at $g \approx 2.00$ is present in the spectrum of non-substituted sample. It indicates the presence of a small amount of paramagnetic centers, which are not related to $Fe^{3+}$ impurities. Moreover, Zn only containing β-TCP powders did not reveal any EPR signals different from that arose from pristine β-TCP. The Fe-containing samples expectedly exhibited EPR spectra characteristic to $Fe^{3+}$ in the high spin $S = 5/2$ state. Therefore, in addition to the Zeeman effect, zero field splitting (ZFS) of the ground state is also expected. When magnitude of ZFS is comparable to the Zeeman term, it is reflected in an EPR signal, which spans a wide magnetic field range [52]. EPR signal intensities scale with Fe content in the samples, which suggests that regardless of the substitution level $Fe^{3+}$ is the preferable charge state in this matrix. The shape of the signal becomes broader and there is a systematic shift in the major peak position as the Fe content increases. The additional broadening is most likely a consequence of increased dipole-dipole interactions of nearby paramagnetic centers [53]. The EPR resonance positions of high $S$ systems are determined by the values of ZFS parameters, therefore a shift in peaks of powder spectra indicates variations in the parameter values and their distributions [54]. This, in turn, implies concentration-dependent distortions in the $Fe^{3+}$ local structure from site to site, which could be associated with slight changes in Fe—O distances and bond angles as well

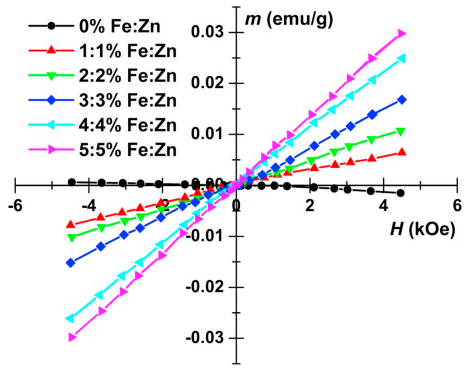


**Fig. 7.** Magnetization dependence on magnetic field strength for TCP powders with different amounts of Fe and Zn.

as increased long-range disorder in the β-TCP crystal structure. No significant changes are observed in the relative intensities of the spectral features up to 5 mol% co-substitution. It indicates that $Fe^{3+}$ ions either occupy one unique position in the crystal structure or are distributed across several site positions in similar proportions regardless of $Fe^{3+}$ content. Taking into account previous investigations, which suggested that incorporation of $Fe^{3+}$ ions in β-TCP occurs *via* substitution in Ca(5) and Ca(4) sites of the crystal lattice [55,56] and results of XRD analysis, the most plausible explanation is that the observed EPR signals originate from $Fe^{3+}$ ions in the Ca(5) position. An additional weaker signal at $g \approx 2.03$ can be observed in the sample with 5 mol% substitution level and could be related to $Fe^{3+}$ ions substituting $Ca^{2+}$ ions in Ca(4) position, however at high doping levels formation of more complicated paramagnetic structures cannot be ruled out. Recent studies of Fe-doped β-TCP system [35,43] have presented EPR spectra, which consisted of two major features located at $g = 4.27$ and 2.08. The reported spectra bear resemblance to $Fe^{3+}$ EPR spectra in glasses [57–59] and are quite different from our obtained results. While it is difficult to comment on the specifics of the spectra, it clearly demonstrates that incorporation of $Fe^{3+}$ ions in the β-TCP structure is sensitive to the substitution level as well as synthesis conditions.

Room temperature dependence of magnetization of β-TCP powders of all compositions on applied magnetic field strength is illustrated in Fig. 7. Different magnetic behavior of β-TCP samples depending on the presence of foreign ions is evident. Pristine sample shows weak diamagnetic properties, which is in agreement with previously reported data on magnetic properties of undoped HAp and β-TCP [60–62]. Different behavior is observed for Fe and Zn-containing powders, which clearly exhibit paramagnetic behavior. Magnetization values are linearly proportional to applied magnetic field strength, moreover magnetization obviously increases as Fe content in the samples increases. No saturation of magnetization was observed regardless of chemical composition of the samples in studied magnetic field range.

Mössbauer spectra of selected Fe-containing β-TCP samples measured at different temperatures and magnetic fields are presented in Fig. 8. Broadened magnetic structure of Mössbauer spectra shows that $Fe^{3+}$ spins experience dynamics, which characteristic time is within $10^{-7}$–$10^{-9}$ s time range, where Mössbauer spectroscopy is sensitive to

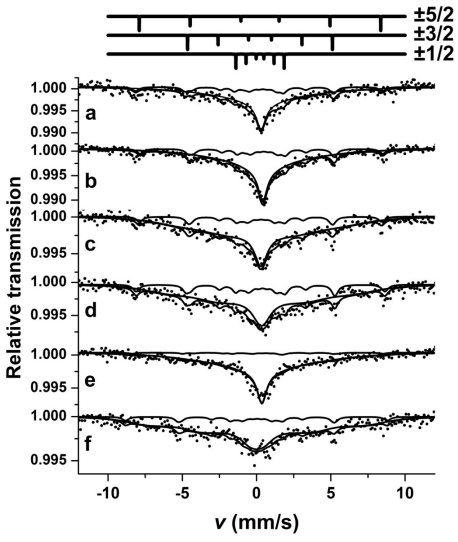


**Fig. 8.** Mössbauer spectra of 5:5% Fe:Zn-TCP (a,b,c), 4:4% Fe:Zn-TCP (d), 3:3% Fe:Zn-TCP (e), 5:5% Fe:Zn-TCP measured at 11 K (a) and room temperature (b-f) at applied magnetic field $B = 0$ T (a,b,e) and $B = 0.42$ T (c,d,f).

hyperfine interactions changes. Hyperfine magnetic structure of Mössbauer spectra of paramagnetic $Fe^{3+}$ is observed when paramagnetic ions are diluted [63]. It was observed that Mössbauer spectra of β-TCP samples at low temperature and room temperature are quite similar. The shape of Mössbauer spectra can be explained by the influence of spin-spin relaxation which has weak dependence on temperature whereas the spin-lattice relaxation is obviously temperature-dependent.

$Fe^{3+}$ spin Hamiltonian is a sum of contributions of interactions with crystal field, Zeeman interaction with magnetic field, and magnetic dipole interactions [63]. Exchange interactions between spins which could result in the magnetic ordering are not present when Fe ions are diluted in a non-magnetic matrix. The application of magnetic field may have considerable influence on spectra and can help to simplify the analysis of Mössbauer spectra if the interaction with magnetic field would become stronger than with existing crystal field. However, the applied magnetic field of 0.42 T (perpendicularly the gamma rays) was not sufficient to fully distinguish the magnetic structure of Mössbauer spectra.

Influence of relaxation on Mössbauer spectra was expressed in simplified form using multistate relaxation model [64,65] when nuclear Hamiltonian is diagonal for all stochastic spin states considering that magnetic hyperfine interaction is much stronger than quadrupole one. The line shape was separately expressed for each nuclear transition defining the static line positions of spectrum $v_i$:

$$I(\omega) = 2\,\mathrm{Re}(\mathbf{P}\cdot((i(\nu - \nu_i) - \Gamma/2)\cdot\mathbf{I} - \mathbf{W})^{-1}\cdot\mathbf{1}) \quad (1)$$

Probabilities of stochastic spin states which were defined by vector **P** components were taken to be equal. **I** was diagonal unit matrix and **1** is column vector with all components equal to unity. Tridiagonal matrix **W** defined transition probabilities between stochastic states. The transition probability from i to j state was given by matrix element $W_{ij}$ and the diagonal element $W_{ii} = -\sum_{j\neq i} W_{ij}$ [64].

The spin relaxation can be sufficiently well characterized by $Fe^{3+}$ spin states $S_z = \pm\frac{5}{2}; \pm\frac{3}{2}; \frac{1}{2}$ when sextets have splitting ratios of approximately 5:3:1 [63]. Positions of the lines of sextets corresponding to the hyperfine field of 50.5 T and $S_z$ values are shown in Fig. 8. The probability corresponding to $S_z - S_z \pm 1$ transition is $W_{S_zS_z\pm1} = (S(S+1) - S_z(S_z \pm 1)) \cdot R$ where $R$ is relaxation rate. With increase in relaxation rate in the range of $10^7$–$10^{10}$ $s^{-1}$ the shape of Mössbauer spectrum lines changes causing rise of intensity at the center of spectrum.

As observed, smaller part of Mössbauer spectra, up to 19% of all area (see Table 2), can be attributed to Fe spins, which relax with slower rates in comparison to Mössbauer spectroscopy sensitivity limit ($R < 10^7$ $s^{-1}$) and gives expressed hyperfine magnetic structure of spectra attributable to $S_z$ states. The clearly observed sextet with hyperfine field $B_h \approx 50$ T is attributed to $S_z = \pm\frac{5}{2}$. The isomer shift $\delta \approx 0.4$ mm/s relatively to α-Fe is characteristic of $Fe^{3+}$. Spin-spin relaxation is explained by cross relaxation processes [63] when the increase in Zeeman and crystal field energies of one spin is accompanied by almost equal decrease in energy of another spin. The results obtained by fitting Mössbauer spectra (see Table 2) indicate that the application of magnetic field of 0.42 T causes considerable decrease in relaxation rate $R$. It can be noted that applied magnetic field determines changes in energy related to spin states depending on the magnetic field direction relatively to the main axis of crystal field.

In β-TCP crystal structure $Fe^{3+}$ ions substitute Ca ones [56] while in Fe-doped hydroxyapatite the differently coordinated $Fe^{3+}$ interstitial sites can be found to be located in the hexagonal channel [55]. Mössbauer spectra of hydroxyapatite consist of doublets and hyperfine magnetic structure is not observed at Fe content as low as in $Ca_{10}Fe_{0.15}(PO_4)_6(OH)_{1.55}O_{0.45}$. However, relaxation rate should depend on local Fe concentrations. Properties of Fe sites are also possibly important determining rates of spin-spin and spin-lattice relaxations.

SEM was employed in order to investigate influence of foreign ions and their concentration on morphological features of β-TCP samples. SEM micrographs of pristine β-TCP powders and powders substituted with the highest amount of Fe and Zn are shown in Fig. 9 as representative. It is seen that non-substituted β-TCP powders consist of mostly uniform particles of irregular shape, which are highly connected to each other and form porous aggregates. The grain size varies from approximately 200 to 500 nm. Substitution with Fe and Zn does not change porous nature of the aggregated powders, however it obviously affects the grain size, which was reduced significantly. The observed particles showed prolonged irregular shape with thickness of around 150–200 nm and length up to 1 μm.

In order to determine toxicity of the synthesized products, *in vivo* cytotoxicity assay was performed in solutions containing 1 wt% of β-TCP powders using zebrafish embryos. Digital photographs of zebrafish embryos taken at different time of presence in TCP-containing solutions are demonstrated in Fig. 10. Evidently, embryos grown in different media visually do not differ from control zebrafish embryos, there are no visible hybridizations or anomalies caused by interaction with pristine or co-substituted β-TCP. Detailed data on hatching rate, survival rate and body length of zebrafish embryos grown in solutions with β-TCP powders for 72 h are summarized in Table 3. It is seen that hatching and survival rate for all samples vary in the range of 80 to 100%, which is very close to the values obtained for control species, which are 90% for both parameters. Moreover, there are no trends which could be associated with amount of Fe and Zn in investigated

**Table 2**
Parameters of fitting of Mössbauer spectra measured at temperature $T$ and applied magnetic field $B_{appl}$. $R$ is relaxation rate, $S$ is relative area of spectrum attributed to slow relaxation ($R = 0$). $\delta$ is isomer shift relatively to α-Fe, $2\varepsilon$ is quadrupole shift and $B_h$ is hyperfine field.

| Sample | $T$, K | $B_{appl}$, T | $R$, $10^8$ $s^{-1}$ | $S$,% ± 1 | $\delta$, mm/s | $B_h$, T | $2\varepsilon$, mm/s |
|---|---|---|---|---|---|---|---|
| 5:5% Fe:Zn | 11 | 0 | 2.7 ± 0.4 | 19 | 0.41 ± 0.03 | 51.6 ± 0.7 | 0.13 ± 0.1 |
| 5:5% Fe:Zn | 296 | 0 | 2.9 ± 0.3 | 19 | 0.52 ± 0.03 | 50.8 ± 0.3 | 0.08 ± 0.06 |
| 5:5% Fe:Zn | 296 | 0.42 | 1.14 ± 0.15 | 15 | 0.40 ± 0.04 | 50.5* | 0.0* |
| 4:4% Fe:Zn | 296 | 0.42 | 0.73 ± 0.15 | 19 | 0.44 ± 0.03 | 52.0 ± 0.03 | 0.07 ± 0.04 |
| 3:3% Fe:Zn | 296 | 0 | 2.3 ± 0.3 | 4 | 0.45 ± 0.05 | 50.5* | 0.0* |
| 3:3% Fe:Zn | 296 | 0.42 | 0.46 ± 0.09 | 13 | 0.49 ± 0.1 | 48.6 ± 1.6 | −0.08 ± 0.08 |
| 2:2% Fe:Zn | 296 | 0.42 | 0.33 ± 0.06 | 11 | 0.38 ± 0.05 | 50.5* | 0.0* |
| 1:1% Fe:Zn | 296 | 0.42 | 0.51 | 16 | 0.38* | 50.5* | 0.0* |

*Fixed value.

samples. On the other hand, there is a visible trend in the body length of the embryos. With the only exception for β-TCP with 1 mol% of Fe and Zn, mean values of the body length of the embryos monotonically increases as a concentration of foreign ions in β-TCP powders increases and exceeds body length of control embryos. Such behavior of zebrafish embryos in TCP-containing media together with an absence of visible anomalies indicate non-toxic nature of the synthesized powders.

Fig. 11 shows concentrations of Fe and Zn ions released to SBF solution from β-TCP powders after soaking for 72 h. It is evident that concentration of foreign ions depends on chemical composition of powders and samples with higher content of Fe and Zn released higher amount of these ions. However, co-substituents show different behavior. For the samples with low substitution level (< 3 mol%) determined concentrations of both metals were very similar (even after recalculating to molar concentrations). On the other hand, for powders with high substitution level an increase of concentration of Fe stayed nearly linear, whereas concentration of Zn increased drastically. In this way, maximal concentration of Zn was determined to be 0.45 mg/L, whereas for Fe it reached only 0.1 mg/L.

All synthesized β-TCP powders were pressed into pellets and sintered in order to prepare ceramic bodies. The XRD patterns of the sintered pellets are shown in Fig. S3. After sintering procedure analyzed samples remained single-phase β-TCP and no additional phases such as high-temperature α-TCP polymorph were observed. Reflection peaks became sharper indicating higher crystallinity and grain growth in ceramic discs in comparison to powders. Fig. 12 represents SEM images of polished and thermally etched surface of pristine β-TCP pellet and β-TCP pellet substituted with 5 mol% of Fe and Zn. Surface of pure β-TCP pellet is composed of the grains varying in size in the range of approximately 1.5 to 7 μm. No cracks, holes or other clearly visible defects were observed. Substitution with foreign ions did not suppress or promote grain growth, which remained nearly the same in terms of size. Unfortunately, the highest substitution level resulted in formation of some visible cracks, moreover some deposits were observed in the grain boundaries. Such observations suggest that sintering procedure needs to be optimized further. Linear shrinkage, densities and Vickers hardness of sintered β-TCP pellets are given in Table 4.

It was observed, that linear shrinkage of the sintered pellets did not correlate with substitution level. Linear shrinkage was determined to be the highest for powders with 5 mol% of foreign ions and the lowest for powders with 2 mol% of Fe and Zn. Calculated relative densities of the sintered species also did not reveal any trends and varied in the range from 90 to 98% with the highest value for pellets with the highest substitution level. Vickers hardness measurements did not reveal improvement in mechanical properties of the prepared ceramics induced by substitution of Ca ions. Determined average Vickers hardness ranged from 1.81 to 4.05 GPa, however the highest value was observed for pristine β-TCP ceramics and was in good agreement with previously reported values [66–69]. The obtained results indicate, that while partial substitution of Ca with Fe and Zn resulted in phase pure, non-toxic and magnetic powders, this approach did not lead to superior mechanical properties.

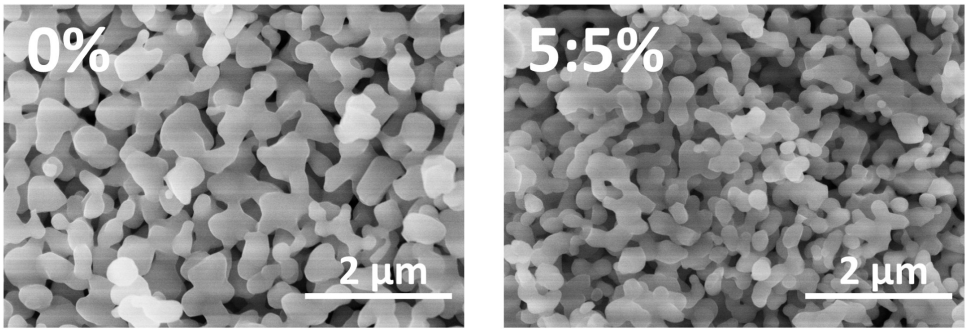


**Fig. 9.** SEM images of pristine TCP and TCP powders co-substituted with 5 mol% of Fe and Zn.

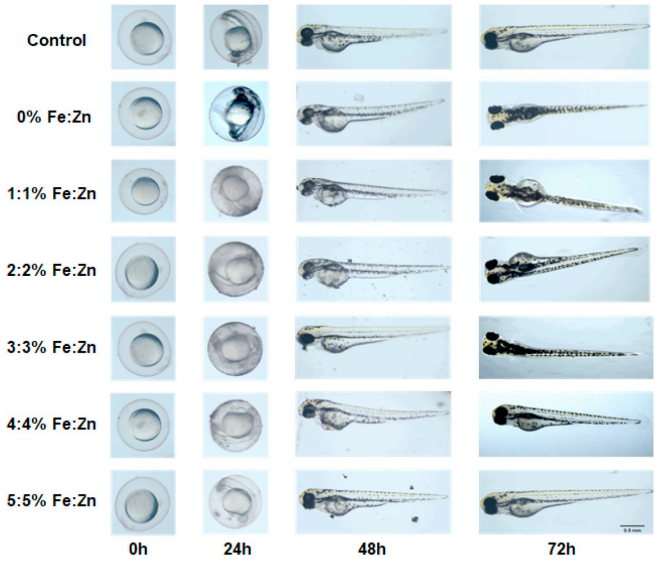


**Fig. 10.** Digital photographs of zebrafish embryos at different stages of growth in solutions containing TCP powders with different amounts of Fe and Zn.

**Table 3**
Hatching rate, survival rate and body length of zebrafish embryos grown in solutions containing TCP powders for 72 h ($N$ = 10).

| Sample | Hatching rate (%) | Survival RATE (%) | Body length (mm) |
|---|---|---|---|
| E3 Medium* | 90 | 90 | 3.26 ± 0.21 |
| 0% Fe:Zn | 80 | 80 | 3.42 ± 0.24 |
| 1:1% Fe:Zn | 90 | 90 | 3.27 ± 0.42 |
| 2:2% Fe: Zn | 80 | 80 | 3.50 ± 0.27 |
| 3:3% Fe: Zn | 100 | 100 | 3.55 ± 0.24 |
| 4:4% Fe: Zn | 90 | 90 | 3.55 ± 0.13 |
| 5:5% Fe:Zn | 100 | 90 | 3.61 ± 0.17 |

*E3 medium (5 mM NaCl, 0.17 mM KCl, 0.33 mM $CaCl_2$, 0.33 mM $MgSO_4$, and 0.1% ($w/v$) methylene blue) for Zebrafish embryos.

## 4. Conclusions

Series of β-TCP powders co-substituted with equal amounts of $Fe^{3+}$ and $Zn^{2+}$ ions in the range of 1–5 mol% have been successfully synthesized by simple and reliable co-precipitation method. Structural analysis revealed gradual decrease in lattice parameters of the synthesized samples with increase of substitution level. XRD and EPR studies showed that both foreign ions preferably occupy octahedral Ca(5) site and Ca(4) at the highest substitution level. Raman spectroscopy confirmed lattice distortion of co-substituted samples by gradual change in shape of the obtained spectra. All substituted samples exhibited paramagnetic behavior, magnetization values were found to be proportional to Fe percentage in the synthesized powders. *In vivo* cytotoxicity assay did not reveal toxic behavior of the synthesized powders even with the highest content of foreign ions. Mechanical properties of sintered β-TCP pellets were not improved by substitution of Ca by foreign ions. Vickers hardness values were determined to be lower for substituted samples in comparison to those of pristine β-TCP ceramics. The dual-substituted ($Fe^{3+}$ and $Zn^{2+}$) TCP bioceramics could play significant role in biomedical applications and could be considered to be an effective material for bone tissue regeneration applications.

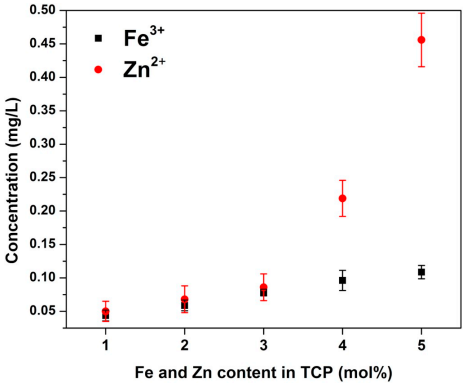


**Fig. 11.** Concentrations of Fe and Zn ions in SBF solution after soaking of TCP powders with different amounts of Fe and Zn for 72 h.

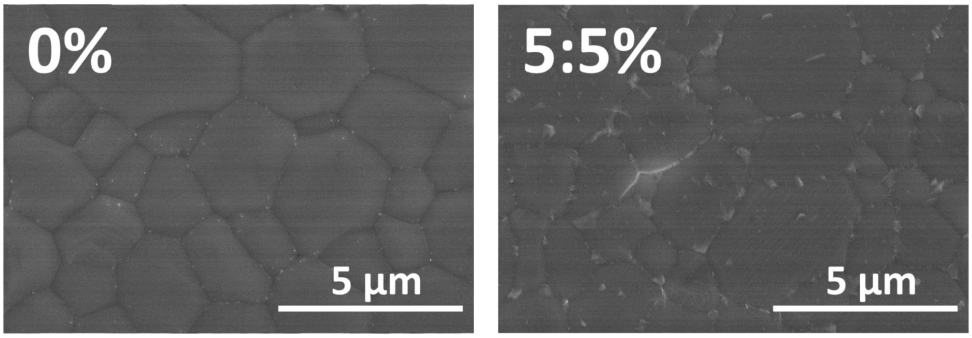


**Fig. 12.** SEM images of polished and thermally etched surface of pristine TCP pellet and sample co-substituted with 5 mol% of Fe and Zn and sintered at 1100 °C.

**Table 4**
Linear shrinkage, density and Vickers hardness of TCP ceramics.

| Sample | Linear shrinkage (%) | Density (%) | Vickers hardness (GPa) |
|---|---|---|---|
| 0% Fe:Zn | 13 | 95 | 4.05 ± 0.27 |
| 1:1% Fe:Zn | 11 | 91 | 3.08 ± 0.18 |
| 2:2% Fe: Zn | 8 | 90 | 1.82 ± 0.05 |
| 3:3% Fe: Zn | 14 | 92 | 2.66 ± 0.06 |
| 4:4% Fe: Zn | 15 | 98 | 2.87 ± 0.11 |
| 5:5% Fe:Zn | 16 | 98 | 2.60 ± 0.06 |

## CRediT authorship contribution statement

**Lauryna Sinusaite:** Investigation, Writing - original draft, Visualization. **Anton Popov:** Investigation, Formal analysis. **Andris Antuzevics:** Investigation, Formal analysis, Visualization. **Kestutis Mazeika:** Formal analysis, Visualization. **Dalis Baltrunas:** Investigation, Visualization. **Jen-Chang Yang:** Methodology, Resources, Validation. **Jiun Lin Horng:** Formal analysis, Resources. **Shengfang Shi:** Investigation, Formal analysis. **Tohru Sekino:** Methodology, Resources, Supervision. **Kunio Ishikawa:** Formal analysis, Resources. **Aivaras Kareiva:** Conceptualization, Resources, Funding acquisition. **Aleksej Zarkov:** Conceptualization, Methodology, Writing - review & editing, Supervision, Project administration.

## Declaration of competing interest

The authors declare that they have no known competing financial interests or personal relationships that could have appeared to influence the work reported in this paper.

## Acknowledgements

This project has received funding from European Social Fund (project No. 09.3.3.-LMT-K-712-16-0157) under grant agreement with the Research Council of Lithuania (LMTLT). AK would like to express sincere gratitude for Fellowship administrated by The Japan Society for the Promotion of Science (JSPS). Fellow's ID No.: L12546. The World Federation of Scientists is highly acknowledged for the National Scholarship to AZ. Authors are grateful to R. Vargalis (Vilnius University) for taking SEM images.

## Appendix A. Supplementary data

Supplementary data to this article can be found online at https://doi.org/10.1016/j.msec.2020.110918.

## References

[1] W. Habraken, P. Habibovic, M. Epple, M. Bohner, Calcium phosphates in biomedical applications: materials for the future? Mater. Today 19 (2016) 69–87.
[2] E.A. Chudinova, M.A. Surmeneva, A.S. Timin, T.E. Karpov, A. Wittmar, M. Ulbricht, A. Ivanova, K. Loza, O. Prymak, A. Koptyug, M. Epple, R.A. Surmenev, Adhesion, proliferation, and osteogenic differentiation of human mesenchymal stem cells on additively manufactured Ti6Al4V alloy scaffolds modified with calcium phosphate nanoparticles, Colloids Surf. B Biointerfaces 176 (2019) 130–139.
[3] S.V. Dorozhkin, Calcium orthophosphate-based bioceramics, Materials 6 (2013) 3840–3942.
[4] R.G. Carrodeguas, S. De Aza, α-Tricalcium phosphate: synthesis, properties and biomedical applications, Acta Biomater. 7 (2011) 3536–3546.
[5] S.V. Dorozhkin, M. Epple, Biological and medical significance of calcium phosphates, Angew. Chem. 41 (2002) 3130–3146.
[6] M. Ebrahimi, M.G. Botelho, S.V. Dorozhkin, Biphasic calcium phosphates bioceramics (HA/TCP): concept, physicochemical properties and the impact of standardization of study protocols in biomaterials research, Mater. Sci. Eng. C 71 (2017) 1293–1312.
[7] E. Boanini, M. Gazzano, A. Bigi, Ionic substitutions in calcium phosphates synthesized at low temperature, Acta Biomater. 6 (2010) 1882–1894.
[8] B. Yilmaz, A.Z. Alshemary, Z. Evis, Co-doped hydroxyapatites as potential materials for biomedical applications, Microchem. J. 144 (2019) 443–453.
[9] J.T.B. Ratnayake, M. Mucalo, G.J. Dias, Substituted hydroxyapatites for bone regeneration: a review of current trends, J Biomed Mater Res B Appl Biomater 105 (2017) 1285–1299.
[10] T. Tite, A.-C. Popa, L.M. Balescu, I.M. Bogdan, I. Pasuk, J.M.F. Ferreira, G.E. Stan, Cationic substitutions in hydroxyapatite: current status of the derived biofunctional effects and their in vitro interrogation methods, Materials 11 (2018) 2081.
[11] M. Šupová, Substituted hydroxyapatites for biomedical applications: a review, Ceram. Int. 41 (2015) 9203–9231.
[12] C. Qi, J. Lin, L.H. Fu, P. Huang, Calcium-based biomaterials for diagnosis, treatment, and theranostics, Chem. Soc. Rev. 47 (2018) 357–403.
[13] S. Sprio, L. Preti, M. Montesi, S. Panseri, A. Adamiano, A. Vandini, N.M. Pugno, A. Tampieri, Surface phenomena enhancing the antibacterial and osteogenic ability of nanocrystalline hydroxyapatite, activated by multiple-ion doping, ACS Biomater. Sci. Eng. 5 (2019) 5947–5959.
[14] A. Rajendran, S. Balakrishnan, R. Kulandaivelu, S.N.T.S. Nellaiappan, Multi-element substituted hydroxyapatites: synthesis, structural characteristics and evaluation of their bioactivity, cell viability, and antibacterial activity, J. Sol-Gel Sci. Technol. 86 (2018) 441–458.
[15] L. Sundarabharathi, M. Chinnaswamy, D. Ponnamma, H. Parangusan, M.A.A. Al-Maadeed, Investigation of antimicrobial properties and in-vitro bioactivity of $Ce^{3+}$-$Sr^{2+}$ dual-substituted nano hydroxyapatites, J. Am. Ceram. Soc. 102 (2019) 144–157.
[16] A. Ballardini, M. Montesi, S. Panseri, A. Vandini, P.G. Balboni, A. Tampieri, S. Sprio, New hydroxyapatite nanophases with enhanced osteogenic and anti-bacterial activity, J. Biomed. Mater. Res. A 106 (2018) 521–530.
[17] N. Abbaspour, R. Hurrell, R. Kelishadi, Review on iron and its importance for

human health, J. Res. Med. Sci. 19 (2014) 164–174.
[18] R. Morrissey, L.M. Rodríguez-Lorenzo, K.A. Gross, Influence of ferrous iron incorporation on the structure of hydroxyapatite, J. Mater. Sci. Mater. Med. 16 (2005) 387–392.
[19] A. Adamiano, M. Iafisco, M. Sandri, M. Basini, P. Arosio, T. Canu, G. Sitia, A. Esposito, V. Iannotti, G. Ausanio, E. Fragogeorgi, M. Rouchota, G. Loudos, A. Lascialfari, A. Tampieri, On the use of superparamagnetic hydroxyapatite nanoparticles as an agent for magnetic and nuclear in vivo imaging, Acta Biomater. 73 (2018) 458–469.
[20] A. Adamiano, V.M. Wu, F. Carella, G. Lamura, F. Canepa, A. Tampieri, M. Iafisco, V. Uskokovic, Magnetic calcium phosphates nanocomposites for the intracellular hyperthermia of cancers of bone and brain, Nanomedicine 14 (2019) 1267–1289.
[21] A. Marrella, M. Iafisco, A. Adamiano, S. Rossi, M. Aiello, M. Barandalla-Sobrados, P. Carullo, M. Miragoli, A. Tampieri, S. Scaglione, D. Catalucci, A combined low-frequency electromagnetic and fluidic stimulation for a controlled drug release from superparamagnetic calcium phosphate nanoparticles: potential application for cardiovascular diseases, J. R. Soc. Interface 15 (2018) 11.
[22] Y. Cherasse, Y. Urade, Dietary zinc acts as a sleep modulator, Int. J. Mol. Sci. 18 (2017) 2334.
[23] E.S. Thian, T. Konishi, Y. Kawanobe, P.N. Lim, C. Choong, B. Ho, M. Aizawa, Zinc-substituted hydroxyapatite: a biomaterial with enhanced bioactivity and antibacterial properties, J. Mater. Sci. Mater. Med. 24 (2013) 437–445.
[24] V. Graziani, M. Fosca, A.A. Egorov, Y.V. Zobkov, A.Y. Fedotov, A.E. Baranchikov, M. Ortenzi, R. Caminiti, V.S. Komlev, J.V. Rau, Zinc-releasing calcium phosphate cements for bone substitute materials, Ceram. Int. 42 (2016) 17310–17316.
[25] A. Turlybekuly, A.D. Pogrebnjak, L.F. Sukhodub, L.B. Sukhodub, A.S. Kistaubayeva, I.S. Savitskaya, D.H. Shokatayeva, O.V. Bondar, Z.K. Shaimardanov, S.V. Plotnikov, B.H. Shaimardanova, I. Digel, Synthesis, characterization, in vitro biocompatibility and antibacterial properties study of nanocomposite materials based on hydroxyapatite-biphasic ZnO micro- and nanoparticles embedded in Alginate matrix, Mater. Sci. Eng. C 104 (2019) 109965.
[26] F.N.S. Raja, T. Worthington, M.A. Isaacs, K.S. Rana, R.A. Martin, The antimicrobial efficacy of zinc doped phosphate-based glass for treating catheter associated urinary tract infections, Mater. Sci. Eng. C 103 (2019) 109868.
[27] L. Robinson, K. Salma-Ancane, L. Stipniece, B.J. Meenan, A.R. Boyd, The deposition of strontium and zinc Co-substituted hydroxyapatite coatings, J. Mater. Sci. Mater. Med. 28 (2017) 51.
[28] N. Lowry, M. Brolly, Y. Han, S. McKillop, B.J. Meenan, A.R. Boyd, Synthesis and characterisation of nanophase hydroxyapatite co-substituted with strontium and zinc, Ceram. Int. 44 (2018) 7761–7770.
[29] N. Matsumoto, K. Sato, K. Yoshida, K. Hashimoto, Y. Toda, Preparation and characterization of β-tricalcium phosphate co-doped with monovalent and divalent antibacterial metal ions, Acta Biomater. 5 (2009) 3157–3164.
[30] D. Xiao, F. Yang, Q. Zhao, S. Chen, F. Shi, X. Xiang, L. Deng, X. Sun, J. Weng, G. Feng, Fabrication of a Cu/Zn co-incorporated calcium phosphate scaffold-derived GDF-5 sustained release system with enhanced angiogenesis and osteogenesis properties, RSC Adv. 8 (2018) 29526–29534.
[31] I. Ullah, W. Li, S. Lei, Y. Zhang, W. Zhang, U. Farooq, S. Ullah, M.W. Ullah, X. Zhang, Simultaneous co-substitution of $Sr^{2+}$/$Fe^{3+}$ in hydroxyapatite nanoparticles for potential biomedical applications, Ceram. Int. 44 (2018) 21338–21348.
[32] S. Basu, A. Ghosh, A. Barui, B. Basu, (Fe/Sr) Codoped biphasic calcium phosphate with tailored osteoblast cell functionality, ACS Biomater. Sci. Eng. 4 (2018) 857–871.
[33] W. Pon-On, S. Meejoo, I.M. Tang, Substitution of manganese and iron into hydroxyapatite: core/shell nanoparticles, Mater. Res. Bull. 43 (2008) 2137–2144.
[34] M. Vlasova, A. Fedotov, I. Mendoza Torrez, M. Kakazey, V. Komlev, P.A. Marquez Aguilar, Mechanosynthesis of hydroxyapatite–ferrite composite nanopowder, Ceram. Int. 43 (2017) 6221–6231.
[35] R. Singh, M. Srivastava, N.K. Prasad, S. Awasthi, A. Kumar Dhayalan, S. Kannan, Structural analysis and magnetic induced hyperthermia of $Fe^{3+}$ and $Mn^{2+}$ substituted β-$Ca_3(PO_4)_2$, New J. Chem. 41 (2017) 12879–12891.
[36] P. Baskaran, A. Udduttula, V. Uthirapathy, Development and characterisation of novel Ce-doped hydroxyapatite–$Fe_2O_4$ nanocomposites and their in vitro biological evaluations for biomedical applications, IET Nanobiotechnology (2018) 138–146.
[37] T. Kokubo, H. Takadama, How useful is SBF in predicting in vivo bone bioactivity? Biomaterials 27 (2006) 2907–2915.
[38] Legislation for the protection of animals used for scientific purposes, https://eur-lex.europa.eu/legal-content/EN/TXT/?uri=CELEX:32010L0063 Accessed 26 November 2019.
[39] R.D. Shannon, Revised effective ionic radii and systematic studies of interatomic distances in halides and chalcogenides, Acta Crystallogr. A 32 (1976) 751–767.
[40] C. Mellier, F. Fayon, V. Schnitzler, P. Deniard, M. Allix, S. Quillard, D. Massiot, J.-M. Bouler, B. Bujoli, P. Janvier, Characterization and properties of novel gallium-doped calcium phosphate ceramics, Inorg. Chem. 50 (2011) 8252–8260.
[41] G. Renaudin, S. Gomes, J.-M. Nedelec, First-row transition metal doping in calcium phosphate bioceramics: a detailed crystallographic study, Materials 10 (2017) 92.
[42] K. Matsunaga, T. Kubota, K. Toyoura, A. Nakamura, First-principles calculations of divalent substitution of $Ca^{2+}$ in tricalcium phosphates, Acta Biomater. 23 (2015) 329–337.
[43] R.K. Singh, M. Srivastava, N.K. Prasad, S. Awasthi, A. Dhayalan, S. Kannan, Iron doped β-Tricalcium phosphate: synthesis, characterization, hyperthermia effect, biocompatibility and mechanical evaluation, Mater. Sci. Eng. C 78 (2017) 715–726.
[44] A. Bigi, E. Foresti, M. Gandolfi, M. Gazzano, N. Roveri, Isomorphous substitutions in β-tricalcium phosphate: the different effects of zinc and strontium, J. Inorg. Biochem. 66 (1997) 259–265.
[45] A. Jillavenkatesa, R.A. Condrate, The infrared and raman spectra of β-and α-tricalcium phosphate ($Ca_3(PO_4)_2$), Spectrosc. Lett. 31 (1998) 1619–1634.
[46] P.N. de Aza, C. Santos, A. Pazo, S. de Aza, R. Cuscó, L. Artús, Vibrational properties of calcium phosphate compounds. 1. Raman spectrum of β-tricalcium phosphate, Chem. Mater. 9 (1997) 912–915.
[47] P.M.C. Torres, J.C.C. Abrantes, A. Kaushal, S. Pina, N. Döbelin, M. Bohner, J.M.F. Ferreira, Influence of Mg-doping, calcium pyrophosphate impurities and cooling rate on the allotropic α↔β-tricalcium phosphate phase transformations, J. Eur. Ceram. Soc. 36 (2016) 817–827.
[48] L. Sinusaite, I. Grigoraviciute-Puroniene, A. Popov, K. Ishikawa, A. Kareiva, A. Zarkov, Controllable synthesis of tricalcium phosphate (TCP) polymorphs by wet precipitation: effect of washing procedure, Ceram. Int. 45 (2019) 12423–12428.
[49] B.C. Cornilsen, R.A. Condrate, The vibratonal spectra of β-$Ca_2P_2O_7$ and γ-$Ca_2P_2O_7$, J. Inorg. Nucl. Chem. 41 (1979) 602–605.
[50] L. Sinusaite, A.M. Renner, M.B. Schuetz, A. Antuzevics, U. Rogulis, I. Grigoraviciute-Puroniene, S. Mathur, A. Zarkov, Effect of Mn doping on the low-temperature synthesis of tricalcium phosphate (TCP) polymorphs, J. Eur. Ceram. Soc. 39 (2019) 3257–3263.
[51] C. Stahli, J. Thuring, L. Galea, S. Tadier, M. Bohner, N. Dobelin, Hydrogen-substituted β-tricalcium phosphate synthesized in organic media, Acta Crystallogr. Sect. B 72 (2016) 875–884.
[52] A. Abragam, B. Bleaney, Electron Paramagnetic Resonance of Transition Ions, Clarendon Press, Oxford, UK, 1970.
[53] J.A. Weil, J.R. Bolton, Electron Paramagnetic Resonance, Wiley, 2007.
[54] G. Morin, D. Bonnin, Modeling EPR powder spectra using numerical diagonalization of the spin hamiltonian, J. Magn. Reson. 136 (1999) 176–199.
[55] S. Gomes, A. Kaur, J.M. Greneche, J.M. Nedelec, G. Renaudin, Atomic scale modeling of iron-doped biphasic calcium phosphate bioceramics, Acta Biomater. 50 (2017) 78–88.
[56] G. Renaudin, S. Gomes, J.M. Nedelec, First-row transition metal doping in calcium phosphate bioceramics: a detailed crystallographic study, Materials 10 (2017) 92.
[57] A.M. Bishay, L. Makar, Role of iron in calcium phosphate glasses, J. Am. Ceram. Soc. 52 (1969) 605–609.
[58] I. Ardelean, C. Andronache, C. Cimpean, P. Pascuta, EPR and magnetic investigation of calcium-phosphate glasses containing iron ions, J. Optoelectron. Adv. Mater. 8 (2006) 1372–1376.
[59] J. Kliava, EPR of impurity ions in disordered solids distributions of the spin hamiltonian parameters, Phys. Status Solidi B 134 (1986) 411–455.
[60] S.Y. Park, S.K.M. Perikamana, J.H. Park, S.W. Kim, H. Shin, S.P. Park, H.S. Jung, Osteoinductive superparamagnetic Fe nanocrystal/calcium phosphate heterostructured microspheres, Nanoscale 9 (2017) 19145–19153.
[61] T. Ates, S.V. Dorozhkin, O. Kaygili, M. Kom, I. Ercan, N. Bulut, F. Firdolas, S. Keser, N.C. Gursoy, I.H. Ozercan, Y. Eroksuz, T. Ince, The effects of Mn and/or Ni dopants on the in vitro/in vivo performance, structural and magnetic properties of β-tricalcium phosphate bioceramics, Ceram. Int. 45 (2019) 22752–22758.
[62] M.E. Zilm, L. Yu, W.A. Hines, M. Wei, Magnetic properties and cytocompatibility of transition-metal-incorporated hydroxyapatite, Mater. Sci. Eng. C 87 (2018) 112–119.
[63] A. Vertes, D.L. Nagy, Mössbauer Spectroscopy of Frozen Solutions, Akadémiai Kiadó, Budapest, 1990.
[64] D.H. Jones, K.K.P. Srivastava, Many-state relaxation model for the M″ossbauer spectra of superparamagnets, Phys. Rev. B 34 (1986) 7542–7548.
[65] M.A. Chuev, Multi-level relaxation model for describing the Mossbauer spectra of single-domain particles in the presence of quadrupolar hyperfine interaction, J. Phys.-Condes. Matter 23 (2011) 11.
[66] A. Tricoteaux, E. Rguiti, D. Chicot, L. Boilet, M. Descamps, A. Leriche, J. Lesage, Influence of porosity on the mechanical properties of microporous β-TCP bioceramics by usual and instrumented Vickers microindentation, J. Eur. Ceram. Soc. 31 (2011) 1361–1369.
[67] C. Shuai, P. Feng, L. Zhang, C. Gao, H. Hu, S. Peng, A. Min, Correlation between properties and microstructure of laser sintered porous β-tricalcium phosphate bone scaffolds, Sci. Technol. Adv. Mat. 14 (2013) 055002.
[68] R. Ghosh, R. Sarkar, Synthesis and characterization of sintered beta-tricalcium phosphate: a comparative study on the effect of preparation route, Mater. Sci. Eng. C 67 (2016) 345–352.
[69] M. Trabelsi, I. AlShahrani, H. Algarni, F. Ben Ayed, E.S. Yousef, Mechanical and tribological properties of the tricalcium phosphate - magnesium oxide composites, Mater. Sci. Eng. C 96 (2019) 716–729.

Vilnius University Press
9 Saulėtekio Ave., Building III, LT-10222 Vilnius
Email: info@leidykla.vu.lt, www.leidykla.vu.lt
Print run copies 20